Final Report

Federal Agency & Organization: Department of Energy – Bioenergy Technologies Office
Project Title: Poly(oxymethylene) Ethers as a High Cetane, Low Sooting Biofuel Blendstock for Use in Medium to Heavy Duty Mixing Controlled Compression Ignition Engines
Award Number: DE- EE0008726

Recipient Organization: Colorado State University
Principal Investigator: Bret Windom

Reporting Period: June 1, 2019 to October 31, 2023
Date of Report: December 31, 2023

Acknowledgment: This material is based upon work supported by the U.S. Department of Energy's Office of Energy Efficiency and Renewable Energy (EERE) under the Bioenergy Technologies Office Award Number DE-EE0008726.

Contents

Abstract/Executive Summary

Compression ignition (CI) engines are currently the most common prime mover for medium and heavy duty vehicles; these engines contribute roughly a quarter of US greenhouse gas emissions from transportation, and even higher percentages of particulate and nitrogen oxide emissions. As a result, there have been significant efforts made to reduce these emissions, particularly through selection of low-emissions alternative fuels. Oxymethylene ethers (OMEs) are a class of molecule, typically structured R-O-(CH2O)n-R', which have been considered as a possible blendstock in CI fuels for the goal of soot reduction. Generally, past work has focused on methyl-terminated OMEs, CH3-O-(CH2O)n-CH3, which by virtue of containing no C--C bonds, produce negligible soot. These molecules show significant reductions in soot emission from engines when blended in moderate to high ratios with traditional diesels, however, they have been shown to have inferior physical properties and poor compatibility with some legacy systems. Recent theoretical work has shown that OMEs with non-methyl alkyl groups may have superior performance, albeit at the cost of increased soot formation. In this work, a variety of OMEs with terminating alkyl groups from methyl to butyl are considered for their suitability as CI fuels. The synthesis of these extended OMEs is studied, including formation of n=1 OMEs from common chemical sources, and extension of the chain length to heavier molecules, via reactions over acidic ion exchange resins. Following the synthesis, the properties of these OMEs are studied with respect to their engine applicability. It is found that heavier (propyl- and butyl-terminated) OMEs have superior properties for diesel compatibility, particularly in reactivity, volatility, and water solubility. Extended-alkyl OMEs are found to have higher soot production than methyl-terminated OMEs, but remain superior to diesel soot production on a per-unit-energy basis. A sample of a butyl-terminated OME mixture, n=2-4, is selected as the ideal OME blend for close compatibility with legacy diesel systems. This mixture is blended with certified diesel and tested for ASTM D975 compatibility, passing all required tests but lubricity; decreased heat of combustion is observed but not governed by the diesel standard. Fundamental combustion tests of various mid-weight OMEs are performed in a rapid compression machine, where it is shown that low-temperature chemistry causes a region of decreased dependence of ignition delay on temperature, consistent with methyl-terminated OME behavior. An isopropyl-terminated OME is observed to have low reactivity compared to other OMEs; this fuel is investigated via further rapid compression machine testing and CFR engine testing. It is found that this OME has strong negative-temperature-coefficient ignition behavior - a first for OMEs - and has reactivity lower than other OMEs, but insufficient for direct spark ignition engine testing.

Chapter 1- Background/Introduction

Mixing Controlled Compression Ignition (MCCI) engines which make up the majority of the heavy duty and medium duty market share experience a NOx/PM tradeoff, such that it is difficult to through engine calibration to suppress both criteria emissions without aftertreatment systems. Fuel chemistries that give low NOx and/or PM over a wide operating range would be ideal for maximizing fuel efficiency. MCCI by definition generates a combustion environment that is highly susceptible to particulate matter (PM) and/or NO_x formation, especially when petroleum-based fuels are used. As such, current MCCI engines require costly and energy-intensive exhaust aftertreatment units that demand regular maintenance to comply with vehicle certification requirements. Oxygenated biofuel species, when blended with a petro-diesel, have the ability to reduce in-cylinder soot formation within MCCI engines by altering kinetic pathways, diluting soot forming hydrocarbon species, and enhancing fuel-air mixing. Furthermore, many oxygenated species derived from bio-feedstocks offer kinetic pathways that can improve the ignition characteristics important for optimal MCCI operation relative to their petroleum counterparts. Ultimately, there is a need to understand and forecast, based on the structure of the biofuel molecule, fuel ignition tendencies and propensity to form PM, NO_x, and other undesirable emissions in MCCI engines. This ability to predict key performance and emission criteria will ultimately assist in selection of biofuels to power future high-efficiency, low-polluting engines.

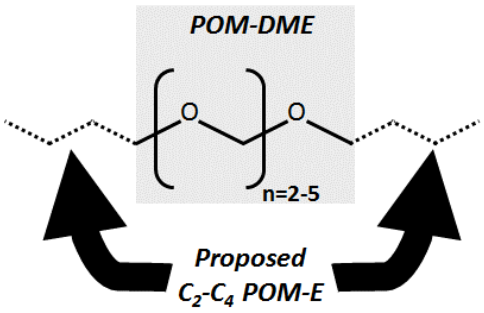

Figure. 1.1. Chemical structure of POM-DME and the proposed C_2 – C_4 POM-E.

Poly(oxymethylene) dimethyl ether (POM-DME, Fig. 1.1 - structure in shaded region) refers to a class of molecules with the general structure CH_3-O-$(CH_2O)_n$-CH_3, where n is the number of oxymethylene units. Among POM-DME oligomers, those with n = 2-5 have garnered interest as diesel blendstocks stemming from their favorable properties compared to conventional diesel fuel, including the ability to enhance cetane numbers (CN) while offering significant soot reduction potential (50% reduction at 20% blending)[1,2]. Although POM-DMEs perform well in these regards, they suffer from poor lower heating values (LHV), poor oxidative stability, and excessive water solubility, all of which arise from their high oxygen content and limit their suitability as an MCCI fuel blendstock. Poly(oxymethylene) ethers (POM-E) in which the terminating functional groups are increased to C_2-C_4 — illustrated in Fig. 1 by the addition of the dotted structures — offer a way to address the shortfalls that plague POM-DMEs, while still maintaining a high potential for soot reduction and favorable ignition characteristics. Furthermore, POM-Es can be produced from alcohols derived from lignocellulosic biomass so they can potentially achieve > 50% GHG reduction compared to conventional diesel and qualify as a renewable fuel.

The overarching objective of the proposed research program is to identify a biofuel blendstock that when blended with diesel fuel (at concentrations of 5-30% by volume) is able to enhance the combustion performance and reduce the emissions when utilized in a MCCI engine. ***The primary goal of the proposed project is to identify the soot reduction potential, cetane number enhancement, and physico-chemical properties of poly(oxymethylene) ethers and identify an optimal biofuel blendstock comprised of POM-Es that presents viable production pathways from lignocellulosic feedstocks and that enhances the performance and reduces criteria PM emissions of traditional MCCI fuels.*** To achieve this goal, the following four key project objectives are proposed:

1. Synthesize a variety of POM-E molecules and evaluate their physio-chemical properties applicable for MCCI operation.
2. Fundamentally understand synthesis pathways and the chemical mechanisms responsible for soot reduction and cetane enhancement in POM-E molecules, which is necessary to predict critical properties of various POM-E compounds and mixtures based on their molecular structure.
3. Understand synergistic and antagonistic blending properties between down selected POM-E candidates and diesel fuel and identification of POM-E blends with attractive fuel properties that have low-cost and sustainable conversion pathways.
4. Provide a comprehensive evaluation of POM-E/diesel fuel blends by way of fuel certification (ASTM D975) and medium duty MCCI engine testing.

The comprehensive work plan devised to carry out these objectives used a combined experimental and computational approach exploiting expertise at Colorado State University, University of Colorado – Boulder, and Yale University, while also leveraging the capabilities and know-how of Co-Optima laboratory partner, the National Renewable Energy Laboratory. Initial efforts focused on the synthesis of POM-E species with varying molecular structures for initial measurements aimed at understanding how variations in POM-E chemical structure impact the chemistry responsible for soot suppression and ignition. Speciation measurements from the μR-PIMS coupled with Yield Sooting Index (YSI) and ignition delay measurements for the variable POM-E structures were conducted and electronic structure theory calculations were carried out and used to develop combustion mechanisms that will enable the prediction of these important performance combustion criteria required for optimal MCCI operation. Critical physical property measurements, including LHV, oxidative stability, water solubility, and cold-flow properties, along with technoeconomic and life cycle analyses were carried out on the synthesized POM-E species (both neat and blended with certification petroleum diesel), which was critical information to down select POM-E blends with attractive fuel properties that have a low-cost conversion strategy to production. ASTM D975 fuel certification as well as engine testing was carried out on the down selected POM-E blends.

1.1. Nomenclature

Numerous shorthand, abbreviations, and symbols will be used throughout this text. A listing of these is provided in Table 1.1.

Table 1.1. List of symbols and abbreviations

Symbol / Abbreviation	Meaning
γ	Specific heat ratio
λ	Equivalence ratio
ν	Kinematic viscosity
ρ	Density
ACS	American Chemical Society
AFIDA	Advanced Fuel Ignition Delay Analyzer
ASTM	American Society for Testing and Materials
BP	Boiling Point
CFR	Cooperative Fuels Research
CI	Compression Ignition
CN	Cetane Number
Co-Optima	Co-Optimization of Fuels and Engines Initiative
CR	Compression Ratio
CSU	Colorado State University
CVCC	Constant Volume Combustion Chamber
DCN	Derived Cetane Number
DoD	United States Department of Defense
DoE	United States Department of Energy

Symbol / Abbreviation	Meaning
EC	Elemental Carbon
EGAI	End Gas Autoignition
FA	Formaldehyde
FIT	Fuel Ignition Tester
FP	Flash Point
GC-FID	Gas Chromatograph - Flame Ionization Detector
GHG	Greenhouse Gas
HHV	Higher Heating Value
ICE	Internal Combustion Engine
ICN	Indicated Cetane Number
IDT	Ignition Delay Time
KI	Knock Index
LHV	Lower Heating Value
MON	Motor Octane Number
NOx	Nitrogen Oxides
NREL	United States National Renewable Energy Laboratory
OC	Organic Carbon
OME	Oxymethylene Ether
ON	Octane Number
P-H	Pseudo-Homogeneous
PM	Particulate Matter
PRF	Primary Reference Fuel
RCM	Rapid Compression Machine
RON	Research Octane Number
SAF	Sustainable Aviation Fuel

Symbol / Abbreviation	Meaning
SI	Spark Ignition
THC	Total Hydrocarbons
TXN	1,3,5-Trioxane
ULSD	Ultra-Low-Sulfur Diesel
WS	Water Solubility
YSI	Yield Sooting Index

The fuels of primary interest in this thesis are Oxymethylene Ethers (OMEs). These OMEs will be referred to using the shorthand X-n-Y, where X and Y are abbreviations for the terminating alkyl groups (M = methyl, E = ethyl, P = propyl, B = butyl, iP = iso-propyl, and iB = iso-butyl), and n is the number of oxymethylene units in the molecule (note that the number of oxygen atoms will be n+1). An example structure, for B-2-B, is provided in Figure 1.1. This shows a linear OME with symmetric end groups, however, some OMEs studies have assymetric end groups (e.g. M-1-B) or have branched structures (e.g. iP-1-iP).

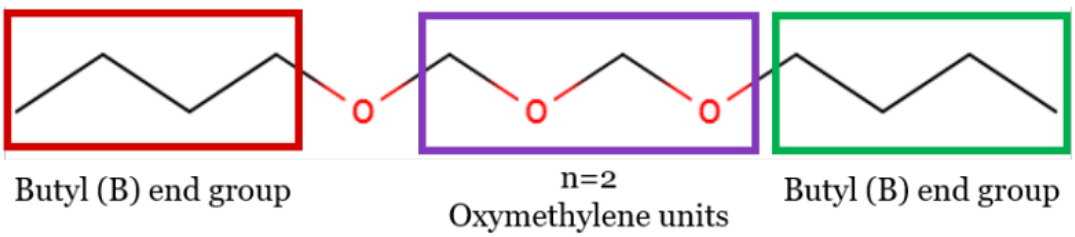

Figure 1.2. Example OME structure for B-2-B showing general layouts of OMEs.

Chapter 2- Synthesis of POM-E

2.1. Background

The simplest possible oxymethylene ether is dimethoxymethane (M-1-M). Several methods are discussed in the literature for synthesis of M-1-M. The primary industrial method is a two-step process from methanol, first via partial oxidation of methanol to formaldehyde, and then via acetalization of methanol with the formaldehyde from the prior process [3–5]. This is described in the reaction mechanism below from [3], where R1.3.1.4 is the overall reaction producing M-1-M:

$$CH_3OH + \frac{1}{2}O_2 \longrightarrow CH_2O + H_2O \qquad \text{(R1.3.1.1)}$$

$$CH_2O + CH_3OH \longleftrightarrow CH_3OCH_2OH \qquad \text{(R1.3.1.2)}$$

$$CH_3OH + CH_3OCH_2OH \longleftrightarrow CH_3OCH_2OCH_3 + H_2O \qquad \text{(R1.3.1.3)}$$

$$CH_2O + 2CH_3OH \longleftrightarrow CH_3OCH_2OCH_3 + H_2O \qquad \text{(R1.3.1.4)}$$

In this reaction mechanism, the formation of the hemiformal (R1.3.1.2) can proceed in a neutral environment and monomeric formaldehyde is present in very low amounts at equilibrium, but the formation of M-1-M requires an acidic catalyst to proceed and is rate limiting [6]. An additional mechanism for production of M-1-M is via selective catalytic oxidation of methanol. This process requires a bifunctional catalyst that can perform the full reaction mechanism above in a single system and typically results in lower yields [7]. Similar to the acetalization process, the oligomerization also occurs in the presence of an acid catalyst. As reviewed by Baranowski [8], these oligomerization reactions can be performed with both liquid and solid catalysts. Synthesis of higher OMEs has received less attention in literature. Lautenschütz et al. synthezise E-n-E from E-1-E and trioxane over Amberlyst 36 catalyst [9] in order to isolate and characterize these OMEs, following a similar process to that described above. No recent work has been published regarding the synthesis of P-n-P OMEs. Recent work by Arellano-Trevino synthesized a mixture of M-n-M, M-n-B, and B-n-B OMEs from trans-acetalization of an M-n-M mixture, primarily n=3-5, with butanol over Amberlyst 46. The resultant mixture contains a large number of oligomers, as well as formaldehyde, asymmetric OMEs, and large quantities of M-1-M, however, no attempt was made to isolate individual OMEs. Stoichiometric ratios of butanol with M-n-M (2:1) were shown to produce larger quantities of FA and asymmetric OMEs; reactants rich in butanol showed much less FA and asymmetric OME production. Similar trans-acetalization reactions are documented by Drexler [10] where linear OMEs, E-1-E, P-1-P, and B-1-B, are reacted with a branched OME to produce more complicated asymmetric structures. These reactions are performed over a zeolite catalyst with Si/Al ratio of 25. Leveraging methods developed and discussed in these previous works, here we provide a more detail description of our techniques. We highlight the synthesis of our butyl-terminate OMEs below, but note that similar methods and approaches were taken to synthesize the other alkyl terminated varieties.

2.2. Synthesis of Butyl-Terminated Oxymethylene Ethers

All synthesis experiments for this section were conducted in a 300 mL Parr 4651 stirred autoclave reactor. Reactants were purchased from Millipore Sigma and Fisher Scientific. M-1-M, n-butanol, and s-trioxane were used as reactants with purity >99%, as purchased from either Sigma Aldrich or Fisher Scientific. Bio-

derived isobutanol was acquired from Gevo with purity 98.7%, balance isopentanol. Reactions were performed at stoichiometric conditions for the respective reactions, with 0.5 mass% catalyst. The idealized stoichiometry is presented below. As will be discussed later, the equilibrium products included other components.

$$2\ C_4H_9OH + CH_3OCH_2OCH_3 \longrightarrow 2\ CH_3OH + C_4H_9OCH_2OC_4H_9 \qquad \text{(Pathway 1)}$$

$$6\ C_4H_9OH + (CH_2O)_3 \longrightarrow 3\ C_4H_9OCH_2OC_4H_9 + 3\ H_2O \qquad \text{(Pathway 2)}$$

All reactions were performed under 5 bar N2, with the reactor being filled and purged 3 times prior to final pressurization. The reactor was then heated to the target temperature and maintained under constant stirring at 600 rpm for the duration of the experiment (except during sample removal).

Liquid samples were primarily analyzed in a HP 5890 Series II gas chromatograph equipped with a flame ionization detector (GC-FID) and a Restek Rtx-Wax 0.25µm x 0.25 mm x 30 m column with helium carrier gas at 50:1 split ratio. The device was operated at 200°C inlet and detector temperature with a temperature profile of 1 minute hold at 60°C, followed by 20°C ramp to 200°C and held at that temperature for 7 minutes. For reactions with H2O products, water content was measured using Karl Fischer titration in a Metrohm 831 KF titrator with Hydranal Coulomat AG reagent. In one case, gas chromatography-mass spectroscopy was used to identify an unknown peak in the GC-FID chromatogram; this device used a 0.25µm x 0.25 mm x 30 m VF5-MS column, operating under the same temperature ramp as the GC-FID, where dichloromethane was used as a solvent in 100:1 volume ratio to the synthesis sample. In Pathway 2, formaldehyde and water cannot be accurately quantified with GC-FID. As a result, we determined the mole fractions of these components algebraically, given the known fractions of B-1-B, butanol, and B-2-B (when present), and verified by comparison of calculated water content with measured water content via Karl Fischer titration. Insufficient thermodynamic data exists for the B-1-B and B-2-B products to perform a free-energy minimization equilibrium calculation, so this method was used instead. The fractions are determined as follows and then normalized to sum to 1:

$$x\ C_4H_9OH + y/3\ (CH_2O)_3 \longrightarrow a\ C_4H_9OH + b\ C_4H_9OCH_2OC_4H_9 + c\ C_4H_9O(CH_2O)_2C_4H_9 + d\ CH_2O + e\ H_2O$$

$$a, b, c = known\ from\ GC-FID$$

$$x = a + 2b + 2c, \quad y = x/2, \quad d = y - b - 2c, \quad e = b + c$$

Four commercially available cation exchange resins were examined in this study: Amberlyst 15 (Millipore Sigma), Amberlyst 46 (Sigma Aldrich), Amberlite IRC 120H (Fisher Scientific) and Dowex G26 (Millipore Sigma). Following tests with each catalyst under consistent reaction conditions of 60°C and 0.5 mass % catalyst with stoichiometric butanol and dimethoxymethane (2:1), it was found that the Amberlyst 15 catalyst provided the highest Yield of our target POME and thus was used in subsequent testing and fuel synthesis.

2.2.1. Results

Figure 2.1. Butoxymethoxymethane – intermediate product, formed via (R2.1.1)

Figure 2.2. Dibutoxymethane – target product, formed via (R2.1.2) or (R2.2.2)

In evaluating Pathway 1 for this synthesis, we must consider the production of both the final product, dibutoxymethane, as well as an intermediate, butoxymethoxymethane (see Figure 2.1, Figure 2.2). This intermediate molecule is formed when only one of the methyl groups on the original OME, dimethoxymethane, is replaced by the butyl group from the alcohol. Dibutoxymethane is then formed when a butoxymethoxymethane has its remaining methyl group exchanged as well. This two-step reaction is described below in (R2.1.1) and (R2.1.2), producing dibutoxymethane, butoxymethoxymethane, and methanol.

$$C_4H_9OH + CH_3OCH_2OCH_3 \longleftrightarrow CH_3OH + C_4H_9OCH_2OCH_3 \qquad \text{(R2.1.1)}$$

$$C_4H_9OH + C_4H_9OCH_2OCH_3 \longleftrightarrow CH_3OH + C_4H_9OCH_2OC_4H_9 \qquad \text{(R2.1.2)}$$

Pathway 2 did not produce any measurable intermediates in the same way as Pathway 1; however, it is expected that the acetalization proceedes through a hemiacetal which is fully consumed. This reaction is presented as a four-step process of trioxane decomposition followed by acetalization producing both water as a byproduct, and under certain conditions, a small amount of a chain-extended molecule, butoxy-(methoxy)2butane (Figure 2.4).

Figure 2.3. B-2-B – oligomerized product, formed via (R2.2.3)

$$(CH_2O)_3 \longleftrightarrow 3CH_2O \qquad \text{(R2.2.1)}$$

$$C_4H_9OH + CH_2O \longleftrightarrow C_4H_9OCH_2OH \qquad \text{(R2.2.2)}$$

$$C_4H_9OH + C_4H_9OCH_2OH \longleftrightarrow C_4H_9OCH_2OC_4H_9 + H_2O \qquad \text{(R2.2.3)}$$

$$C_4H_9OCH_2OC_4H_9 + CH_2O \longleftrightarrow C_4H_9O(CH_2O)_2C_4H_9 \qquad \text{(R2.2.4)}$$

2.2.2. Effect of Temperature on Pathway 1 Reactions

Having determined that Amberlyst 15 is the most effective catalyst for production of dibutoxymethane, we proceed with investigation of the temperature effect on the Pathway 1 reactions. We continued to use stoichiometric reactant ratio and 0.5mass% catalyst. Three temperature conditions were tested – 40°C, 60°C, and 80°C. As shown below in Figure 2.4 and Figure 2.5, the production rate of both products was highly temperature dependent, while the equilibrium composition appeared to be independent of temperature.

$$y = a\frac{t}{b+t} \qquad \text{(Eq. 2.1)}$$

A saturation growth model (see (Eq. 2.1)) well describes the change over time of the desired products, and is used for comparison of time constants and to estimate equilibrium for reactions which do not reach equilibrium in the 24 hours measurement period, where y is the mole fraction, a is the asymptotic equilibrium, and b is a rate modifier. In the 40°C case, butoxymethoxymethane reached the equilibrium fraction, albeit at a slower rate, but dibutoxymethane did not reach equilibrium in the measured time (24 hours). The time constants τ to reach $1-1/e \cdot a$ at 40°C, 60°C, and 80°C, are 8.57 hours, 2.40 hours, and 9.64 minutes, respectively. The dibutoxymethane yield in the first hour roughly doubled for every 20°C increase in temperature. The 80°C reaction had comparable yield of products to the lower temperatures, however, it is established that higher temperatures promote hydrolysis of dimethoxymethane to methanol and formaldehyde [11], and we observed higher methanol concentrations at 80°C than 60°C despite the comparable target product yields.

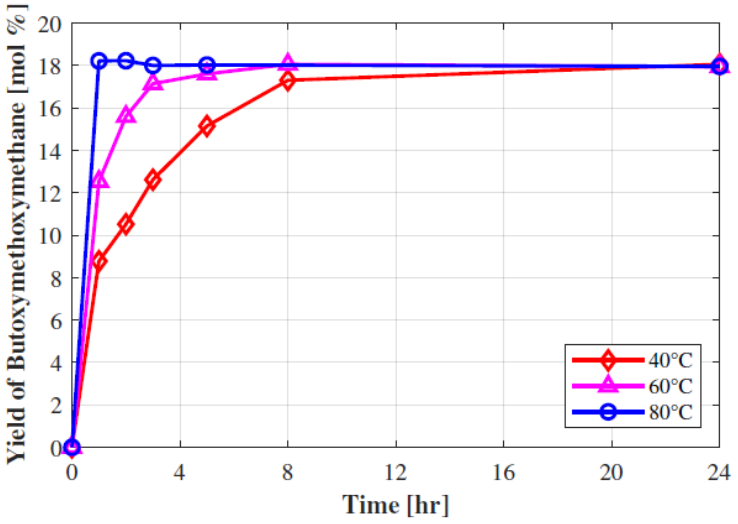

Figure 2.4. Pathway 1 mole fraction yield of M-1-B with 0.5 mass % Amberlyst 15, 2 mol butanol : 1 mol dimethoxymethane

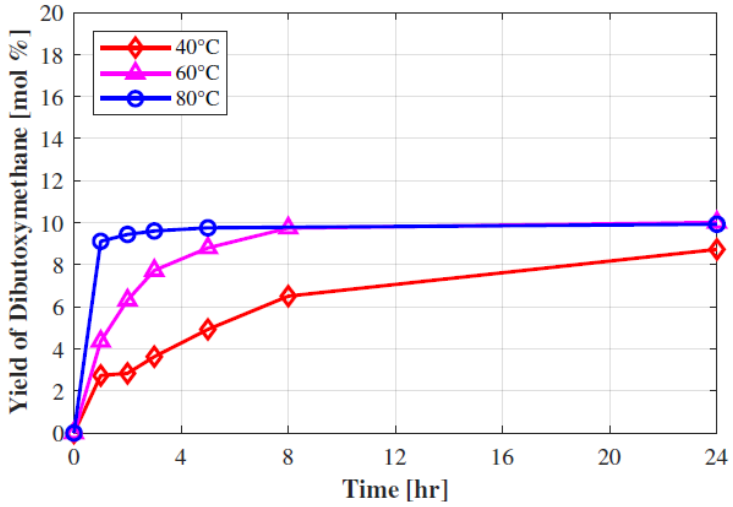

Figure 2.5. Pathway 1 mole fraction yield of B-1-B with 0.5 mass % Amberlyst 15, 2 mol butanol : 1 mol dimethoxymethane

2.2.3. Effect of Temperature on Pathway 2 Reactions

Again using Amberlyst 15 as the preferred catalyst, we applied these reaction conditions to the Pathway 2 synthesis method. Unlike Pathway 1, where all reactants and products can be measured with GC-FID techniques, for Pathway 2, formaldehyde and water cannot be accurately quantified with GC-FID. As a result, we determined the mole fractions of these components algebraically, given the known fractions of B-1-B, butanol, and B-2-B (when present).

These calculations were verified by testing the water content by mass at the end of the reactions with Karl-Fischer titration. It was found that at 60°C, the water mass fraction was 92% of what was predicted from Eqs. 1-5, and for the 80°C and 100°C cases, the water mass fractions was 84%and 72% of the prediction

respectively. As there will be some water loss to evaporation, and some consumption of H and OH radicals may occur as terminating groups in the formation of paraformaldehydes ormethanediol [12] from unreacted formaldehyde is to be expected (which is not predicted in the above equations), and for the higher temperature cases some water precipitated out of solution into a separate phase at the bottom of the container due to higher dibutoxymethane concentration (and thus lower water solubility [13]), we consider this result to be reasonable. Additionally, as the higher temperature cases will more rapidly depolymerize trioxane [14], there will be additional time and concentration of formaldehyde for formation of these possible OH consumers. Further work may be warranted to determine the exact forms of the unreacted formaldehyde, which may lend greater accuracy to the calculation of water content.

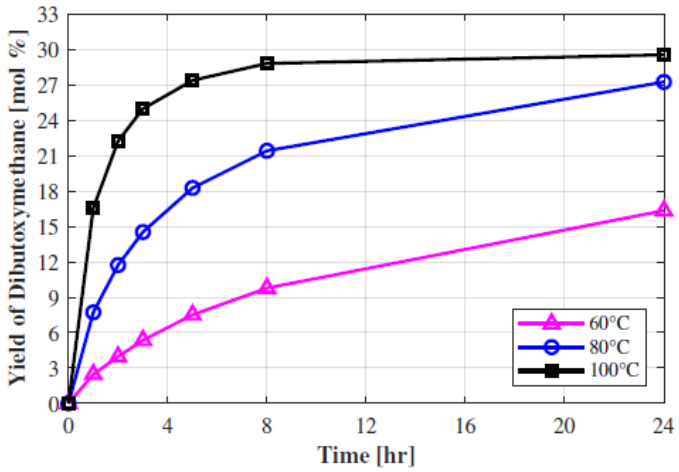

Figure 2.6. Pathway 2 mole fraction yields of B-1-B with 0.5 mass % Amberlyst 15, 2 mol butanol : 1 mol formaldehyde (6 mol butanol : 1 mol trioxane). B-2-B was present in small (<2 mol% after 24 hours) concentrations for 80°C and 100°C tests.

Of the prior three reaction conditions – 40°C, 60°C, and 80°C – only the latter two were successful for this case. In stoichiometric proportions, 2:1 molar ratio of butanol to formaldehyde (in our case, specifically 6:1 butanol to trioxane), the trioxane will dissolve fully at elevated temperatures, but at room temperature some trioxane will remain solid. It was observed that all samples until the 24 hour sample at the 40°C condition had trioxane crystallizing out of solution once the sample cooled to room temperature, which both posed a risk of damage to the GC-FID instrument if solids formed in the injector, and indicated that there was very little conversion of trioxane. Even after 24 hours, some solidified, unreacted trioxane was observed on the interior of the reactor vessel. Thus, this condition was discarded as being unsuitable, and a higher temperature third case, 100°C, was added. The reactions at 60°C, 80°C, and 100°C were much more successful, showing no apparent crystallization of trioxane at any point, and are presented in Figure 2.6.

It may be immediately observed from Figure 2.6 that this reaction proceeds differently than Pathway 1; the different temperatures produced significantly different yields at 24 hours, rather than simply accelerating the reaction to a temperature-independent equilibrium – an apparent equilibrium of 29.5%by mole of dibutoxymethane was reached only for the highest temperature case. Saturation growth models fitted to these indicate that the 60°C case may approach a lower equilibrium dibutoxymethane yield of 23% while the 80°C and 100°C both approach an equilibrium of approximately 31% for extended time. The

time constant for 60°C to the lower equilibrium was 17.6 hours, while the higher temperature cases, 80°C and 100°C, had shorter time constants, 5.62 hours and 1.43 hours respectively, acknowledging that the asymptotic equilibrium value here is an estimate from (Eq. 2.1).

Pathway 2 was a significant improvement in yield of the desired product (dibutoxymethane), with the 80°C case producing more than twice the yield by mole of its Pathway 1 equivalent. In addition, we observed that the oligomerized product, B-2-B, was produced in small but measurable quantities at later stages of the 80°C reaction, up to about 1%, and at all stages in the 100°C case up to 1.6%, while the 60°C reaction produced negligible amounts of this product, even at 24 hours. As this reaction did produce water as a byproduct, and contained some amount of unreacted formaldehydes, industrial applications may require additional processing steps to be viable, however, from the standpoint of yield of desired product (specifically B-1-B), Pathway 2 was the clearly superior method, yielding higher equilibrium mole fraction of B-1-B at the cost of slower reaction times.

2.2.4. Synthesis of Butyl-terminated Ethers using Bio-Butanol

Desire to reduce CO2 emissions has driven attempts to find alternative, non-combustion powertrains for many vehicle types. As reviewed by Kluschke et al. [15], even in an optimistic scenario for alternative powertrains for heavy duty vehicles, combustion engines remain relevant, occupying approximately 40% of market share by 2050, and biofuels for these engine systems are an option studied in a number of the reviewed articles and the most competitive option in at least one. Biofuels are an attempt to approximate a “net zero” or “carbon neutral cycle” approach, wherein all carbon emitted into the environment is both reused for future energy, and is itself sourced from carbon in the environment. An “ideal” net zero fuel would emit no more carbon into the atmosphere (as CO2 or otherwise) than is contained in the source material (e.g. biomass) for the fuel, so that upon combustion, the CO2 produced can then be reabsorbed by plant matter and later turned into more biofuel [16] without changing the total amount of carbon in the atmosphere.

Bio-derived n-butanol is a well-studied process, but hindered by lowthrough put due to poisoning of the fermentation species by the produced butanol [17,18]. Further, it is established that sulfur and nitrogen compounds, which are commonly found in bio-derived feedstocks, may have a negative effect on catalytic activity by poisoning active sites [19,20]. Thus, we acquired a sample of iso-butanol from Gevo Inc. with a bio-derived source, specifically from #2 yellow dent corn, as a proof-of-concept for synthesis of an extended-alkyl OME from a known bio-source. Following the Pathway 2 reaction process at 80°C with stoichiometric reactants and 0.5 mass% Amberlyst 15, a similar yield curve was found. A curve-fit suggests a slightly lower equilibrium of 29 mol% iB-1-iB. An additional peak is found in the chromatogram in addition to expected peaks from the iB-1-iB and iB-2-iB; GC-MS lookup was unable to accurately identify this compound, but we tentatively propose that it may be the acetalization of iso-pentanol, present at 1.3% in the provided sample, to a new iso-pentyl-terminated oxymethylene ether.

2.3. Synthesis and Chain Growth of Other OMEs

The synthesis of B-1-B was investigated directly as it was identified early on as a likely candidate for diesel substitution; structure-property relations indicated a high likelihood of ideal properties [13]. However, other OMEs were investigated in the course of this study, many of which needed to be synthesized in-house. M-n-M is commercially available and a supply was provided by Oak Ridge National Laboratory for this study; additionally, E-1-E – B-1-B are easily acquired from Fisher, Sigma, or other chemical providers. However, the branched (iP and iB) OMEs, and extended-chain / extended-alkyl OMEs were not

commercially available. These were synthesized in-house; the processes for doing so are discussed here in this section. Several of the conclusions from the detailed study of B-1-B were applied here, most particularly the catalyst and pathway selection. For (relatively) large-scale production, a flow reactor was used rather than the batch reactor discussed above; additionally, once the methods were established as effective, measurements were taken merely for quality control purposes rather than scientific characterization, so much of the discussion in this section will be less detailed.

2.3.1. Method of Production of X-1-X OMEs

For property and engine testing, larger quantities of fuel were required. P-1-P and B-1-B could be acquired by the barrel and tested as is, or extended to longer chains as described in the following section. iB-1-iB was tested only for properties, and little was required. Thus for the general description of the production of other OMEs, iP-1-iP is used as the example, as multi-liter-scale production was required for engine testing. A flow reactor was assembled for this task. The flow reactor was built in house, consisting of an Eldex piston pump and a 3/4 inch stainless reactor tube in a split tube furnace. The reservoir, tubing, and pump piston housing were heat-traced to prevent crystallization of trioxane in the system. The reactor itself was filled with 15g Amberlyst 15 catalyst, in 3 layers separated by glass wool (this makes the system easier to clean and replace catalyst, and should not have any effect on the reactions), as the B-1-B testing indicated that of the four tested catalysts, this was superior for OME production. Figure 2.14 demonstrates the full process, using iP-1-iP as a representative OME.

Production of OMEs for testing was performed using the Pathway 2 methods as described in reactions R2.2.1-R2.2.3. The ratio of trioxane to alcohol was kept at the stoichiometric value, with reactants being prepared bymass (for trioxane) and volume (for the alcohol) in 1 L batches to be added to the reactant vessel as needed. Using iP-1-iP as an example, this synthesis produces a mixture of iP-1-iP, water, and unreacted iPrOH and trioxane. For the conditions selected (80 °C in a flowreactor with 15 g Amberlyst 15 catalyst, approximately 0.64 min-1 space velocity), the product mixture is described in Table 2.5. While the mass fractions are dependent on the alkyl groups, the mole fractions provided in this table are reasonably representative of the synthesis in the flow reactor with other alcohols. The hemiacetal is not observed and is expected to be consumed completely in the reaction. As a GC/FID was used for quantification, where concentrations are calculated using the effective carbon number method [21], only iPrOH and iP-1-iP could be observed; the remaining components were calculated via stoichiometry. Extended oxymethylene chains can be formed in acidic environments with a formaldehyde source given sufficient time to reach equilibrium [6], however, negligible chain growth is observed at these conditions.

The presence of unreacted formaldehyde and/or trioxane or paraformaldehydes, as well as water and unreacted alchohol, requires additional treatment steps for the fuel to be ready for later use. Before separation, the product mixture was treated with a buffer solution. Collaborators at NREL provided the specifications for this buffer solution; its purpose is to simultaneously neutralize the acidity of the product mix (pH = 5 as measured via test strips) and dissolve out water and formaldehyde from the mixture. The buffer solution consists of 1 L of purified (ASTM Type II or better) water mixed with 0.764 g sodium bicarbonate and 0.095 g sodium carbonate. This is mixed 1:1 by volume with the product mixture for several minutes (the products are to a greater or lesser extent immiscible in water, so vigorous shaking by hand was found to be more effective than stirrers or other mechanical methods) and then placed into a separation funnel to split into phases. As will be highlighted later, nearly all OMEs other than heavy M-n-M are lighter than water, so the lower phase is the water phase and is removed and disposed of. In cases where the alcohol is completely miscible in water, this buffer solution treatment also serves to extract a

large portion of the alcohol. Specifically, for iP-1-iP, the affinity of iPrOH for dissolving in water was much higher than in iP-1-iP, and so after just two buffer solution treatments, the amount of iPrOH was found to be an order of magnitude lower than the product mix directly out of the reactor. This treatment is performed a total of three times; fewer than three tended to leave enough paraformaldehyde and/or trioxane to foul the distillation column. Following the buffer solution treatment, purification was performed in a B/R Instruments spinning band distillation column, operated typically under vacuum with a Teflon band providing 200 maximum theoretical plates, per manufacturer specifications. For very high temperature distillations (>225°C), a stainless-steel band with 36 theoretical plates was required. Using atmospheric equivalent temperature methods, the cut temperatures under vacuum were selected and the column performed automatic cut separation.

Table 2.1. Mass and molar yields of iP-1-iP production reaction at 80°C and 0.64 min-1 space velocity over Amberlyst 15 acid catalyst

Component	CH_2O	H_2O	i-C_3H_7OH	$C_3H_7OCH_2OC_3H_7$
Mass %	11.2	5.2	45.1	38.3
Mole %	22.0	17.0	44.0	17.0

2.3.2. Methods for Chain Growth of OMEs

Chain growth of the OMEs is performed in the flow reactor over Amberlyst 15 catalyst, determined above to be best catalyst for use with OMEs, using trioxane as a formaldehyde source. All oligomerization reactions were performed at a 1:1 mol ratio of X-1-X basic OME to formaldehyde (3:1 OME:trioxane). When possible, the reactor was held at 80°C +/- 3°C, although for E-n-E oligomerization the temperature was lowered to 70°C to ensure that temperature fluctuations would not result in the mixture boiling in the feed tube due to the low boiling temperature of E-1-E. Reaction R3 shows the general process, using B-n-B as an example.

$$C_4H_9O(CH_2O)_{n-1}C_4H_9 + CH_2O \longleftrightarrow C_4H_9O(CH_2O)_nC_4H_9 \qquad \text{(R3)}$$

2.3.3. Results

Under these conditions, the mixtures were able to achieve an equilibrium yield of various chain lengths as described below. Testing with B-n-B indicates that the time on catalyst is long enough that changes in flow rate did not significantly affect yield; the only observed change with lower flow rates (longer time on catalyst) was an increase in the production of the associated alcohol due to decomposition of X-1-X to X-OH, which was observed to be present in low quantities at all flow rates. At a nominal flow rate of 8 mL/min, the yields are as shown in Figure 2.7 - Figure 2.9. The mean MW of the E-n-E mixture is 120.2 g/mol, with 10.2 mol% / 3.9 mass% of ethanol. This indicates a mean oligomerization length of E-1.63-E. For P-n-P, the mean MW is 147.8 g/mol with 5.5 mol% / 3.7 mass% propanol, and a mean oligomer length of P-1.65-P. For B-n-B, the mean MW is 177.2 g/mol with 6.8 mol% / 2.8 mass% butanol, and a mean oligomer length of B-1.70-B.

For engine testing and blending with diesel, a 200°C - 305°C distillation cut has been identified as the desired blendstock; this cut has superior properties and the volatility better matches the typical distillation curve of diesel (Figure 2.10). The composition of this cut is provided below in Figure 2.11. Negligible

butanol remains in this distillation cut. Approximately 95% by mass of this cut lies between 220-300°C boiling temperatures, appropriate for diesel.

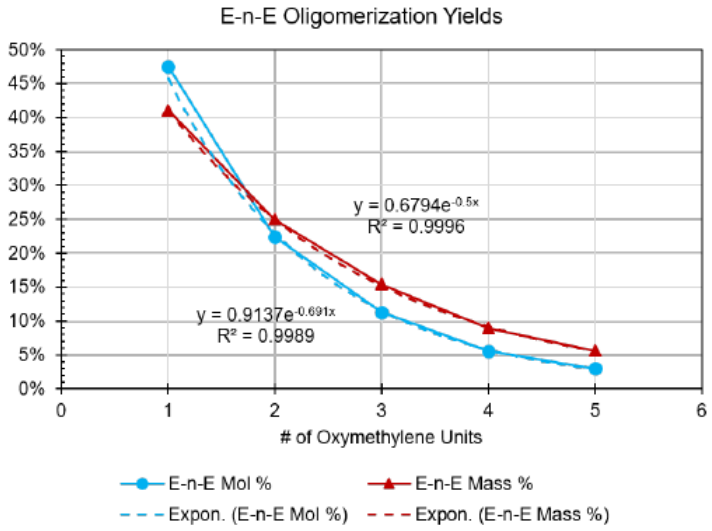

Figure 2.7. Oligomerization yield of 3mol E-1-E : 1 mol trioxane over Amberlyst 15, 70°C, 8 mL/min

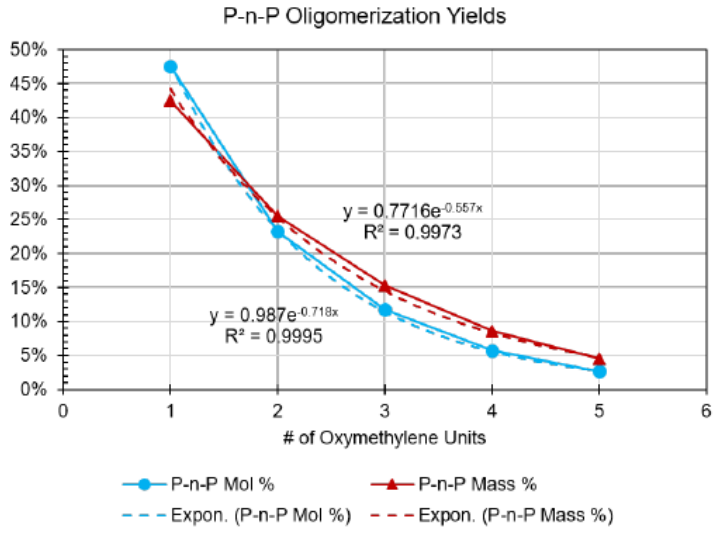

Figure 2.8. Oligomerization yield of 3 mol P-1-P : 1mol trioxane over Amberlyst 15, 80°C, 8mL/min

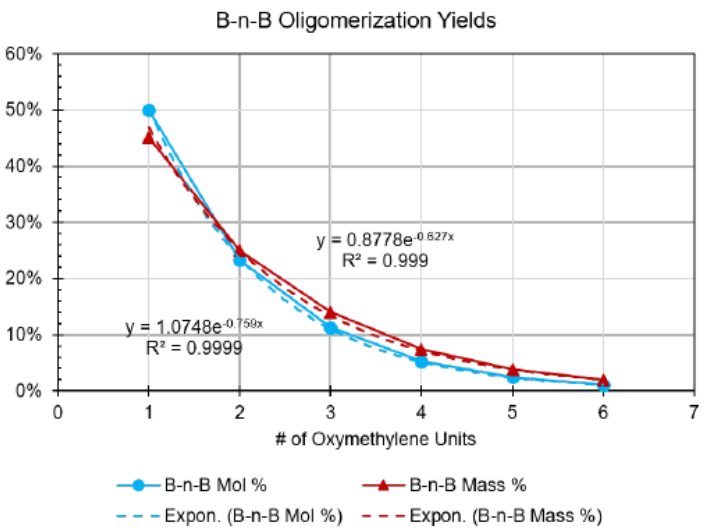

Figure 2.9. Oligomerization yield of 3 mol B-1-B : 1 mol trioxane over Amberlyst 15, 80°C, 8 mL/min

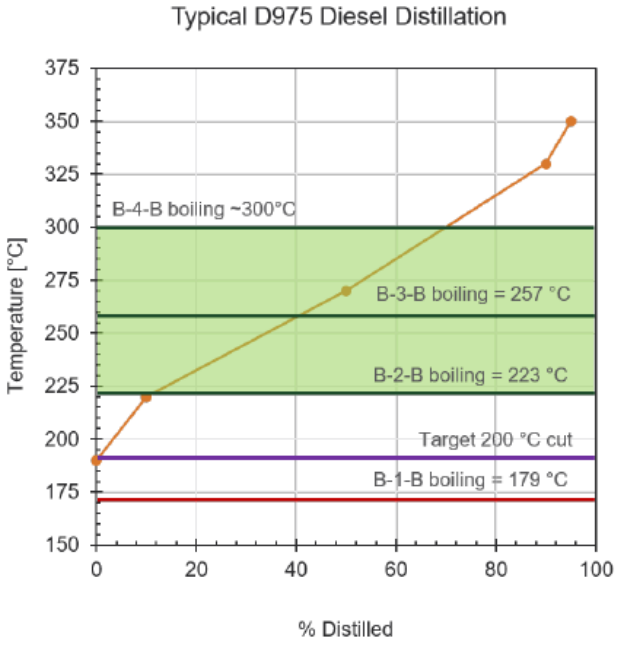

Figure 2.10. Typical D975 distillation curves with boiling points of some B-n-B compounds

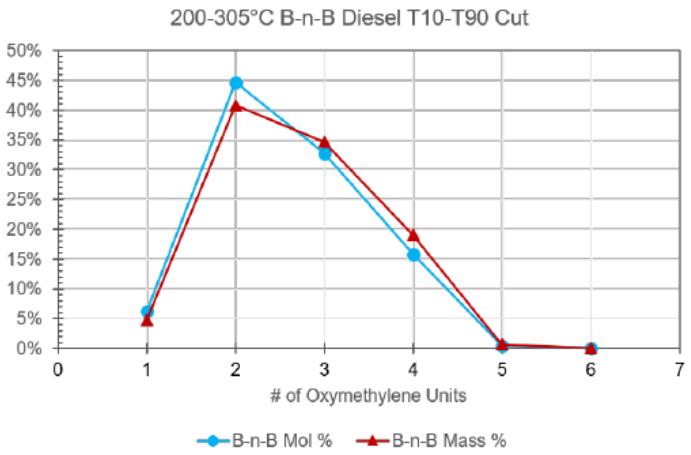

Figure 2.11. Composition of 200-305°C cut of B-n-B oligomerization products

Chapter 3 Individual POME Characterization

To identify most promising OME molecular structures ahead of expensive and time-consuming bulk synthesis and MCCI engine testing, multiple OMEs with variable oxyethylene chain structure length and alkyl endgroups were synthesized and characterized. Properties relevant to MCCI engine operation and combustion were measured on the matrix of OME species. The following section highlights these results, emphasizing the sooting tendencies of the OMEs quantified by the Yield Sooting Index (YSI) and the autoignition tendencies of the OMEs marked by ignition delays using the CSU rapid compression machine (RCM) and the indicated cetane number (ICN). The last section in this chapter shows results from additional physio-chemical property tests, many of which part of the ASTM MCCI fuel certification procedures, which describe fuel behaviors important for fuel distribution and handling and suitability in legacy fuel systems/engines.

The OMEs tested in this study are a combination of commercially available and those synthesized in-house. All methyl-terminated OMEs were acquired commercially. M-1-M was purchased from Fisher Scientific and Sigma Aldrich, purity >98%. M-2-M was purchased from AstaTech Inc., purity >97%. M-3-Mthrough M-5-Mwere acquired as amixture fromASG Analytik-Service GmbH, and was distilled in-house to purity >95%. E-1-E was purchased from Fisher Scientific and Sigma Aldrich, purity >98%. P-1-P was provided as a sample without charge by Lambiotte & Cie, purity >97%. B-1-B was purchased from Fisher Scientific and Sigma Aldrich, purity >98%. E-2-E, E-3-E, P-2-P, P-3-P, B-2-B, and B-3-B were synthesized via oligomerization of the appropriate X-1-X with trioxane, as described earlier and distilled to purity >95%. iP-1-iP and iB-1-iB were synthesized from trioxane and the appropriate iso-alcohol over Amberlyst 15 catalyst as described earlier and distilled to purity >95%.

3.1. Yield Sooting Index

One of the most beneficial properties of POMEs is their low tendency to form soot. Therefore, a major objective of this project was to quantify the sooting tendencies of POMEs. The ultimate arbiter of sooting behavior is emissions from engines, so engine studies were included in this project and are reported in Chapter 6. However, engine studies suffer from several drawbacks for determining the effect of fuel structure on sooting tendency: (1) running an engine requires large fuel volumes, (2) changing the fuel structure usually indirectly affects soot by changing factors such as ignition timing, and (3) the results are specific to the test engine. Therefore laboratory-scale sooting tendency measurements were also included in the project using the yield sooting index (YSI) methodology. This section presents the results for individual POMEs (and mixtures of POMEs), then Section 5.a presents the results for POMEs mixed with conventional diesel and other fuels.

This section is organized as follows. 3.1.1 describes the YSI methodology, the modifications necessary to account for the very low sooting tendencies of methyl-terminated POMEs, and experiments that validated these modifications. 3.1.2 presents results that quantify the soot tradeoff when methyl-terminated POMEs are converted to butyl-terminated POMEs by end-group exchange, and it shows that the sooting tendencies are still much lower than conventional diesel fuel. 3.1.3 lists the 28 YSIs measured for individual POMEs and related compounds, discusses how the YSIs depend on structural factors such as the end-group size, and explains some of these trends based on the kinetic pathways developed in this project (see Chapter 4). 3.1.4 presents results for a set of POME mixtures that were synthesized at NREL using alternative alcohols to expand the range of reactants available for end-group exchange, and it shows that they also soot much less than conventional diesel fuels. 3.1.5 describes how the pure compound results

have been made available to all stakeholders via the online NREL YSI Estimator tool. Finally, 3.1.6 summarizes sooting tendency measurements that were performed in support of the other FY18 Co-optima university projects and several of the Co-optima National Laboratory projects.

3.1.1. YSI Methodology

In this project sooting tendencies were measured as yield sooting indices (YSIs). YSI was originally developed at Yale in 2007 [22] as an alternative to the ASTM D1322 smoke point test [23]. It has been further developed in this project and the FY16 Co-optima university project DE-EE0007983. Many research groups around the world are now using YSI for fuel screening (e.g., [24–26]). The Coordinating Research Council (CRC) has incorporated it into a new particulate matter (PM) index for predicting emissions from direct-injection spark ignition engines [27].

YSI offers several benefits compared to smoke point, which proved to be critical to this project:

1. A YSI measurement requires 50 µL of sample, which is orders of magnitude less than the 10 mL required for a smoke point measurement [23]. Most of the POMEs tested in this project were custom-synthesized and the volumes were inadequate for smoke point but sufficient for YSI. The results from this large set of compounds then allowed the project to rationally downselect to the most promising compounds to produce in large volumes.

2. YSI has a much larger dynamic range than smoke point. Some of the POMEs have drastically lower sooting tendencies than conventional fuel molecules and are outside the range of smoke point. For example, Tan et al. [28] attempted to measure smoke points of MnM compounds, but they were only able to show that they were negligible compared to conventional diesel fuel. In this project quantitative YSIs were successfully measured for these same compounds.

3. The YSI flames have much simpler boundary conditions than the wick burner smoke point flames and can be directly simulated. For example, Kwon et al. [29] simulated the YSI flames for 20 bio-derived spark-ignition fuel molecules with a mechanism from William Pitz's group at LLNL; the results showed that the mechanism could predict soot formation accurately from most of the molecules, but more work was needed for furanic species. It is anticipated that eventually the kinetic mechanisms developed in this project (see Chapter 4) will also be tested against YSI data.

The YSI procedures used in this project mostly followed earlier work [30]. However, modifications were required due to the very low sooting tendencies of some POMEs. In particular, a new scale was defined, as shown in the figure below. Every YSI measurement is referenced to two endpoint species. Normally these species are n-heptane and toluene (the blue range in the figure). These endpoints are well-suited to normal internal combustion (IC) engine fuels since they bracket n-alkanes, isoalkanes, cycloalkanes, olefins, and aromatics. However, the YSIs of the methyl-terminated POMEs (green diamonds) are much lower than n-heptane, so this scale requires a large extrapolation. The new scale uses water as the lower endpoint and n-heptane as the upper endpoint (the orange range in the figure), and it requires no extrapolation. The YSI of water is defined to be zero since it contains no carbon atoms. Water is well-suited to be an endpoint since it is a liquid that can be injected into the fuel mixture with the same procedures as regular hydrocarbons, and it has a volatility similar to gasoline.

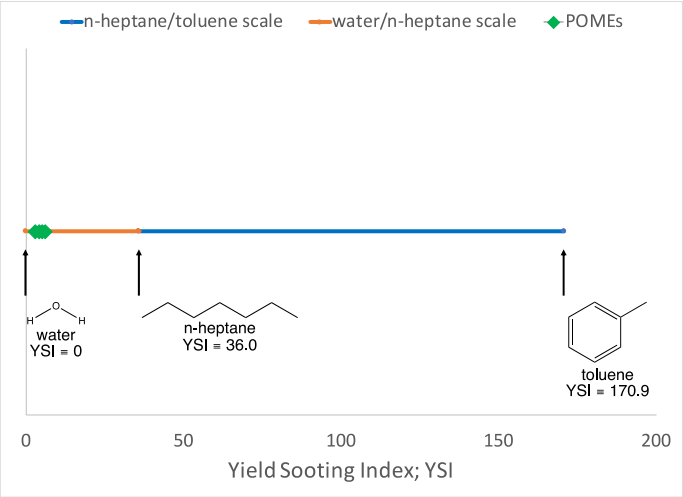

Figure 3.1. Visualization of YSIs for common compounds (water, n-heptane, and toluene) compared to those of POMEs.

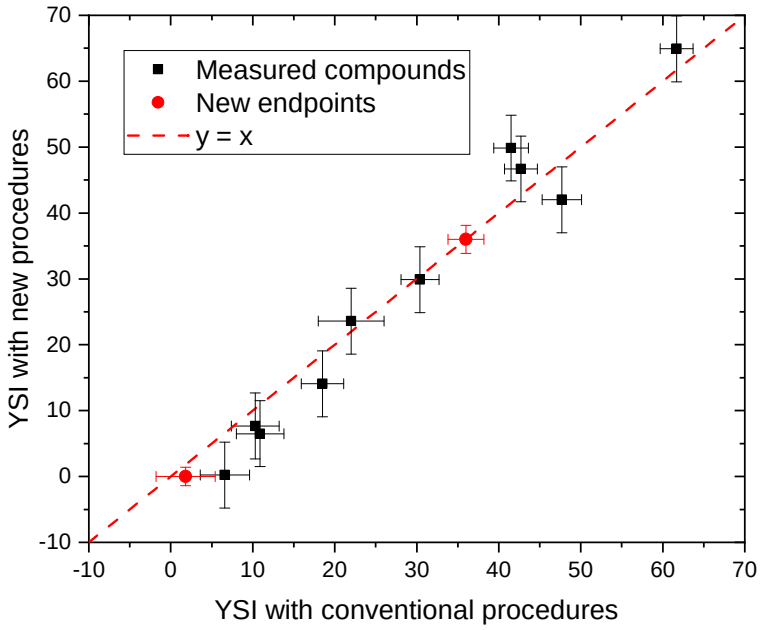

Figure 3.2. YSIs measured for a diverse set of hydrocarbons with the new and conventional scales agree to within experimental error.

3.1.2. Sooting Tendencies of POMEs Following Butyl End-Group Exchange

Methyl-terminated POMEs have extremely low sooting tendencies (see next section), but they also have low heats of combustion and high water-solubilities. A potential method for improving these properties is to exchange the methyl end-groups for butyl-groups. However, this will increase the sooting tendencies. To quantify the tradeoffs between these properties, sooting tendency measurements were performed for a methyl-terminated POME mixture before and after end group exchange. The results are presented in detail in [31] and are discussed here briefly.

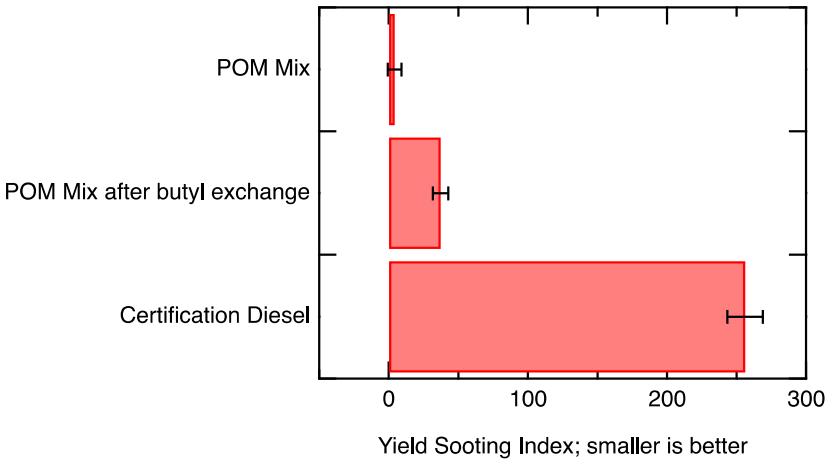

Figure 3.3. YSI results for (1) a commercial POME mixture with methyl end-groups (supplied by Lisa Fouts, NREL), (2) a portion of the same POME mixture after butyl end-group exchange (supplied by Martha Arellano-Treviño, NREL; see [31]), and (3) a certification diesel fuel (supplied by Charles Mueller, Sandia National Laboratories, see [32]).

The YSI of the methyl end-group mixture (fuel #1) is extremely low; indeed, it is so low that only an upper limit for its value, 4, could be determined with the standard YSI procedures that were used in these measurements. (As discussed in 3.a.1, a new YSI procedure was subsequently developed that is more sensitive to very low sooting tendencies, and it was used to generate the quantitative YSIs of the methyl-terminated compounds presented in 3.a.3.) This occurs because the M-n-M components of this fuel all contain zero carbon-carbon bonds. It demonstrates the tremendous soot reduction benefits of POME fuels.

The YSI of the sample after butyl end-group exchange (fuel #2) is significantly higher, 37. This increase is expected since end-group exchange adds either 3 carbon-carbon bonds (M-n-B compounds) or 6 carbon-carbon bonds (B-n-B compounds). However, the YSI is still less than 15% of the YSI of the diesel fuel (fuel #3, YSI = 256). This occurs because the diesel fuel contains about 27 mol% single-ring aromatics and 11 mol% multi-ring aromatics [32]. Thus, butyl end-group exchange allows the fuel to have much better heating value and water solubility, while still offering large soot reduction benefits over conventional diesel fuels.

3.1.3. Sooting Tendencies of Individual POMEs

This section discusses the YSIs measured for individual POMEs and related compounds. Most of these compounds are not commercially available and were synthesized as part of this project (see Chapter 2). Isooctane was included in each experimental set as an internal standard; the value listed in the table (63.3) was the average over all the experiments and it agrees well with the previously measured value (61.7) [33]. Based on the standard deviation of the isooctane results, the random uncertainty in the measured YSIs is ±2%. There is an additional systematic uncertainty of ±1% due to the possible error in the property values necessary to calculate the flowrates in the measurements. There is also uncertainty associated with comparing the new measurements with previous YSI measurements, which is estimated to be ±2%. Thus, the overall uncertainty in the results in the table is ±5% or ±5 YSI units, whichever is larger.

Table 3.1. Tabulated YSI measurements for various compounds.

Name	Abbr.	Structure	YSI
n-heptane[1]	n/a		36.0
toluene[1]	n/a		170.9
water[1]	n/a		0
isooctane[2]	n/a		63.3
CF diesel[3]	CF	n/a	246.0
dimethoxymethane	M1M	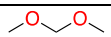	6.6
2,4,6,8-tetraoxanonane	M3M		0.5
2,4,6,8,10-pentaoxaundecane	M4M	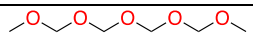	−2.5
2,4,6,8,10,12-hexaoxatridecane	M5M	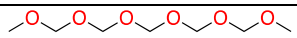	−4.8
diethoxymethane	E1E	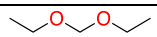	15.5
3,5,7-trioxanonane	E2E	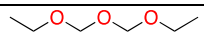	13.8
3,5,7,9-tetraoxaundecane	E3E	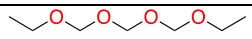	11.9
dipropoxymethane	P1P	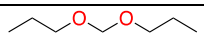	30.8
4,6,8-trioxaundecane	P2P	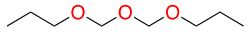	25.5
4,6,8,10-tetraoxatridecane	P3P		21.3
dibutoxymethane	B1B		46.0
5,7,9-trioxatridecane	B2B	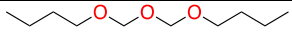	42.7
5,7,9,11-tetraoxapentadecane	B3B	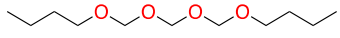	37.8
1-(methoxymethoxy)-propane	M1P	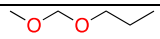	15.9
1-(methoxymethoxy)-butane	M1B	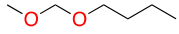	24.5
1,1-dimethoxyethane	M1M-M	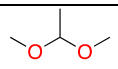	14.2
2,2-dimethoxypropane	M1M-MM	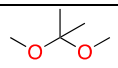	16.4
3,3-dimethoxyprop-1-ene	M1M-V	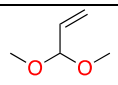	15.5
1,1-diethoxyethane	E1E-M	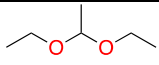	22.4
1,1-diethoxypropane	E1E-E	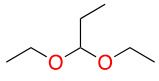	27.3

3,3-diethoxyprop-1-ene	E1E-V	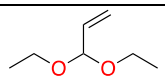	26.6
1,1-diethoxyhexane	E1E-Pe	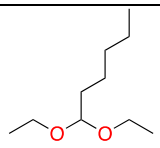	42.9
1,1-diethoxyoctane	E1E-Hep	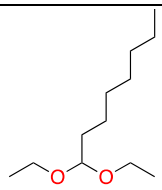	59.6
1-(1-(isopentyloxy)ethoxy)-3-methylbutane	iPe1iPe-M	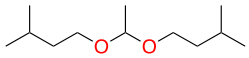	75.7
2-methoxyethanol	n/a	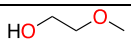	5.9
diethylene glycol	n/a	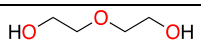	7.9
diethylene glycol diethyl ether	n/a	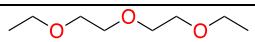	17.7
tetraethyl orthocarbonate	n/a	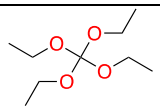	25.1

[1]These species are endpoints that were used to define the YSI scale, so their YSIs are defined values.
[2]Isooctane was included in each experimental set as an internal standard.
[3]This is a certification diesel fuel; it is described in [32].

Figure 3.4. depicts a comparison of the YSIs for the POMEs against certificate diesel. The results show that the POMEs soot much less than conventional diesel fuel. However, the POMEs also have lower heats of combustion than diesel. Therefore, the figure also shows YSI/LHV (blue data), where LHV is lower heating value in MJ/mol. YSI provides a measure of (soot/mol) since a fixed mole fraction (either 1000 ppm or 3000 ppm) of the test compound is added to the flame, so YSI/LHV provides a measure of (soot/energy) when LHV is in units of (energy/mole). The results show that YSI/LHV is also much lower for the POMEs than for diesel, so the POMEs reduce soot formation even when the difference in heat of combustion is accounted for. I.e., it may be necessary to burn more of a POME than conventional diesel fuel for an engine to do a certain amount of work, but the total soot emissions will likely still be reduced. Interestingly, while the YSI of B1B is 7 times larger than the YSI of M1M, the YSI/LHV for B1B is only 2 times larger than the YSI/LHV of M1M. This shows that the "soot penalty" associated with butyl exchange is much smaller on a (soot/energy) basis than a (soot/mole) basis.

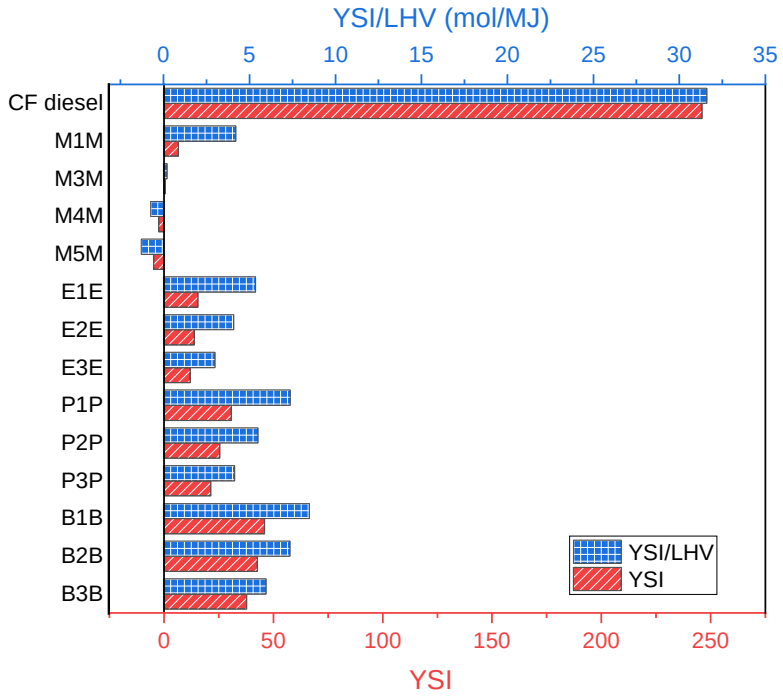

Figure 3.4. Comparison of the YSIs for the POMEs to the CF diesel (red data).

Depicted in Fig. 3.5., for each type of end group, the YSI systematically decreases as OI increases. This trend is attributed to increased dilution of the flame gases by formaldehyde (CH_2O) product molecules as OI increases. Based on the kinetic analysis in Chapter 4, the pyrolysis of the POMEs is expected to approximately follow the reactions:

M-OI-M	→	(OI+1) * CH_2O + CH_3	(R1)
P-OI-P	→	(OI+1) * CH_2O + C_2H_5 + C_3H_7	(R2)
B-OI-B	→	(OI+1) * CH_2O + C_3H_7 + C_4H_9	(R3)

The carbon atoms in formaldehyde do not contribute significantly to soot formation since they already have a double bond to an oxygen atom (e.g., the formula can be written $H_2C{=}O$). Thus, as OI increases, the molecules that contribute to soot (e.g., CH_3 for MnM) are diluted by an increasing number of molecules that are inert with respect to soot formation.

The figure also shows that the sooting tendencies increase for a given OI as the end group gets larger, e.g., YSI(B1B) > YSI(P1P) > YSI(M1M). This is presumably a consequence of the larger hydrocarbons formed in reactions R1, R2, and R3.

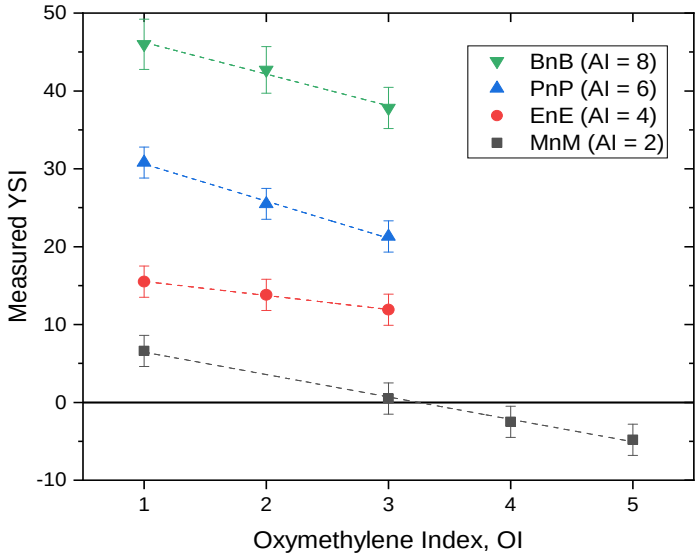

Figure 3.5. Sooting tendencies of methyl, ethyl, propyl, and butyl terminated POMEs as a function of the oxymethylene index (OI), which is the number of oxymethylene units in the POME.

The measured YSIs for the MnM compounds are extremely low, and in fact negative for M4M and M5M. These negative YSIs are attributed to dilution of soot formation from the methane background fuel by the formaldehyde formed from the larger MnM compounds. Figure 3.6. indicates that addition of M-1-M enhances soot concentrations, while addition of the other compounds suppresses soot. Argon and water both reduce the soot concentration, presumably because they are diluting the methane fuel. A similar mechanism is likely occurring for M4M and M5M. The magnitude of the suppression is larger as the number of oxymethylene units increases.

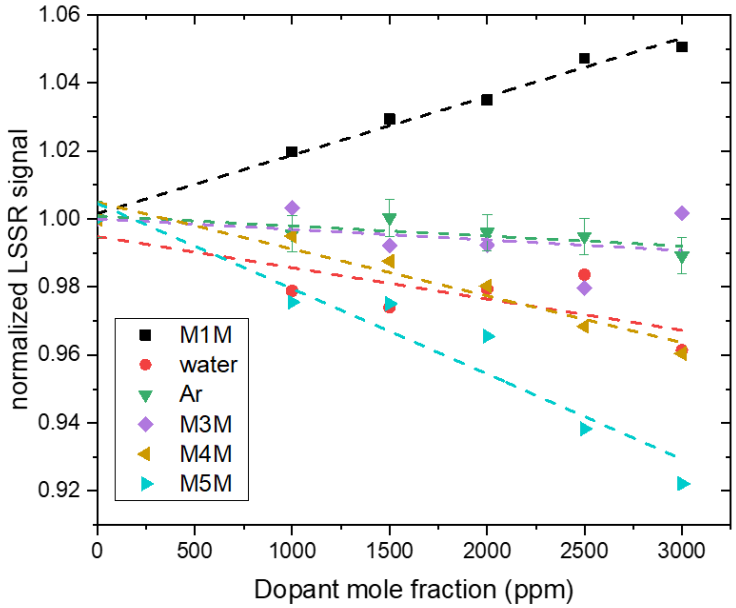

Figure 3.6. Normalized soot concentrations measured in flames doped with various concentrations of methyl-terminated POMEs (M1M, M3M, M4M, and M5M) and of inert species (water, argon).

Figure 3.7 below shows that 2-methoxyethanol has the same sooting tendency as M1M. These compounds are isomers with the same molecular formula ($C_3H_8O_2$), however, 2-methoxyethanol has one C-C bond whereas M1M has no C-C bonds. This result suggests that the low sooting tendencies of the methyl terminated MnM compounds are not solely a consequence of them having no C-C bonds.

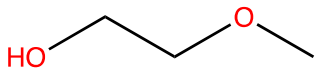

2-methoxyethanol

YSI = 5.9

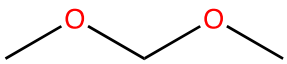

dimethoxymethane (M1M)

YSI = 6.6

Figure 3.7. Sooting tendency and molecular structure of 2-methodyethanol compared to M1M.

Based on the reaction kinetics analysis discussed in Chapter 4, the main chemical consumption pathways of POMEs in the YSI flames are likely to be unimolecular fission of C-C and C-O bonds, at nearly equal rates for each bond, followed by beta-scission of the resulting radicals. As an example, these reactions for E2E are:

CCOCOCOCC → 2/8 C* + *COCOCOCC → C* + 3 C=O + C=C + *H

CCOCOCOCC → 2/8 CC* + *OCOCOCC → H* + C=C + 3 C=O + *C

CCOCOCOCC → 2/8 CCO* + *COCOCC → C* + 3 C=O + C=C + *H

CCOCOCOCC → 2/8 CCOC* + *OCOCC → H* + C=C + 3 C=O + *C

Results of this type can be generalized to show that a general POMEs with non-branched end-groups and no side-chains on the backbone will decompose as follows:

POMEs → OI C=O + H* + (AI/2 – 1) C=C + *C

where OI = oxymethylene index = the total number of oxymethylene units in the backbone, and AI = alkyl index = the total number of carbon atoms in the two end-groups. The formaldehyde molecules (C=O) do not contribute to soot production since the carbon atom is already double-bonded to an oxygen atom; instead they suppress soot production by diluting soot formation from the other products. On the other hand, the methyl radical (*C) and ethylene molecules (C=C) do contribute to soot production. These ideas suggest that YSI should be roughly proportional to the number of carbon atoms in the hydrocarbon product molecules divided by the total number of product molecules, i.e., (AI − 1) / (OI + AI/2 + 2). Figure 3.8. below shows that this quantity does indeed correlate well with the measured YSIs.

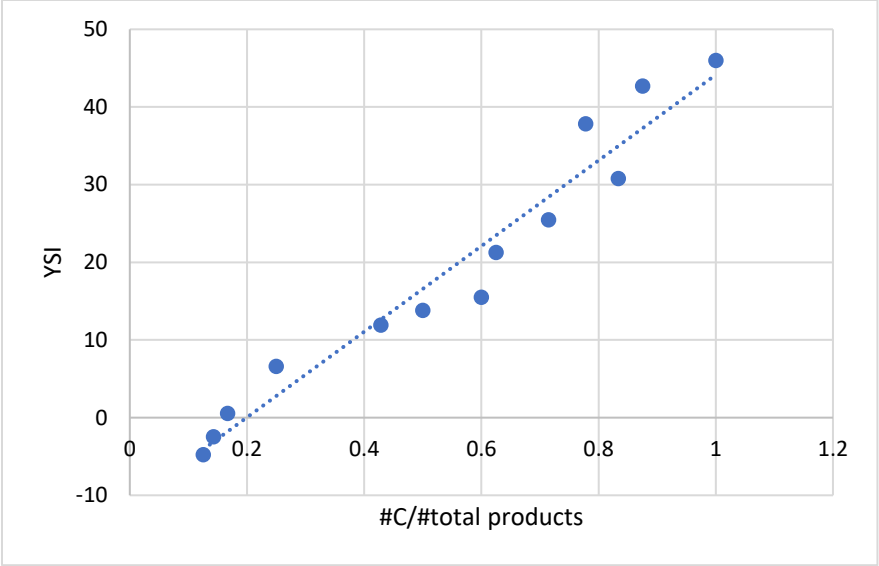

Figure 3.8. Proportionality of number of carbon atoms in the hydrocarbon product molecules to YSI.

Figure 3.9. shows how the YSI of M1M changes as the methyl end-groups are exchanged with either propyl (blue) or butyl (orange) groups. The data point on the left is M1M itself, the two data points in the middle are M1P and M1B, and the data points on the right are P1P and B1B. For both propyl and butyl end-groups, the YSI varies linearly with the number of exchanges. They show that the sooting tendency of a compound with exchange at one end-group is the average of the compounds with no exchange and with exchange at both end-groups.

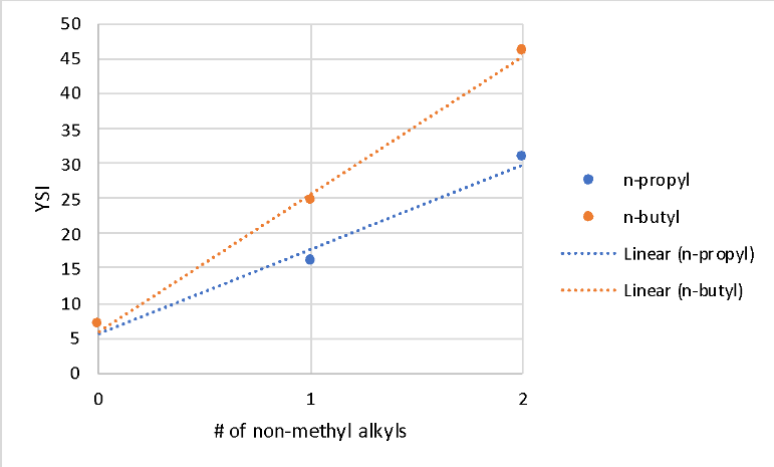

Figure 3.9. Relationship between the number of non-methyl alkyl groups in the POME molecule with its sooting tendency (YSI).

Figure 3.10. below shows the YSIs for compounds with a pendant group attached to the interior of the oxymethylene chain, and it compares them to conventional POMEs with similar carbon numbers. The compounds with red oxygen atoms are conventional POMEs with end-groups only, while the compounds with black oxygen atoms are the new compounds with both end-groups and interior pendant groups. For a given total number of carbon atoms, the sooting tendencies are similar regardless of whether the carbon is in end-groups or interior groups. For example, M1M-MM (top row center) and E1E (top row, 2nd from

right) are both $C_5H_{12}O_2$ isomers and have YSI = 16.4 and 15.5. These results show that if POMEs with interior groups have beneficial fuel properties – e.g., low melting points – then they can be used as fuels while preserving the soot reduction benefits of POMEs.

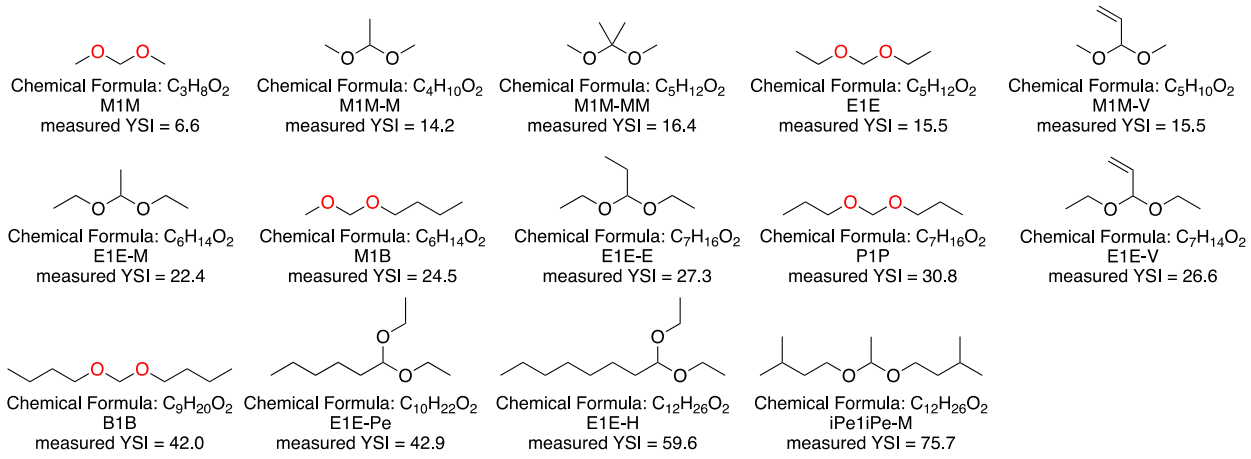

Figure 3.10. Summary of the sooting tendencies and molecular structures of the POME molecules studied.

3.1.4. Sooting Tendencies with Alternative Alcohols Used for End-Group Exchange

Most of the POMEs in this project were generated by end-group exchange with *n*-alcohols (ethanol, *n*-propanol, and *n*-butanol); however, production of these alcohols from biomass is not guaranteed to be cost-effective, so alternatives are desirable. This section discusses YSI results for a set of POME mixtures that were produced in Daniel Ruddy's group at NREL using alternative alcohols for end-group exchange. These results are presented in detail in [34].

The mixtures are summarized in Table 3.2. below. The first mixture used isobutanol as the alcohol and therefore produced POMEs with branched C4 end groups. The starting POME sample was a commercial POME mix that contained methyl-terminated POMEs with various numbers of oxymethylene units in the backbone. The second mixture used tetrahydrofurfuryl alcohol (THFA) as the alcohol and therefore produced POMEs with cyclic oxygen-containing end groups. THFA is a platform chemical that can be readily produced from sugars after deconstruction of cellulose and hemicellulose. The third mixture used a fusel alcohol mixture (sometimes referred to as fusel oil) as the alcohol. The fusel mixture mainly contained isopentanol, so the final POMEs mainly contained branched C5 end groups. Fusel alcohol is readily produced by variations of the fermentation process that produces ethanol.

Table 3.2. Structure of exchanged alcohols in POME mixtures.

Name	Exchanged Alcohol	Main Components
iB-POMEs	Isobutanol	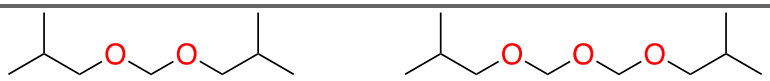
THF-POMEs	Tetrahydrofurfuryl alcohol (THFA)	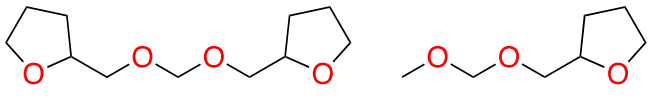

FOil-POMEs	Fusel alcohol mixture	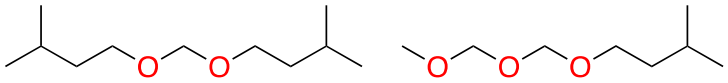

Table 3.3. below lists the YSIs measured for these samples. All the values are much smaller than the values for petroleum-derived diesel fuels, which are typically around 250. Thus these mixtures significantly expand the pool of POME structures demonstrated to have favorably low sooting tendencies.

The table also lists predicted YSIs that were obtained by (1) using the NREL YSI estimation tool discussed in Section 3.a.5 to predict the YSIs of the individual components, and (2) combining these values with a linear mixing rule:

$$\mathrm{YSI}_{\mathrm{mix}} = \sum_{j} x_j \times \mathrm{YSI}_j$$

where $\mathrm{YSI}_{\mathrm{mix}}$ is YSI of the mixture, x_j is the mole fraction of component j, and YSI_j is the predicted YSI for component j.

Table 3.3.YSIs measured for the POME mixtures.

Name	Measured YSI	Predicted YSI	Predicted YSI for linear analogue
iB-POMEs	39.7	38.5	29.9
THF-POMEs	28.2	35.5	n/a
FOil-POMEs	49.9	45.9	38.1

Figure 3.11. compares the measured and predicted YSIs. The predictions are quite accurate for the iB-POME and FOil-POME mixtures, but the YSI of the THF-POME mixture is significantly overpredicted. The YSI of THFA is similarly overpredicted, which suggests that the overprediction is associated with the cyclic structure. The NREL tool relies on an empirical group contribution method (GCM) which only considers the interaction of each carbon atom with its nearest neighbors; thus, it often has difficulty with cyclic structures where longer-range interactions are important.

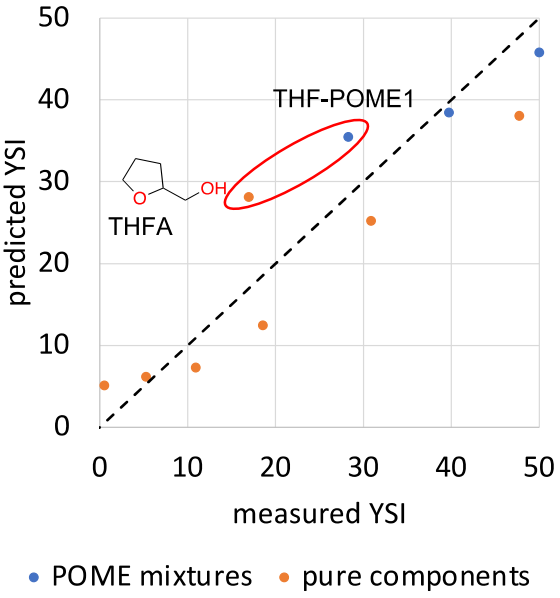

Figure 3.11. Comparison of the measured and predicted YSIs of the POME mixtures.

The THF-POME mixture contains components with both end groups exchanged (THFA-1-THFA) and with only one end group exchanged (THFA-1-M), so it is not possible to directly determine the YSI of these components. However, the YSIs can be estimated if the YSI is assumed to vary linearly from compounds with no end group exchange to compounds with one end group exchanged to both end groups exchanged. This analysis leads to the progression of values shown below in Fig. 3.12. Interestingly, the YSI for THFA-1-THFA is nearly the same as the value for B-1-B (46.0), even though THFA-1-THFA has an additional carbon atom at each end. This shows that the tetrahydrofuranic structure can reduce the soot penalty associated with additional carbon atoms.

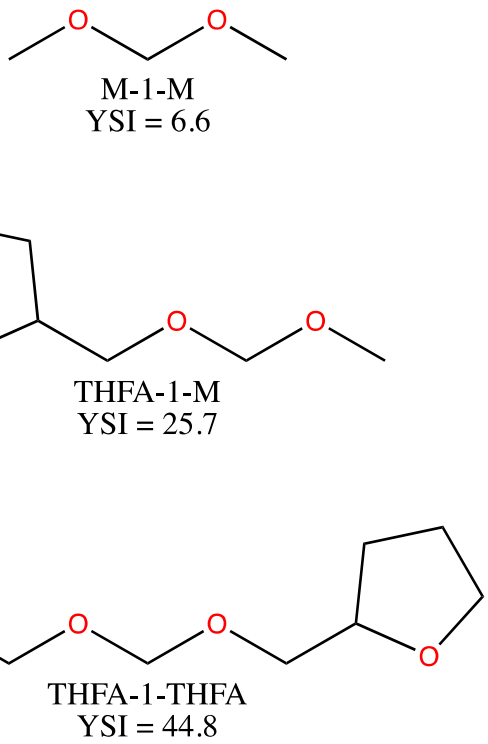

Figure 3.12. Progression of YSIs based on the assumption that YSIs vary linearly from compounds with no end group exchange.

Reaction pathway analysis indicates that pyrolysis of the branched end groups leads to larger alkenes and oxygenates than pyrolysis of the linear end groups. To test the effects of this difference on formation of aromatic hydrocarbons and soot, well-mixed reactor simulations were performed at 1500 K and 1 atm for methane doped with either (A) 10,000 ppm CH_2O + 20,000 ppm C_2H_4 or (B) 10,000 ppm CH_3CHO + 10,000 ppm C_3H_6. These mixtures have the same total number of carbon and oxygen atoms, but in (A) all the carbon atoms in a butyl end group have been converted into alkenes, whereas in (B) some of the carbon atoms have partitioned into the oxygenated product. Figure 3.13. below shows that case (B) produces significantly more benzene; this result is consistent with the higher sooting tendencies measured for the branched end group POMEs.

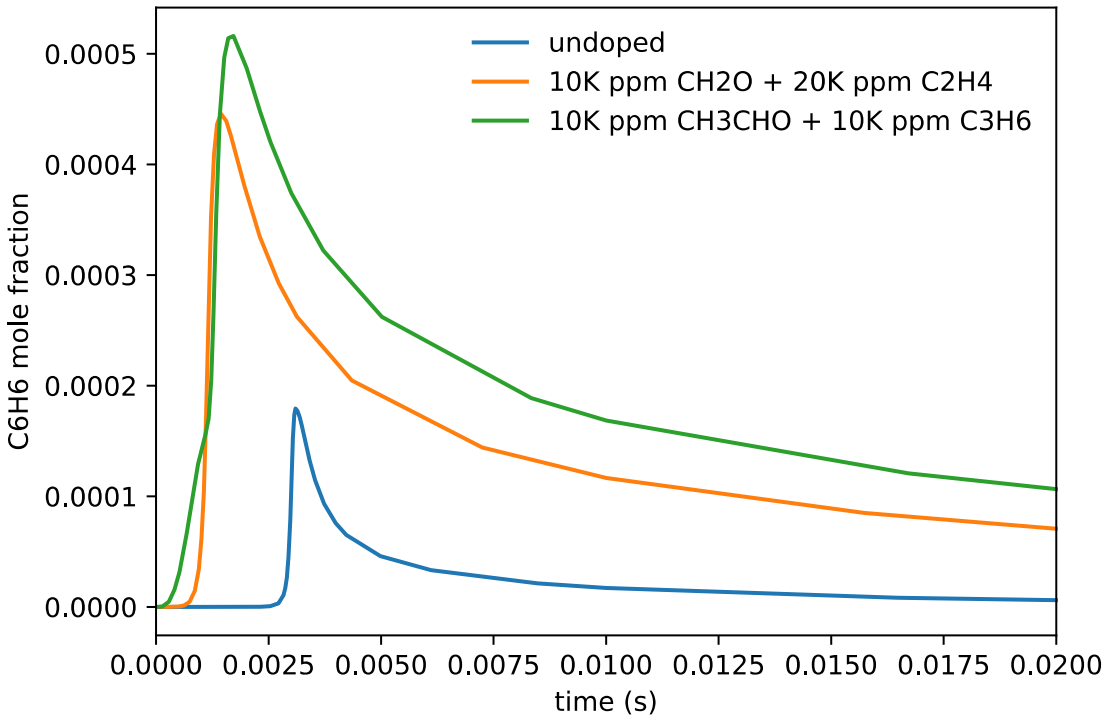

Figure 3.13. Temporal soot formation in a well-mixed reactor simulation for methane doped with either (A) 10,000 ppm CH_2O + 20,000 ppm C_2H_4 or (B) 10,000 ppm CH_3CHO + 10,000 ppm C_3H_6. Simulations performed at 1500 K and 1 atm.

3.1.5. Dissemination of Results

All the sooting tendencies measured in this study have been made available to all stakeholders via the NREL YSI Estimator. This tool is available at https://ysi.ml.nrel.gov. It allows users to search for a molecule, either by entering its SMILES code or drawing it. The tool then lists the measured YSI (if one exists) and predicts the YSI using the structure-property relationship developed in [33]. A key attribute of this tool is that it recalculates the structure-property relationship on-the-fly each time it generates a prediction; thus, as new compounds are added to the training database, the predictions become more accurate and applicable to a larger set of potential fuel molecules.

The training set is maintained as a CSV file on Peter St. John's Github account at https://github.com/pstjohn/YSIs_for_prediction. All the YSIs measured in this project have been added to this file. Thus, they are available via the YSI estimator tool and its predictions for POMEs are significantly improved. The screenshot below shows the output for M3M as an example.

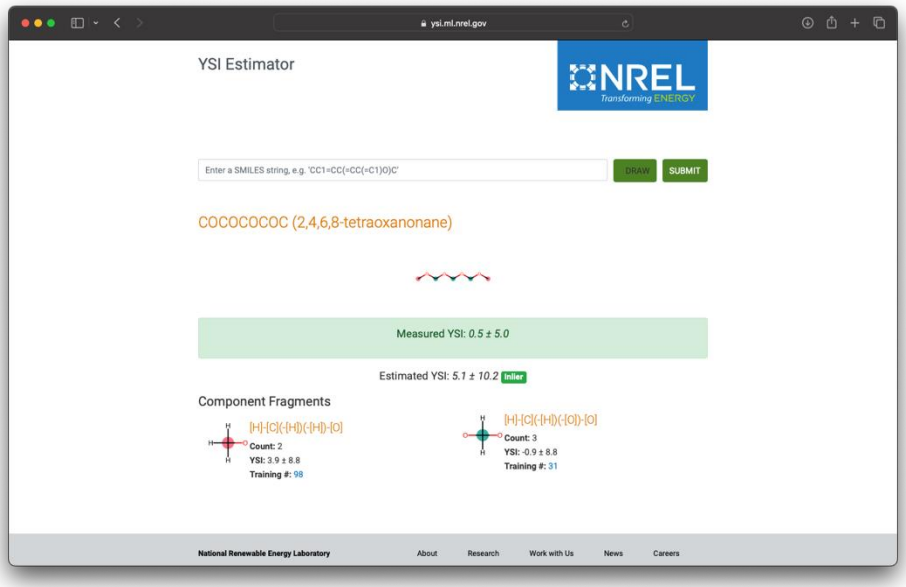

Figure 3.14. Screenshot of the YSI Estimator available at https://ysi.ml.nrel.gov.

3.1.6. Sooting Tendency Measurements for Other Co-optima Projects

The sooting tendency measurements were focused on POMEs since they were the topic of this project. However, collaboration was one of the keystones of the Co-optima Project, so YSIs were also measured for fuels produced by several DOE National Lab partners and for several of the other FY18 Co-optima university projects. These results are briefly summarized here.

- Sooting tendencies were measured for a series of bicyclic and multicyclic alternative diesel fuels synthesized from biomass by Lelia Cosimbescu's group at PNNL. The results are presented in [35]. They showed that these fuels produced 24 to 51% less soot than conventional diesel fuel.
- Sooting tendency was measured for a sustainable aviation fuel (SAF) derived from food wastes by Derek Vardon's group at NREL. The results are presented in [36]. They showed that this fuel produced 34% less soot than conventional jet fuels.
- Sooting tendencies were measured for two algae-derived alternative diesel fuels produced by the Michigan/André Boehman university project. The results showed that these fuels produced 34 and 41% less soot than conventional diesel fuel.
- Sooting tendencies were measured for a series of surrogate mixtures prepared by the Stony Brook/Dimitris Assanis university project to represent possible compositions of their naphthenic alternative diesel fuels. The results showed that these fuels produced 15% to 30% less soot than conventional diesel fuel and provided input for formulating the final fuels to have the lowest soot emissions possible.
- Structure-property relationships for predicting YSI were developed in collaboration with the UMass-Lowell/Hunter Mack university project. This work is reported in [37]. Based on this model and a corresponding model for cetane number, the four compounds shown below were identified as promising alternative diesel fuel components. These compounds had not been previously considered as fuels but had low predicted YSI and high predicted cetane number. The YSIs of these compounds were then measured and their favorable soot properties were confirmed.

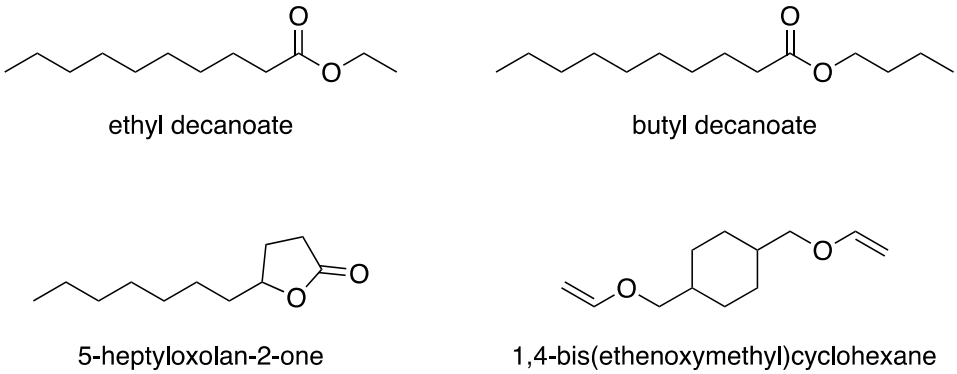

Figure 3.16. Compounds identified as promising alternative diesel fuel components based on the structure property relationships used to predict YSI developed here.

3.2. Ignition Behaviors

Here we present the ignition behaviors of the synthesized POMEs. Measured indicated cetane numbers (ICN) are provided for select POMEs, which emulates/describes the spray/two-phase ignition process experience by the fuel in an MCCI engine. In addition, ignition delays were also measured using the CSU RCM, which play a important role in the validation and construction of chemical mechanisms.

3.2.1. Indicated Cetane Numbers

Indicated Cetane Number (ICN), ASTM D8183 [38]. This method is certified in the range of 35 < *ICN* < 85, and while it can measure results outside this range, the accuracy is not guaranteed in the standard. Work by Abel et al. has shown that this method has good agreement with other CN measurement standards in normal diesel ranges, and that only for extremely high or low reactivity fuels do the several common methods start to diverge [39]. These tests were performed in a Seta Analytics Advanced Fuel Ignition Delay Analyzer (AFIDA).

3.2.1.1 ICN Results

ICN was measured as the average of two tests due to the larger quantity of fuel required (approximately 40 mL per test). For all fuels, 2000 ppm of Infineum R655, a lubricity additive, was mixedwith the fuel to ensure proper injector operation. Testswith P-1-P and B-1-Bwithout the lubricity additive showed negligible (<0.3) change in ICN due to this additive. The values are presented in Table 3.1. On-road diesel fuels in the US are typically ICN>40, with Texas requiring ICN>48 and California requiring ICN>53. The EU requires ICN>51.

Based upon these criteria, it is found that M-2-M and longer methyl OMEs, and all ethyl, propyl (except iP-1-iP), and butyl OMEs meet the minimum US requirements, and for maximum compatibility, M-2-M and higher, E-2-E and E-3-E, and all propyl (except iP-1-iP) and butyl OMEs are the best candidates. Larger alkyl groups are less sensitive to the length of the oxymethylene chain on ICN, up to the point where the ICN of butyl-terminated OMEs appears entirely independent of the number of oxymethylene units. The kinetics of extendedalkyl OMEs are a new frontier in combustion chemistry; some recent works by Kroger et al. [40], Jacobs et al. [41], and Li et al. [26] have considered the kinetics of E-1-E, but no detailed chemical studies of larger extended-alkyl OMEs have been published. In a later section, this work considers ignition behavior of E-1-E, E-2-E, P-1-P, and iP-1-iP in a rapid compression machine, wherein it is hypothesized that the additional sites available for RO2 pathways on the longer alkyl groups such as propyl have significant effects on ignition, which may cause the decreased effect of chain length as alkyl groups are extended. Understanding the full causes of these ignition behaviors will require significant future study in fundamental theory and experiments.

Of particular note are the behaviors of the iso-OMEs, iP-1-iP and iB-1-iB. These have significantly lower ICN than their linear counterparts P-1-P and B-1-B, by 79% and 30% respectively. This is not an entirely unexpected result; for example, n-octane has a CN of approximately 65 (depending on the exactmeasurement method), while its branched counterpart iso-octane has CN approximately 17 [42]. While detailed chemical mechanisms have not been developed for any propyl- or butyl-terminated OMEs, work onmethyl- and ethyl-terminated OMEs indicates that RO2 chemistry remains an important step in the ignition of these fuels [26,40,41], and thus similar effects on inhibition of RO2 pathways via branched structures are to be expected. While ICN cannot be directly converted to either formof octane number (RONorMON), it is clear that many fuels with high octane numbers have low cetane numbers; the ICN of iP-1-iP is similar to that of iso-octane, and this may warrant investigation of iP-1-iP as a potential gasoline, rather than diesel, additive.

In the corrigendum to their 2016 analysis of M-n-M and E-n-E OMEs, Lautenschütz et al. review cetane numbers, also using an AFIDA device [9]. We find lower ICN for all comparable OMEs than Lautenschütz, with an average difference of 13% lower ICN; the least difference is in the E-2-E measurement (4.5% lower) and the highest in M-2-M (21% lower). Drexler et. al. [10] tested E-1-E, P-1-P, and B-1-B in an AFIDA; we find similar results to this work, where the highest difference is a 3.2% higher ICN for P-1-P. In either case, the conclusions are similar – most OMEs other than M-1-M, and in some jurisdictions E-1-E, meet diesel requirements for reactivity.

Table 3.4. Indicated Cetane Number of various OMEs

End Group	Number of CH2O Units				
	1	2	3	4	5
Methyl	25.6	56.1	64.0	71.1	85.2
Ethyl	41.1	60.3	59.4		
Propyl	53.2	59.3	66.1		
Butyl	76.3	76.9	76.0		
iso-Propyl	11.2				
iso-Butyl	53.2				
Typical Diesel	>40				

3.2.2. Ignition Delay

3.2.2.1 Rapid Compression Machine

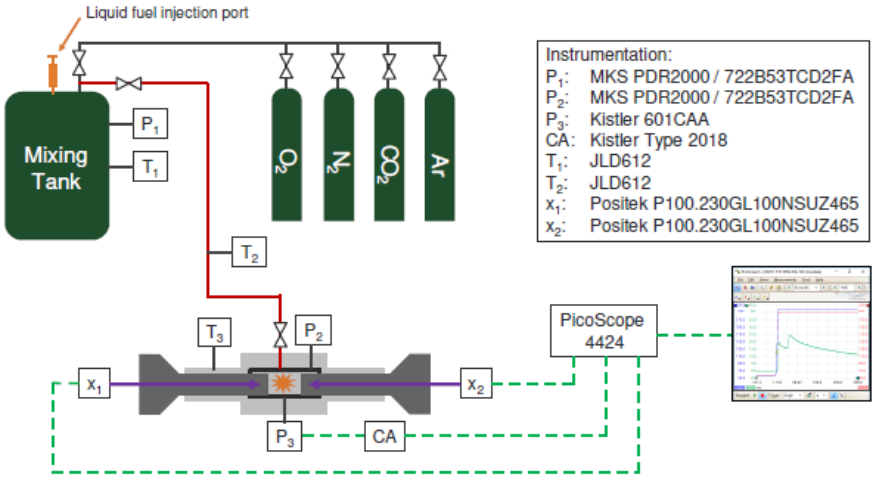

Figure 3.17. RCM system schematic.

The CSU Rapid Compression Machine was the focus of the majority of the combustion experiments. RCMs are a common device for testing of fundamental combustion behaviors; along with shock tubes, they are often used for measurement of prevaporized IDT to characterize fuels and provide data for kinetic model development. Sung and Curran [43], and recently Goldsborough et al. [44] provide excellent reviews of the uses of these machines. In summary, RCMs operate via rapid compression of a gas and fuel mixture to simulate the stroke of a reciprocating engine, or more generally to quickly create high-temperature conditions for combustion. Ideally, RCMs could be treated as true isentropic devices, however, heat losses to the walls prevent true isentropic behavior. As pressure can be more easily measured than temperature at high rates, the temperature is typically calculated as an integral over the actual pressure trace, incorporating changes in specific heat ratio γ [43]. This is referred to as the adiabatic core hypothesis and assumes that while heat losses occur at the wall, the core of the gas mixture at compression can be evaluated as the isentropic compression of the pressure-based compression ratio (as opposed to the geometric, volume-based compression ratio). Modern RCMs typically use pistons with creviced faces to reduce vortices around the perimeter of the piston (“roll-up vortices”), which improves the accuracy of the adiabatic core hypothesis [45].

In addition to the heat loss to the walls, an additional facility effect which can have significant effect on IDT measurement accuracy is the presence of reactions during the compression stroke. Shock tubes have extremely rapid heating, with the gas being heated and compressed through the extremely thin shock wave which travels at greater than sonic speed, effectively eliminating this facility effect, however, RCMs are capable of lower compressed pressures and thus continue to be of interest despite this flaw [46]. As opposed to the near-instantaneous shock heating effect, the heating in the RCM happens on millisecond ranges; e.g. the CSU shock tube compression stroke is approximately 18 ms in duration. Particularly at higher temperatures or for more reactive fuels, a significant portion of the reaction can occur during the compression stroke so that IDT is not effectively measured from piston top-dead-center (TDC). Mittal et al. show this using dimethyl ether as a test fuel [47], wherein including the compression stroke in the model allowed more accurate prediction, indicating the presence of significant reaction during the stroke.

The CSU machine is a dual-piston, pneumatically-driven, hydraulically-locked device with multiple available chambers for different purposes. The geometric compression ratio of this device is approximately 11.4 in the chamber used for autoignition; the chamber for flame speed has larger dead volume from windows and has a geometric compression ratio of approximately 10.7. Creviced pistons are used to minimize roll-up vortex effects on the gas core. Pressures and temperatures are controlled via initial settings (fill pressure and sleeve temperature via heat tape) and variation of γ of the gas mixture by changing composition of the inert mixture between CO2, N2, and Ar. Monitored low-speed variables are initial pressure and initial sleeve temperature. High speed variables are piston positions (easily convertible to volume) and chamber pressure. Gas mixtures are created in a heated mixing tank. Liquid fuel is first added volumetrically to a tank at vacuum, and then gases are added via partial pressure to achieve the desired inert mixture and equivalence ratio (Φ). The gas mixing code accounts for temperature changes during the filling process to reduce errors in mixture composition. A system schematic in Figure 3.17 details the instrumentation used.

For spark ignition testing, a laser spark was used. Use of a focused laser spark as an ignition source is reviewed by Phuoc et al. [48] and Morsy et al. [49], and has some advantages and disadvantages. A major advantage is the lack of physical objects in the core of the compressed gas, as would be the case for electrodes or a spark plug – this allows for improved visibility of the gas and flame expansion. However, initial flame kernels from laser sparks are not spherical; two counter-rotating regions on opposite sides of the laser path are the initiation regions for combustion. In some cases, a third lobe is also observed on the laser path; this is documented but the physics are less well understood [48]. In the tests here, this asymmetric flame initiation is observed, but in most cases rapidly transitions to mildly wrinkled spheroids and does not cause significant difficulty in measurement of flame speed, although as will be shown, lower temperature flames may retain the lobed asymmetry. In lean and rich combustion, laser ignition has been shown to have similar ignition energy requirements to electric sparks, but at near-stoichiometric conditions, it has been shown to require higher energy input for ignition [48]. The laser ignition system used on the CSU RCM consists of a Quantel Q-smart laser, model QSM100-20-G, focused down to a point in the center of the chamber with a 60mm focal length plano-convex lens. For flame measurements, an optical system is required. A chamber with large (26 mm visible diameter) windows was used, and an LED light source used for Schlieren imaging following the schematic in Figure 4.2. The camera used is a Photron FastcamSA5, model 775K-M4, set at 42000 fps and 512x320 resolution (equivalent to 10.8 pixel/mm in this particular setup). Figure 4.3 shows a sample flamefront from this method, showing the initial asymmetric flame kernel and subsequent development to an approximately spherical flame.

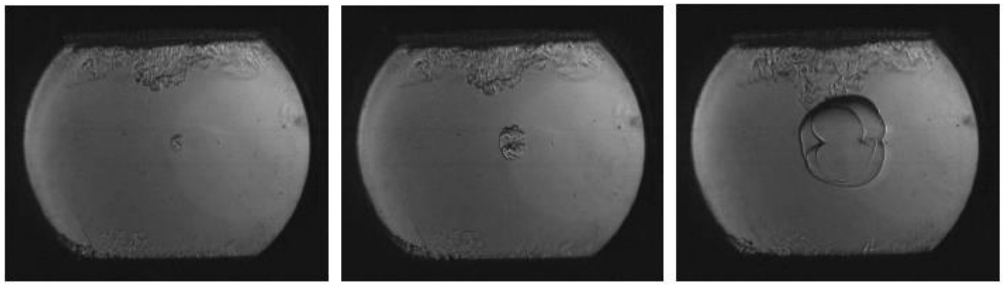

Figure 3.18. Representative Schlieren images of flamefront at 1, 10, and 100 frames (0.024, 0.24, and 2.4 ms) after the laser spark, from stoichiometric iP-1-iP in N2.

3.2.2.2. RCM Autoignition Analysis

RCM high-speed and low-speed data are analyzed in MATLAB to identify TDC conditions and autoignition events. Some prior code from A. Zdanowicz was used as the skeleton for this analysis, but significantly modified and rewritten for this work.

Output data from the PicoScope is saved as a CSV file and imported into MATLAB. Piston positions are extracted and converted to volume. Pressure data is filtered at two separate levels with low-pass Butterworth filters. A higher passband filter is used to identify TDC location with minimal phase shift or loss of resolution, and a lower passband filter applied for the actual analysis to reduce noise. Time is offset to TDC = t0. TDC conditions are calculated using the adiabatic core hypothesis, where the initial temperature is set, and then at each timestep (Δ = 5.0x10-7) the new temperature is calculated from the ΔP across that timestep. γ is recalculated at each timestep. The polynomials for gases – Ar, N2, O2, and CO2 – are calculated from the polynomials in Lawrence Livermore's n-Heptane v3.1 mechanism [50]. Polynomials for OMEs are either taken from literature (available for E-1-E from Li et al. [51]), or generated via group contribution methods from the MIT Reaction Mechanism Generator (RMG) [52]. The MIT RMG calculation of thermodynamic polynomial coefficients was compared to the polynomials in Li and found to be within 5% for 600 K - 1000 K, indicating acceptable accuracy of RMG for the undocumented fuels.

In the first set of RCM tests, highly dilute conditions were used (12:1 inert:O2 ratio), which produced low dP/dt, and thus necessitated a slightly different definition of the start of autoignition. Typically, RCM IDT is defined either by the inflection point in the pressure rise from ignition, where IDT is assigned either as the time of the inflection, or the time of the root of the tangent to the pressure at this inflection point [53]. For high dP/dt, this method produces IDT which are essentially indistinguishable, however, for low dP/dt, the root of the tangent can occur well before the time when pressure rise begins, or the inflection point itself well after. Thus, we use a method where the tangent to the inflection point is intersected with the (horizontal by definition) tangent to the local minimum in pressure before pressure rise. This is similar to a method often applied to OH* measurements for IDT [54], however, here it is applied to pressure rather than OH*. For high dP/dt, there is little difference between this and the common methods, while for lower dP/dt, this method sits in between the two. As two-stage ignition was observed at low temperatures, this method had to be applied twice in these cases. A sample pressure trace showing this methodology is provided in Figure 3.19.

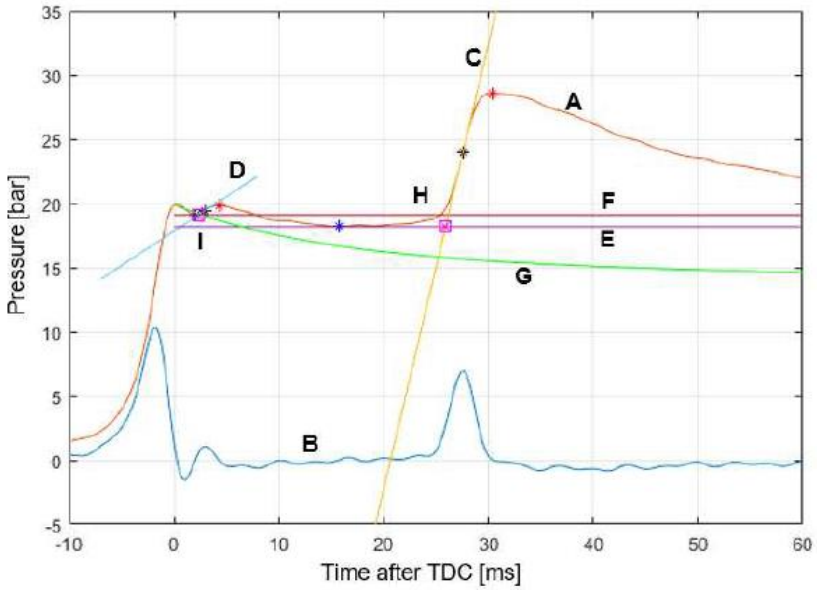

Figure 3.19. Example algorithm for solving IDT with a low *d*P/*d*t. *Line A*: Filtered pressure trace. *Line B*: Gradient of pressure. *Line C*: Tangent to pressure at maximum gradient (primary event). *Line D*: Tangent to pressure at maximum gradient (first stage event). *Line E*: Tangent to local minimum pressure (between first and primary event). *Line F*: Tangent to local minimum pressure (between TDC and first event). *Line G*: Nonreactive pressure curve, calculated from double-exponential function fitted to normalized and scaled average of three nonreactive pressure traces for the appropriate gas mixture. *Point H*: Intersection of Line C and Line E. Defines primary ignition delay. *Point I*: Intersection of Line D and Line F. Defines first stage ignition delay. For single-stage ignition, lines D and F and point I are not calculated, and Line E occurs between TDC and primary ignition.

As the compression temperature at TDC is calculated from the pressure trace, assuming an isentropic core [43], the method of pressure trace filtration can affect the peak (TDC) temperature and pressure. The variance was found to be approximately +/-5 K and +/-0.1 bar within the range of half power frequencies that produce an accurate, low-noise pressure curve from a lowpass filter. The compression stroke produced the target pressures to an average of 20.1 bar with 1.55% (0.311 bar) standard deviation. Initial temperatures were measured via a thermocouple to an accuracy of +/- 1 K, which transforms to +/- 3.55 K for an average effective compression ratio of 10 (see Table S1 for these values) in a 40%N2 / 60% Ar bath gas environment (the highest γ gas mixture used). Combining errors, the pressure is accurate to +/- 0.327 bar, and the temperature to +/- 6.13 K. Using sample E-1-E pressure traces at 720 K and 915 K (2 stage and single stage ignition), testing the range of reasonable filtering techniques provided a range of +/-7% for first stage IDT and +/-5% for primary IDT. Temperature errors of +/-6.13 K at 720 K and 915 K produce IDT errors of +/-6% and +/-1%, respectively. Combining these errors, we expect an accuracy of +/-11% for IDT measurements.

3.2.2.2. Pre-Vaporized Ignition of E-1-E, E-2-E, P-1-P, and iP-1-iP

Four OMEs were selected for this analysis, each representing a unique modification in the structure of the OME. The structures and calculated bond energies for these molecules are presented in Figure 3.20. Here we label each of the carbons for ease of discussion, starting with the end group carbon closest to the ether oxygen labeled as α, and so forth. For all OMEs presented, all carbons between the ether moieties are labeled δ for consistency.

The simplest OME tested in this study is E-1-E, the ignition and kinetics of which have been previously studied, providing a basis for comparison to our results [40,55–57]. P-1-P is a fuel which, to my knowledge, has not been studied for its ignition or fuel characteristics in any previously published work; this fuel is used to consider the effects of lengthening the alkyl terminations. The fuel-relevant properties of E-2-E have been studied prior by Lautenschutz [9], but no kinetics or ignition delay experiments have been performed. Finally, iP-1-iP is a new, unstudied molecule, representing a change from a linear OME structure analogous to normal alkanes, to a branched OME structure analogous to iso-alkanes. Each of these molecules have similar bond dissociation energies (BDEs) for equivalent bonds as shown in units of kcal/mol in Figure 3.20. All BDE values were obtained using the ALFABET tool from the National Renewable Energy Laboratory (NREL) [58,59]. When available, density functional theory values were preferred over machine learning values.

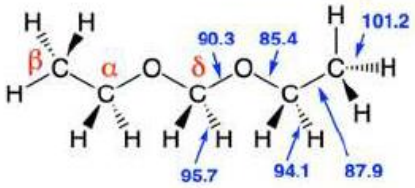

E-1-E Structure

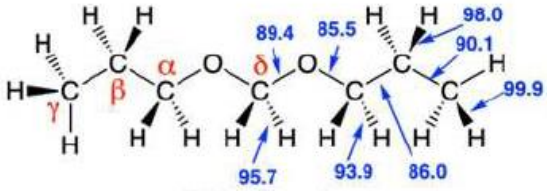

P-1-P Structure

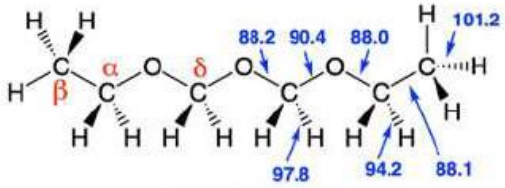

E-2-E Structure

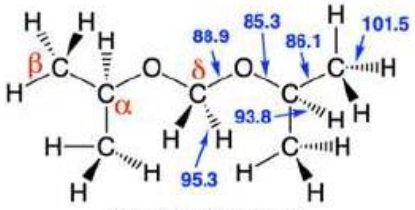

iP-1-iP Structure

Figure 3.20. OME Structures: Red greek letter indicate carbon labels. Blue numbers indicate bond dissociation energies in kcal/mol from [58,59]

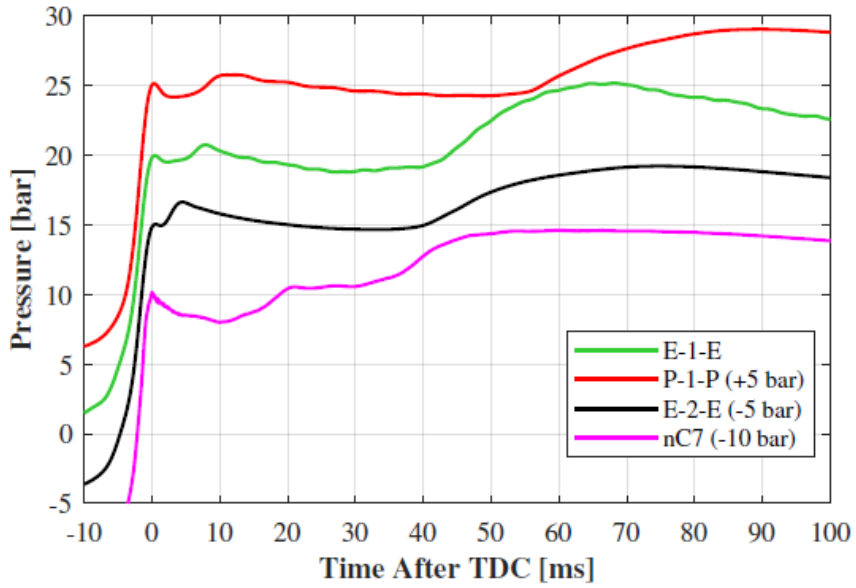

Figure 3.21. Pressure traces for representative tests at 700K and 20 bar compressed pressure, F= 1.0, 12:1 inert:O2. (note that pressure offsets have been applied to prevent overlap)

The observed ignition behavior of the OMEs generally fell into three categories: at lower temperatures, the linear OMEs (E-1-E, E-2-E, and P-1-P) demonstrated multi-stage ignition with relatively low pressure gradients (see Figure 3.21). As the temperature increased, the first stage ignition disappeared, resulting in single stage ignition with a faster rate of pressure rise. Finally, the branched OME (iP-1-iP) only ever demonstrated single stage ignition; further, this fuel was incapable of ignition at the 20 bar compressed pressure used in earlier tests. At 30 bar, high temperatures were required to initiate ignition and the IDT fell rapidly with increasing temperature afterward.

The primary IDT for all of the tests at 20 bar where ignition occurred (tests at temperatures too low for ignition were performed, but are not shown here) is shown in Figure 3.22. First stage IDT, when observed, are shown in Figure 3.23. In Figure 3.24, the calculated IDT of n-heptane [50] using Chemkin simulation provides a reference to a more well-studied fuel; similarly, Figure 3.25 includes calculated iso-octane IDT. Additionally, Figure 3.23 contains simulations of M-1-M [51], M-2-M [60], M-3-M [61], and E-1-E [41] from literature to show where the measured values compare to kinetic mechanisms for other, primarily methyl-terminated, OMEs. We consider the chemical basis of observed behavior later in this section; however, on a broad scale there are some basic observations. First, we observe that all of the tested linear OMEs show strong nonlinear temperature dependencies, but not true negative temperature coefficient behavior as seen with n-heptane. Secondly, iP-1-iP behaves similar to iso-octane without apparent nonlinearity, but has delayed ignition.

Prior literature, e.g. [62], notes that discontinuities in IDT curves may occur with changes in diluent gas composition, particularly with increasing argon concentration, where ignition slows for a given temperature condition due to thermal effects. We note some of this behavior in our data, most apparently for the P-1-P at just above 1000/T = 1.1; for E-1-E and E-2-E these effects are observable but less apparent

as they occur in a region where the IDT is nearly unaffected by the temperature and thus thermal effects will produce less noticeable changes in IDT. Prior literature studying fuels with established chemical mechanisms, e.g. [47,63], have noted that at higher temperatures and shorter IDTs, the effects on IDT of radical formation during the compression stroke may not be negligible. Consequently, we caution the reader that the reported high-temperature IDT may be shorter than would occur if TDC conditions were achieved instantaneously without facility effects, and simulations of these conditions should include the compression stroke.

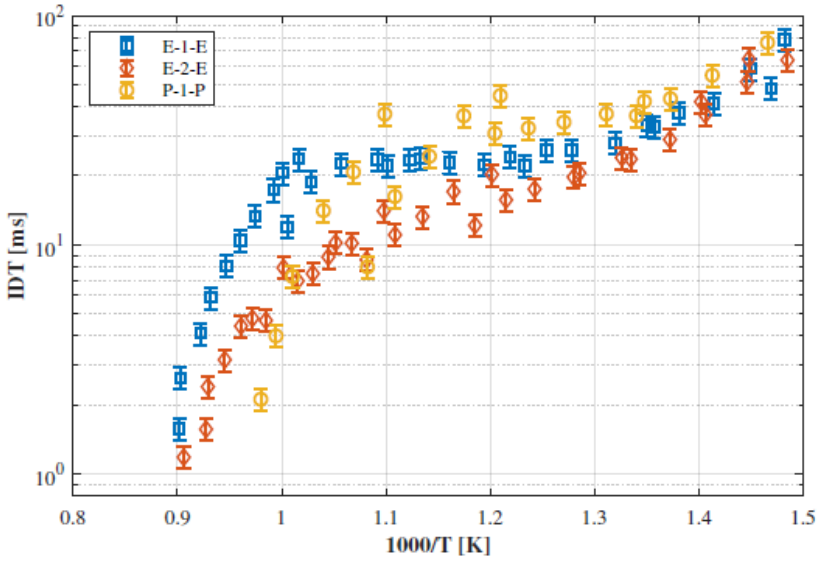

Figure 3.22. Calculated primary IDT of linear OMEs at 20 bar compressed pressure, F= 1.0, 12:1 inert:O2

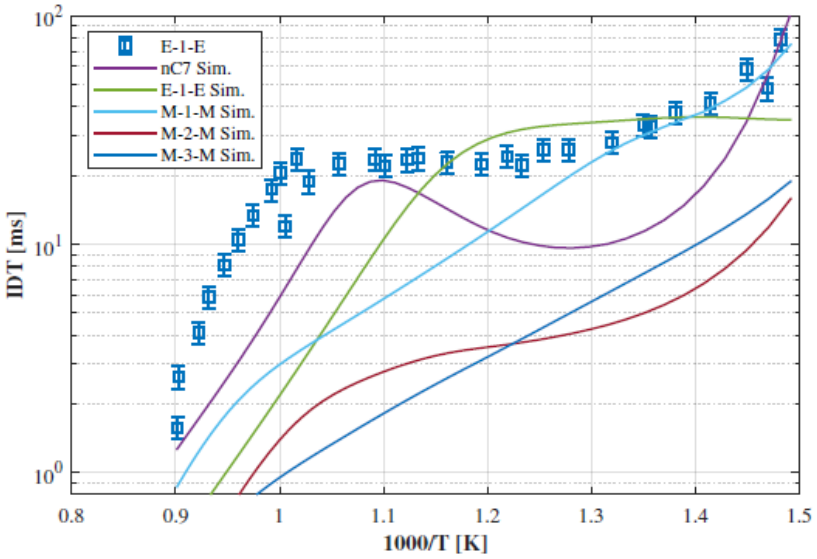

Figure 3.23. Calculated primary IDT of E-1-E with various mechanisms of nC7 and OMEs at 20 bar compressed pressure, F= 1.0, 12:1 inert:O2 [64–68].

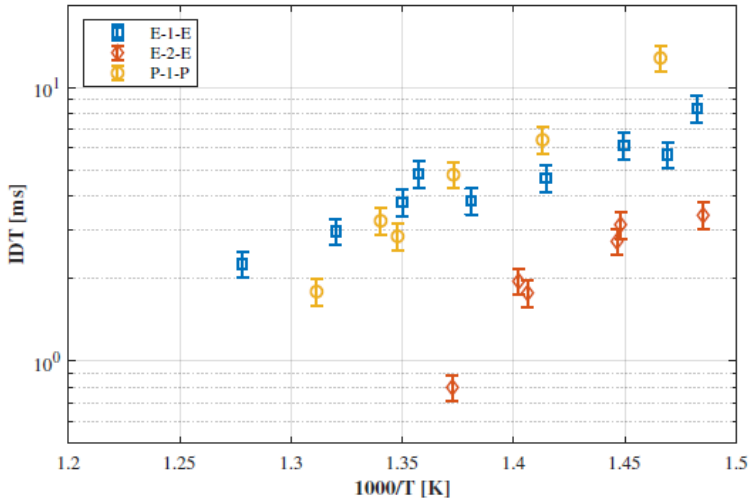

Figure 3.24. Calculated first stage IDT of linear OMEs at 20 bar compressed pressure, F= 1.0, 12:1 inert:O_2

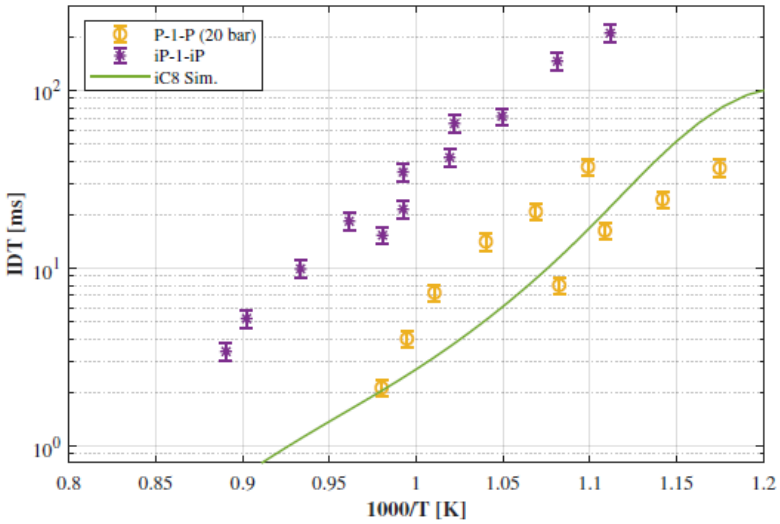

Figure 3.25. Calculated IDT of iP-1-iP at 30 bar compressed pressure, F= 1.0, 12:1 inert:O2 compared with P-1-P at 20 bar and simulation of iC8 via LLNL v3.0 mechanism [69]

As a primary point of comparison, we will first consider the behavior of E-1-E, as its ignition has been characterized; we direct the reader to [40,66,70] for detailed discussion of the kinetics of this fuel. Here, E-1-E shows a wide region (750 - 1000 K) where IDT is essentially independent of temperature. Lehrheuer et al. [71] observed similar behavior in prior RCM testing of this fuel at these dilute conditions (we note that their observed IDT is faster as their tests were performed at 30 bar compressed pressure); similarly, kinetic modeling by Li et al. [70] shows a small temperature-independent region, although their modeling is primarily performed with standard air (3.76:1 inert to oxygen ratio).

Effect of Extending the Oxymethylene Chain - Using E-1-E as a reference, it can be observed that adding an additional oxymethylene unit (E-1-E –> E-2-E) advances the ignition at moderate to high temperatures (although it is worth noting that at low temperatures, <750 K, E-1-E and E-2-E have comparable IDT), and

advances the temperature where IDT begins to rapidly decrease. This behavior is similar to that observed by Cai et al. [68] when transitioning between methyl-terminated OMEs of various oxymethylene chain lengths, although one can note from the above work that this reduction appears to have a diminishing effect as the chain length continues to increase, with the largest change occurring with an increase from one to two oxymethylene units. Additionally, as shown in Fig. 3.21, at low temperatures, the first stage ignition of E-2-E is faster by a few milliseconds - not a large change in comparison to the primary IDT, but roughly twice as fast as E-1-E for the first stage only. A test of n-heptane at comparable conditions shows that the n=1 OMEs have similar first stage ignition timing to n-heptane, while the all of the OMEs have slower primary ignition at these low-temperature conditions.

In their analysis of diethoxymethane decomposition, Jacobs et al. [66] found that as temperature was increased, the diethoxymethane radical formed after H-abstraction from the central methylene group (analogous to the δ-E-1-E radical) and rapidly β-scissioned to form ethyl formate rather than react bimolecularly with O2 to form a peroxyl radical, essentially inhibiting hydroxyl formation and retarding ignition. Notably, the reaction rates for the decomposition of δ-E-1-E used in their model were the highest pressure rates from Kroger et al. [40] and may be too fast by as much as a factor of 20 for the 10 bar IDT experimental conditions, potentially exaggerating the observation. Li et al. [70] similarly noted the importance of the δ-E-1-E radical on inhibiting ignition at higher temperatures, though they attributed the effect to the lesser number of unique peroxyl radicals that can be formed as compared to the other diethoxymethane radicals. Similar arguments may be made to explain the faster reactivity of E-2-E. Fig. 3.20 shows that the C-O bond attached to α-carbon is slightly stronger for E-2-E (2.6 kcal/mol), which would slow β-scission of the δ-E-2-E radical and provide more opportunity for ROO formation. Furthermore, the symmetry of E-1-E is broken with the addition of another methylene group. The extended chain would allow for 5 unique QOOH products to be made from the δ-E-2-E ROO, which would increase possible reaction paths leading to OH-radical production.

At low temperatures, Li et al. [70] and Jacobs et al. [66] both conclude that reactions of the α-E-1-E ROO and β-E-1-E ROO radicals are the primary drivers of ignition. Cai et al. [68] confirmed that this remains true for n=2 methyl-terminated OMEs. Thus, the additional central H-atom sites would not be expected to affect the low-temperature IDT, as observed in Fig. 3.22. However, the first stage IDT for lowtemperature reactions does decrease with the oxymethylene addition (see Fig. 3.24). Merchant et al. [72] note the first stage IDT can be directly attributed to generation of ketohydroperoxides (KHPs) in the lowtemperature ignition regime. In order for KHPs to form, ROO must isomerize to QOOH, undergo a second O2 addition to formOOQOOH, and finally undergo an internal H-atom abstraction before decomposing to form a KHP. Comparing the BDEs for E-1-E and E-2-E in Fig. 3.20 highlights why E-2-E has a faster first stage IDT. With the addition of another oxymethylene unit, the influence of the O-atoms on neighboring bonds is enhanced, slightly increasing the C-O bond strengths. This creates a stabilizing effect, slowing down β-scission to increase likelihood of O2 addition to the E-2-E radicals. Paired with the previously discussed increased number of possible QOOH configurations for E-2-E, which in turn, increases the number of possible second O2 addition sites, E-2-E is more likely to form KHPs, enhancing first stage IDT.

Effect of Lengthening the Terminating Alkyl Groups - Again referencing E-1-E as a base, the shift to P-1-P demonstrates the effect of extending the alkyl termination groups by one additionalmethylene per side. In this case, the larger molecule shows similar trends to E-1-E, but at lower temperatures (up to approximately 900 K) is less reactive, and transitions towards rapid ignition at lower temperatures (around 1000 K compared to 1100 K for the E-1-E), leading to a smaller region of temperature independence than

E-1-E. The rapid ignition at high temperatures speeds up to the point that above 1000 K, P-1-P reacts an order of magnitude faster than E-1-E, and slightly faster than E-2-E. Despite observable differences in the primary IDTs for E-1-E and P-1-P, the first stage ignition of both fuels have quite similar behavior.

To understand the variations in ignition behavior with the increase of the end group alkyl chain length, we consider the differences in H-abstraction kinetics between methyl ethyl ether (MEE) and methyl propyl ether (MPE).MEE andMPE are similar to E-1-E and P-1-P respectively, terminating the molecule at the first oxymethylene group. In a theoretical kinetics study of HO2 + various ethers, Mendes et al. [73] calculated the reaction rates for abstraction at each unique H-atom site in MEE andMPE. At low temperatures (up to 500 K), 99% of all H-abstraction from the C2 and C3 end groups occurs on the α-carbon, and the total rates for H-abstractions at all sites on the C2 and C3 end groups are similar (within a factor of 1.5 with DEE abstraction occurring slightly faster). It is reasonable to expect that abstraction at the α-carbon on E-1-E and P-1-P would dominate at low temperatures, and the resultant fuel radicals would combine with O2 to form α-ROO radicals. It is facile for the α-ROO radicals to form 6-membered ring transition states to internally abstract an H-atom. For E-1-E, a 6-centered transition state is formed to abstract the weakened δ-hydrogen, and would be expected to be the only competitive route. P-1-P has two 6-centered transition state options: internal abstraction of the δ-hydrogen similar to E-1-E, or to abstract the stronger (4.2 kcal/mol stronger) γ-hydrogen, which is unlikely to occur. Given the similar chemistry for low-temperature oxidation of E-1-E and P-1-P, it is unsurprising that first stage ignition behavior and low-temperature primary IDTs are similar.

As temperature increases, so do the deviations between the IDTs of E-1-E and P-1-P. E-1-E H-abstraction reactions increase in total rate, but continue to occur >97% at the α-hydrogen site. Thus, the E-1-E oxidation mechanism is unchanged with temperature, though temperature can affect subsequent branching of the ROO/QOOH/OOQOOH radical cascade to HO2 and OH. For P-1-P, the chemistry begins to change around 1000 K, at which point only 87% of abstraction occurs at the α-hydrogen site, with the balance occurring at the β-hydrogen site. This opens a second possible OOQOOH pathway, in which the expected second O2 addition site is still expected to be the δ-carbon. With the relocation of one peroxyl group one atom further from the oxymethylene backbone, the subsequent β-C-O bond would be expected to be weakened, promoting faster decomposition to reactive radicals. This may account for the rapid increase in P-1-P reactivity but warrants further study to confirm the role of β-hydrogen abstraction on IDTs.

Effect of Branching Terminating Alkyl Groups - The final molecule to consider is the branched OME, iP-1-iP. For this, we will compare to linear P-1-P, which shares the same chemical composition but with a different structure. In this case, iP-1-iP did not react at all in the measured time frame (400 ms after TDC) under the original test conditions of 20 bar compressed pressure, even at temperatures exceeding 1000 K. Therefore, to get reliable ignition, the pressure was increased to 30 bar, and even at these elevated pressure conditions, measurable ignition still did not occur until 900 K. However, upon reaching a pointwhere ignition occurs, the IDT advanced rapidly, decreasing two orders of magnitude from more than 200 ms to slightly more than 3 ms in a very small temperature range, as seen in Fig. 3.25. No multi-stage ignition behavior occurred with this molecule at any test condition, although the ignition required temperatures outside of the multi-stage region for P-1-P.

To explain this behavior, we compare the ignition of P-1-P and iP-1-iP to previously published work by Johnson et al. [74], who studied the ignition of n-propanol and isopropanol in a shock tube at 1 atm and

found that isopropanol has a longer IDT than n-propanol. However, the somewhat increased IDT for isopropanol is not enough to explain the disparate IDT behavior of P-1-P and iP-1-iP. A theoretical study on H-abstractions of n-propanol and isopropanol by OH may further clarify this behavior. Guo et al. [75] showed that for n-propanol, abstraction at the α-carbon is preferred at all temperatures above room temperature. The equivalent H-atoms in P-1-P would be either the α-hydrogens or potentially the δ-hydrogens. Both resultant radicals can readily accept addition of O2, promoting low-temperature ignition kinetics. In contrast, Guo et al. [75] showed that for isopropanol, abstraction at the α-carbon is only preferred below »1000 K (above »1000 K methyl group abstraction is preferred). This has significant consequences for iP-1-iP ignition. Even more so than isopropanol, the α-hydrogens in iP-1-iP are crowded. O2 would be unlikely to add at the α-site; β-scission to less reactive products such as acetone, formaldehyde, and propene is preferred. The result would be an arresting of the ROO cascade necessary for ignition at low temperatures.

As temperature increases, the abstraction at the β-carbon sites becomes more important. At 900 K, Guo et al. [75] observed »40%of all abstraction from isopropanol occurs at the terminal methyl sites. Similarly for iP-1-iP, abstraction at the terminal methyl sites is expected to become significant at »900 K, creating β-iP-1-iP radicals which are unencumbered enough to accept the addition of O2. These ROO radicals can then begin the ROO cascade required for ignition, and hence, this phenomenon explains the lack of observed ignition until »900 K in this work.

3.3 Additional MCCI Engine Relevant Physiochemical Properties

3.3.1. Testing Methods

For this segment of the study, several properties were measured for the matrix of OME variations. For some properties, ASTM standard methods were available, however, a number did not have ASTM standard methods available, or the available methods were not designed to handle the range of values encountered in the testing. As much as possible, each test was attempted to be performed on all of the desired molecules; however, due to limited quantities of some of the more difficult molecules to isolate, some tests were performed only on a subset in order to show the likely trends.

For the ASTM standard methods, the following tests were performed:

• Indicated Cetane Number (ICN), ASTM D8183 [38] - describe earlier.

• Lower Heating Value (LHV), ASTM D240 [76]. Note that this method directly measures the higher heating value; LHV can be calculated via stoichiometry and the known heat of vaporization of water. These tests were performed in an IKA C200 calorimeter.

• Flash Point (FP), ASTM D93A [77]. These tests were performed in an Anton-Paar PMA4 closed-cup flash point tester. This method was not able to process flash points below ambient conditions, and so some lighter OMEs could not be safely tested.

• Density and Viscosity (ρ and ν), ASTM D7042 [78]. Measurements were conducted over a range of temperatures from 20-100°C where possible. These tests were performed in an Anton-Paar SVM-3000 viscometer.

• Vapor Pressure, ASTM D6378 [79]. From this data, a curve-fit was applied to calculate Antoine equation coefficients. These tests were performed in a Grabner Instruments VPXpert-L vapor pressure tester.

• Oxidative Stability, ASTM D7545 [80]. These tests were performed in a Petrotest PetroOXY device as 20 vol.% blends in tridecane to simulate likely blending conditions.

For non-ASTM test methods, the following tests were performed:

• Yield Sooting Index (YSI) – described earlier

• Water Solubility (WS) - measured in a HP 5890 Series II gas chromatograph with a flame ionization detector (GC-FID) in a 30mRestek Rtx-Wax column, 0.25mmdiameter with 0.25 µm film. As water cannot be accurately measured in a GC-FID device, a relative response ratio (RRR) method was used. The target OME was blended with 99% ethanol (n-propanol was used for the iP-1-iP case due to simultaneous elution of ethanol and iP-1-iP) at known masses after drying overMS4Å molecular sieves, and the responses recorded:

$$RRR = \frac{area_{ethanol} / mass_{ethanol}}{area_{OME} / mass_{OME}} \tag{3.1}$$

From here, the OMEs were blended with Type I deionized water in individual vials (five samples per OME), shaken vigorously, and left to diffuse to equilibrium for 72 hours. The water layer was extracted, added to clean vials and the mass recorded, then a known mass of ethanol added. This mixture was tested in the GC-FID, and from the known mass of ethanol and measured response areas, the mass of OME can be calculated. From here, the mass of water is the remainder of the measured mass of OME/water blend, and water solubility in g/g is calculated:

$$mass_{OME} = RRR * \frac{area_{OME}}{area_{ethanol} / mass_{ethanol}} \tag{3.2}$$

This method provides good coefficient of variance (CoV, <5% for most samples), but the very low solubility of butyl-terminated OMEs resulted in higher CoV (approximately 15%) as the samples used masses of OME and ethanol only one order of magnitude higher than the resolution of the balance used. This method was verified with n-pentanol to within 2% of literature values (22.1 g/L vs 22.5 g/L [81]).

• Boiling Point (BP) - Boiling points were not measured directly, but calculated from reduced pressure boiling points during purification. The reduced pressures were converted to atmospheric equivalents using the Atmospheric Equivalent Temperature calculation described in ASTM D1160 [82].

• Seal material compatibility - Material compatibility was tested on small (approximately 1mmx 10mmx 25mm) coupons of the selected materials submerged in the OME fuels. Four representative materialswere tested – silicone rubber, nitrile rubber (NBR), and flouroelastomer (FKM), which represent a number of common flexible seal materials, and poly-ether ether ketone (PEEK), a hard polymer sometimes used as a valve seat material. Polytetrafluoroethylene (PTFE) is one of the most common chemical-resistant hard sealing and valve seat materials, but it has been shown in literature to be resistant to OMEs [36] and so PEEK was selected as an interesting alternate material. Two coupons of each material had the mass taken before immersion, then at 24, 48, 72, and 144 hours of exposure to test for fuel absorption, and then again after drying in a fume hood for 24 and 48 hours to test for any permanent damage. When possible, the

OME sample was unchanged, but some of the volatile OMEs required replenishing during the measurements to ensure the samples remained fully submerged.

3.3.2. Property Measurement Results

3.3.2.1. Lower Heating Value

LHV was not measured directly; the calorimeter used (IKA C200) combusts a known mass fuel sample in an oxygen environment and measures the change in temperature of a water bath to determine energy released. As the water formed from combustion will condense when cooled, this method measures the higher heating value (HHV). For engine operation, LHV is the more applicable measurement as the combustion chamber is maintained at high temperature with very short dwell times, so under typical operation none of the latent heat of the water vapor will be released. Thus, HHV is converted to LHV via the assumption of complete combustion and subtraction of the latent heat of the produced water mass; the results of this analysis are presented in Table 3.5.

$$LHV = HHV - m_{H_2O}(\Delta h_{vap}) \tag{3.3}$$

ASTMD975 and EN590 diesel standards do not specify a minimum acceptable value for LHV or HHVof diesel; however, typical diesels have LHV>42MJ/kg [83], and while biodiesel LHV will depend in part on the oxygen content, some traditional biodiesels have been found to have LHV between 37 and 40 MJ/kg [83,84]. Synthetic diesels from processes such as Fischer-Tropsch or hydrotreatment of bio-oils may have much higher LHVs, up to 49 MJ/kg [85]. The high oxygen content of OMEs results in significantly lower LHVs than traditional diesels, a weakness noted in prior work [86]. OMEs with extended alkyl groups reduce the oxygen:carbon ratio and thus should produce higher LHVs, and one would further expect longer oxymethylene chain OMEs to produce lower LHV than their shorter counterparts.

Table 3.5. Lower Heating Value of various OMEs [MJ/kg]

End Group	Number of CH2O Units				
	1	2	3	4	5
Methyl	23.2	21.0	20.0	19.3	18.8
Ethyl	28.8	25.9	24.1		
Propyl	32.0	29.0	27.0		
Butyl	34.1	31.2	29.2		
Isopropyl	31.4				
Isobutyl	33.7				
Typical Diesel	>42				

These results are consistent with expectations; higher alkyl groups produce higher LHV, and longer oxymethylene chains produce lower LHV. There is a diminishing effect on the reduction in LHV per oxymethylene unit as the ratio of oxygen:carbon approaches unity with longer chains. The iso-OMEs diverge again from their linear counterparts, but only slightly. This is also consistent with alkane behavior, where LHV of branched molecules is slightly reduced in comparison to linear variants [87]. The reported values here for M-n-M, E-n-E, P-1-P, and B-1-B are in good agreement with literature, [86,88–90] with a maximum difference of 4.9%higher LHV reported here for E-1-E compared to measurements from Drexler et al. [88] In our data, an average coefficient of variance (CoV) of 1.2% is found, with M-1-M showing the highest CoV of 4.6%.

None of the tested OMEs show what could be considered “high” LHV; even the highest tested value, for B-1-B, is still approximately 3MJ/kg less than many typical biodiesels [83]. For maximizing energy content, we recommend usage of OMEs with as long of terminating alkyl groups as other requirements may permit.

3.3.2.1. Flash Point

Flash point (FP) is an important factor in the safety of handling fuels; while gasolines typically have FP well below ambient and are treated as flammable liquids, diesel fuels typically have FP >52°C (>55°C in the EU) and are classified as combustible liquids [91]. As documented by Härtl et al. and Lautenschütz et al. [86,89], smaller OMEs such as M-1-M and E-1-E have FP below or close to this requirement, but the most commonly studied OMEs (M-3-M and higher) will meet this requirement.

As shown in Table 3.6, FP appears to be a significant weakness in compatibility of OMEs with diesel; about half (M-3-Mand higher, E-3-E, P-2-P and higher, and B-1-B and higher) meet this requirement, while others do not. Our measurements have an average coefficient of variance (CoV) of 0.98%, with B-1-B showing the highest CoV of 1.8%, for five tests performed for each fuel. The reported values for M-n-M and E-n-E are in good agreement with Lautenschütz’s work, with a maximum deviation of <1% higher for M-3-M [86]. We also find comparable FP to Drexler et al. [88] for P-1-P and B-1-B, with <1% difference. Some of these fuels had FP too low to safely test in the PMA4 device, which is not natively equipped to test FP below ambient temperatures, and while some cooling of the test cup is possible, a different device with native cooling capability may be required for testing of low-FP OMEs; we note that Lautenschütz et al. report FP values for M-1-M and E-1-E of -32°C and -5°C respectively [86] and Deutsch et al. report a FP of 16°C forM-2-M [90], below the safe testing limits of the methods used here.

Table 3.6. Flash Point of various OMEs [°C]

End Group	Number of CH2O Units				
	1	2	3	4	5
Methyl	<20[a]	<20[a]	56.4	85.6	116
Ethyl	<20[a]	35.5	69.4		
Propyl	31.7	66.5	91.0		
Butyl	58.6	89.6	114		
Isopropyl	21.3				
Isobutyl	49.4				
Typical Diesel	>52				

[a]Flash point too low to safely test in PMA4

3.3.2.3. Density and Viscosity

Physical properties of the liquid fuel will have significant effects on the behavior of the spray in the fuel injector for a CI engine; the influential work of Lefebvre on sprays indicate that ρ and ν are of high importance for spray development [92]. The effect of biodiesels on the performance of CI engine injectors has been a matter of concern due to typically higher ρ and ν; as reviewed by Algayyim et al., many studies have been conducted which find that typical biodiesels produce sprays with greater penetration and larger diameter droplets, hindering evaporation due to lower area:volume ratios [93]. Further, some work suggests that larger droplets may increase soot formation [94]. CI engines are designed around combustion of a particular ideal fuel spray, so rather than preferring some minimum (e.g. YSI) or maximum (e.g. LHV), the ideal OME for diesel blending will match as closely as possible to typical diesel values. We present density of the OMEs at 20°C in Table 3.7, and the viscosity at 40°C in Table 3.8 below.

None of the OMEs tested match perfectly with typical diesel for ρ except M-1-M; however, all of the n=1 and n=2 OMEs are very close to diesel and may be good substitutes in this respect. Longer oxymethylene chains produce higher ρ due to higher oxygen content, which helps offset some LHV losses by allowing for more fuel mass per unit volume. Only two tested OMEs, M-5-M and B-3-B, even approached the ν values typically seen in diesels, with most being less than half that of the minimum diesel ν. The average CoV for ρ and ν measurements was less than 0.1% for 3 tests per fuel.

Table 3.7. Density at 20°C of various OMEs [g/mL]

End Group	Number of CH2O Units				
	1	2	3	4	5
Methyl	0.860	0.992	1.03	1.07	1.10
Ethyl	0.829	0.912	0.971		
Propyl	0.834	0.900	0.948		

Butyl	0.837	0.888	0.931
Isopropyl	0.818		
Isobutyl	0.824		
Typical Diesel	0.84-0.87		

Table 3.8. Kinematic Viscosity at 40°C of various OMEs [mm2/s]

End Group	Number of CH2O Units				
	1	2	3	4	5
Methyl	n/a[b]	0.617	0.876	1.32	1.98
Ethyl	0.346	0.652	0.963		
Propyl	0.644	0.949	1.39		
Butyl	0.945	1.32	1.85		
Isopropyl	0.515				
Isobutyl	0.904				
Typical Diesel	2.0-3.2				

[b]At lab ambient pressure (84 kPa), M-1-M will boil at approximately 37°C, so no density or viscosity at 40°C can be measured without a device to maintain the viscometer above ambient pressure

In comparison with literature, we find nearly identical ρ measurements to Lautenschütz [95] and Drexler [88], with the largest observed difference as a 1.5% higher ρ for M-2-M. For ν, Lautenschütz et al. measure ν at 25 °C and Drexler et al. measure at 20 °C, while Deutsch et al. measure at 40 °C, as reported in Table 3.8 above. We find good agreement with Deutsch et al. for all values except M-2-M, where we observe a 9.2% higher ν. A temperature sweep was performed for ρ and ν (Figs. 3.26 – 3.29) with a step of 10°C, so to compare with Lautenschütz et al. we take an average of our 20°C and 30°C values. Acknowledging that ν is nonlinear with temperature, and thus some small error is to be expected from this approximation, we nonetheless find good agreement except for M-1-M and E-1-E, where we observed significantly (16% and 19% respectively) lower ν than Lautenschütz et al. For E-1-E, P-1-P, and B-1-B, we find a 15% lower ν for E-1-E than Drexler et al. [88], but find good agreement (within 5%) for the remaining fuels.

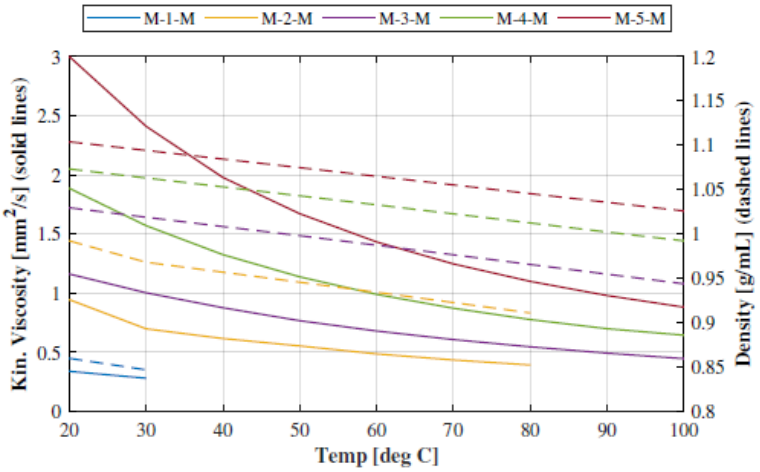

Figure 3.26. Viscosity and density curves of M-n-M OMEs between 20°C and 100°C.

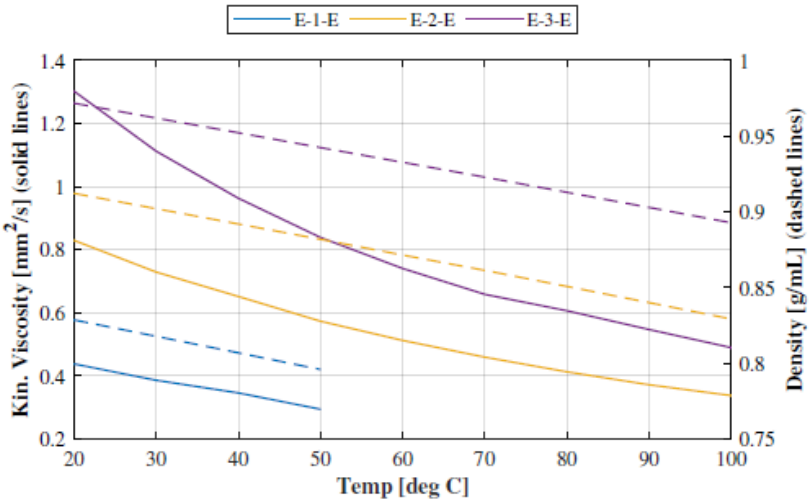

Figure 3.27. Viscosity and density curves of E-n-E OMEs between 20°C and 100°C.

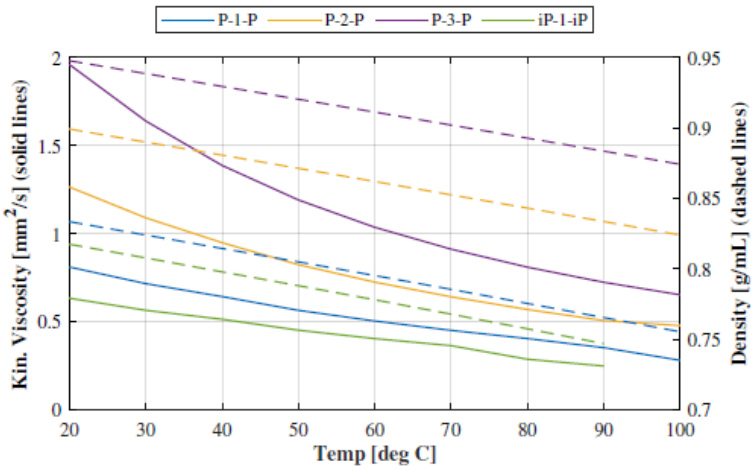

Figure 3.28. Viscosity and density curves of P-n-P and iP-1-iP OMEs between 20°C and 100°C.

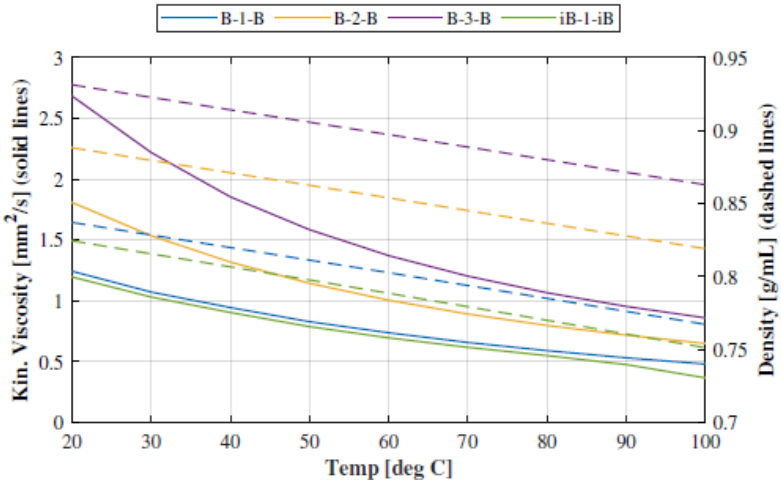

Figure 3.29. Viscosity and density curves of B-n-B and iB-1-iB OMEs between 20°C and 100°C.

3.3.2.4. Vapor Pressure

A subset of the OMEs were tested for vapor pressure, however, due to high fuel volume requirements not all were tested. The tested OMEs were M-1-M, M-3-M, M-4-M, M-5-M, E-1-E, P-1-P, and B-1-B. Antoine equation (Eq. 3.4) parameters were calculated for these OMEs and are presented below; M-1-M and E-1-E have Antoine coefficients provided in the NIST Webbook [96,97] and produce curves within 5% of our calculated values. The average CoV for five tests per fuel was 5.5%, driven primarily by exceptionally high CoV (29%) for M-5-M (the average CoV for the other tests, excludingM-5-M, was a more reasonable 1.8%). Generally, CoV increased with decreasing volatility. Due to limits of the testing device and the fuels, different temperature ranges were tested, up to either just below the boiling temperature or the device maximum temperature (120°C), and starting at 0°C or a temperature providing above 5 mbar vapor pressure (to prevent damage to the machine due to low vacuum). Coefficients are reported in Table 3.8 as calculated from the curve fit, but we note that the measured values from which these are produced are accurate to 3 significant figures and calculated values from these should be treated as such.

$$log_{10}(P_{vap}) = A - \frac{B}{C+T} \quad (3.4)$$

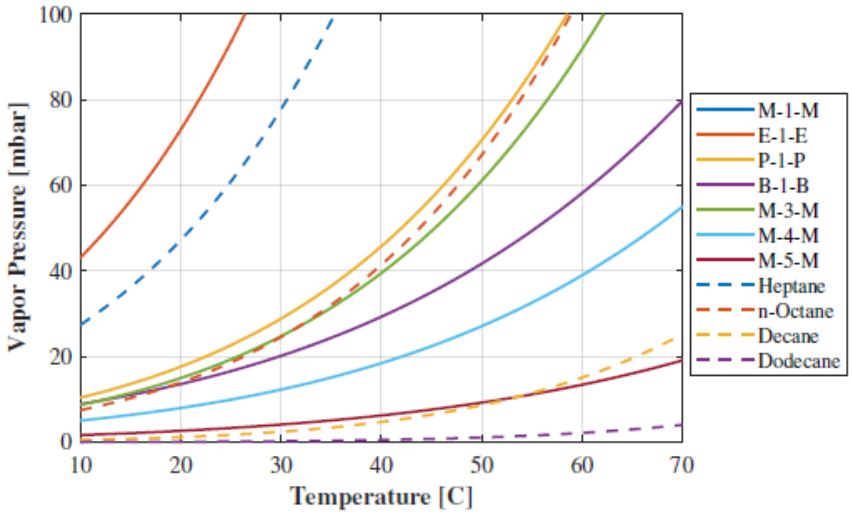

Figure 3.30. Antoine curves of OME vapor pressure, from calculated Antoine coefficients, compared to some typical alkanes.

Table 3.9. Antoine equation coefficients for some OMEs [bar, K]

Fuel	Temp Range Tested [°C]	A	B	C
M-1-M	0-35	3.881	991.89	-59.23
E-1-E	0-80	3.995	1201.2	-59.07
P-1-P	20-120	4.762	1920.2	1.598
B-1-B	30-120	3.911	1882.5	32.66
M-3-M	20-120	4.246	1629.4	-24.69
M-4-M	30-120	4.309	2130.2	39.43
M-5-M	50-120	4.142	2301.4	49.54

The vapor pressure of diesel will vary with the various volatile components, so several common alkanes are shown on the plot below (Figure 3.6) using Antoine parameters from NIST [76,98,99] to provide a point of reference.

3.3.2.5. Oxidative Stability

The most common test for oxidative stability of biodiesels is the Rancimat test (EN 15751). This testwas attempted for oxidative stability, however, the nature of the method caused significant difficulties and was

determined to be ineffective for testingOMEs. First and most relevant, the Rancimat test is by nature an open-system test. The oxidation is accelerated by pumping air through a heated fuel sample, and the volatiles (nominally acids) are collected in water, with changes in the conductivity of the water indicating the presence of acids formed from autooxidation. As a result of heating to the test temperature of 110°C and simultaneously enforcing a gas flow, many of the OMEs will rapidly vaporize or even boil and be lost – further, as will be discussed in a later section, the water solubility of many OMEs is very high and vapors will contaminate the measuring water. The second problem is the nature of the test, which uses conductivity change of a water sample as a proxy for oxidation. This has been shown to work well for fatty-acid methyl ester biofuels [100], but it was not clear prior to the tests whether the auto-oxidation products of anOMEwill necessarily ionize or otherwise change the conductivity of the measuring water.

As a result of these difficulties, a different test was used. The Petro-Oxy testing device is often used for gasoline and gasoline additives [101], which makes it more suitable for the OMEs, some which have been shown to have higher volatility. Additionally, it is a closed-system measurement, preventing the vapor losses seen in some initial failed attempts to use the Rancimat method. The Petro-Oxy device subjects a small (5 mL) sample of the fuel to 140 °C under 7 bar of oxygen, and measures the induction time as defined by the time to a 10% reduction from the maximum pressure of the test [80]. Some past work has applied this method to biodiesel in comparison with the Rancimat method and determined minimum equivalent Petro-Oxy induction times [102], proposing that the 8 hour Rancimat induction time required for European biodiesel is comparable to 27 minutes in a Petro-Oxy device, and the US standard of 3 hours is comparable to 17 minutes of Petro-Oxy testing, where longer induction times are indicative of higher oxidative stability. Due to limited equipment availability, only a subset of OMEs were tested in this device, focusing primarily on larger alkyl groups (E-1-E, P-1-P, P-2-P, B-1-B, B-2-B, B-3-B, iP-1-iP, and iB-1-iB). These were blended at 20 vol% in tridecane to simulate common blending ratios in diesel and allow for higher resolution due to lower concentrations of OME. The induction times for the tests are presented in Table 3.10. GC-MS testing was performed on the oxidized sample to determine the products of the auto-oxidation reaction. Common products included alkyl esters, carboxylic acids, and alcohols. The presence of carboxylic acids indicates that Rancimat tests may be effective for heavier OMEs which can survive the heated open system environment without significant vapor loss.

Table 3.10. Induction times of select OMEs in Petro-Oxy test, 20 vol% in tridecane.

End Group	Number of CH_2O Units		
	1	2	3
Ethyl	228 min		
Propyl	86 min	91 min	
Butyl	106 min	152 min	174 min
Isopropyl	38 min		
Isobutyl	88 min		
Tridecane	154 min		

A trend is observed with the oxymethylene chain length; longer chains lead to improved stability. However, no clear trend can be seen for alkyl groups – E-1-E is more stable than any of the propyl or butyl OMEs, however, all of the butyl OMEs are more stable than the propyl ones. The iso-alkyl OMEs do show significantly reduced stability in comparison to their linear counterparts. The mechanisms by which this is occurring are unclear and warrant further investigation. All of the tested OMEs, in 20% blends, exceed the biodiesel oxidative stability standards, but it is unclear whether these fuels will exhibit stability issues when tested neat. Single tests were performed for each fuel, and so we refer to the ASTM standard, section 14.1.5, [80] where the reproducibility R of this method can be calculated as $R = 0.0863X + 1.3772$, to estimate an average R of 10% of the measured values.

3.3.2.5. Water Solubility

Table 3.11. Water solubility of various OMEs [g OME / kg water]

End Group	Number of CH2O Units				
	1	2	3	4	5
Methyl	481	469	394	338	283
Ethyl	56.0	60.7	52.3		
Propyl	3.16	3.72	3.23		
Butyl	0.215	0.189	0.251		
Isopropyl	9.76				
Isobutyl	6.62				
Typical Diesel	<0.1				

Water interaction with fuels is important for a number of reasons, but most importantly, there are environmental and combustion concerns. A fuel which is highly soluble in water poses risks in case of spillage; it will be significantly harder to separate from water sources due to lack of distinct phases, and there is a risk of fuel becoming dissolved into groundwater in high concentrations and being spread from the spill site. Further, a fuel which can carry high concentrations of water dissolved in the fuel itself, while less of an environmental concern, poses risks to engine and fuel system operation and can reduce the effective LHV of the fuel.

As shown in Table 3.11, the effect of additional oxymethylene units on the water solubility is negligible compared to the alkyl group effect, where increasing the alkyl group by one carbon per side reduces water solubility by roughly an order of magnitude each time. The mean CoV of these data is 6.9%, with B-3-B having the highest CoV at 19%. All of the B-n-B fuels exhibited high CoV due to measurable amounts of the fuels being only one order of magnitude greater the resolution of the balance used. Of the various properties tested, this one makes one of the strongest cases for the suitability of extended-alkyl (particularly butyl) OMEs for diesel blending. One anomaly is the behavior of iB-1-iB – while iP-1-iP is slightly higher than P-1-P, but within the same order of magnitude, iB-1-iB is an order of magnitude higher in water solubility than B-1-B. This result was sufficiently surprising that the entire series of iB-1-iB was

retested with fresh samples, and the same result was found. It is currently unclear what the chemical basis for this significant difference is, and more investigation is warranted.

3.3.2.6. Boiling Temperatures

Boiling temperatures were measured as a necessary result of the distillation process for purification. Distillation was generally performed under vacuum (150 torr, 100 torr, or 30 torr, depending on the lightest component) except for when M-1-M was expected to be present. The equivalent temperature at standard conditions (AET) was calculated using the procedure in ASTM D1160 Appendix A7 [82], assuming a *K* factor of 12 (this value is recommended in the standard unless another value can be clearly established) and using units of torr and °C. A pressure correction *A* is first calculated from the distillation pressure *P*, a temperature correction Δ*t* from K and the pressure *P*, and then the AET calculated from *A*, *T*, and Δ*t*:

$$\Delta t = -1.4(K-12)log_{10}\left(\frac{760}{P}\right) \tag{3.5}$$

$$A = \frac{5.994295 - 0.972546log_{10}P}{2663.129 - 95.76log_{10}P} \tag{3.6}$$

$$AET = \frac{748.1A}{(T+273.15)^{-1} + 0.3861A - 0.00051606} - 273.15 + \Delta t \tag{3.7}$$

The most likely source of error in these measurements is not from average boiling temperatures observed at reduced pressure, which were typically within +/- 1°C, but rather the uncertainty of the K factor. This is recommended in the standard as 12, but differing behavior of OMEs from typical distillate fuels may require a different K value. As an example, a +/-2 difference in K produces (at 30 and 150 torr reduced pressures, respectively) +/-3.93°C and +/-1.97°C differences (where higher K leads to lower calculated temperature).

Table 3.12. Boiling temperature of various OMEs [°C]

End Group	Number of CH2O Units				
	1	2	3	4	5
Methyl	42	112	161	207	243
Ethyl	88	142	186		
Propyl	141	184	223		
Butyl	179	223	257		
Isopropyl	119				
Isobutyl	164				
Typical Diesel (T10)	200				

The 10% distillation and 50% distillation temperatures (T10 and T50) of diesel fuel vary based on the specific blend but are often around 200°C and 250°C, respectively [83]. From the data in Table 3.12, it is

clear that most of the tested OMEs are more volatile than even the low distillation components of a diesel; the only OMEs tested with boiling temperatures above T10 are M-4-M, M-5-M, P-3-P, B-2-B, and B-3-B, and only one tested OME (B-3-B) has a boiling temperature comparable to diesel T50. Consequently, diesels with OME components may experience preferential vaporization effects; effects of this on the combustion characteristics of diesel sprays is worthy of investigation.

3.3.2.6. Material Compatibility

Due to high required volumes of fuel for the material compatibility, this testing was performed only on a subset of OMEs with n=1. The effect of various chain lengths of M-n-M has been documented in literature [103–105], so this work focuses on the end group effect. Additionally, there is a wide range of possible sealant materials, and varying properties within categories of material, so it will be necessary for any engine development programs to do in-depth testing of the specifically selected materials. Thus, we present these data as being informative, but not necessarily generalized.

The results of the material compatibility tests are provided in Figure 3.31 and Figure 3.32, where the results are shown as mass increase due to fuel absorption (i.e. a 50% change represents the material absorbing a mass of fuel equal to 50% of the original material), and thus the desired result is to minimize this effect. The largest change in mass (due to fuel absorption) occurred in the first 24 hours (Fig. 3.31), and equilibrium was reached by 72 hours (Fig. 3.32) for all fuels and materials. For most, the change from the first measurement to equilibrium was negligible; only FKM and NBR in M-1-M, silicone in E-1-E, and FKM in iP-1-iP had significant (>5% by mass) changes after 24 hours. These measurements are an average of 2 samples, where the average deviation from the mean is 1.6%, with iP-1-iP having the widest variation at 5.5%. The largest change in mass (due to fuel absorption) occurred in the first 24 hours, and equilibrium was reached by 72 hours for all fuels and materials. For most, the change from the first measurement to equilibrium was negligible; only FKM and NBR in M-1-M, silicone in E-1-E, and FKM in iP-1-iP had significant (>5% by mass) changes after 24 hours. In the plots below, the PEEK samples are not shown for the simple reason that they proved to be highly resistant and did not absorb any fuel for the entire duration of the test.

One of the most important takeaways is the suitability of PEEK as a hard sealing or handling material for OMEs; no absorption was observed for any of the tested OMEs at any duration of exposure. For the elastomers, FKM was the only one which was suitable for use with OMEs, and only for the extended alkyl OMEs - it has worse performance for M-1-M, but shows significant reductions in mass of fuel absorbed as the alkyl group is lengthened. Additionally, it is noted that the common trend observed in most other properties regarding the iso-OMEs, namely that they have somewhat inferior properties to their linear counterparts, is reversed here - iP-1-iP and iB-1-iB had less absorption than P-1-P and B-1-B for NBR and FKM samples, and essentially comparable effects on silicone.

An effect that is difficult to quantify is leaching into the fuels. No apparent change was observed for PEEK, silicone, or FKM, but the NBR sample caused discoloration of all of the OMEs. Anecdotally, similar discoloration was observed when a nitrile rubber stopper was used for a flask storing B-1-B, so we believe that this may not simply be a flaw with the specific lot of NBR used in this testing.

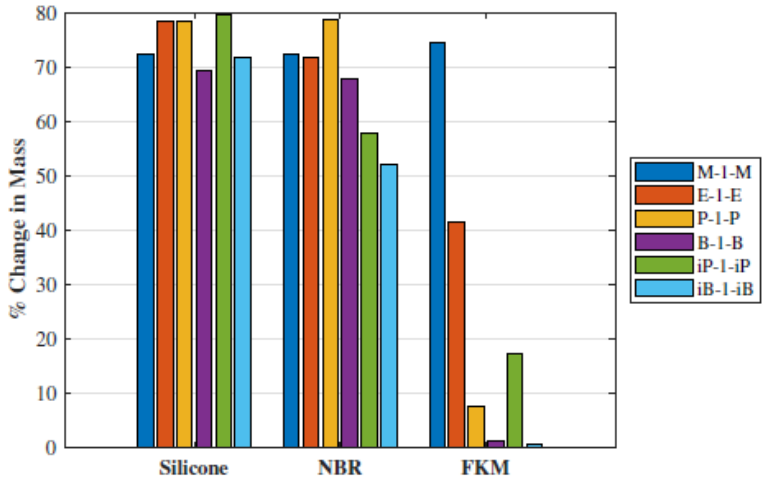

Figure 3.31. Percent change in mass of elastomer sample coupons after 24hr submerged exposure

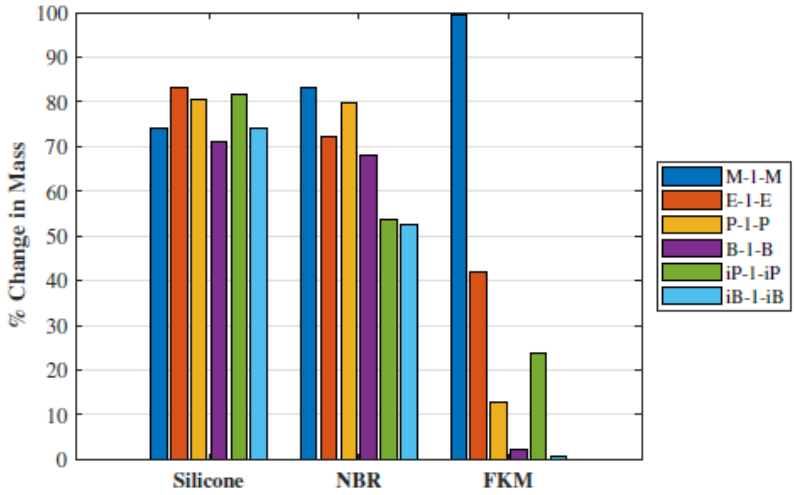

Figure 3.32. Percent change in mass of elastomer sample coupons after 72hr submerged exposure

Chapter 4 – POME Chemical kinetics/Mechanism Development

4.1. Reaction Calculations for POMEs

If POMEs are to be used as practical diesel additives, the creation of accurate chemical kinetics models to predict their flame behavior under practical combustion conditions across a plethora of operating conditions is critical, both to predict conditions under which adverse effects may occur and to optimize engine design and performance with the use of a new blendstock. Furthermore, the development of fundamentally accurate kinetics models can provide insight as to why POMEs are so successful at reducing soot productivity in diesel blends, leading to chemical insights that can further lead to drop in additives with similar soot reduction tendencies.

This section is organized as follows. Section 4.1 and its subsections focuses on the theoretical calculations of reaction rates for several POMEs and the development of kinetics models for use in simulations of flames and engines. In this section, the methods used to calculate high accuracy reaction rates and thermodynamics are outlined, comparisons to existing studies are highlighted, and insights as to how changing chain length and end group functionalities change the fundamental behavior of POMEs are discussed. In particular, the role of carbenes and well skipping reactions highlight how theory can both solve long standing discrepancies on reaction mechanisms in the literature concerning POMEs and how it can also reveal reaction dynamics that otherwise would not have been detected in experiments. Section 4.2 and its subsections presents the fundamental microreactor experiments to further validate the theoretical reaction rate calculations and provide direct detection of pyrolysis reaction intermediates. It also highlights the model accuracy against other published experiments on POMEs. Finally, Section 4.3 delves into the extension of the kinetics models to other POMEs that have been identified as potentially viable POMEs for production.

4.1.1. Kinetics Calculation Methodology

In this work, high level electronic structure calculations combined with master equation theory were employed to calculate accurate pressure dependent kinetics for POMEs. The quantum chemical and reaction rate constant computational methods used by this research group are more completely outlined in a previous study by Lockwood et al. [106]. In short, potential energy surfaces were generated primarily via KinBot [107] in conjunction with Gaussian 16 [108]. Occasionally KinBot failed to find an expected reaction, at which point a manual search using Gaussian 16 was also performed. For example, pericyclic reactions were often missed by KinBot. A maximum energy threshold of 120 kcal / mol was selected for the KinBot reaction search and the calculations were performed at the B3LYP/6-311G* level of theory. This level of theory was chosen for its combination of computational efficiency and accuracy compared to other density functional methods.

After initial structures were found at the B3LYP/6-311G* level of theory, the reactant, transition states, and products for each reaction were re-calculated at the M06-2X/cc-pVTZ level of theory (calculation of harmonic frequencies are also performed at this time). The M06-2X method is more computationally expensive than B3LYP but has been shown to yield greater accuracy for a wide range of molecule classes and types of calculation [109,110]. 1-D hindered rotor scans of every rotatable bond were performed at a 10 degree interval for 360 degrees, using the M06-2X/cc-pVTZ level of theory. After geometry optimization

and rotor scan calculations are completed, the geometries of the lowest energy conformers of a given species are extracted and single point energies are calculated using a coupled cluster method, CCSD(T). This method can have a chemical accuracy of ~0.3 kcal mol^{-1} when paired with a basis set of the appropriate size making it one of the most accurate methods currently available. The cc-pVDZ and cc-pVTZ basis sets were chosen to estimate the infinite basis set via extrapolation.

The temperature and pressure dependent rate constant were computed by RRKM model using the MESS [111] (Master Equation System Solver Code) developed by Argonne National Laboratory. MESS [111] models bond fission potential energy profiles as an attraction potential

$$V_{attr}(r) = -C/r^n$$

This attractive potential may be fit to long range force calculations which are cost prohibitive for such large molecules as POMEs, so an approximation of the attractive forces between reaction fragments had to be made. Based upon the work of Jacobs et al. [41], we calculated the morse potential analytically for bond fissions using the Morse potential:

$$V_{Morse}(r) = D_E\left(1 - exp\left(-\alpha(r - r_0)\right)\right)^2$$

The dissociation threshold and minimum energy bond length was taken from the single point energy calculation and optimized geometry structures respectively. The Morse potential's curvature parameter,

$$\alpha = 2\,\pi\nu_0\sqrt{\mu/2D_E}$$

was calculated from the averaged stretching oscillator harmony frequencies ν_0 of the bond undergoing dissociation and is the averaged reduced mass of the fragments. The harmonic frequencies were calculated for the optimized geometry structure. Numerically fitting the MESS [111] code's attraction potential with the analytically calculated morse potential can compute the potential pre-factor (C) and potential power exponent (n) but the attraction potential can only trace a region of Morse potential and fails to trace near inflation points due to not accounting for repulsion. To avoid the resulting inaccuracies due to the subjectiveness in the selection of Morse potential range to fit with, a modified Buckingham Potential

$$V_{Buckingham}(r) = Aexp(-Br) - C/r^n$$

was used to numerically fit the Morse Potential. The first term of the Buckingham Potential accounts for the repulsion potential and second term accounts for the attraction potential which allows the numerical fitting methods to trace the Morse Potential for a wider range and accurate near inflation points.

Energy collision parameters for the unimolecular systems present the largest uncertainties in master equation calculations. The parameters in the ΔE_{down} model for collisional energy transfer,

$$\langle\Delta E_{down}\rangle = \langle\Delta E_{down}\rangle_{298K}(T/300)^n$$

were computed by numerically fitting of dimethoxymethane (or PODE-1) total decomposition rates with the experimental data of Golka et al. [112] and Peukert et al. [113] as shown in Figure 4.1. The numerical fitting resulted in the selection of $\langle\Delta E_{down}\rangle_{298K} = 150\ cm^{-1}$ and $n = 0.8$. The reaction rates were calculated for temperatures ranging from 300 to 2500 K and pressures ranging from 0.0001 to 100 atm for

two different bath gases: argon and nitrogen, and were generated as either single or double Arrhenius expressions in the PLOG format of CHEMKIN [114]. The complete reaction mechanism along with the thermodynamic data files can be found in supplementary material.

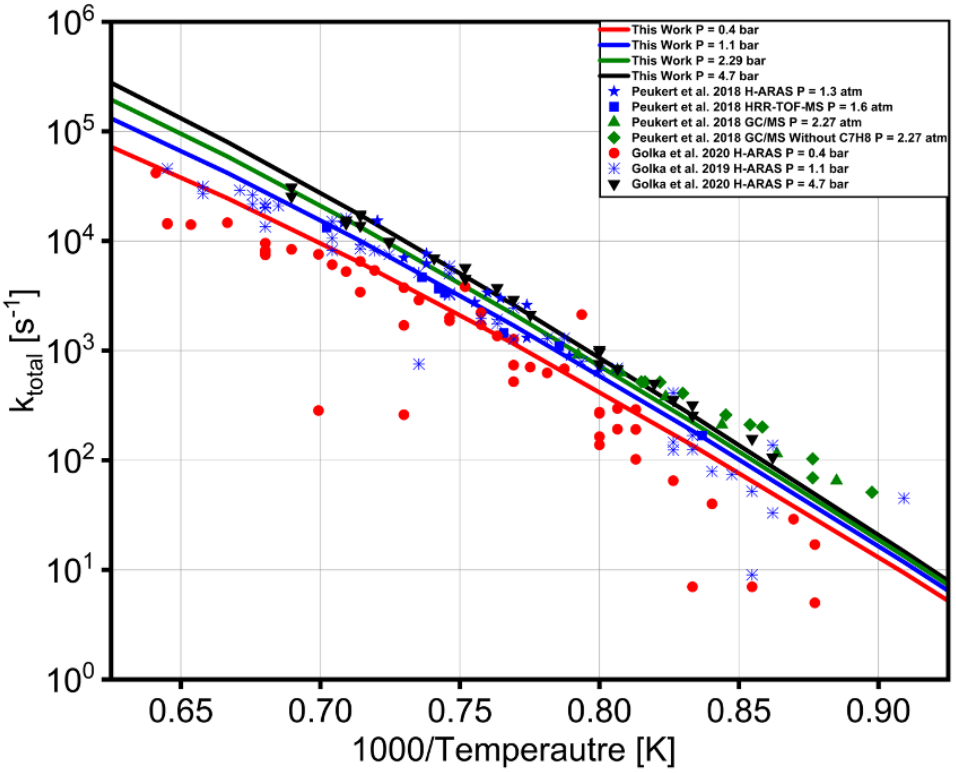

Figure 4.1: Comparison of this work's calculated Arrhenius expression for total rate constants of PODE-1 decomposition with the H-ARAS experimentally calculated rates. The solid lines represent the total rate constant of this work and symbol represents experimental data from Golka et al. [112] and Peukert et al. [113].

4.1.2 PODE-1 Theory Justification and Model Validation

The potential energy surface (PES) showing the relative energies for the thermal decomposition of PODE-1 is shown in Figure 4.2. The difference in energy between the lowest transition state barrier and the lowest bond dissociation energy of 11.5 kcal / mol implies that the bond fissions may be more competitive than the molecular routes, given the entropic favorability of bond fissions over molecular routes. However, some of the prior studies shown in Figure 4.2 have suggested that the formation of the carbene is the dominant reaction pathway, leading to a critical question over the fundamental mechanism of PODE-1 reaction. It was interesting to note that overall, prior literature studies were in agreement generally with our PES energetics, despite very different reaction rate calculations.

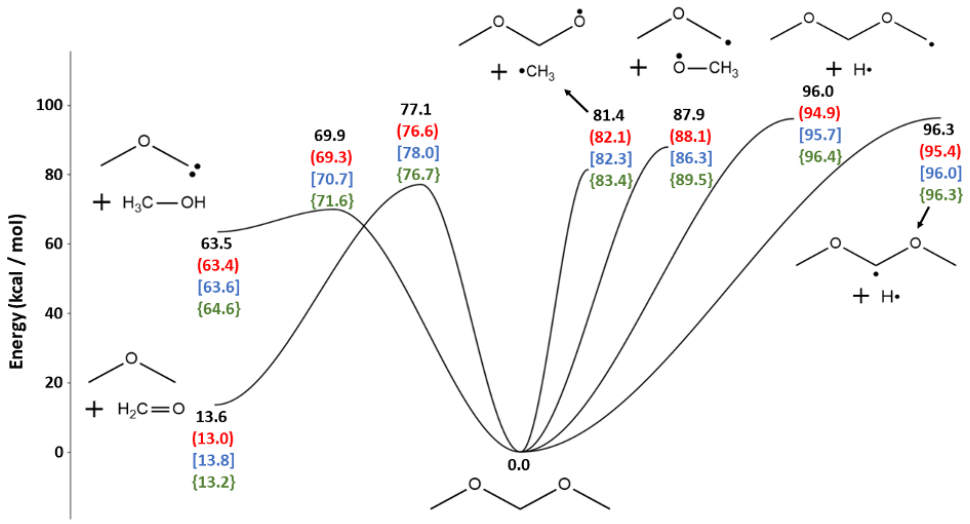

Figure 4.2: Potential energy surface for PODE-1. Energies calculated in this work (black without brackets) at the CCSD(T)/cc-pV∞Z//M06-2X/cc-pVTZ level of theory, Pazdera et al. [115] (red with parenthesis), Döntgen et al. [116] (blue with square brackets), and De Ras et al. [64] (green with curly brackets) are shown next to each stationary point.

The total of all PODE-1 unimolecular decomposition reaction rate constants from 1053 – 1667 K at 1 atm for this work is compared with several literature mechanisms [64,115–119] in Figure 4.3. The total rate for most studies presented here lie within a tighter grouping, while De Ras et al. [120] and Al-Otaibi et al. [118] reporting substantially higher total rate constants across the full temperature range. The total rate coefficient in this work had the closest agreement with Pazdera et al. [115] due to the similar levels of theory and rate constant calculation methods used in both studies. The spread of total pyrolysis rate constants versus temperature in the various studies demonstrates the historical lack of consensus in the decomposition chemical kinetics of PODE-1, which has only recently started to converge.

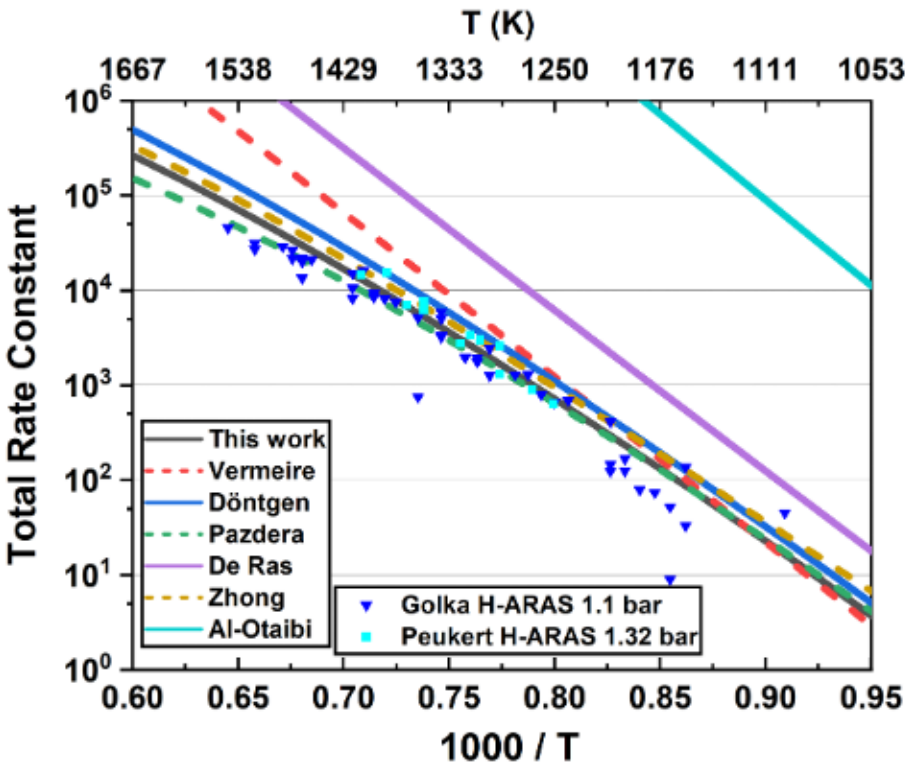

Figure 4.3: Total rate coefficients versus 1000/T and T (K) for PODE-1 unimolecular decomposition at 1 atm for this work (black line), Vermeire et al. [117] (red dashed line), Döntgen et al. [116] (dark blue line), Pazdera et al. [115] (green dashed line), De Ras et al. [120] (purple line), Zhong et al. [119] (gold dashed line), and Al-Otaibi [118] (light blue line). Experimentally determined PODE-1 decomposition rates from Golka et al. [112] at 1.1 bar (dark blue triangles) and Peukert et al. [113] at 1.32 bar (light blue squares).

However, the total rate constant is not the only factor in correctly describing decomposition chemical kinetics. The speed of specific reactions contributing to the total rate is also very important, as it dictates the mixture of intermediate products which are formed. These intermediate products undergo multiple steps of subsequent decomposition, adding to the complexity of determining the final product mixtures (i.e. emissions) and combustion parameters such as rates of heat release and ignition delay, and emphasizing the importance of accurate branching ratios for decomposition reactions. While a consensus on the total decomposition rate constants has been gradually forming, there has been much less agreement in the branching ratios of the individual reactions contributing to the total rate constants. The branching ratio for PODE-1 pyrolysis are shown in Figure 4.4, which displays the branching ratios versus temperature at 1 atm for this study and four literature studies [115–117,120]. The results from Pazdera et al. [115] again match the branching ratios produced in this work most closely due to the similar calculation methods used, also suggesting that methyl fission dominates PODE-1 reaction. Döntgen et al. [116] predicted that the carbene pathway remains dominant over the full range of temperatures, and Vermeire et al. [117] predicted that methoxy fission is the fastest rate over the full temperature range. De Ras et al. [120], while predicting a dominant R1.1 reaction at low temperatures and a dominant R1.3 reaction at high temperatures, predicted that the formaldehyde elimination would be the dominant reaction in the range of ~700 – 1200 K.

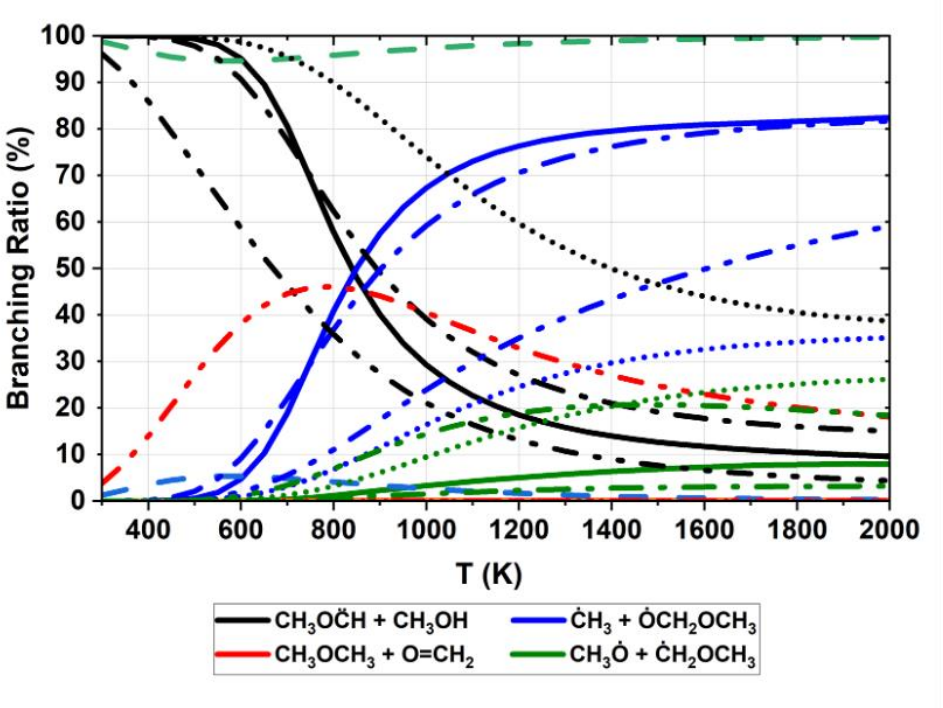

Figure 4.4. Branching ratios versus temperature for PODE-1 unimolecular decomposition at 1 atm for this work (solid lines), Vermeire et al. [117] (dashed lines), Döntgen et al. [116] (dotted lines), Pazdera et al. [115] (dash-dot lines), and De Ras et al. [120] (dash-dot-dot lines)

As Figure 4.4 highlights, there is a large fundamental question in the literature over what the true dominant pathway for PODE-1 decomposition is. The difference in these 3 routes could yield significant changes in prediction of intermediate species, influence the prediction of pollutant formation such as soot and NOx, and change the predicted flame structure. It was critical not only to confirm that our theoretical methods were indeed appropriate for this system to test our model, but also to answer this long-standing question in the literature of just how these POMEs behave in a flame. To assess the validity of our kinetic model in predicting the rates of POME decomposition reactions, to address the unresolved disparities pertaining to the branching ratio of PODE-1 decomposition, and to gain insights into the kinetics of POMEs in general, we conducted numerical simulations using our kinetic model which is compared against various experimental data as well as other kinetic model found in literature. One particularly important series of experiments were the H-ARAS experiments of Peukert et al. [113], since H-ARAS experiments were the only dilute direct measurements of PODE-1 decomposition found in the literature. Our model versus the other literature models compared to an H-ARAS trace of Peukert et al. [113] can be found in Figure 4.5.

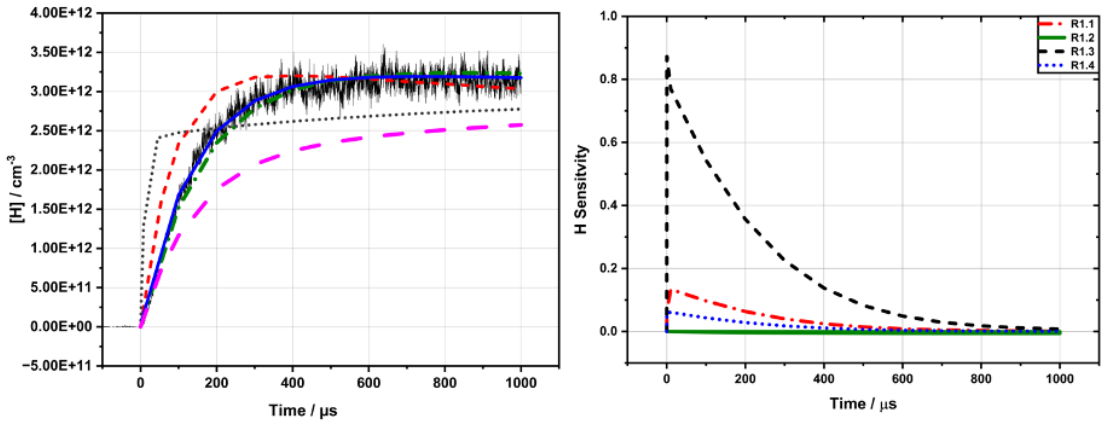

Figure 4.5. (Left) H-ARAS Experimental data [113] at 1370 K and 1.33 bar with initial mole fraction of PODE-1 being 0.48 ppm. The solid blue line represents our kinetic model, magenta long dashed line is Zhong et al. [119], red short dashed line is the Pazdera et al. [115], green dash dotted line is Döntgen et al. [116] and black dashed line is De Ras et al. [120]. (Right) Hydrogen atom sensitivity analysis of our kinetic model.

The clean nature of the H-ARAS experiments is evident from the sensitivity analysis shown in Figure 4.5 (Right), which indicates that primarily methyl fission exhibits the sensitivity. The mechanism developed in this work, as well as of Pazdera et al. [115], exhibit good agreement with the experimental data. Pazdera et al. [115] overall PODE-1 decomposition rates are 20% slower than our findings. Consequently, their prediction of hydrogen concentrations is slower up to the 600 ms, after which their predictions align more closely to our model's prediction. However, the kinetic model of Döntgen et al. [116], overpredicts the production of hydrogen radical concentrations until around 500 ms, failing to capture the early rise. This discrepancy is largely attributed to Döntgen et al. [116] artificially increasing their reaction rates to match other experimental datasets. They also made certain modifications to secondary chemistry reaction rates, leading to an overcorrection of the total reaction rate for PODE-1 decomposition. De Ras et al. [120] incorrectly predicted that methoxy fissions dominate PODE-1 decomposition, resulting in their erroneous fit to the H-ARAS data [113]. Zhong et al. [119] also fails in accurately predicting the hydrogen radical concentrations likely due to fitting rates to less accurate jet stirred reactor (JSR) experiments [121].

What is clear from this careful examination of our rates versus the literature is that our theoretical methods are both appropriate and accurate for PODE-1 decomposition, leading to confidence in using our theoretical methodology to approach POME kinetics.

4.1.3 PODE-2 and PODE-3 Related Reaction Rates

The longer PODE molecules such as PODE-2 ($CH_3OCH_2OCH_2OCH_3$) and PODE-3 ($CH_3OCH_2OCH_2OCH_2OCH_3$) have better applicability as diesel additives due to their higher flash points, boiling points, and cetane numbers without losing the excellent yield sooting index (YSI) of PODE-1 [122]. However, these extended chain PODEs have even greater uncertainty in their pyrolysis sub-mechanisms than PODE-1 due to the smaller number of theoretical reaction rate calculation studies performed on them in the literature. In addition, there are likely valuable chemical insights that can be drawn from the analysis of multiple PODE molecules of various chain lengths. Chain length is only one of the variations in the OME structure that can be explored, but if these variations are combined to make a longer OME with branching and different

end groups, it will likely to be difficult to determine what the contribution of the individual variations have on the ultimate chemistry. Determining whether the reaction pathways for the longer PODE molecules follows the same trends as the shorter ones, or entirely new trends, may enable future researchers to separate the effects of chain length from the effects of other variations in an OME's structure.

To understand the relative energetics between the possible reactions for the extended PODEs, we first consider the reactions of PODE-2. The PES for PODE-2, including the unimolecular decomposition routes explored in this study and De Ras et al. [120], is shown in Figure 4.6. PODE-2 has similar reaction pathways to PODE-1, but with more possible reactions due to the additional oxymethylene unit. We studied six reaction routes for PODE-1 and nine routes for PODE-2, including two carbene producing reactions, two formaldehyde eliminations, three C-O bond fissions, and two C-H bond fissions.

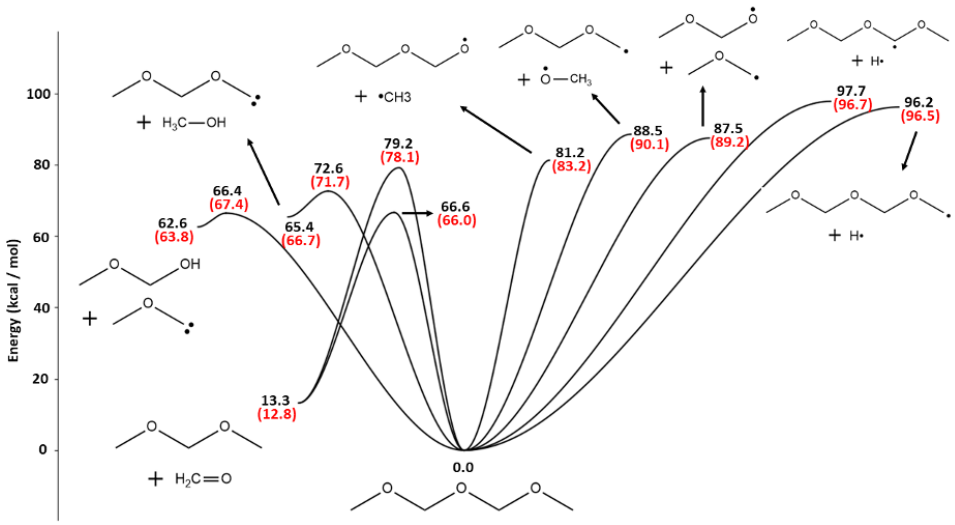

Figure 4.6. Potential energy surface for PODE-2. Energies calculated in this work (black without brackets) at the CCSD(T)/cc-pV∞Z//M06-2X/cc-pVTZ level of theory, and De Ras et al. (red with parenthesis) are shown next to each stationary point.

Notably, the calculations in this study determined that the reaction with the lowest energy barrier was still a carbene-forming transition state 66.4 kcal/mol, but with one of the formaldehyde elimination routes being just slightly above it at 66.6 kcal/mol. As compared to PODE-1, the lowest carbene-forming TS decreased by ~3.5 kcal/mol, while the lowest formaldehyde elimination TS decreased by ~10.5 kcal/mol. This can be explained by the reduced crowding of the TS pseudo-cylic structure by hydrogen atoms. Figure 4.6 shows that the calculations by De Ras et al. [120] resulted in formaldehyde elimination instead being the reaction with the lowest energy barrier at 66.0 kcal/mol. Finally, both this study and De Ras et al. [120] showed the lowest energy C-O bond fission reaction decreasing in barrier energy by less than 0.5 kcal / mol. The greater decrease in barrier energy for the TS reactions between PODE-1 and PODE-2 indicates that the TS reactions may receive a greater portion of the reaction flux in PODE-2 pyrolysis. A similar analysis was conducted for PODE-3. The calculations in this work show that for PODE-3, formaldehyde elimination becomes even more favorable with the lowest reaction barrier at 65.8 kcal/mol. Although a formaldehyde elimination is now the lowest barrier energy reaction, these types of reactions have a relatively tight TS structure involving more bending in the molecular backbone than the carbene producing reactions.

The change in barrier energy between similar TS reactions in PODE-1 and PODE-2 was much greater than the same comparison between PODE-2 and PODE-3. The lowest barrier carbene producing reaction for PODE-3, R3.1, is only 0.2 kcal / mol lower than R2.1. This is encouraging for creating analogy-based models to extend the oxymethylene chain in POMEs.

The results of the rate calculations for individual PODE-2 pyrolysis reactions in this work, De Ras et al. [120] , and Zhong et al. [119] are shown in Figure 4.7, which displays the branching ratios between the various reaction pathways from 300 – 2000 K, at 1 atm. This work suggests that the carbene producing route is dominant reaction from 300 – 1500 K, which is a much wider temperature range of reaction flux dominance than observed with PODE-1. Similarly to PODE-1, the terminal carbon-oxygen bond fission is the next fastest reaction at temperatures from about 800 – 1500 K becoming the dominant reaction at temperatures above 1500 K. The third carbon-oxygen bond fission in the PODE-2 chain also makes up a significant portion of the reaction flux at temperatures from about 900 – 2000 K. The increased dominance of the lowest barrier carbene producing route for PODE-2 compared to PODE-1 could be due to the large drop in barrier energy for this type of reaction, while the lowest barrier C-O bond only saw a slight reduction in energy. The De Ras et al. [120] mechanism for PODE-2 departs quite strongly from the current work. The fastest PODE-2 pyrolysis reaction in their mechanism is one which produces formaldehyde and PODE-1. The Zhong et al. [119] mechanism was found to have a similar branching ratio for the carbene pathway as the current work over the temperature range from 300 K to 1300 K, but with the 2nd carbene forming reaction, and formaldehyde elimination playing significant roles at higher temperatures unlike what our calculations suggest. In addition, a reversal in the importance of the various C-O bond fissions can be observed in the branching ratios of Zhong et al. [119] compared to this work.

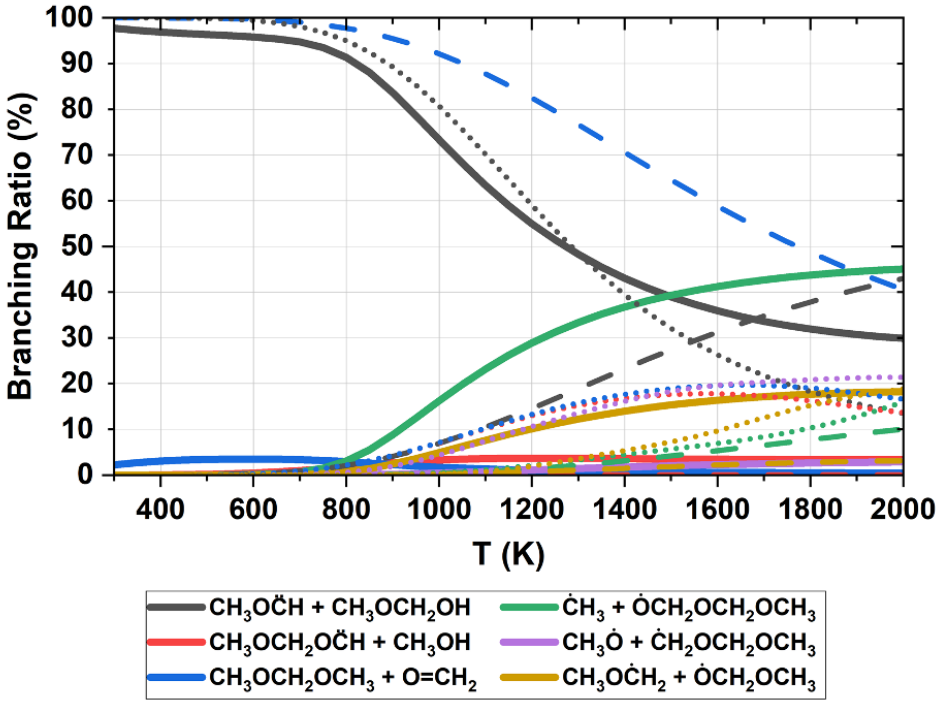

Figure 4.7. Branching ratios versus temperature for PODE-2 unimolecular decomposition at 1 atm for this work (solid lines), De Ras et al. [120] (dashed lines), and Zhong et al. [119] (dotted lines)

A few trends emerge from the rate constant calculation results presented herein. Most importantly, the carbene-forming transition states increase in their reaction flux dominance as PODE-n chain length increases. While this trend was predicted by the Zhong et al. [119] mechanism, the branching ratio between various carbene routes was in question since the rate expressions for the two fastest carbene-producing routes were assumed to be the same.

Another trend worth discussing is that of the carbon-oxygen bond strength with increasing chain length. For all three of the PODE-n molecules studied in this work, the terminal carbon-oxygen bond fission was the lowest energy, with this energy generally decreasing as chain length increases. The second C-O bond fission in the chain increases in energy with chain length, and the third C-O bond fission in the chain decreases in energy with chain length. Overall, this energy trend seems to alternate between higher and lower BDE's as one travels up the PODE-n backbone from either end. The fragmentation of PODE-n molecules appears to favor the smaller product fragment having a radical on the terminal carbon and the larger product fragment having a radical on the terminal oxygen. This is presumably due to oxygen atoms having a higher electronegativity value than carbon atoms, and thus oxygen radicals causing greater instability when located on short-chain molecules when compared to carbon radicals on shorter chains.

Another important trend is the change in total pyrolysis rate with increasing chain length, as can be seen in Figure 4.8. The pyrolysis rate of these molecules generally goes up with increasing chain length, with the difference in total rate being most prominent at lower temperatures of ~800 K. This trend can be explained by two phenomena present in PODE-n molecules of increasing chain length. The first phenomenon is the decreasing barrier energy of the lowest barrier reaction in all three types of reactions considered in this study (carbene producing, formaldehyde eliminations, and bond fissions) as chain length increased from n=1 to n=3. The formaldehyde elimination reactions decreased in barrier energy the most, but the decreasing barrier energy of the carbene producing reactions turned out to be the most impactful on total reaction rate constant. The lowest barrier carbene reaction for PODE-1 was found to be 69.9 kcal / mol, while that of PODE-3 was 66.2 kcal / mol. The second phenomenon that contributes to increasing reactivity with increasing chain length is the result of longer molecules undergoing less strain to form transition states than their shorter chain length equivalents. The longer the chain, the less each bond angle needs to change for a molecule chain to bend into a "tight" configuration.

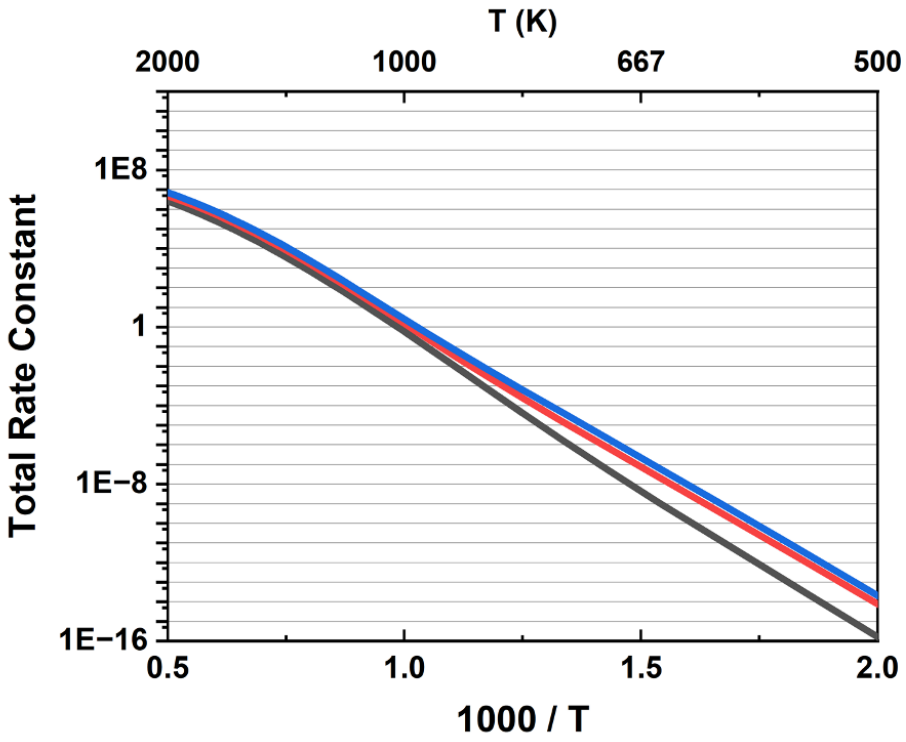

Figure 4.8. Total rate coefficients versus 1000/T for PODE-1 (black line), PODE-2 (red line), and PODE-3 (blue line) unimolecular decomposition at 1 atm for this work.

4.1.4 PODE Radical Reaction Phenomena

While understanding the chemistry of the parent fuel molecules (POMEs), perhaps even more important is the accurate prediction of the resultant radicals. These radical intermediates are fast reacting and dictate the ultimate products of combustion of POMEs. Often in the literature, the reaction rates of these species are estimated at the high-pressure limit and can yield major inaccuracies in kinetic models. In this work, we also calculated the pressure dependent rates for the POME radicals of interest. Here we highlight some of the more significant findings using PODE-1 (dimethoxymethane) as the primary example.

The PES for the unimolecular decomposition of the PODE-1 radical which forms as a result of the dominant reaction (methyl cleavange), $\dot{O}CH_2OCH_3$, in Figure 4.9. Four decomposition routes are available to the $\dot{O}CH_2OCH_3$ radical; two isomerizations through internal H-abstraction and two β-scissions. The large energy difference of 11.3 kcal/mol between the lowest barrier energy reaction and the next closest barrier implies that R4.3 will be the dominant reaction. Unlike early models which suggested these O-terminating radicals unzipped rapidly to formaldehyde monomers, the dominant reaction for this radical is the β-scission of an H-atom, leaving an aldehyde group, and in the case of PODE-1, forming methyl formate. It is interesting to see that given the dominance of methyl cleavage in PODE-1, the characteristics of PODE-1 combustion are expected to be similar to a biodiesel surrogate, methyl formate. In fact, methyl esters are formed so readily in the thermal decomposition of PODEs generally, that it is unsurprising that many of their reactive properties are similar to that of diesel.

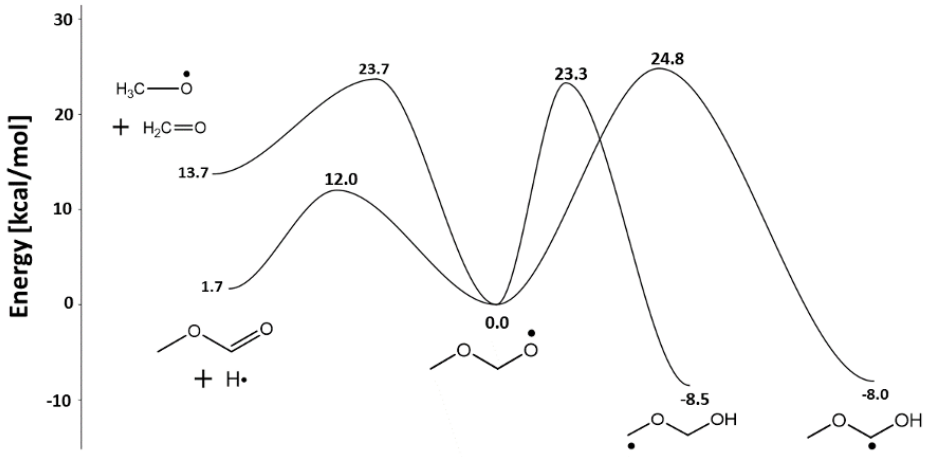

Figure 4.9. Potential energy surface for the unimolecular decomposition of $\dot{O}CH_2OCH_3$ at the CCSD(T)/cc-pV∞Z//M06-2X/cc-pVTZ level of theory

The PES for the unimolecular decomposition of the PODE-1 H-abstraction radicals, $\dot{C}H_2OCH_2OCH_3$ and $CH_3OC\dot{H}OCH_3$, is shown in Figure 4.10. These species are less flexible in terms of potential reactions. Although these two H-radical isomers can and do isomerize to one another, the terminal H-atom radical primarily unzips to formaldehyde and a smaller radical, while the central H-atom radical unzips again to methyl formate, this time also producing a methyl radical.

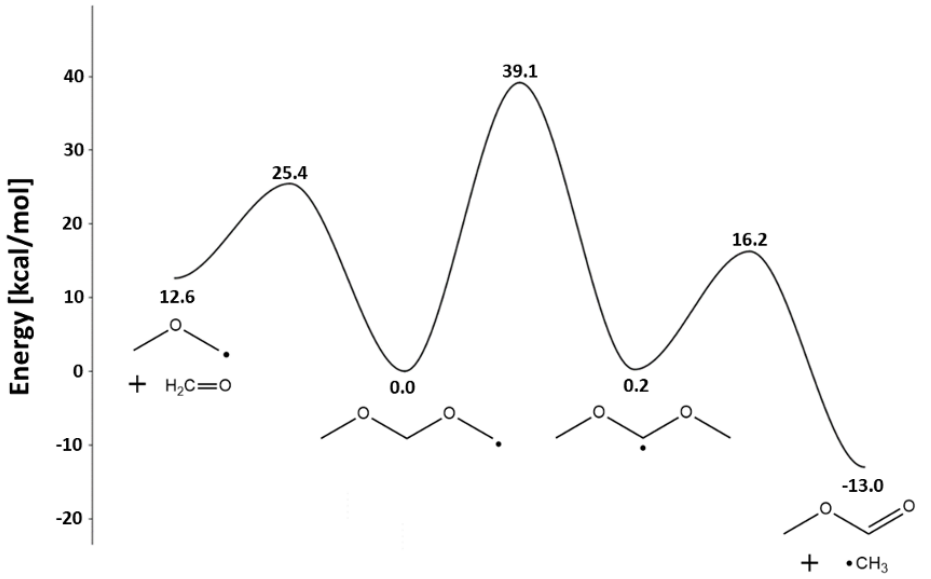

Figure 4.10. Potential energy surface for the unimolecular decomposition of and C at the CCSD(T)/cc-pV∞Z//M06-2X/cc-pVTZ level of theory

Though the decomposition of these reactive radicals is relatively straight forward to predict, the stability of these radicals and the likelihood that they will survive long enough to react bimolecularly is less clear.

To determine the likelihood that fuel radical + flame radical (H-atom for example) reactions may occur, we compare our calculated reaction rates for the radical unimolecular decomposition for both $\dot{C}H_2OCH_2OCH_3$ and $CH_2O\dot{C}HOCH_3$, and compare them to pseudo unimolecular reaction rates for reaction with H-atoms assuming ~1% concentrations of H-atoms exist in the flame sheet. The results are shown in Figure 4.11 and Figure 4.12.

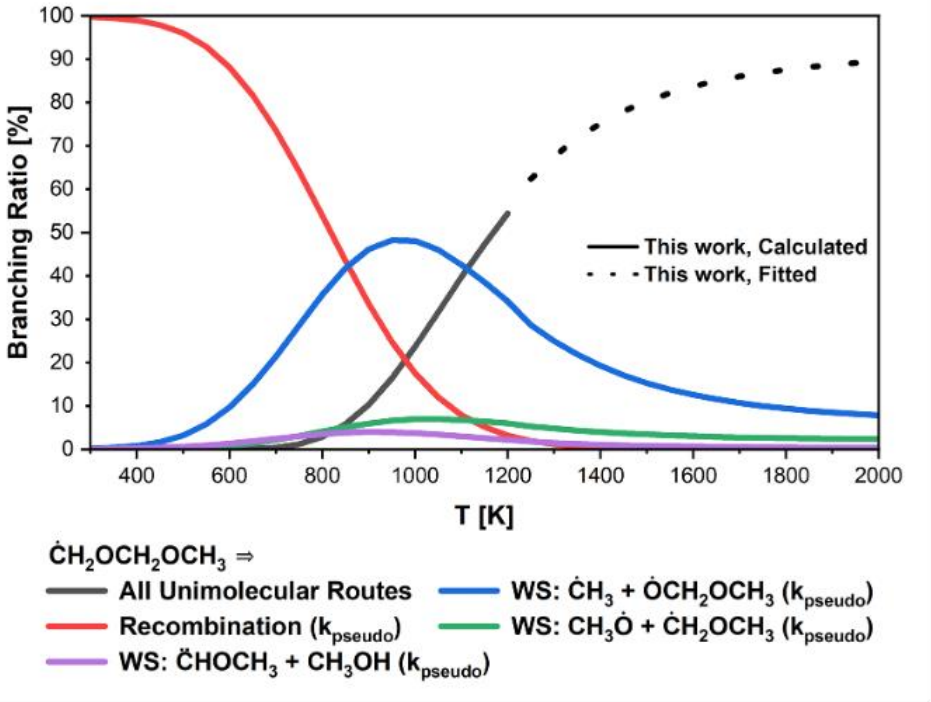

Figure 4.11. Branching ratios versus temperature at 1 atm for the unimolecular decomposition and bimolecular H-radical recombination and H-radical well-skipping of the $\dot{C}H_2OCH_2OCH_3$ radical. k_{pseudo} is indicated for pseudo-unimolecular rate constants generated assuming 1% H-radical mole fraction.

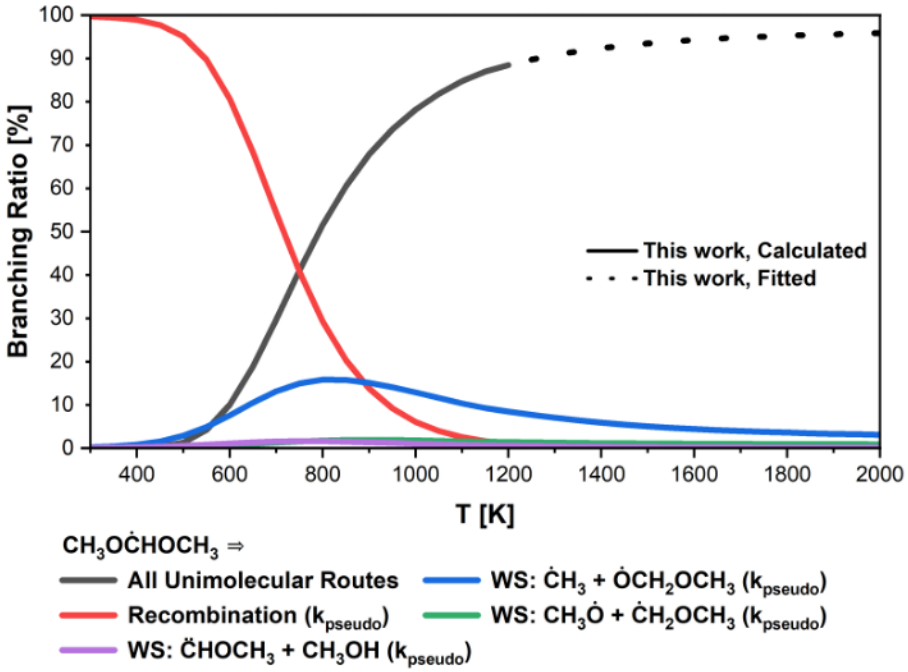

Figure 4.12. Branching ratios versus temperature at 1 atm for the unimolecular decomposition and bimolecular H-radical recombination and H-radical well-skipping of the $CH_3O\dot{C}HOCH_3$ radical. k_{pseudo} is indicated for pseudo-unimolecular rate constants generated assuming 1% H-radical mole fraction.

As Figures 4.11 & 4.12 indicate, well skipping reactions have the potential to play a significant role in the combustion of POMEs. Up to 50% of $\dot{C}H_2OCH_2OCH_3$ destruction may in fact be bimolecular rather than unimolecular. Rather than unzipping to formaldehyde then, H-atoms could force the $\dot{C}H_2OCH_2OCH_3$ radical to instead form methyl radical and the O-terminating radical, which subsequently forms more methyl formate. This can change the reactive behavior in models for these fuels and well skipping will be an important phenomenon to consider for POMEs. Well skipping was calculated and included for all POMEs studied in this work.

4.1.5 Diethyoxy- and Dipropoxy- Methane Related Reaction Rates

Exchanging the end groups in POMEs from methyl to larger hydrocarbons was also suggested to increase the properties of POMEs in such a way to make them more favorable as fuel additives while still maintaining significant reductions in yield sooting index [123]. However, the information available on these end group exchanged POMEs is very limited.

Diethyoxymethane (DEM) involves the extension of the methyl end groups by one carbon each to form two ethyl end groups. The increase in chain length of the end groups increases the energy density of the POME, though it also increases the YSI of the fuel modestly as well. Limited literature data is available for this particular molecule, and the perhaps most relevant study for DEM is that of Herzler et al [124]. The molecular and bond fission rates for DEM were measured by Herzler et al [124] using a single-pulse shock-tube experiment for pressures and temperatures between 2-4 bar and 1150-1260 K, respectively. They found that for every DEM molecule destroyed, 1.2 and 0.5 molecules of ethylene and ethanol were formed, respectively. They used the formation of ethanol as a measure for the total rate from molecular channels and subtracted this rate from the total DEM rate of destruction to derive the total rate coming

from bond fission channels. Jacobs et al. [66] also published a comprehensive study of DEM, measuring ignition delay times, laminar burning velocities, and extinction rates. They used these results to develop a kinetic reaction mechanism for DEM that includes ab initio calculations describing the unimolecular decomposition of DEM. Their electronic structure, and single point energy calculations were carried out at the calculations were down at the at the DLPNO-CCDD(T)/CBS//B3LYP- D3BJ/def2-TZVP level of theory.

The comparison of the total rate constant for the unimolecular decomposition of DEM predicted in this study to those calculated by Jacobs et al. [66] and Herzler et al. [124] is shown in Figure 4.13. Once again, our theoretical methodology is supported via fundamental experimental measurements with remarkable agreement, leading to further confidence in our theoretical abilities.

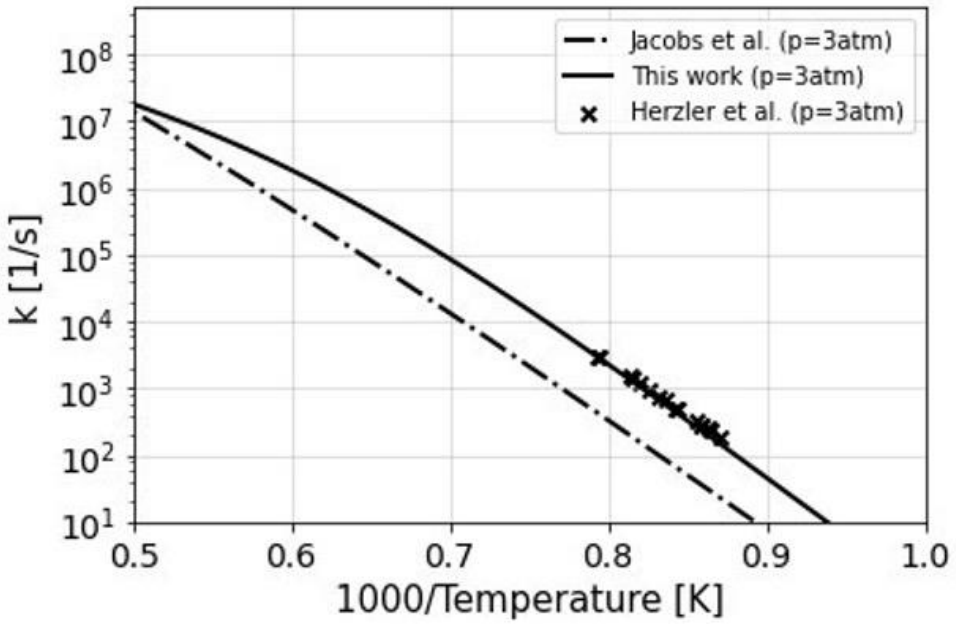

Figure 4.13. Comparison of the total rate constant for the unimolecular decomposition of DEM. Solid line is this work. Dash-dot line is Jacobs et al. [66]. Experimental points (x) from Herzler et al. [124].

With the increase in end group length, the chemistry of DEM decomposition varies somewhat from that of PODE-1. Rather than the terminal methyl group fission dominating DEM decomposition, this time the new ethyl end group is what cleaves, though the methyl cleavage does play about a 20% role at highest temperatures. Figure 4.14 highlights the reaction rates and branching ratios calculated for the main reaction pathways for DEM. However, when compared to DPM in Figure 4.15, there are some deviations from this reactivity pattern. For DPM (dipropoxymethane), we would expect that following the PODE-1 and DEM pattern, that propyl cleavage would dominate. Instead, it second to ethyl cleavage. Methyl and propoxy cleavage play minor roles in comparison.

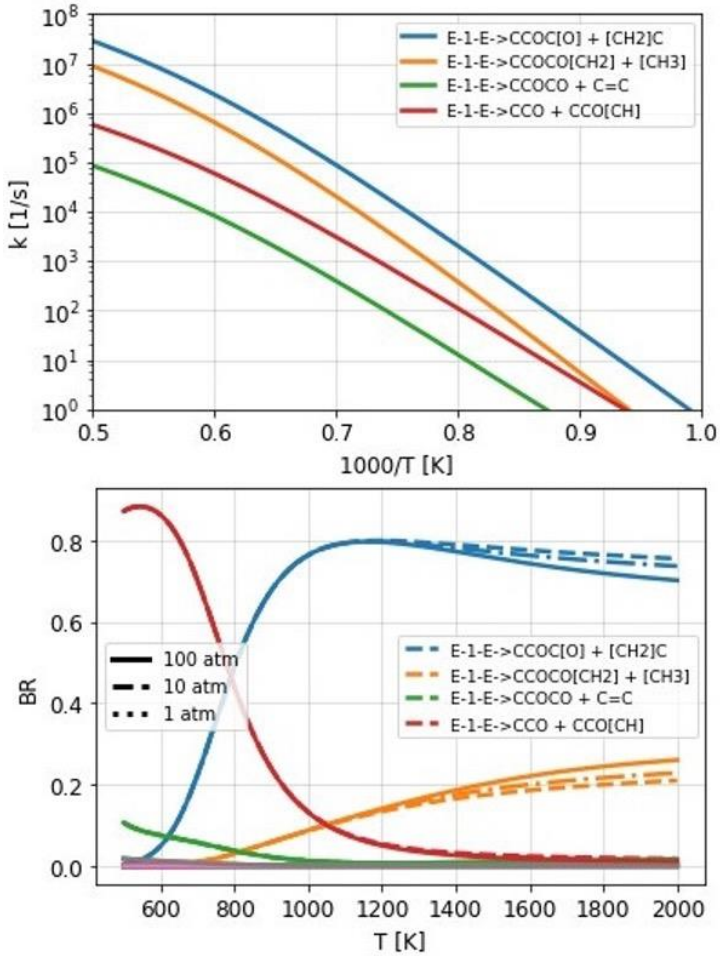

Figure 4.14. Reaction rates and branching ratios for DEM calculated in this work.

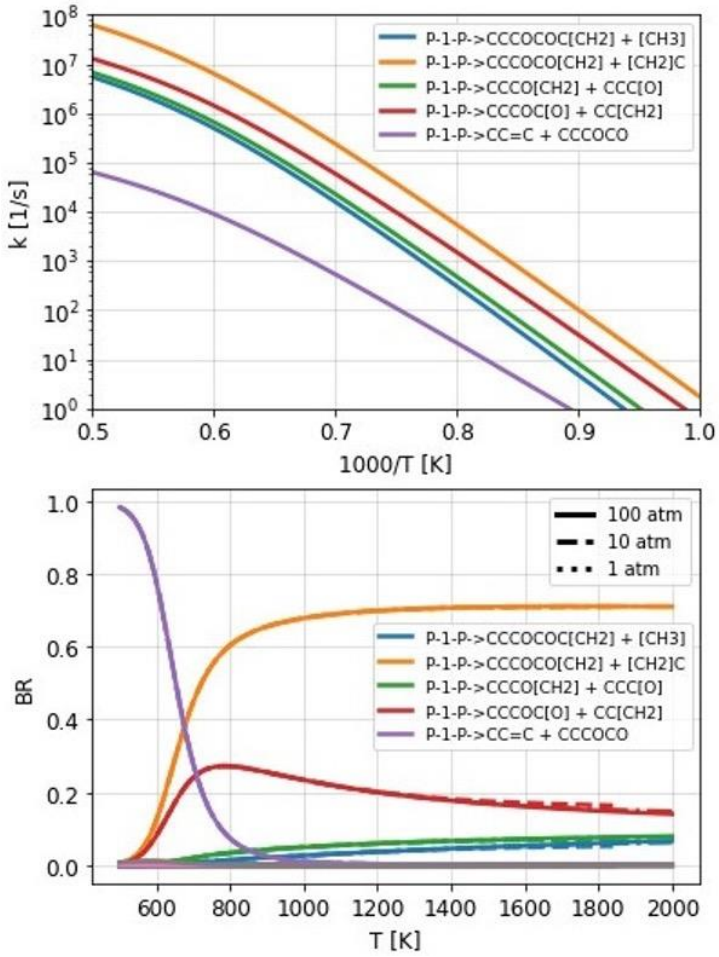

Figure 4.15: Reaction rates and branching ratios for DEM calculated in this work.

4.2 Fundamental POME Kinetics Experiments and Model Validation

Experimental studies play a foundational role in the development of kinetic mechanisms. Not only do they provide benchmarking data to probe not only the chemistry of the fuel molecules themselves, but the subsequent chemistry of the intermediate species that follow. The goal of comparison of a theory-based model to experiments is two-fold. 1) To make sure that the theory is accurately predicting nature and 2) that beyond the scope of the immediate study, that other assumptions do not cloud predictions. In the previous section, we saw that the total rates for the theory-based reaction rate constants were in line with previous experimental studies, but we have not discussed more broadly the accuracy of the developed kinetic models. In this section we aim to do that.

4.2.1 Benchmarking Models versus Literature Data

We conducted several more reaction model studies for dimethoxymethane to test both the reaction kinetics that were calculated as well as the base chemistry for our model to ensure accuracy. To start, we conducted numerical simulations using the other sets of shock tube experimental data from Peukert et al. [113], namely HRR-TOF-MS and GC/MS. These experiments have higher concentrations of PODE-1, which leads to significant involvement of secondary chemistry due to which these experiments are not as clean as the H-

ARAS experiment for gaining a comprehensive understanding of PODE-1 pyrolysis kinetics. Nevertheless, they provided valuable insight into the kinetics of important species, such as the competition between decomposition and abstraction reactions of PODE-1, as well as the key pathways for CO species formation.

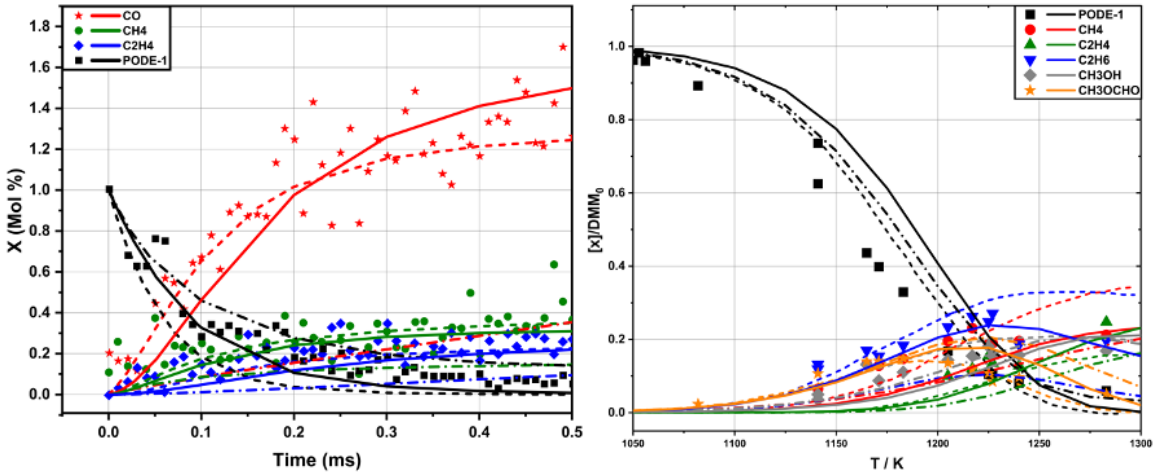

Figure 4.16. (Left) HRR-TOF-MS Experimental data [113] at 1358 K and 1.42 bar with initial mole fraction of PODE-1 being 1% with Kr 1% and Ne 98%. The solid line represents our kinetic mode, dashed dotted line is the Pazdera et al. [115], dashed line is Döntgen et al. [116]. (Right) GC/MS Experimental data [113] at 2.3 bar and 1.8 ms residence time with initial mole fraction of PODE-1 being 560 ppm with Argon as bath gas. The solid line represents our kinetic model, dashed dotted line is the Pazdera et al. [115], dashed line is Döntgen et al. [116].

The mechanism derived from our work and that of Döntgen et al. [116] exhibited good agreement, while Pazdera et al. [115] consistently underpredicted the speciation data of HRR-TOF-MS [113], as observed in Figure 4.16 (left). The underprediction by Pazdera et al. [115] could be attributed to their lack of radical chemistry. The Döntgen et al. [116] model demonstrates good accuracy in predicting CO species, even though they did not consider well-skipping reactions for PODE-1. This accuracy can be attributed to the fact that Döntgen et al. [116] adjusted their theoretical rates for PODE-1 decomposition, as discussed earlier.

The numerical simulation of GC/MS shock tube data [113] reveals that consumption of PODE-1 is slower for our mechanism compared to that of Pazdera et al. [115] and Döntgen et al. [116]. Pazdera et al. [115] PODE-1 decomposition rates become faster than our theoretical rates as pressure increases. The GC/MS experiment was conducted at higher pressure compared to the previous two shock tube experiments. Hence, on contrary to the previous two numerical simulations, decomposition of PODE-1 is faster for GC/MS simulation for Pazdera et al. [115]. On the other hand, the Döntgen et al. [116] model doesn't exhibit overprediction of consumption of PODE-1 as it has been seen with the previous two experimental data sets. However, they accurately predict PODE-1 consumption, primarily because the GC/MS shock tube experiment [113] was one of the datasets they used to calibrate the reaction rates for PODE-1 decomposition.

The accuracy in prediction of PODE-1 consumption falls short for our kinetic model compared to Pazdera et al. [115] and Döntgen et al. [116] is primarily attributed to the large variability in the GC/MS experimental dataset [113]. It is reasonable to assert that out kinetic model falls well within the experimental variability of the GC/MS dataset [113].

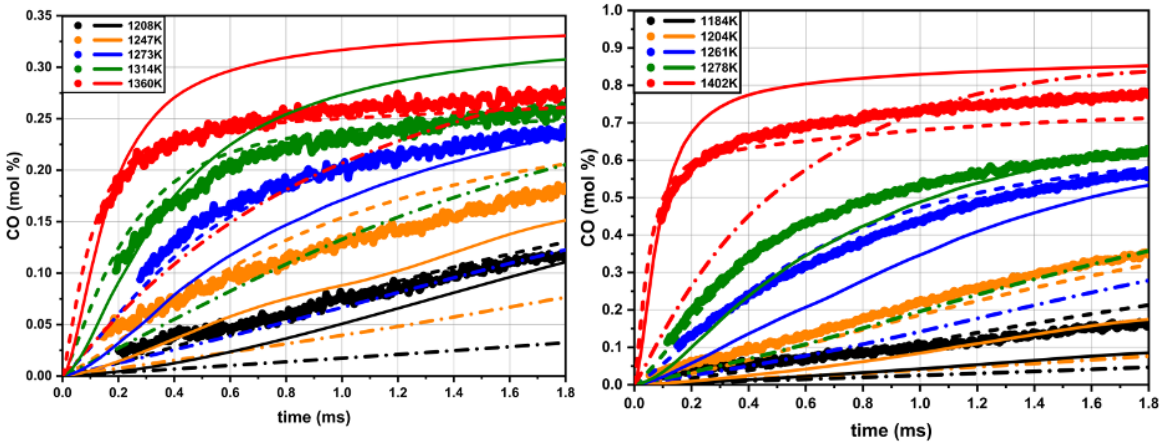

Figure 4.17. CO speciation data obtained via laser absorption spectrometry [116] at different temperatures and ~2 bar pressure, initial mole fraction of 0.2% (left) and 0.5% (Right) PODE-1 with bath gas Argon. The solid line represents our kinetic model, dashed dotted line is the Pazdera et al. [115], dashed line is Döntgen et al. [116].

We also conducted a comparative analysis of our PODE-1 kinetic model with a set of shock tube data collected by Döntgen et al. [116] which have CO speciation data obtained through laser absorption spectrometry. The results from the kinetic model of Pazdera et al. [115] and Döntgen et al. [116] is similar to what has been observed from the investigation of CO speciation in TOFMS shock tube data [116]. In case of our kinetic model, which has shown good performance when tested against other experimental datasets, we encounter a different behavior with laser absorption spectrometry data [116]. At lower temperatures, our model underpredicts CO speciation, and as the temperature increases, it starts to overpredict CO speciation. In our supplementary material we have included our sensitivity analysis results, which revealed that two reactions are most sensitive to the CO speciation and H abstraction reaction of formaldehyde (CH2O+H=HCO+H2). Apart from these two reactions, there are several other reactions which exhibit mild sensitive to CO speciation. The involvement of the secondary chemistry due to the fact that this experiment has ran at higher pressure and with higher concentrations of PODE-1 when compared to the cleaner experiment for PODE-1 pyrolysis, H-ARAS shock tube experiment [113].

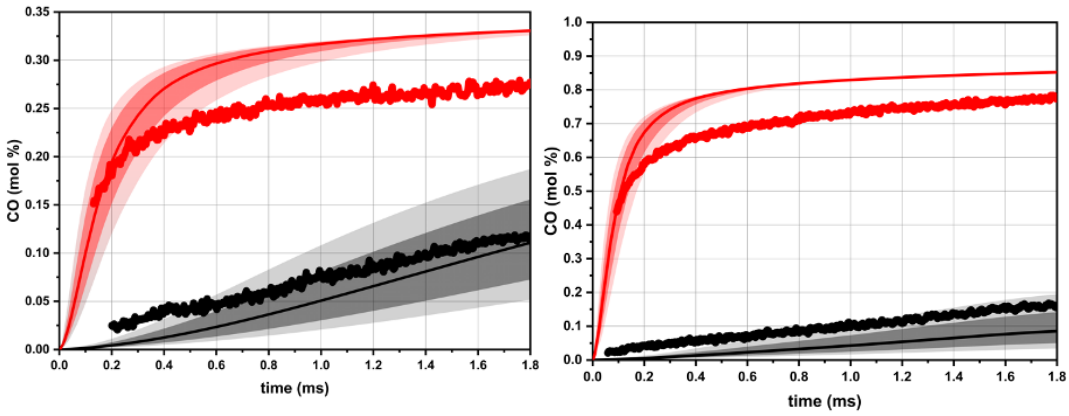

Figure 4.18. CO speciation data obtained via laser absorption spectrometry [115]. The solid line represents our kinetic model. (Left): Initial mole fraction of 0.2% PODE-1, red is CO %mol fraction at 1208K and black is CO %mol fraction at 1360K. (Right): Initial mole fraction of 0.5% PODE-1, red is CO %mol fraction at 1184K and black is CO %mol fraction at 1402K.

To differentiate the effects resulting from PODE-1 decomposition reactions on CO speciation from those caused by other CO-sensitive reactions, we conducted simulations by scaling rates of PODE-1 decomposition by a factor of 2 and 1.5. The resulting bands are shown in Figure 4.18: for two temperature points. Figure 4.18: illustrates that as the temperature increases, the modification to PODE-1 decomposition rates lead to less variation in CO speciation. Furthermore, it is noticeable that the bands representing CO for initial PODE-1 mol fraction of 0.5% is even narrower compared to the bands for CO speciation at an initial PODE-1 mol fraction of 0.2%. This observation may be attributed to the increasing prominence of secondary chemistry effects as the concentration of PODE-1 is increased.

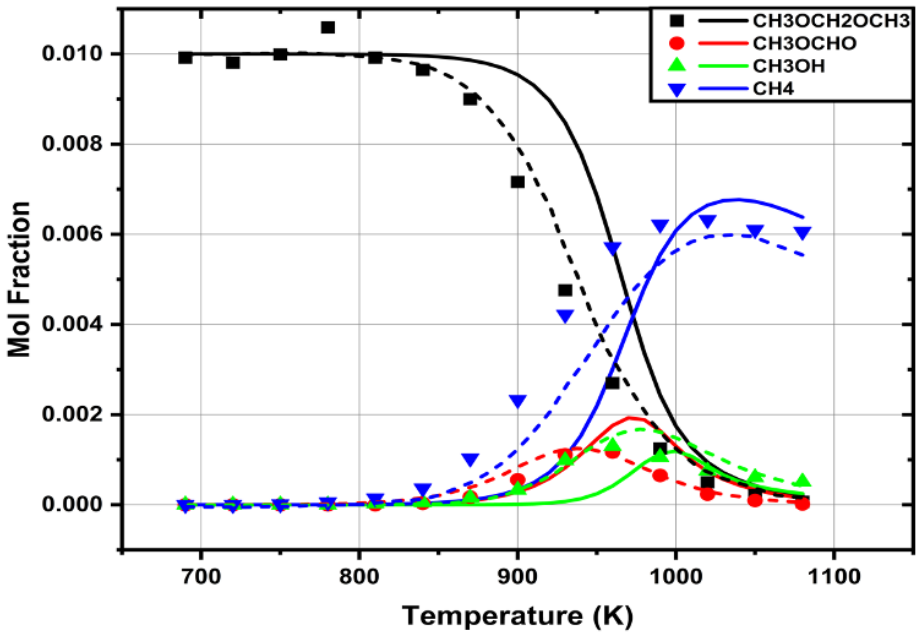

Figure 4.19. JSR Experimental Data [119] at 1.07atm and 2s residence time with initial PODE-1 mole fraction being 1 % and Argon as bath gas. The solid line represents our kinetic model and dashed line of Zhong et al. [119].

Figure 4.19 highlights our final experimental comparison to our model by comparing JSR experiments from Zhong et al. [119]. Of note, the Zhong et al. [119] kinetic model is accurate with the species prediction for JSR experiment which is largely due to the fact that this JSR experiment [119] along with JSR experiment from Vermeire et al. [117] was used by Zhong et al. [119] to numerically fit their analogy-based PODE-1 pyrolysis rates. Based on the accuracy shown by our kinetic model for the PODE-1 pyrolysis with experiments which have less impact of secondary chemistry on PODE-1 pyrolysis compared to JSR, it is fair to conclude that the slight shift seen in our kinetic model is caused due to the accuracy of external hydrogen abstraction reactions rather than our theoretically computed PODE-1 pyrolysis rates. In addition to JSR experimental data of Zhong et al. [119] we also compared our model with JSR experimental data from Vermeire et al. [117], where we saw similar behavior of our kinetic model as we see with Zhong et al. [119] JSR experimental.

4.2.2 Experimental Methodology for Microreactor Experiments

Experiments regarding the direct detection of decomposition species for POMEs was very limited in prior work. Those relevant studies have been discussed prior in this section. However, given the history of disagreement as to the primary decomposition pathways of dimethoxymethane (PODE-1) and the

subsequent uncertainty that places on the decomposition of other POMEs, experimental observation of the direct decomposition of POMEs is warranted.

Experiments, used to confirm initial decomposition pathways, were performed in a micro-reactor in tandem with photoionization mass spectrometry (PIMS) for mass detection. In summary, POMEs were studied by entraining a dilute sample of the molecule in helium. This sample mixture is flowed continuously through the reactor at 200 SCCM using an MKS 4B013202RB70 Mass Flow Controller. The following molecules were analyzed - dimethoxymethane (Sigma Aldrich >99% purity), 2,4,6 Trioxaheptane (Asta Tech Chemicals >99% purity), and 2,4,6,8 Tetraoxanonane (synthesized at CSU >95% purity). Each of these molecules' vapor pressure is large enough to prepare static sample volumes of between 0.025% and 0.1% reactant in standard lecture bottles.

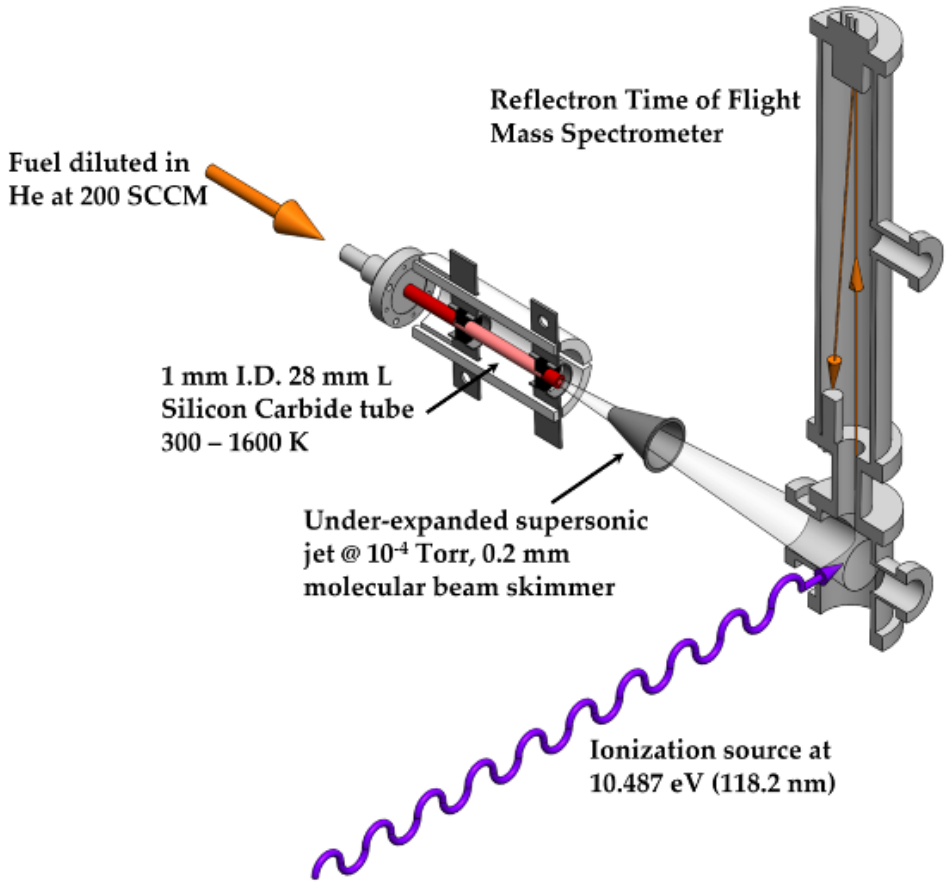

Figure 4.20. Reflectron photoionization time-of-flight mass spectrometer with fixed frequency photons at 118.2 nm

The microreactor assembly consists of a tubular silicon carbide reactor of 30 mm in length, with a 1 mm inner diameter. The reactor material is chosen for its ability to withstand very high temperatures and thermal cycling while remaining inert and not participating in any of the pyrolysis reactions. The reactor is resistively heated to 1800K through Carbon discs fitted to the reactor's outer diameter. These discs are approximately 15 mm apart and form the contact points for the electrical circuit used to heat the reactor resistively. The temperature at the exterior surface of the reactor is monitored by a TIM Microtek thermal

camera, between the two heating. The residence time is roughly 100 μs enabling the identification of the first decomposition products.

The flow properties in the reactor were modeled using CFD by Guan et al. [125]. The temperature was calculated to reach within 100 K of the measured wall temperature by 1/3 of the reactor length. This temperature profile and the falling pressure profile affect the product distribution as the reaction rates are temperature and pressure dependent. A low Peclet number of the flow results in any wall reactions being constrained to the thin layer of fluid directly adjacent to the walls and not affecting the bulk of the flow.

In the PIMS experiment, gases flow continuously through the reactor, with the products exiting the reactor entering a 0.2 mm diameter molecular beam skimmer. The resulting beam is intersected and ionized by the 9th harmonic of an Nd:YAG laser (118.2 nm or 10.487 eV). The laser is aligned with the flow entering an ionization chamber maintained at 5 X 10-7 torr by a 1200 L/s Pfieffer TPU 1201 P turbomolecular pump. The internal frequency tripled the output of an Nd: YAG laser is directed into a cell that is pressurized to 150 Torr with a 10:1 argon: xenon mixture. This mixture is optimized to promote sum-frequency generation that creates 118.2 nm VUV photons, which have sufficient energy to ionize most hydrocarbon molecules. The generation of 118.2nm photons by Xe/Ar tripling cells has been studied at great length. We expect the use of 30 mJ pulse per pulse power at 355 nm from the YAG laser and the established tripling efficiency of 1×10-5 in pure Xenon and the transmission efficiency of the MgF2 lens to produce roughly 30 nJ per pulse at 118.2 nm light. Post ionization, the molecules in the expansion are accelerated into a Jordan reflectron time of flight spectrometer with a Micro Channel Plate (MCP) detector producing voltage signals which are converted to digital traces in an interfacing computer. This data is converted into a spectra format and is analyzed for the decomposition products.

As a complement to the PIMS, infrared spectroscopy in an argon matrix provides structural information for the pyrolysis products, differentiating thermal products of identical mass. Additionally, those molecules and radicals whose ionization energy lies beyond the energy of the photons produced by the fixed wavelength light source can also be characterized. The molecular beam formed at the reactor exit impinges on a cold window. The products, now trapped in frozen argon, are detected by FT-IR spectroscopy, as shown in Figure 4.21.

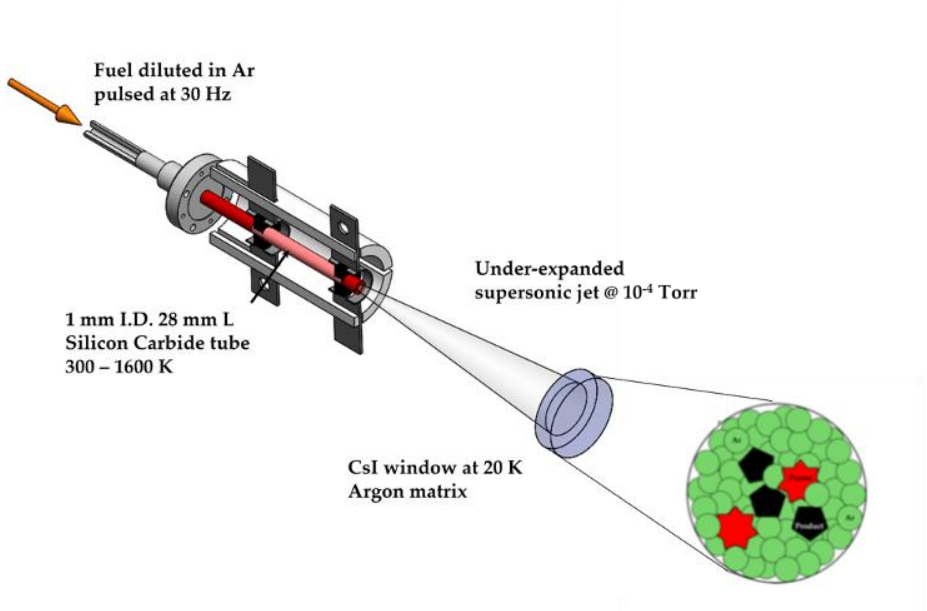

Figure 4.21. Pyrolysis products entrained in Ar exit the μ-tubular reactor and become trapped on a cryogenic window.

A Varian Turbo V 81 AG, backed by a mechanical pump (Edwards Vacuum Systems), produces the high-vacuum conditions (10^{-6} Torr) necessary for matrix isolation spectroscopy. The flow reactor assembly is mounted to the vacuum shroud of a two-stage closed-cycle helium cryostat (APD Cryogenics, model DE-202, 60 Hz and 2.5W cooling capacity at 20 K; compressor model HC-2D), which cools an infrared transparent cesium iodide (CsI) window to 10 K. Figure 2.6 shows a detailed cross-sectional view of the matrix assembly and the positions for deposition and collection of the FT-IR spectrum. The CsI window is mounted in a metallic holder, which is screwed into the cold finger of the He-cryostat expansion unit. Thermal contact between the finger and the window holder is enhanced by a thin layer of indium. Molecules exiting the reactor are aimed at the cold, IR transparent window (approximately 3 cm away). The deposition of many thin layers of the pulsed reactant gas mixture forms a matrix. A pair of CsI windows on opposing sides of the cryostat shroud allow an infrared beam to pass for spectroscopic detection.

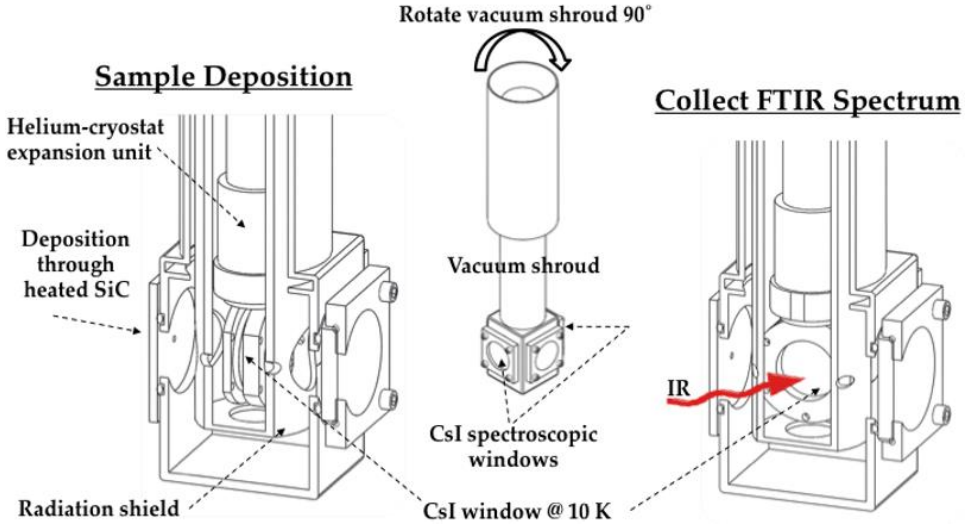

Figure 4.22. After deposition on the cold (10 K) window, the outer shroud is rotated 90 for spectroscopic analysis of molecules frozen in Ar.

Gaseous reactant mixtures are prepared in a glass 1.2 L reservoir upstream of the reactor in concentrations of 0.04−0.1% in approximately 800 Torr Ar. To achieve resolved IR spectra, typical deposition rates through a pulsed valve were 0.8 to 1 Torr min^{-1} from the reservoir (equivalent to 3−3.6 mmol hr^{-1}), depositing between 3 to 6.5 mmol total onto the cold window. Based on the concentration of the reactants in argon, this is equivalent to about 10^{13} radicals per pulse. The vibrational spectra are measured using a Nicolet 6700 infrared spectrometer equipped with a liquid N_2-cooled mercury/cadmium/telluride detector (MCT/A, 4,000−650 cm-1). The spectrometer is purged with purified dry air, and the spectra are collected with the OMNIC software package on a Windows operating system. A background scan is taken approximately 1 to 2 hours before the sample scan; all spectra averaged 500 scans at 0.25 cm^{-1} resolution.

4.2.3 Microreactor Experimental Results

The experimental results from the decomposition of the POM-E molecules in the heated microreactor experiments are presented first, followed by the electronic structure calculations. Figure 4.23 shows PIMS Spectra for 0.1% dimethoxymethane (PODE-1) in He at four temperatures, labeled on the right. Two peaks are observed at room temperature when ionized by the light source at 10.47 eV. All three POM-E molecules chosen in this experimental study show strong dissociative ionization. The presence of an easily ionizable lone pair of electrons on the multiple oxygen atoms results in a direct elimination of hydrogen in the form of a radical from the parent molecule. This manifests in a large peak at m/z 75 corresponding to $CH_3OCH_2OCH_2$+ and the associated Carbon 13 peak at m/z 76. At 900K, an additional peak at m/z 45 (methyl methoxy radical CH_3OCH_2+) appears. This is due to breaking the weak oxygen-carbon bond-forming methoxy radical and the fragment at m/z 45. Since the methoxy radical's ionization energy is beyond the laser's capability, it is not observed. However, the formation of methyl methoxy radical indicates its presence indirectly. As the temperature is raised further, the parent peak reduces in signal intensity, indicating a complete breakdown within the reactor into multiple fragments. Due to the laser's conditions, most of these fragments undergo decomposition to formaldehyde and methyl radical through multiple intermediate radical forms. The laser energy at 10.487eV places a lot of these radical fragments outside the ionizability envelope, resulting in only the methyl peak (IE) being seen at temperatures greater than 1300K and growing in intensity as the temperature is raised. A comprehensive analysis carried out at a tunable synchrotron light source, which eliminates the challenge of dissociative ionization and can access products beyond the capability of the tabletop Nd:YAg laser agrees with these results.

A set of concentration trials was carried out to confirm that none of the products observed (or pathways were being suppressed) due to bimolecular reactions. This involved assessing spectra from evaluations carried out at 0.15% dimethoxymethane as a high concentration limit, followed by trials at 0.1%, 0.05%, and 0.025%. All four evaluations confirmed that none of the observed peaks were due to bimolecular reaction, with peaks across concentrations being identical in mass over charge and varying only in signal intensity.

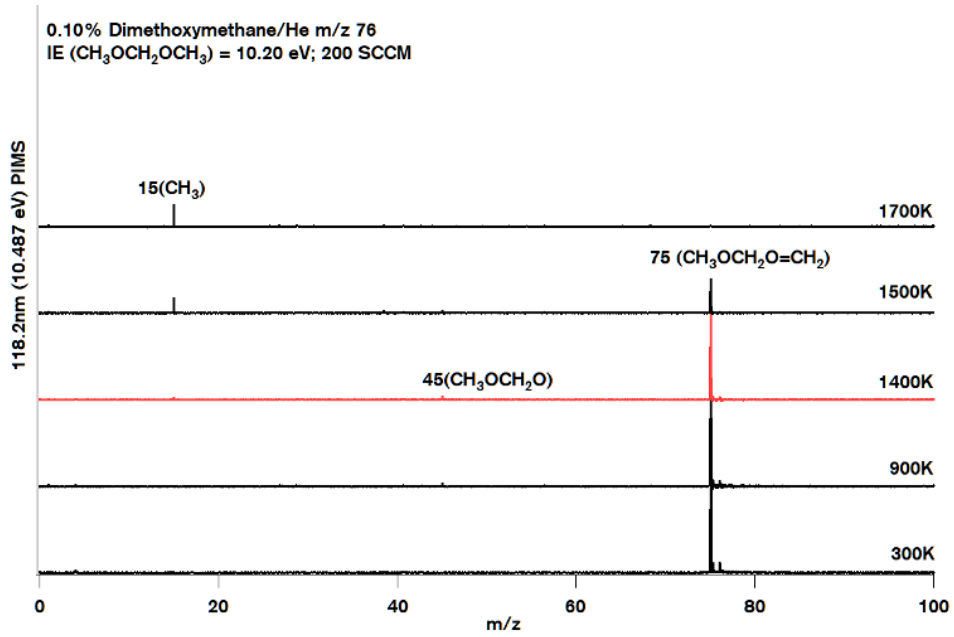

Figure 4.23. PIMS of 0.1% Dimethoxymethane in He in the micro-reactor at 200 SCCM heated from 300 to 1700 K and ionized by 118.2 nm (10.487 eV) photons

Though more difficult to interpret, questions of whether the existence of the carbene could be detected linger, as the carbene would not be stable upon contact with the photoionization laser. Figure 4.24 shows a representative infrared spectrum of PODE-1. No trace of the carbene has been detected with the experiment to date, reaffirming it is likely not important for PODE-1.

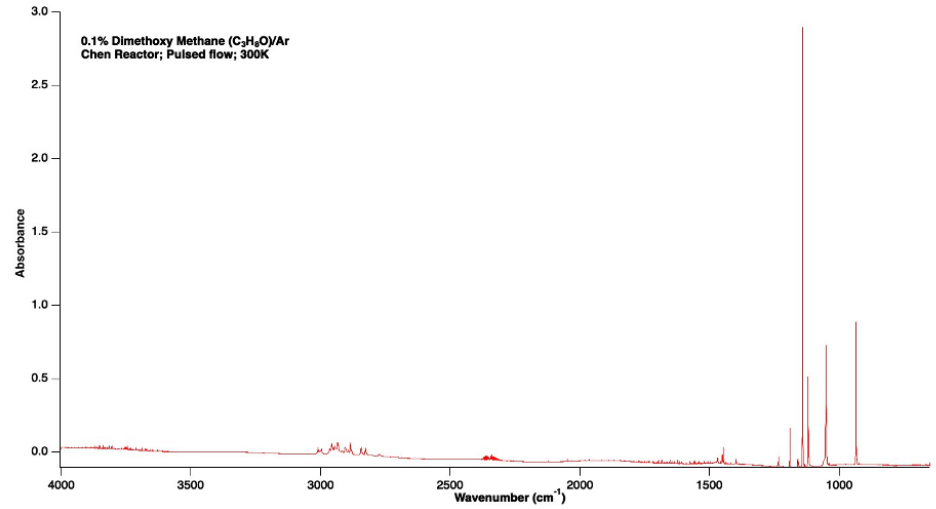

Figure 4.24. Infrared spectrum of 0.1% PODE-1 (dimethoxymethane) in argon.

The next member of the methyl end group POM-E evaluated was 2,4,6 Trioxanonane (PODE-2) - this molecule differs from dimethoxymethane in having an additional O-CH_2 group in the chain. A sample at 99% purity was obtained from Asta Tech for this evaluation and Figure 5.2 shows PIMS spectra for 0.1% of the molecule in a Helium carrier gas. At room temperature, a weak parent peak is observed at m/z 105 (the result of the removal of hydrogen through oxygen lone pair ionization) due to a strong dissociative

ionization effect. Laser intensity coupled with additional oxygen in the second methoxy group results in intense dissociative ionization at room temperature, with peaks at m/z 77 (formyl radical elimination), m/z 76 (formaldehyde elimination), m/z 75(secondary C-O bond fission), m/z 74 (methanol elimination). These dissociative ionization peaks persist till 1500K, with intensity decreasing with increasing temperature. At 900K, the first pyrolytic decomposition product is observed at m/z 45 (CH_3OCH_2 *) and 61 (CH_3OCH_2O*). With a further increase in temperature, the fragment peaks persist with a progressive reduction in parent peak intensity. At 1300K, the first sign of methyl peak (m/z 15) is observed - with peak height growing with increasing temperature, consistent with observations made with dimethoxymethane. By 1500K, all other pyrolytic fragmentation peaks disappear, with only the methyl peak and weak fragmentation peaks at m/z 74 and m/z 75. This indicates the strong tendency of the molecule at elevated temperatures to fragment in the short residence time of the reactor to form methyl radical and formaldehyde. At temperatures beyond 1500K, the parent peak at m/z 105 disappears, and only the methyl peak at m/z 15 endures.

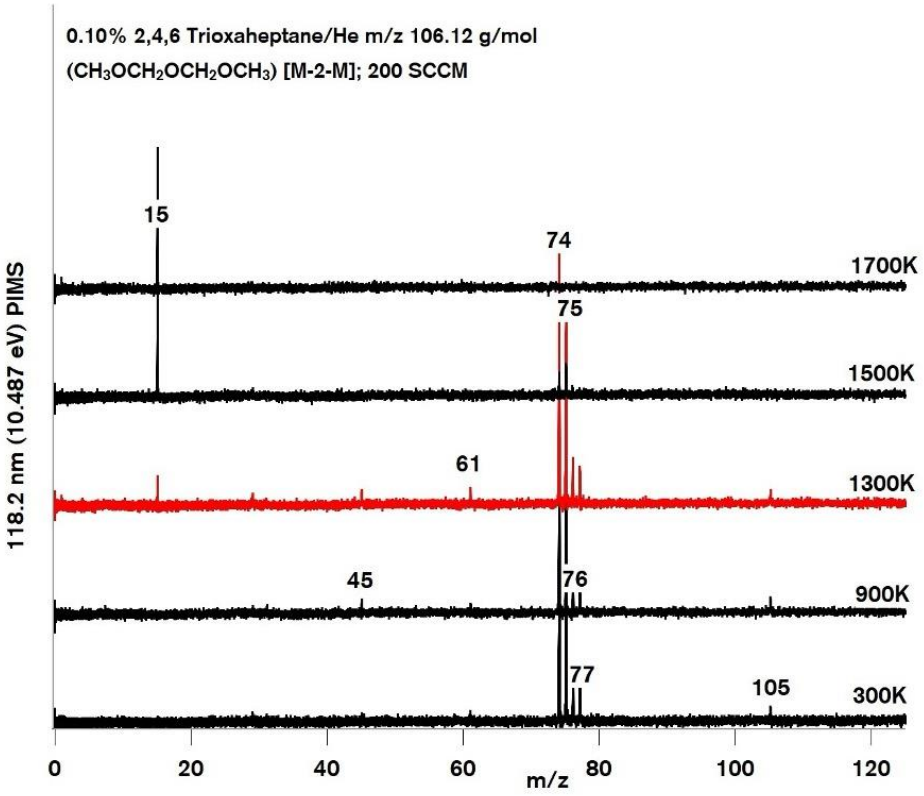

Figure 4.25. PIMS of 0.1% 2,4,6 Trioxanonane (PODE-2) in He in the micro-reactor at 200 SCCM heated from 300 to 1700 K and ionized by 118.2 nm (10.487 eV) photons

The third compound evaluated using the photoionization mass spectrometry setup was 2,4,6,8 Tetraoxanonane (PODE-3), containing two O-CH_2 groups more than dimethoxymethane and weighing 136 g/mol. The sample evaluated was synthesized at CSU to a purity of >96%. Figure 4.26 shows PIMS spectra for 0.1% of the molecule in helium. Like the previous two molecules evaluated, M-3-M also undergoes a very high degree of dissociative ionization. The photon energy of 10.487eV is strong enough to completely break down the parent peak at room temperature into multiple fragments, with a minimal parent peak at m/z 136. Major peaks are observed at m/z 107, m/z 106, m/z 105, and m/z 104, with the peak at m/z 105

being the strongest in relative intensity. These peaks correspond to the elimination of methoxy (CH_3O), formaldehyde (CH_2O), and methanol (CH_3OH) from the parent molecule. The peak at m/z 91 is $CH_3OCH_2OCH_2O^*$, with the other fragment at m/z 45 (CH_3OCH_2). Unlike the other two compounds, where the bond cleavage between the oxygen and carbon atoms is driven through thermal cracking, in this case, bond breakage is achieved through photon impact. A set of peaks is observed at m/z 74, m/z75 ($CH_3OCH_2OCH_2$), m/z 76, and m/z 77 caused by the bond breakage between the oxygen and carbon at different sites along the molecule. The corresponding fragments associated with these masses are also seen at m/z 59, m/z60, and m/z 61. The peak at m/z 44 may be assigned to $^*C_2H_4O$. These dissociative ionization fragments persist up to 1400K, with most peaks disappearing beyond this temperature. The appearance of methyl radical ($^*CH_3$ m/z 15) is first noted at 1200K. This is lower than the 1300K seen across the previous two molecules and concentration evaluations. This can be attributed to the longer chain length of the molecule with relatively weaker bonds binding individual fragments leading them to break down more easily into methyl and formaldehyde at elevated temperatures. By 1800K, the only peaks visible are at m/z 15, which increases in intensity between the temperature range of 1200K to 1800K.

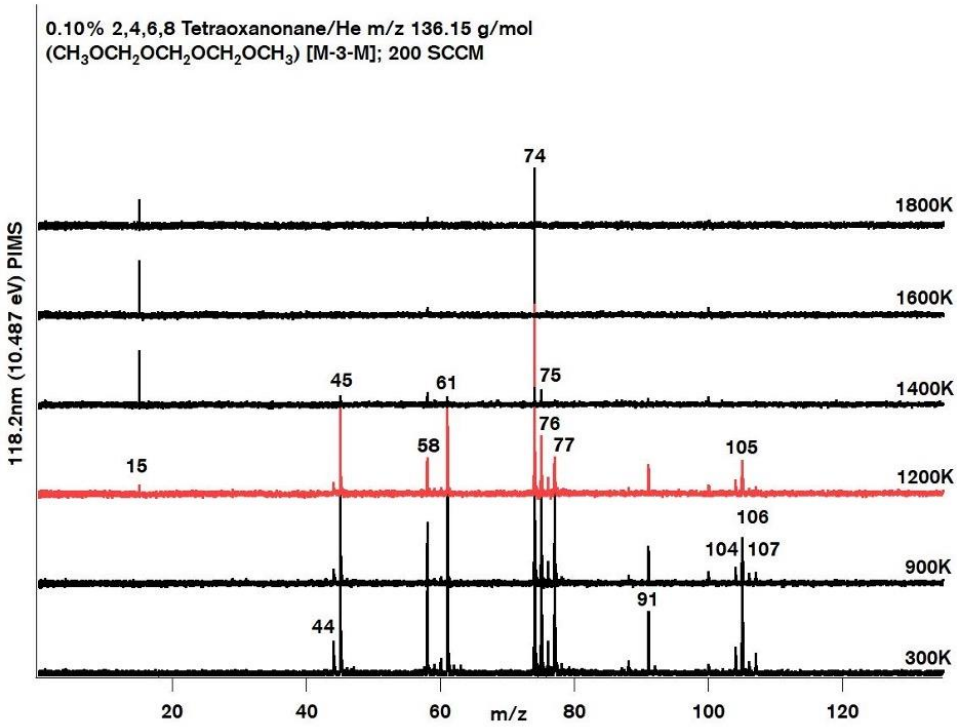

Figure 4.26. PIMS of 0.1% 2,4,6,8 Tetraoxanonane (PODE-3) in He in the micro-reactor at 200 SCCM heated from 300 to 1800 K and ionized by 118.2 nm (10.487 eV) photons

Room temperature spectra for diethoxymethane (DEM) shows significant dissociative ionization with fragments formed at m/z 89 (methyl bond breakage) and m/z 74 (formaldehyde elimination). The first time thermally activated decomposition pathways are reached is between 1300 and 1400K reactor surface temperatures. The presence of m/z 28 also confirms the validity of the transition state route at 67.9 kcal/mol. Other short-lived products fragment into methyl radicals (m/z 15) and formaldehyde (m/z 30, but not ionizable at 10.487 eV). The PIMS spectra are shown in Figure 4.27.

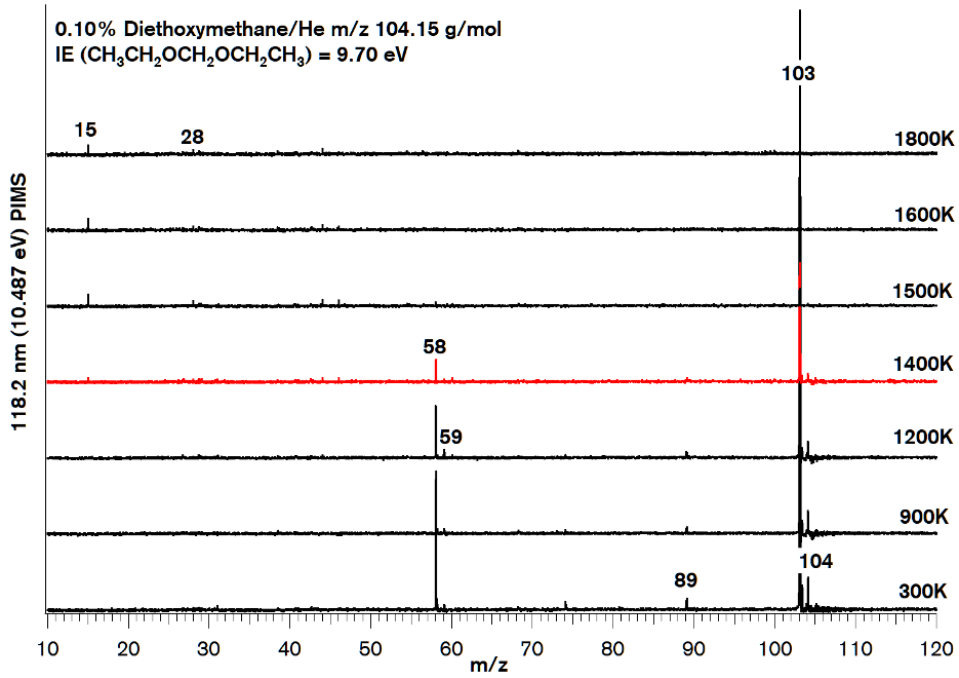

Figure 4.27. PIMS of 0.1% diethoxymethane in He in the micro-reactor at 200 SCCM heated from 300 to 1800 K and ionized by 118.2 nm (10.487 eV) photons.

Room temperature spectra obtained at 300K shows significant dissociative ionization with multiple peaks observed in addition to the parent peak. A weak parent peak signal is seen at m/z 132, with a much larger signal corresponding to the abstraction of a hydrogen atom from the parent molecule internally at m/z 131. A cluster of peaks is observed at m/z 104 (ethylene elimination), m/z 102 (CH_3-CH_2* elimination), and m/z 102 (formaldehyde elimination). The formaldehyde elimination peak is the most dominant route among these three (based on signal intensity). Additional peaks observed at m/z 73 and m/z 72 are due to the fragmentation of the first carbon-oxygen bond and the elimination of propanol. Additional peaks seen at m/z 58 (Propanal) and m/z 43 (CH_3-CH_2-CH_2*) are fragment remnants produced by the laser. The PIMS spectra are shown in Figure 4.28.

As the temperature is raised, the primary decomposition route of elimination of the end propyl and methyl groups is observed at temperatures above 1300K. At these temperatures, the influence of the ionizing medium on the fragmentation is reduced, with bond fission peaks at m/z 43 (CH_3-CH_2-CH_2*) and m/z 15 (CH_3*) becoming dominant.

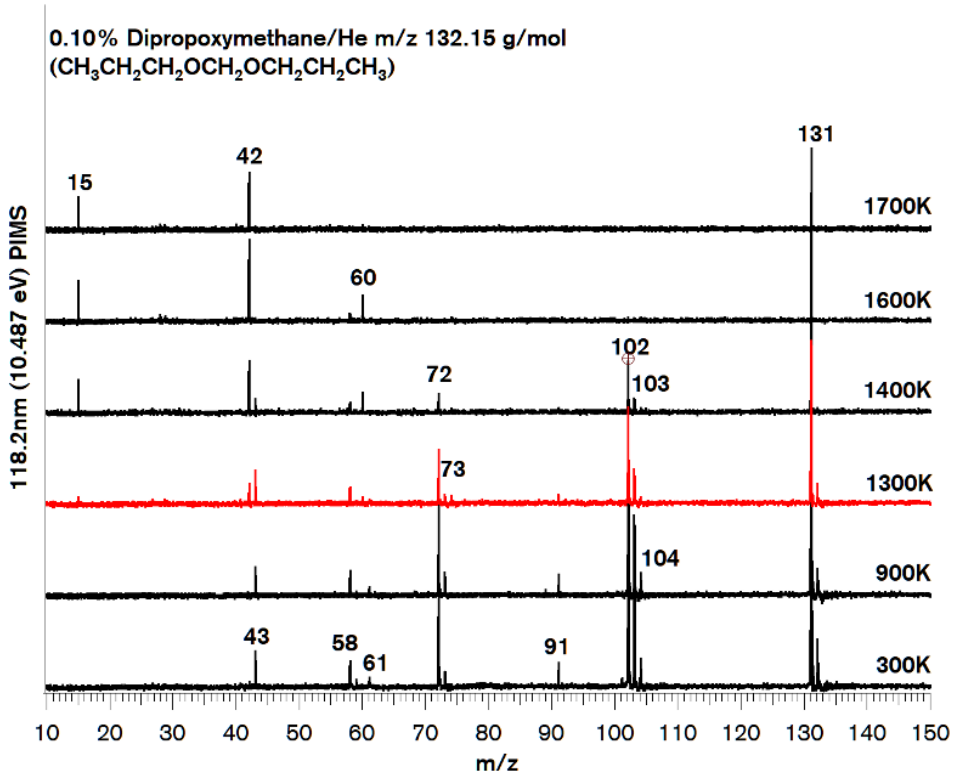

Figure 4.28. PIMS of 0.1% dipropoxymethane in He in the micro-reactor at 200 SCCM heated from 300 to 1700 K and ionized by 118.2 nm (10.487 eV) photons.

4.3 Extending the Models to Practical POMEs

Finally, the work outlined above was in the service of creating a reliable theory based reaction network from which analogies may be created to extend these models to larger, more practical potential POMEs. Here we demonstrate the utility of this with CH_3-CH_2-O-CH_2-O-CH_2-O-CH_2-CH_3 (E2E), which was identified as a potential viable oxymethylene ether for use in diesel blends by Bartholet et al. [123] The foundational work of studying how the kinetics of POMEs change either by 1) extension of the polymeric chain via addition of -OCH_2- groups or 2) by extension of the alkyl end groups to higher carbon number functional groups allowed for analogy based reaction rates to be created for alternative POME fuels with ease and accuracy. Through this, the base reaction mechanism described above was extended for the addition of E2E. Flame speeds were first tested against the work of Jacobs et al. [66] who measured laminar flame speeds of diethoxymethane in air at 1.01 and 2.5 bar. These data were used as a test regarding the accuracy of the base mechanism for use in flame speed predictions.

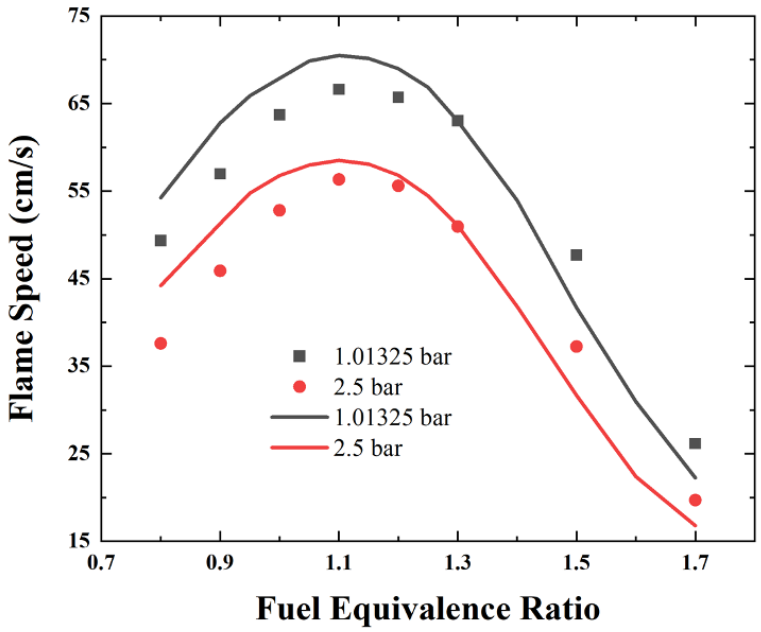

Figure 4.29. Flame speed calculations for E1E (diethoxymethane) in air at 1.01 and 2.5 bar compared to data from Jacobs et al. [66].

Simulations in Figure 4.29 were performed using with the lump POME mechanism in this work using Chemkin Pro. [114] The flame speed predictions overall are quite good considering that the model was not adjusted, and the focus of the prior work was on the pyrolysis and radical decomposition chemistry of the POMEs. At rich conditions, the predictions are within expected uncertainty bounds, though increased discrepancies between the model and the data occur at conditions at or below stoichiometric conditions.

A second flame speed study was conducted to then compare the flame speeds of the methyl and ethyl terminated POMEs. Figure 4.30 shows the differences in predicted flame speeds for the 5 fuels which have been abbreviated in terms of their terminating group (M = methyl, E = ethyl) and the polymer chain length in terms of numbers of oxymethylene units. In other words, dimethoxymethane (PODE-1) would be M1M while PODE-2 would be M2M.

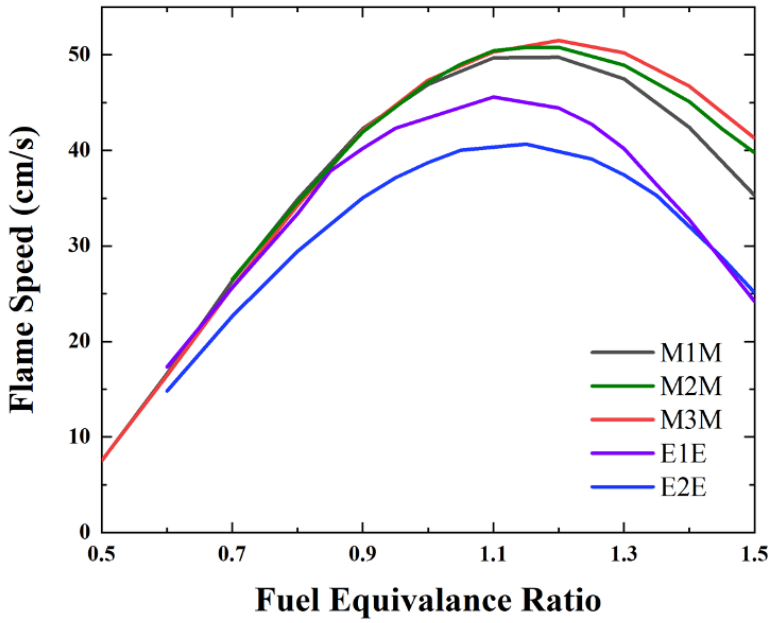

Figure 4.30. Flame speed predictions for the 5 methyl and ethyl terminated POMEs

The first observation is in the relative speeds of the methyl vs. ethyl terminated fuels. Methyl-terminated oxymethylene ethers are generally faster than their ethyl-terminated counterparts and lump quite close together. The addition of the ethyl groups slows the flame speeds considerably. The further slowing of the E2E flame speeds from DEM is somewhat unexpected and likely a symptom of the slower chemistry of several of the E2E radical species that were included from the work of Jacobs et al. [66]. These radicals were estimated to incorporate LTC chemistry for DEM and may not have been estimated from the best analogies. The work for DEM and PODE-2 may provide better analogical reaction rates than provided in the work of Jacobs et al. [66], however given the lack of experimental data to compare to, we have refrained from replacing those rates in this work.

Chapter 5 POME Down Selection and Blended Fuel Characterization

Based on the POME fuel characterization results (Chapter 3) the team agreed that the larger POME variations (i.e., propyl and butyl terminated versions) provided the best combination of soot reduction with highest exhibited LHVs and lowest water solubility while matching best the petrol diesel's volatility and ignition characteristics. These down selected POME molecules were then blended with certification diesel fuel and tests were reconducted. YSI and ICN measurments were taken on the POME-diesel blends followed by a complete ASTM D975 test procedure conducted by an external lab. Additionally, POME blends with distillation ranges targeted to match that of diesel fuel were also produced and tested.

5.1. Yield Sooting Index of Blended POME

This section discusses sooting behavior for POMEs mixed at large concentrations with other fuels. It is organized as follows. 5.1.1 presents sooting tendency results for POMEs mixed with diesel fuel, and it shows that the blending behavior is highly linear. 5.1.2 discusses morphology and composition measurements for soot particles from flames burning POMEs mixed with diesel fuel, and it shows the particles are very similar to those from pure diesel fuel. 5.1.3 presents soot concentration results for M1M blended with methane, and it shows that remarkably the M1M suppresses soot formation from the methane.

5.1.1. Sooting Tendencies of POMEs Blended with Diesel Fuel

Blending experiments were performed for most of the POME mixtures discussed in Section 3.1, mixed with conventional diesel fuel. Since the exact molecule weight of the diesel fuels was not known, the normal mole-based YSI could not be measured. Instead, normalized soot concentrations (NSCs) were measured by adding each fuel blend to the base flame at a fixed volumetric flowrate of 100 µL/h, measuring the soot concentration, subtracting the contribution from the base flame, and normalizing the result to the neat diesel fuel.

- Methyl-terminated POME mix supplied by Lisa Fouts of NREL and discussed in 3.1.2. This fuel was blended at 30 vol% with a certification diesel fuel. The results are discussed in Burton et al. [126] and are summarized here.

Figure 5.1. below shows the results for the POME blend ("OM30") and compares it to several other Co-optima bio-based diesel blendstocks that were also blended at 30 vol%, including a renewable diesel ("RD30"), a high-temperature liquefaction fuel from PNNL ("PN3o"), a soy biodiesel mixture ("BD30"), methyl decanoate ("MD30"), hexyl hexanoate ("HH30"), 1-decanol ("DL30"), and isoamyl ether ("IE30"). The horizontal axis is the NSC results measured for all the blends, while the vertical axis is engine-out soot emissions measured in Robert McCormick's group at NREL.

The NSC for the POME/diesel mixture is 0.7, which is consistent with a linear blending rule, given that the YSI of the POME mix (<4) is negligible compared to the diesel fuel (256) as discussed in 3.1.2. This NSC is significantly lower than all the other Co-optima blendstocks. Similarly, the engine-out emissions are lower for the POME mix than any of the other fuels. Thus, these results show that the soot reduction benefits of POMEs are greater than for other alternative fuels, and that the laboratory-scale YSI/NSC measurements are predictive of engine emissions.

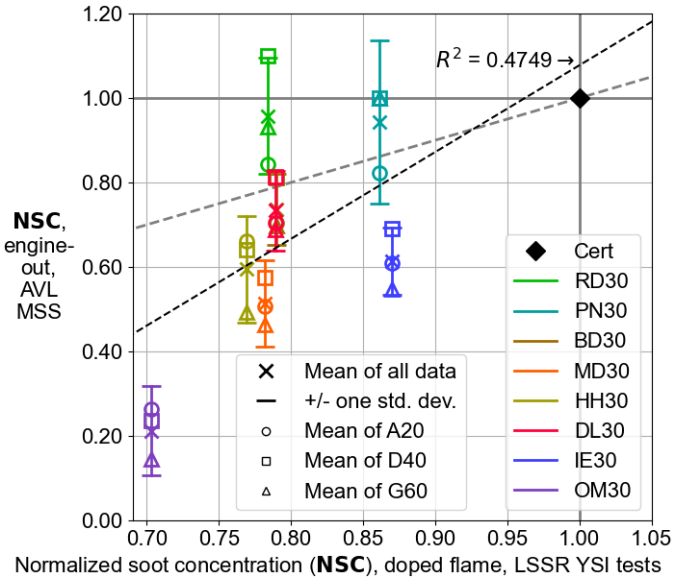

Figure 5.1. Engine out soot emissions for the POME blend ("OM30") against several other bio-based blendstocks also blended at 30% vol-fraction, including renewable diesel ("RD30"), a high-temperature liquefaction fuel from PNNL ("PN3o"), a soy biodiesel mixture ("BD30"), methyl decanoate ("MD30"), hexyl hexanoate ("HH30"), 1-decanol ("DL30"), and isoamyl ether ("IE30").

- The commercial POME mix after butyl-exchange supplied by Martha Arellano-Treviño of NREL and discussed in 3.1.2. This fuel was blended at 20 vol% with a No. 2 diesel fuel that was clay-treated to remove additions and used at NREL for Tier 2 screening of mixing-controlled compression ignition (MCCI) blendstocks [127]. The results are discussed in Arellano-Treviño et al. [128]. The measured NSC for the blend was 0.86, showing that, even after butyl exchange, the POME mix significantly improved the sooting tendency of the blend.

- The POME mixes after end-group exchange with alternative alcohols supplied by Martha Arellano-Treviño of NREL and discussed in 3.1.4. These fuels were blended at 20 vol% with the clay-treated reference diesel. The results are discussed in Arellano-Treviño et al. [129] and are summarized here.

The measured NSCs are shown in Table 5.1. below. The "neat diesel" is the same diesel fuel that was used at NREL for Tier 2 screening of mixing-controlled compression ignition (MCCI) blendstocks [127]. "MM3-6" is the commercial methyl-terminated POME mixture discussed above and in 3.1.2. "Isobutyl POME" and "Fuel Oil POME" are the mixtures of isobutyl-terminated and isopentyl-terminated POMEs generated by Daniel Ruddy's group at NREL that were discussed in 3.1.4.

Table 5.1. Measured NSCs for the candidate POMEs.

POME Sample	POME Mole Percentage	Measured NSC
None (neat diesel)	0	1.000
MM3-6 POME	20	0.802
MM3-6 POME	30	0.703

MM3-6 POME	100	0.028
Isobutyl POME	20	0.836
Isobutyl POME	100	0.226
Fusel Oil POME	20	0.846
Fusel Oil POME	100	0.280

Figure. 5.2. shows the measured NSC as a function of the mole percentage of the POMEs in the mixture. The blending behavior is extremely linear. The results further show that blending any of the POMEs into diesel fuel reduces soot formation in laboratory-scale flames. The largest reduction occurs for the MM3-6 mix, which produces virtually no soot on its own, but large reductions are observed for the other POME mixes as well.

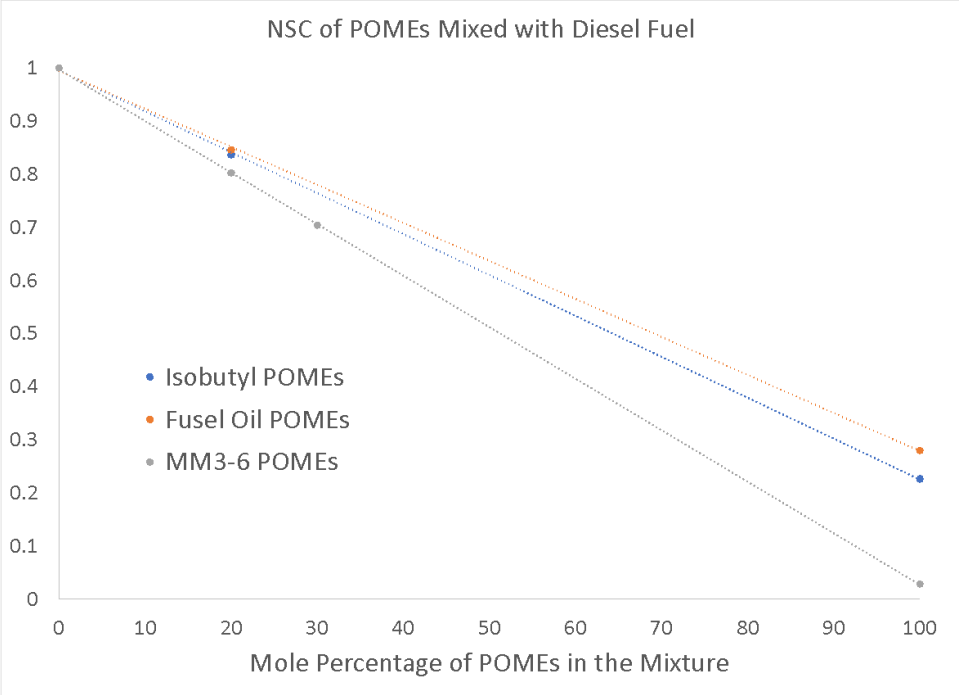

Figure 5.2. Measured NSC as a function of the mole percentage of POME in the blended mixture.

5.1.2. Soot Particle Morphology and Composition for POMEs Blended with Diesel Fuel

The results discussed in 5.1.1 show that the total amount of soot produced from mixtures of POMEs and diesel fuel in laboratory flames is a linear combination of the amounts produced from each component. This part discusses measurements that were performed to determine the blending behavior with regard to particle morphology and composition, since these characteristics may affect the operation of air pollution control equipment and the environmental consequences of emissions.

The photos in Fig. 5.3. below show transmission electron microscopy (TEM) photos of particles sampled from an undoped methane flame and from the same flame doped with 3000 ppm of the NREL diesel surrogate mixture and 3000 ppm of a MnM mixture. In all three cases the particles consist of spherical primary particles aggregated into fractal structures. The particles sampled from the diesel doped flame (center panel) are more aggregated due to the higher number density, but the diameters of the individual primary particles in the fractal aggregates are similar. The atomic composition of the particles was determined with X-ray photoelectron spectroscopy (XPS) and the results are listed in the table below the TEM photos. The particles from all three flames had similar compositions of 95% carbon and 5% oxygen. The oxygen content of the MnM mix did not change the composition of the soot particles. Overall, these results suggest that the particles produced from POME blends in engines will be similar to those from diesel fuel, just less numerous.

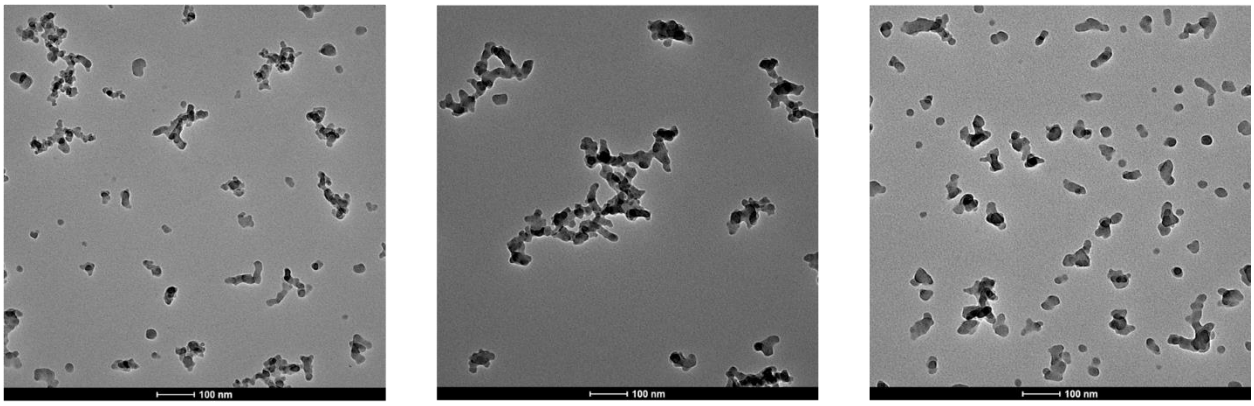

Figure 5.3. Transmission electron micorscopy (TEM) photos of particles sampled from an undoped methane flame and the same flame doped with 3000 ppm of NREL diesel surrogate mixture and 3000 ppm POME.

Table 5.2. Atomic composition of the particles in Fig. 5.3., as determined by X-ray photoelectron spectroscopy (XPS).

HAB = 41 mm	atom concentration (%)				
	C 1s	O 1s	N 1s	Cu 2p3	Si 2p
Intact Cu	62.1	26.9	2.5	3.3	5.2
Graphite 1-2 um	94.6	5.4			
Undoped	95.2	4.8			
Diesel Surrogate	95.3	4.7			
POME	95.2	4.8			

5.1.3. Soot Concentrations in M1M/Methane Flames

The YSI measurements discussed in Section 3.1 doped small concentrations (1000 ppm to 3000 ppm) of the test POME into a methane/air flame. To expand the range of conditions to much higher POME concentrations, a procedure was developed to generate pure POME/air flames. The photographs below show a series of flames where the fuel mixture is M1M (dimethoxymethane) diluted with nitrogen and the oxidizer is air. The fuel mixture flows out of the central tube and the oxidizer from the annular region around it; this non-premixed flame geometry mimics a compression ignition engine where a fuel jet is injected into a hot oxidizer. The M1M flowrates in the liquid phase increase from left to right in the order 15.0, 18.0, 21.0, 24.0, and 27.0 mL/h. The diagonal orange line shows that the flame heights increase in proportion to the M1M flowrates, which provides a consistency check that all the fuel is evaporating. The graph below the photos shows a more quantitative comparison of flame height and fuel flowrate.

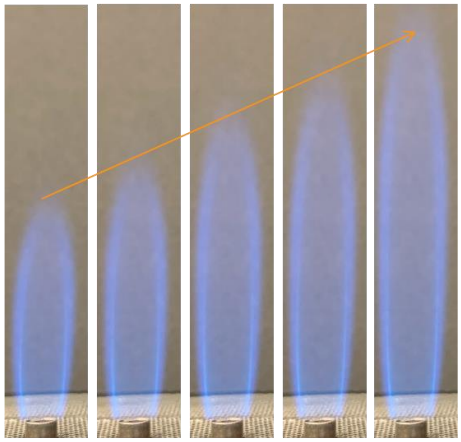

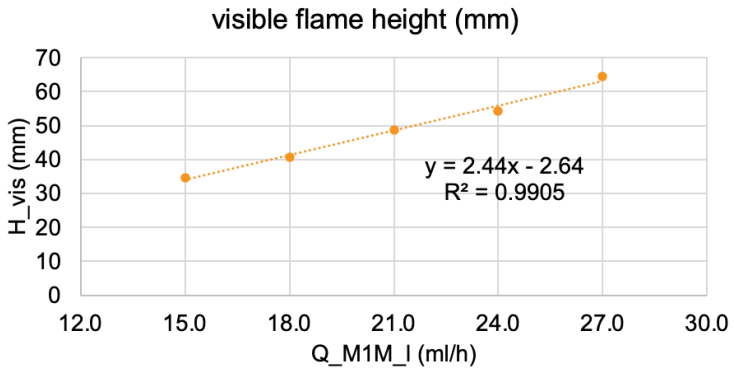

Figure 5.4. (Top) Images of M1M flames diluted with nitrogen with air as an oxidizer. M1M flowrates in the liquid phase increase from left to right in the order 15.0, 18.0, 21.0, 24.0, and 27.0 mL/h. (Bottom) Quantitative comparison of flame height and fuel flowrate.

The photos in Fig. 5.5. below compare a methane flame (left) and a M1M flame (right). The same camera settings were used for both photos. The yellow/white color is blackbody emission from soot particles, while the blue is chemiluminescence from excited state CH molecules. The methane flame contains enough soot to saturate the camera over most of the flame area, whereas the M1M flame contains only a small amount of soot near the tip. Thus, these photos clearly illustrate that M1M produces far less soot than methane.

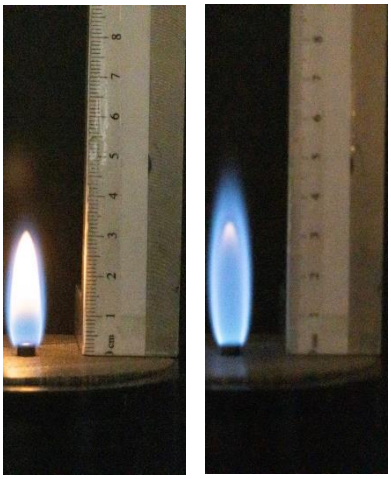

Figure 5.5. Images of a methane flame (left) compared with an M1M flame (right).

Soot concentrations were measured in flames where the fuels were mixtures of M1M (dimethoxymethane) and methane. These measurements were performed using color-ratio pyrometry with the procedures described in [130]. The results are highly nonlinear, which shows that POMEs can suppress soot formation from co-fuels that have low sooting tendencies. This complements the results reported earlier in this section, which showed that the sooting tendencies of POME/diesel mixtures follow a linear blending rule. The difference is that the sooting tendencies of POMEs are negligibly small compared to diesel fuel but are closer to methane. Overall, these results suggest that POMEs may have a synergistic blending effect on reducing soot emission when they are mixed with other alternative diesel fuels that have lower sooting tendency than conventional diesel.

Figure 5.6. below shows the maximum soot volume fraction (in parts-per-million) for a series of methane/M1M flames as a function of the M1M mole fraction in the fuel mixture. The soot concentration is 0.14 ppm for methane by itself (left axis) but decreases rapidly as M1M is added to the fuel. In fact, the soot concentration decreases by over an order-of-magnitude with only 15% M1M added to the fuel mixture. The behavior is very nonlinear, showing a strong synergistic effect.

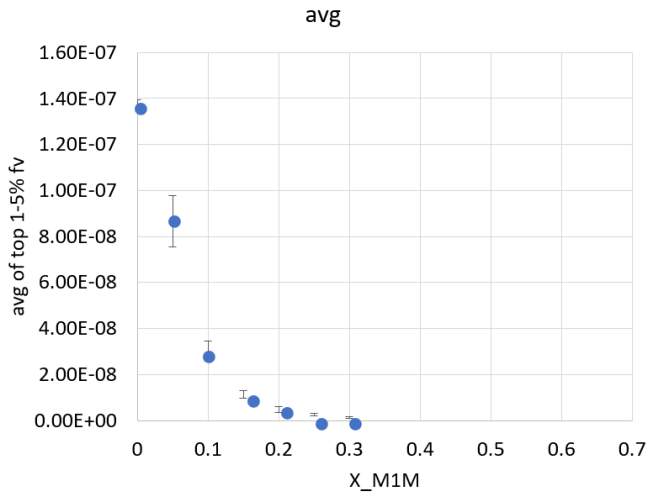

Figure 5.6. Maximum soot volume fraction for a series of methane/M1M flames as a function of the M1M mole fraction in the fuel mixture.

A possible explanation for this synergistic effect is dilution of the methane by the oxygenated products of M1M decomposition. Methane is expected to primarily decompose to methyl radical (CH_3), which can then grow to soot.

$$CH_4 \rightarrow CH_3 + H$$

$$CH_3 \Rightarrow \text{soot}$$

While CH_3 is not a particularly effective soot precursor, it does lead to some soot as illustrated by the soot emission in the methane flame on the left of the figure above. Based on the chemical kinetics developed in this project (see Chapter 4), M1M decomposes to methyl but also formaldehyde (CH_2O), which cannot grow to soot due to the oxygen atom.

$$M1M\ (CH_3\text{-}O\text{-}CH_2\text{-}O\text{-}CH_3) \rightarrow CH_3 + 2\ CH_2O$$

$$CH_3 \Rightarrow \text{soot}$$

$$CH_2O \not\Rightarrow \text{soot}$$

Since it takes many CH_3 radicals to make a soot particle, the dilution of the CH_3 by the CH_2O from M1M has a nonlinear effect on soot production.

5.2. Blended Fuel Indicated Cetane Number

In the literature, neat OMEs as well as OMEs blended with diesel fuel have been tested [131]. Here ICNs were measured for a representative high-ICN OME, B-1-B, blended volumetrically with a certified diesel, ICN=40.7, in increments of 10 volume % (Figure 5.7). Due to the similar densities of B-1-B and diesel, this is essentially equivalent to a mass ratio blend as well. It is observed that the ICN of the mixture is nonlinear with volumetric blending; the presence of B-1-B shows an antagonistic effect on mixture ICN resulting in a lower ICN than would be predicted by linear blending rules; this is in agreement with existing literature on ether blending effects in distillate fuels [85]. The maximum deviation from the linear blending rule is

6.3%, indicating that while the presence of the ether has some negative effect, it is insufficient to overcome the ICN benefit of the high-reactivity OME.

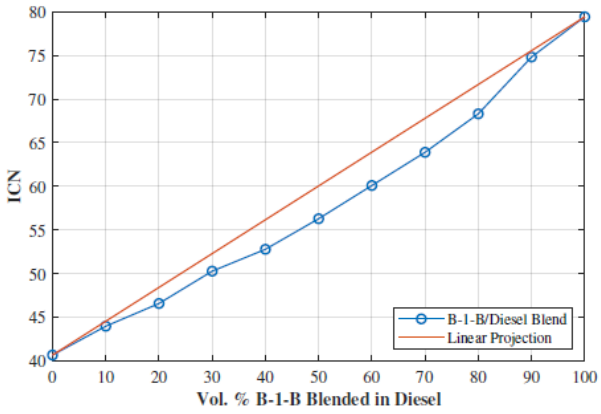

Figure 5.7. Effect of varying B-1-B blending ratio in diesel (ICN=40.7) on ICN of mixture, compared with a linear blending assumption.

5.3. ASTM D975

One of the major goals of the overarching DoE project is the selection of a blend of OMEs which can reduce the soot production of diesel engines in legacy systems. In order to achieve this goal, we must downselect from the variety of OMEs tested for the best compatibility with current diesel standards, as described by ASTM D975. Table 5.3 describes the properties governed under this standard; each of these is measured using its own ASTM standard.

Considering the properties measured above, and the boiling range described earlier, we select a 200°C - 305°C distillation cut of B-n-B as the most appropriate for diesel blending. A sample of this was prepared and sent to an external laboratory – FOI Laboratories in Vancouver, WA – for certification under ASTM D975. All properties except lubricity and flash point passed in the initial report, however, a retest of flash point was requested and passed on the second attempt. Equipment failure is suspected in the first test, as the reported flash point was lower than the flash point of either the certification diesel or the lowest OME component. Lubricity of OMEs, as well as viscosity, is of concern, but may be remedied with lubricity additives. A small sample was kept in a flask for six months to check for phase separation or other miscibility problems. No separation was observed. Some sediment is observed in the bottom of the flask, however, this is expected to stem from the diesel rather than OME components, as no sediment was found in the OME-only sample used to make this blend.

Table 5.3. Properties controlled and limits under ASTMD975 [132], using ULSD 2-D as reference

Property	Governing Standard	Limit Range
Flash Point	D93	>52°C
Water and Sediment	D2709	<0.05 vol%
Distillation Temp., 90% Recovered	D86	282°C - 338°C
Kinematic Viscosity	D445	1.9-41 mm2/s
Ash Mass Percent	D482	<0.01 mass%
Sulfur ppm	D5453 or D2622	15
Copper Strip Corrosion	D130	No. 3
Cetane Number	D613	>40
Aromaticity, Vol. Percent	D1319	<35 vol%
Cloud Point	D2500	No specified
Carbon Residue	D524	<0.35 mass%
Lubricity	D6079 or D7688	<520 µm
Conductivity	D2624 or D4308	>25 pS/m

Table 5.4. ASTM D975 results

FOI LABORATORIES

Certificate of Analysis
Laboratory Number: FOI0711202233

Stephen Lucas		Sample Taken From:	
Colorado State: Chemical Energy Conversion Lab		Type of Fuel:	Diesel
430 N. College Ave.		Sample Collection Date:	
Fort Collins, CO 80524		Date Received:	July 12, 2022
USA		Date Released:	August 11, 2022
509-220-6228		Component Make:	
Sample ID:		Component Model:	
Purchase Order:		Serial Number:	
Work Order:		Quanity in Tank:	
Package:	ASTM D975 - Full	Tank Capacity:	

Test	Limit	Method	Result
Acid Number	report mg KOH/gm max	ASTM D974-08	.04
API Gravity by Hydrometer	report	ASTM D1298-99	31
Ash Content	0.01% wt max	ASTM D482	<.01
Carbon Residue	report % (m/m)	ASTM D189	0.10
Cetane Number	report	ASTM D613	50.6
Cloud Point	report °C	ASTM D2500-99	-21
Conductivity	25 pS/m minimum	ASTM D2624	841
Copper Strip Corrosion	3 maximum	ASTM D130-04	1a
Distillation, 90%	282 - 338 °C	ASTM D86/D2887	305
Flash Point	52 °C minimum	ASTM D93-10	42
ICP Metals-Aluminum(Al)	report in ppm	HL-1158	0
ICP Metals-Antimony(Sb)	report in ppm	HL-1158	0
ICP Metals-Barium(Ba)	report in ppm	HL-1158	0
ICP Metals-Boron(B)	report in ppm	HL-1158	1
ICP Metals-Calcium(Ca)	report in ppm	HL-1158	1
ICP Metals-Chromium(Cr)	report in ppm	HL-1158	0
ICP Metals-Colbalt(Co)	report in ppm	HL-1158	56
ICP Metals-Copper(Cu)	report in ppm	HL-1158	0
ICP Metals-Iron(Fe)	report in ppm	HL-1158	0
ICP Metals-Lead(Pb)	report in ppm	HL-1158	0
ICP Metals-Magnesium(Mg)	report in ppm	HL-1158	0
ICP Metals-Molybdenum(Mo)	report in ppm	HL-1158	1
ICP Metals-Nickel(Ni)	report in ppm	HL-1158	2
ICP Metals-Phosphorus(P)	report in ppm	HL-1158	1
ICP Metals-Potassium(K)	report in ppm	HL-1158	0
ICP Metals-Silicon(Si)	report in ppm	HL-1158	0
ICP Metals-Silver(Ag)	report in ppm	HL-1158	0
ICP Metals-Sodium(Na)	report in ppm	HL-1158	0
ICP Metals-Tin(Sn)	report in ppm	HL-1158	0
ICP Metals-Titanium(TI)	report in ppm	HL-1158	0

(a) FOI Laboratories ASTM D975 Test Report, page 1

ICP Metals-Vanadium(V)	report in ppm	HL-1158	0
ICP Metals-Zinc(Zn)	report in ppm	HL-1158	1
Lubricity, HFRR @ 60°C	520 um maximum (micron)	ASTM D6079	700
Oxidation Stability	minimum 6 hours	ASTM D7545	25.8
Pour Point	report °C	ASTM D97	-49
Sulfur	report ppm	ASTM D5453-09	4
Viscosity @ 40°C	1.3 - 4.1 cst	ASTM D445	2.2
Water and Sediment	0.05 maximum (% volume)	ASTM D2709	0.001

Comments:

Gas aroma present.

Low Flash Point: A low flash point fuel can be a fire hazard, subject to flashing and possible continued ignition and explosion. A low flash point can also indicate contamination with low flash fuels such as gasoline and or Kerosene.

8014 NE 13th Ave., Vancouver, WA 98665

Table 5.5. Flashpoint retest with new flash point exceeding the required diesel fuel specification.

FOI LABORATORIES

Certificate of Analysis
Laboratory Number: 102620225

Stephen Lucas		Sample Taken From:	
Colorado State: Chemical Energy Conversion Lab		Type of Fuel:	Unknown
430 N. College Ave.		Sample Collection Date:	
Fort Collins, CO 80524		Date Received:	October 26, 2022
USA		Date Released:	November 8, 2022
509-220-6228		Component Make:	
Sample ID:		Component Model:	
Purchase Order:		Serial Number:	
Work Order:		Quanity in Tank:	
Package:		Tank Capacity:	

Test	Limit	Method	Result
Flash Point	report °C	ASTM D93-10	77

Comments:

Chapter 6 Compression Ignition Engine Performance of Butyl- and Propyl-Terminated Oxymethylene Ethers

6.1 Introduction

Industry reliance on compression ignition (CI) internal combustion engines (ICEs) for transportation and small- to mid-scale power generation applications is likely to be maintained until carbon-free and carbon-neutral energy system technologies can fully supplement the nation's energy demands. During the ongoing transition, federal agencies have imposed increasingly stringent emissions regulations for CI engine platforms that most manufacturers have complied with using exhaust aftertreatment systems, which, though effective, can be both a financial and functional burden to the end-user. For this reason, some researchers have shifted their focus to the use of oxymethylene dimethyl ethers (OMEs) to reduce CI engine soot production in-cylinder and thereby minimize aftertreatment system sizing and regeneration requirements.

As discussed at length previously, the use of OMEs in CI engines leads to significant mitigation of soot formation in-cylinder [133–135]. The widespread application of OMEs for this purpose, however, has been impeded by their lack of energy density and their poor compatibility with traditional diesel platforms and fuels. The OMEs with larger terminating alkyl groups (e.g., ethyl, propyl, butyl) have superior properties for diesel compatibility compared to the conventional methyl-terminated molecules including improved heating values, cetane numbers, volatilities, water solubilities, and oxidative stabilities. Chapters 3-5 of this report discuss POME candidate fuel and their properties at length, most notable of which were identified to be Dipropoxymethane (P1P) and dibutoxymethane (B1B), featuring heating values greater than 30 MJ/kg and water solubilities less than 10 g/L. Benchtop analysis concluded that the most preferable POME blend is likely oligomerized B1B, in the form of dibut-polyoxymethane (BnB), to be used in 30% by volume blend with conventional diesel fuel - a blend that complied with all ASTM D975 specifications except flash point and lubricity.

This project's engine testing campaign serves as an extension of those benchtop analyses in which the POME fuel blends identified to be most promising were tested in a medium duty offroad CI engine to evaluate their effects on cylinder-out emissions and engine performance. The POME compounds selected for preliminary engine testing were those featuring balanced diesel like properties and high soot emission reduction potential. In its preliminary phase, engine testing was focused on the "drop-in" performance of those compounds (i.e., no changes to the engine's operating map were made) with specific regard to their effects on fuel consumption, brake efficiency, combustion phasing/duration/stability, and both gaseous and particulate emission rates. In so doing, the prevailing question of whether specific POME blends are able to alter the conventional soot/NOx emissions tradeoff in CI engines was addressed.

6.2. Drop-In Performance Assessment

6.2.1. Methods

Table 6.1. outlines the structure, composition, and performance properties of the POME compounds (also referred to herein as "test fuels") studied in this work. The fuels were either procured in bulk (P1P, B1B) or synthesized and distilled in-house (MnM, BnB) using the processes presented in Chapter 2. Fuel properties were evaluated and compared to those of 2007 ultra-low sulfur certification diesel fuel (referred to herein as "2007 ULSD," "ULSD," and/or "cert. diesel"). Two of the compounds, dimeth-

polyoxymethane (MnM) and dibut-polyoxymethane (BnB), are distilled mixtures of oligomerized POMEs with varying numbers of oxymethylene groups, as delineated in Table 6.2.

Table 6.1. Detailed property, structure, and nomenclature information for the fuels tested in this study. Note that elsewhere in this work, the fuel abbreviations are used in combination with a number indicating their volume blend percentage with certificate diesel (e.g., P1P30 is 30%-vol P1P and 70%-vol ULSD).

Compound	Abbv.	Molecular Structure	CAS no.	Oxygen Content (wt%)	Carbon Content (wt%)	Hydrogen Content (wt%)	Indicated Cetane Number (-)	Lower Heating Value (MJ/kg)	Yield Sooting Index (-)	YSI/LHV $(MJ/kg)^{-1}$	Density @ 20 C (kg/m3)	Viscosity @ 20 C (mm2/s)
Dimeth-polyoxymethane	MnM	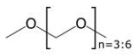	-	46.2	44.7	9.1	N/A	19.2	0.0	0.0	1061	1.685
Dipropoxymethane	P1P		505-84-0	24.2	63.6	12.2	53.4	32.0	30.8	1.0	834	0.812
Dibutoxymethane	B1B		2568-90-3	20.0	67.4	12.6	76.4	34.1	46.0	1.3	837	1.243
Dibut-polyoxymethane	BnB	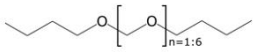	-	28.1	60.8	11.1	N/A	28.9	40.2*	1.4	933	2.394
2007 Ultra-Low Sulfur Certification Diesel	ULSD	-	-	0.0	86.8	13.2	47.6	42.8	200**	4.7	856	3.783

* - derived from known composition and measured constituent values
** - value reported by supplier

Table 6.2. The molecular composition of the oligomerized polyoxymethylene ethers MnM and BnB, whose structure is detailed in Table 6.1.

	Oxymethylene Units (n)					
	1	2	3	4	5	6
MnM (mol%)	0.0	0.0	48.1	29.7	16.6	5.6
BnB (mol%)	7.7	36.9	29.7	16.4	5.1	4.1

Liquid density and kinematic viscosity were measured using an Anton-Paar SVM 3000 Stabinger viscometer at 20 °C and 40 °C respectively. Measurements were repeated four times and the mean values recorded. Higher heating values (HHV) were measured using an IKA C200 calorimeter (repeated four times, mean values recorded). Lower heating values (LHV) were derived using ASTM-D240 and the measured HHV – a conversion method commonly employed for compression ignition fuels with unknown carbon/hydrogen balance. Flashpoints were measured using the Pensky-Martens PMA 4 flashpoint tester according to ASTM D 931. Indicated cetane number (ICN) measurements were taken with an advanced fuel ignition delay analyzer (AFIDA) at NREL's facilities in Golden, CO according to ASTM D81832. Derived cetane number (DCN) measurements were taken with a Waukesha Fuel Ignition Tester (FIT) at the CSU Energy Institute according to ASTM D71703. It should be noted that ASTM has retired its standard for FIT DCN measurement. It should also be noted that cetane number measurements have been documented to vary substantially between types of measurement instruments used (AFIDA, IQT, or FIT) and to varying degrees depending on fuel composition [39]. Detailed results of this comparison are presented in Lucas [136] and summarized in Table 6.1.

A fully instrumented 4.5L, 4-cylinder Deere 4045 Tier 3 compression ignition engine (Fig. 1) was used to assess the performance of the test fuels. Dipropoxymethane (P1P) and dibutoxymethane (B1B) were tested in 30%-vol. blends with certificate diesel (P1P30 and B1B30) and in their pure forms (P1P100 and B1B100). Oligomerized dibut-**poly**oxymethane (BnB30) and dimeth-**poly**oxymethane (MnM30), whose molecular composition is detailed in Table 6.2, were also tested in 30% blend. The engine was operated at steady state according to Mode 4 of ISO 8178 (50% torque at intermediate speed) – Test Cycle Type A,

which outlines testing procedures for heavy-duty diesel engines for use in road vehicles. Mode 4 for this test engine equated to 1700 RPM with 325 Nm of brake torque and 920 kPa brake mean effective pressure (BMEP) (see Table 6.3). The operating mode was selected as the best balance between assessing the performance of a given fuel under reasonable engine load and conserving fuel to perform as many replicate measurements as possible.

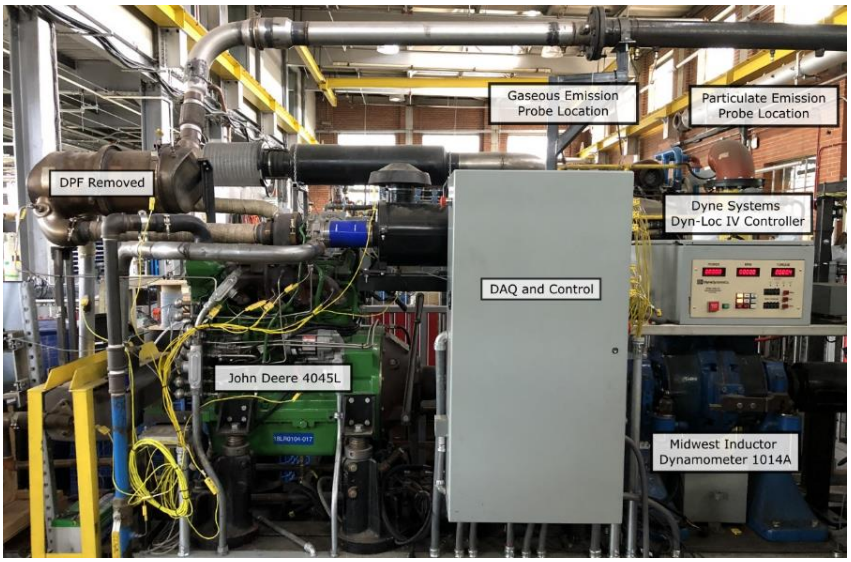

Figure 6.1. Image of the John Deere 4045L test engine and the associated data acquisition and control systems.

Table 6.3. Engine operating conditions that were maintained across all data reported. "ECM" listings indicate values that the engine control module was allowed to modify in response to changing fuel properties.

Engine Operating Conditions					
Speed	Load	BMEP	IMAT	IMAP	Injection Timing/Duration
1700 RPM	325 Nm	48.1 kPa	40 °C	ECM	ECM

The engine's fueling system consisted of a high-pressure common rail (HPCR) with switchable valves on both the pump supply and rail return lines. The valves permitted the engine to either run off standard offroad diesel or off the test fuel contained in a separate dedicated vessel. The engine was first fueled by the standard diesel, brought to the desired operating condition, and allowed to reach steady state as indicated by the stabilization of the engine speed/load and the temperatures of the engine oil, jacket water, and intake/exhaust manifolds. Then, the fuel supply was switched to draw from the test fuel vessel and the fuel rail was allowed to bleed into a waste bucket until stable engine load, exhaust manifold temperature, and fuel return color was achieved.

A low-speed data acquisition system recorded engine temperatures, pressures, and speed/load conditions at a frequency of 2 Hz. A high-speed data acquisition system recorded in-cylinder pressure data from a Kistler 6055 piezoelectric transducer mounted in the glow plug port of cylinder 1. Apparent heat release rate was derived from the time-averaged pressure trace resulting from 500 engine cycles according to Eq. 6.1 below.

$$\frac{dQ}{d\theta} = \frac{\gamma}{\gamma-1} P \frac{dV}{d\theta} + \frac{1}{\gamma-1} V \frac{dP}{d\theta} \tag{6.1}$$

The engine's integrated diesel particulate filter (DPF) was removed such that the raw unfiltered exhaust could be sampled. Heated lines were used to transport exhaust sample at elevated temperature (105 °C) to a 5-gas analyzer and FTIR measuring gaseous composition. The 5-gas analyzer consisted of (1) a non-dispersive infrared (NDIR; Siemens ULTRAMAT 6) sensor to measure the mole fractions of CO and CO2, (2) a paramagnetic detector (Siemens OXYMAT 6) to measure O2 concentration, (3) a chemiluminescence detector (Siemens NOXMAT 600) to monitor NOx, and (4) a flame ionization detector (Siemens FIDAMAT 6) measuring total hydrocarbon emission. Each analyzer was zeroed and spanned at the start of every test day using pure N2 and their appropriate calibration gases. Volumetric measurements (PPM) were converted to report specific emissions according to Eq. 6.2 below, wherein e_i is the specific emission result in g/kWh, PPM_i is the raw volumetric measurement in parts-per-million, MW_i is the molecular weight of the measured compound in kg/kmol, $\dot{m}_{ex}$ is the mass flow rate of the exhaust in kg/s as approximated by the engine speed and exhaust temperature/pressure, P is the engine brake power in kW, and MW_{ex} is the total molecular weight of the exhaust mixture approximated using the exhaust composition measured by the 5-gas analyzer in real time.

$$e_i = PPM_i \; x \frac{[\,MW_i * \dot{m}_{ex}]}{[P * MW_{ex}]} * \; 3.6 \tag{6.2}$$

Particulate emissions were measured using the apparatus illustrated in Fig. 6.2. An isokinetic probe collected exhaust sample and directed it to a Dekati L7 diluter through a heated line. The diluter was supplied with raw exhaust sample along with filtered compressed air fixed at a volume flowrate of 50 SLPM using an Alicat MC-50SLPM-D-DB15/10M mass flow controller. The resulting sample was diluted 10:1 by volume to reduce the sample's relative humidity and thus prevent water dropout upon sample cooling. The diluted sample was then directed into a 200 L buffer volume to minimize transitory error when sampling. A CO2 analyzer located at the outlet of the buffer volume worked in tandem with the NDIR CO2 detector of the 5-gas instrument panel to determine the exact dilution ratio of the sample at any given time. When not sampling, steady flow was maintained through the buffer volume using a bypass line and mass flow controller. When sampling, the ball valves between the dilution tunnel and filter cart were configured such that flow was directed through the parallel filter train, but not through the bypass. In the parallel filter train, the diluted sample first passed through 2.5 µm cut point cyclones (URG Corp. 16.7 LPM 2.5 µm) to ensure that no particles greater than 2.5 µm were passed onto the sample filters. Next, in the top filter train, the sample passed through a 47-mm PTFE filter (Teflon; Whatman 7592-104) followed by a pre-baked quartz-fiber filter (Pallflex Tissuquartz, 2500 QAT-UP). In the bottom filter train, the sample passed over a single quartz-fiber filter of the same make. The Teflon filter was used for gravimetric analysis to determine the total concentration of PM2.5 in the unfiltered exhaust sample. The quartz-fiber filter in the second filter train was used to determine the ratio of organic carbon (OC) to elemental carbon (EC) contained within the total carbon (TC) concentration of the unfiltered exhaust sample. The quartz-fiber filter that backed the Teflon filter in the top filter train was used to correct for the positive measurement artifact caused by the deposition of gas-phase organic compounds on the quartz-fiber filter of the bottom train (the Q-QBT method [137]). The mass flow rate, temperature, and pressure of each filter train were monitored to determine the specific amount of exhaust sample that passed over the filters during the test. PTFE filters were pre- and post-weighed using a balance with a resolution of 0.3 µg after equilibrating in the microbalance room for 24 hours. Quartz filters were analyzed according to NIOSH method 5040 using a Sunset Laboratory OC-EC Aerosol Analyzer.

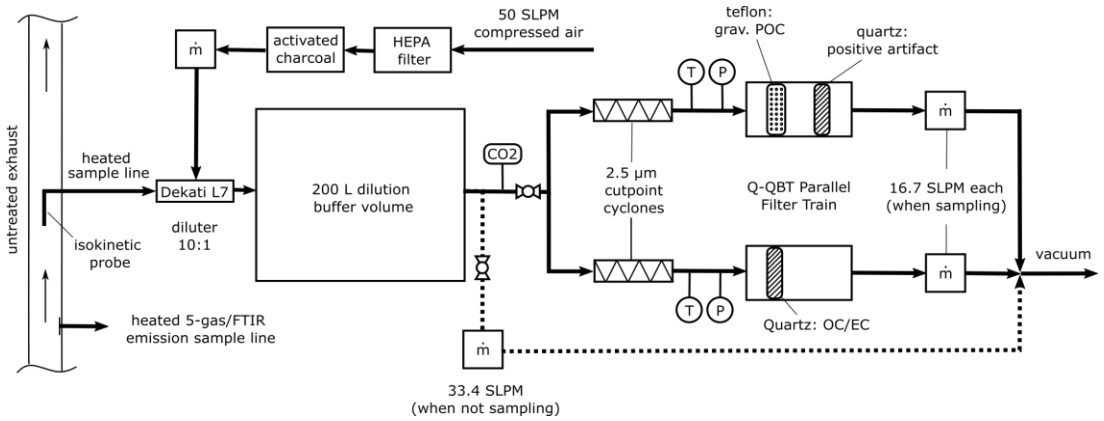

Figure 6.2. Schematic diagram of the exhaust sampling equipment used to make PM and composition measurements.

During testing, the engine was brought to its steady state condition, fuel supply/return lines were switched over to the test vessel, it was again allowed to stabilize (~3 minutes), and then held at steady state for 15 minutes while exhaust sample was directed through the PM filter cart's bypass line. Doing so prior to sampling ensured the dilution tunnel's buffer volume was sufficiently flushed with new sample. Only then were the filter cart's valves configured to direct sample through the filter train. Data was collected for a period of 8 minutes across all instrumentation, and the resulting metrics were time averaged over the complete duration of the data collection period. In between data points, the engine was left at its steady state condition, exhaust flow was directed through the bypass, filters were exchanged, and then another 8-minute data collection period commenced.

6.2.2. Results and Discussion

High-speed in-cylinder pressure measurements revealed the effects of the POME fuel blends on the combustion phasing/duration of the unmodified John Deere 4045L engine at the operating state denoted in Table 6.3. Figure 6.3 presents time averaged apparent heat release rate (AHRR) profiles for the POME neat and blended fuels, along with the averaged injection timing data collected. Here, start of injection (SOI) times are held relatively constant by the engine's default operating map, but injection duration is extended to account for the lower energy densities of the test fuels and thereby maintain fixed load. The center of heat release (CA50) was consistent within 0.5 °CA for all fuels. Most notable was the change to the fraction of energy released in the premixed burn phase, characterized by the autoignition of the vaporized fuel surrounding the injection plume prior to the initiation of a diffusion flame anchored to the plume itself, and indicated by the initial peak in AHRR shortly after SOI. This effect was most pronounced for the neat POMEs – especially B1B100 – and is in direct correlation to the autoignition times and cetane numbers of the fuels. That is, the shorter a fuel's autoignition time, the higher its cetane number, and the lower its premixed burned fraction.

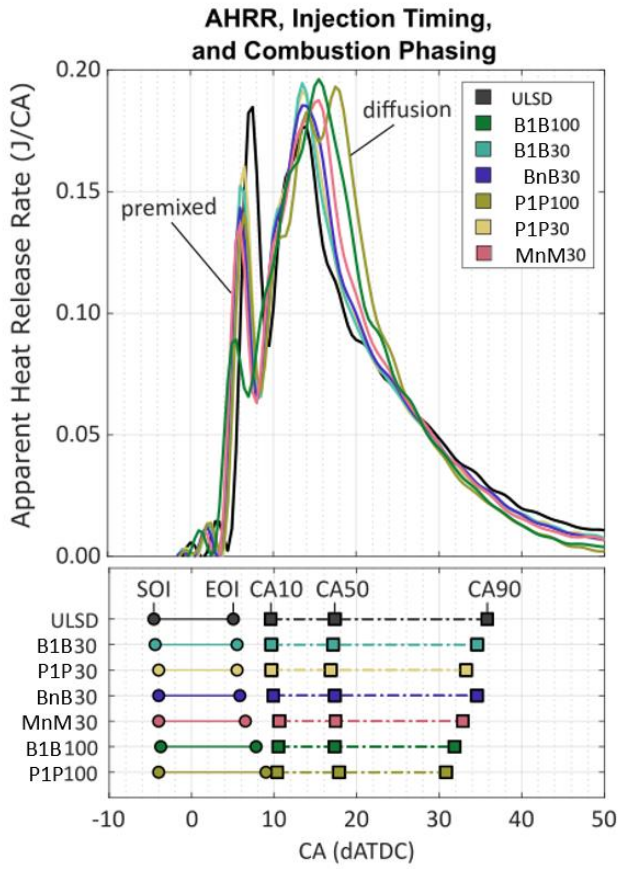

Figure 6.3. Apparent heat release rate profiles averaged across 1000 cycles for all tested fuels. Average start of injection (SOI) and end of injection (EOI) locations indicated by the circle markers on the time-aligned plot below. Average 10%, 50%, and 90% mass fraction burned locations denoted by the square markers on the same plot.

PM emissions were reduced to varying degrees and trended with the oxygen content of the fuels and their blend ratios, though marked increases in NOx emissions were also observed. Figure 6.4 presents the PM to NOx tradeoff data for the set of test fuels, along with the measured organic/elemental carbon fraction within the collected PM samples. Though all tested fuels resulted in increased NOx emissions, likely due to decreasing premixed burn fractions, several fuels featured disproportionate decreases to PM that differentiated their performance from the standard PM/NOx tradeoff. This effect is illustrated in Fig. 6.4 by a fuel's divergence from the linear regression fit through the PM/NOx baseline ULSD data and is most pronounced for B1B30, BNB30, and P1P30. It is proposed, but has not yet been tested, that EGR rates could be adjusted to bring NOx to a normal level while still maintaining realizable soot reduction in-cylinder. Doing so could allow for decreased DPF loading and extended operating time between regeneration cycles and thereby reduce the financial and performance burden of conventional aftertreatment systems.

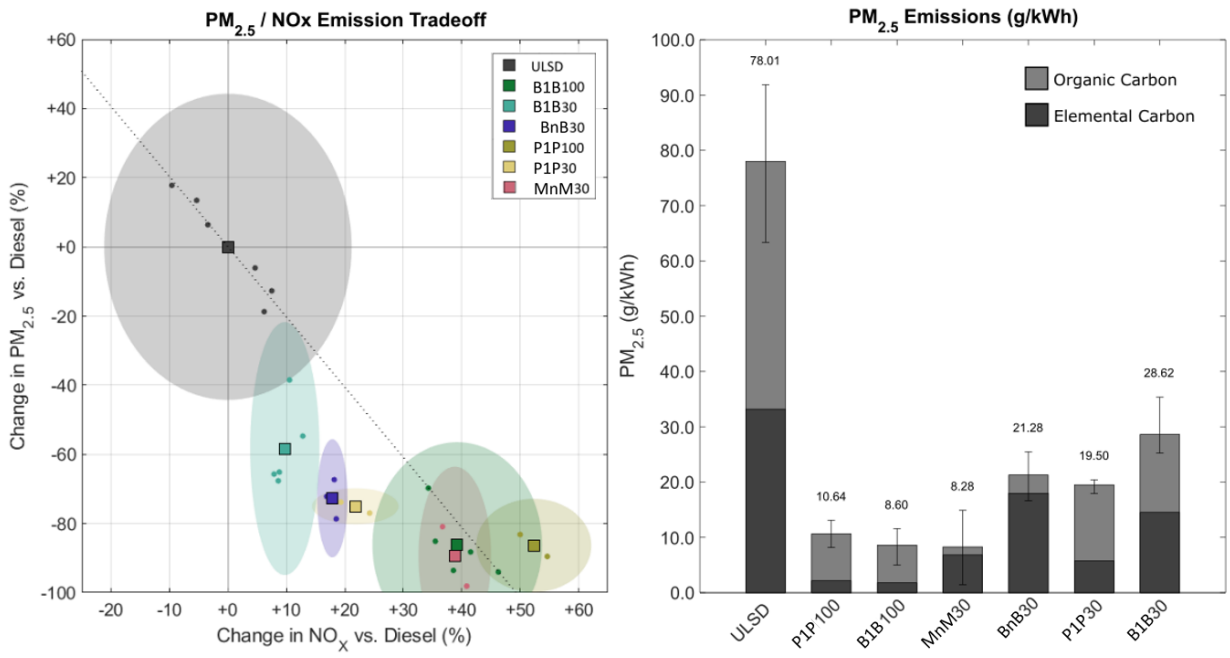

Figure 6.4. (Left) PM 2.5 and corresponding NO_x for all data points taken. Fuel type indicated by color. Small dots represent individual data points. Larger squares represent sample averages. Shaded regions denote 3 standard deviations from the mean in both dimensions. The dotted line is a linear regression through the baseline ULSD data points, representing the standard PM/NOx tradeoff for this engine. (Right) PM 2.5 measurements for all tested fuels. Bars represent total PM 2.5 concentration normalized by brake power. Error bars represent the total range of observed values. Shaded regions differentiate between the average amounts of the elemental and organic carbon composing the measured loading.

Marked increases to brake specific fuel consumption (Fig. 6.5 – top, left) were also observed in direct relation to the test fuels' energy densities. None of the tested fuels, however, featured a statistical difference in brake thermal efficiency (Fig. 6.5 – top, middle). COV of IMEP (Fig. 6.5 – top, right) was affected in both the positive and negative directions depending on fuel but did not exceed a value of 2.1 for the set – indicating there was minimal effect on engine stability. CO emissions (Fig. 6.5 – bottom, left) were significantly reduced across all fuels tested. Formaldehyde emissions (Fig. 6.5 – bottom, middle) increased by over an order of magnitude, but never exceeded 4 ppm overall and differences in the total hydrocarbon emissions (Fig. 6.5 – bottom, right) fluctuated across the set with some statistical significance.

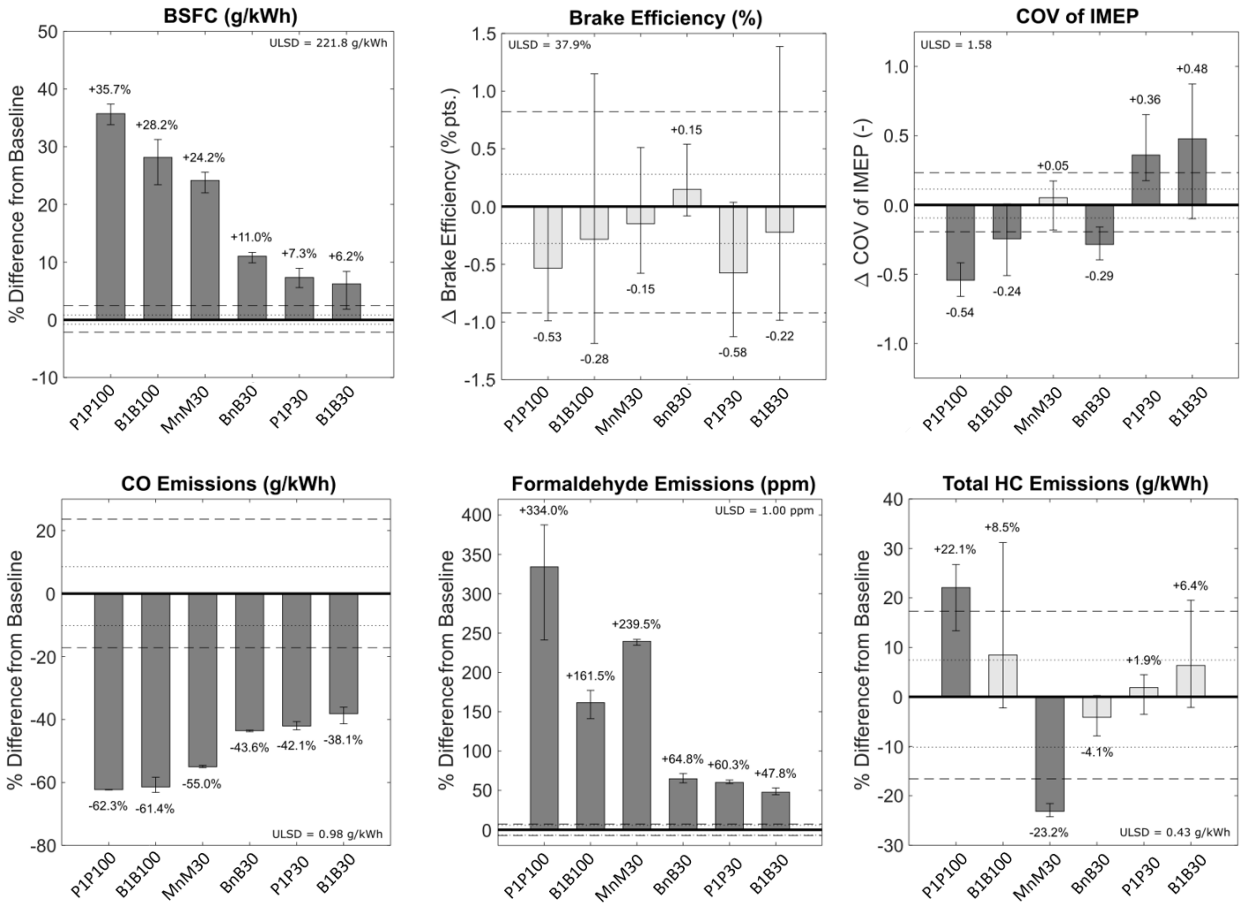

Figure 6.5. Average relative brake specific fuel consumption (BSFC – top, left), brake efficiency (top, middle), indicated mean effective pressure coefficient of variance (COV of IMEP – top, right), carbon monoxide emissions (CO – bottom, left), formaldehyde emissions (bottom, middle), and total hydrocarbon emissions (bottom, right) for all fuels and data points collected. For all plots, the average measured value for the baseline ULSD is referenced at 0 and is listed on the plot. The full range of observed values for the baseline ULSD is denoted by the large, dotted lines above and below the zero-reference. Similarly, the interquartile range of the baseline ULSD values fitted with a normal distribution is depicted by the finer dotted lines within. Dark shaded bars represent values that were identified as being statistically significant by an independent, two-sample t-test with unequal sample size and assumed equal variance. Unshaded bars represent values that failed to disprove the null hypothesis of the same test – i.e., those that were not statistically significant. Error bars represent the full range of observed values for each test fuel.

6.2.3. Drop-In Performance Conclusions

From the observed lower sooting propensities, disruption to the conventional PM/NOx emissions tradeoff, and otherwise unremarkable effects on engine performance, opportunity to use polyoxymethylene ethers to limit reliance on cumbersome exhaust aftertreatment equipment is revealed. Dibut-polyoxymethane (BnB) in 30% blend with diesel fuel proved particularly attractive as a drop-in alternative CI fuel, as it complied with all ASTM D975 specifications except flash point and lubricity, resulted in a 70% reduction in PM emissions with a mere 18% increase in NOx emissions, increased engine stability, and resulted in no statistically significant change to brake efficiency.

6.3. Performance Optimization Studies

The engine performance data collected on the John Deere 4045L suggested the potential for BnB30 to disrupt the conventional PM/NOx tradeoff in compression ignition engines. That is, BnB30 resulted in a reduction of PM emissions that was disproportionately larger than the resulting increase in NOx emissions. The implication of this result is that alterations to the engine's operating map can correct the elevated NOx emissions through conventional means (e.g., exhaust gas recirculation) and still benefit from reduced concentrations of particulate matter. As an extension to the drop-in performance evaluation, it was then of interest to perform tests on an engine with which changes to the operating map could be made and operating states could be optimized.

6.3.1. Methods

To best allocate time and resources, the team partnered with researchers at the University of Alabama (UA) to carry out the performance optimization studies. In so doing, the team hoped to leverage UA's specialties to conduct relevant-scale engine experiments and bypass the instrumentation-related complications that had delayed progress at the Energy Institute. The University of Alabama was positioned well to conduct these tests with a single-cylinder PACCAR MX-11 engine of similar bore/stroke, operating conditions, and end-use application as the 6.7L Cummins diesel originally slotted for this testing at the Energy Institute (see Fig. 6.6 for detailed engine specifications). This engine offered three primary benefits: (1) its ECM was fully "unlocked" with the ability to precisely tune injection timing, injection duration, EGR rate, and boost pressure across its map, (2) it was fully instrumented with cylinder pressure transducers, five-gas emission analyzers, and low-frequency temperature and pressure sensors throughout, and (3) as a single-cylinder, it burned significantly less test fuel while offering equivalent performance insights to the multi-cylinder engine.

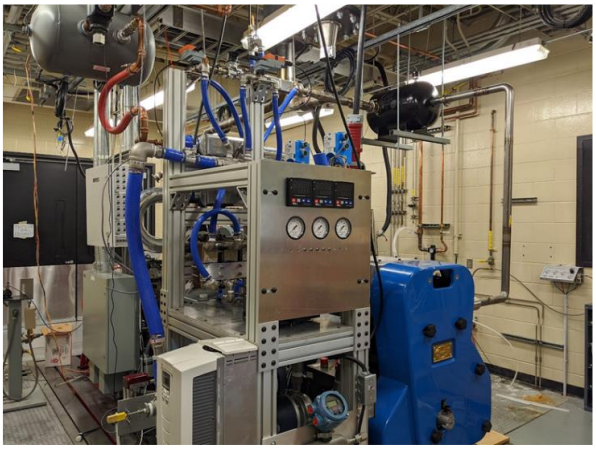

Parameter	Specifications
Engine type	Single cylinder, four-stroke
Bore (mm)	123
Stroke (mm)	152
Displaced volume (L)	1.806
Compression ratio	18.5
Intake valve timings	IVO: 710 CAD, IVC: 190 CAD
Exhaust valve timings	EVO: 495 CAD, EVC: 5 CAD
Diesel Injection system	Common Rail Injection System
Max torque	50 Nm @ 1000 rpm
Max power	53 kW @ 1750 rpm
Max engine speed	2200 rpm
Max cylinder pressure	245 bar

Figure 6.6. Single cylinder research engine at University of Alabama and engine specifications.

Preliminary performance data was first collected to characterize baseline performance of P1P in the PACCAR engine and corroborate the findings of the Energy Institute. Engine testing beyond the baseline was to consist of preliminary EGR sweeps to normalize NOx emissions to the engine's baseline, followed by fine tuning of the operating map (e.g., boost pressure, injection timing/duration) to optimize performance on the alternative fuel blend. Particulate and gaseous emissions were to be measured at this optimized state and compared to the baseline to quantify the NOx-normalized soot reduction potential of

the blended POME fuel. Though extensive baseline data was collected, the final EGR sweeps were not carried out due to repeated catastrophic failures of the test engine during the final months of the project. These failures occurred during unrelated diesel/natural-gas dual fuel studies – the first resulting from a hydraulic-lock condition caused by coolant leaking into the combustion chamber, and the second from oil starvation caused by an abrupt and extensive oil leak.

6.3.2. Baseline Results and Discussion

Baseline performance tests were conducted using 100% P1P. Cylinder pressure, heat release profiles, and five-gas emissions were recorded at 5, 10, and 15 bar IMEP and averaged over 1000 cycles. Three engine speeds – 1099, 1339, and 1578 RPM – were assessed. Injection timing was held constant across both speed and load, with SOI 1 = 350 CAD and SOI 2 = 0 CAD. The in-cylinder pressures for the three load and three speed conditions are presented in Fig. 6.7.

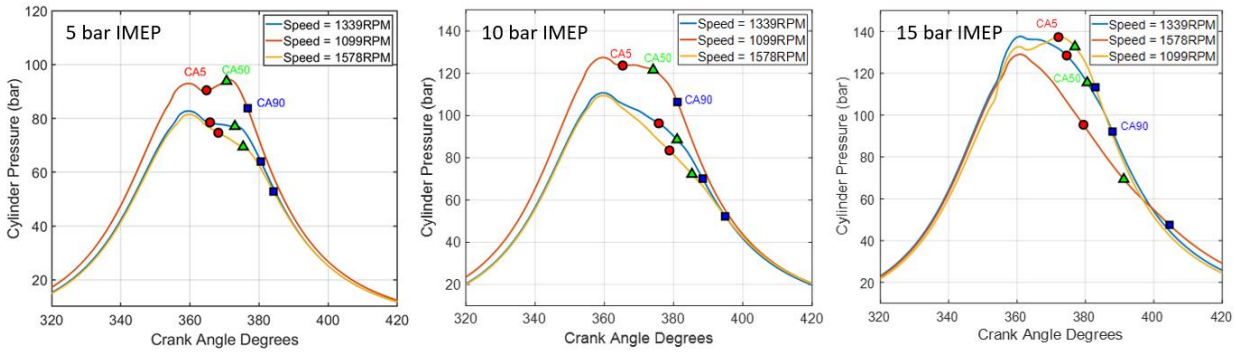

Figure 6.7. Cylinder pressure traces and locations of 5%, 50%, and 90% mass fraction burn for the swept operating conditions.

Combustion phasing advanced at lower speeds due to the relative difference in flame speed and RPM. Combustion duration increased with load. The SOC is the most delayed at the 1578 RPM condition and the duration between SOI and SOC is also maximum for this speed condition. This implies increased fuel – air mixing duration and lower stratification. The lower local temperatures, which are likely to prevail within the combustion chamber due to lower stratification and delayed combustion phasing, contribute to the NOx reduction.

Figure 6.8. shows the indicated fuel conversion efficiency (IFCE) and combustion efficiency for all the speeds. The combustion efficiency is observed to be > 99% at this load for all speeds; this trend is similar to conventional diesel CIDI combustion. The IFCE variations are minimal but the slight increase and decrease in IFCE as speed increases can be correlated with changes in combustion phasing. The combustion phasing for the 1578 RPM operating point is the most retarded from TDC, which is sub-optimal for high efficiencies, which is corroborated by the slight decrease in efficiency compared to the 1339 RPM operating point.

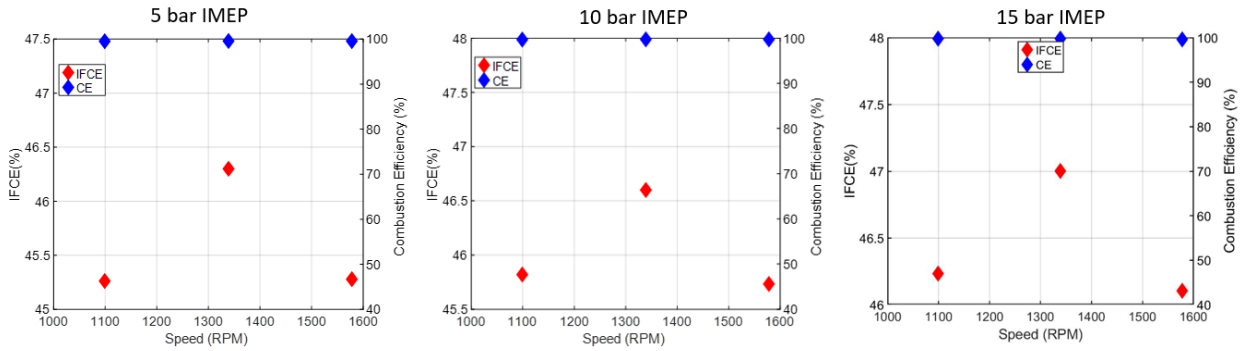

Figure. 6.9. Indicated fuel conversion efficiency and combustion efficiency at different speeds.

Figure 6.9 shows trends in indicated specific HC, CO and NOx emissions with speed for P1P CI combustion at the various load conditions. At 10 bar IMEPg, steady increase at ISNOx from 5 g/kWh to 9 g/kWh is observed as speed decreases. The ISHC and ISCO emissions, however, are lower than 5 bar IMEPg conditions as the values are close to 0.5 g/kWh. At 15 bar IMEPg, both ISHC and ISCO emissions are below 1 g/kWh for this load, however the NOx emissions rise steadily beyond 10 g/kWh as speed is reduced from 1578 RPM to 1099 RPM. The variations in NOx can be attributed to the earlier SOC and combustion phasing advancement at lower speeds. There is no appreciable variation in ISHC and ISCO emissions as they vary only by 0.2 and 0.8 g/kWh respectively from the lowest to the highest speed. The ISHC values are slightly greater in the 15 bar IMEPg case than the 10 bar IMEPg case due to the much greater injection duration and injected quantity of P1P, which might consequently lead to more hydrocarbons being trapped in crevices.

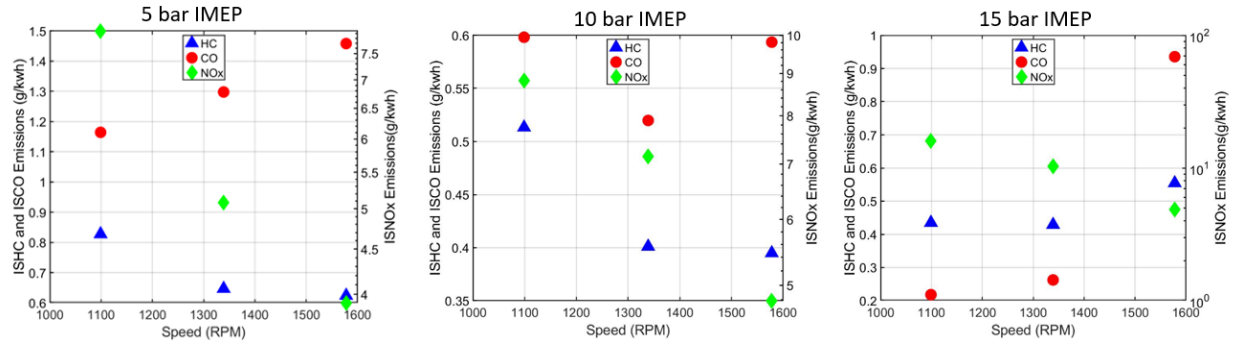

Figure 6.10. Indicated specific emissions across load and speed.

6.3.3. Performance Optimization Conclusions

The key conclusions from this P1P testing are:

- Near zero smoke emissions were recorded by an AVL 415S smoke meter demonstrating the potential of P1P in virtual elimination of engine-out smoke emissions. Future work should focus on quantifying particulate matter number and size distribution measurements.
- ISHC and ISCO emissions < 2 g/kWh and < 1 g/kWh were observed at low and medium loads respectively.
- For a given load, engine-out NOx emissions were typically higher at lower speeds due to earlier combustion phasing and likely higher local temperatures.

- IFCEs were slightly lower than conventional diesel combustion operation at these loads; 49% IFCE for CDC at 5 and 10 bar IMEPg, whereas only 47% and 46.5% were observed for P1P combustion at 5 and 10 bar IMEPg. However, it must be emphasized that the P1P operation was not optimized for efficiencies or emissions at any operating condition.
- At all speed load conditions, locations of CA50 were found to be > 370 CAD, which is sub-optimal for higher IFCEs.
- Parameters like intake pressure, injection timing and rail pressure are known to have an impact on combustion phasing and thereby IFCE.

Chapter 7 TEA/LCA of POME Fuels

7.1. Introduction

Bio-derived liquid fuel will likely continue to have a place in the net-zero transition of hard-to-abate sectors such as aviation and marine transportation. As such, it is important to determine whether emissions from the production of novel bio-derived oxymethylene ethers (OMEs) can meet the requirements of advanced biofuels based on the renewable fuel standard and are economically viable. This chapter summarizes a concurrent life cycle assessment and techno-economic analysis of one of the OMEs, Dibutoxymethane (B-1-B) (C_4H_9-O-CH_2-O-C_4H_9), synthesized, characterized, and tested over the course of this project. B-1-B is compared to, oxymethylene of chain lengths 3–5 (M-n-M) (CH_3-O-(CH_2-O-)$_{3–5}$-CH_3), the previously established state of technology for OMEs, and traditional diesel fuel.

The different production pathways for M-n-M and B-1-B compared in this chapter are summarized in but not limited to Figure 7.1. The production pathways can be broken down into primary feedstock (biomass, H_2, CO_2), intermediate feedstock (butanol, formaldehyde, and methanol), and final products (B-1-B, M-1-M, and M-n-M). Intermediate feedstock can be derived from biomass or synthesized using renewable electricity via carbon capture and water electrolysis. Pathway A results in bio-derived fuels from second generation biomass feedstock [8,136,138–142]. Pathway B results in electricity-based fuels commonly referred to as e-fuels [136,140,143–148]. This project focuses on Pathway A. Final products can be derived from the intermediate feedstock through multiple pathways. In Pathway 1, M-n-M is directly synthesized through the reaction of aqueous formaldehyde and methanol [8,136,138–143,146,147,149]. In Pathway 2, aqueous formaldehyde is first reacted with methanol to produce M-1-M in a well-established process [148]. M-1-M is subsequently reacted with trioxane yielding M-n-M [143,147,149,150]. Additionally, M-1-M can be utilized as a fuel itself [136,143,145,148]. While Pathway 2 is more established, Pathway 1 is more energy efficient [143,145,147,150]. Pathway 3 and Pathway 4 have not been previously studied. This project has focused on establishing pathways 3 and 4 to produces bio-derived B-1-B which will be further discussed in the methods.

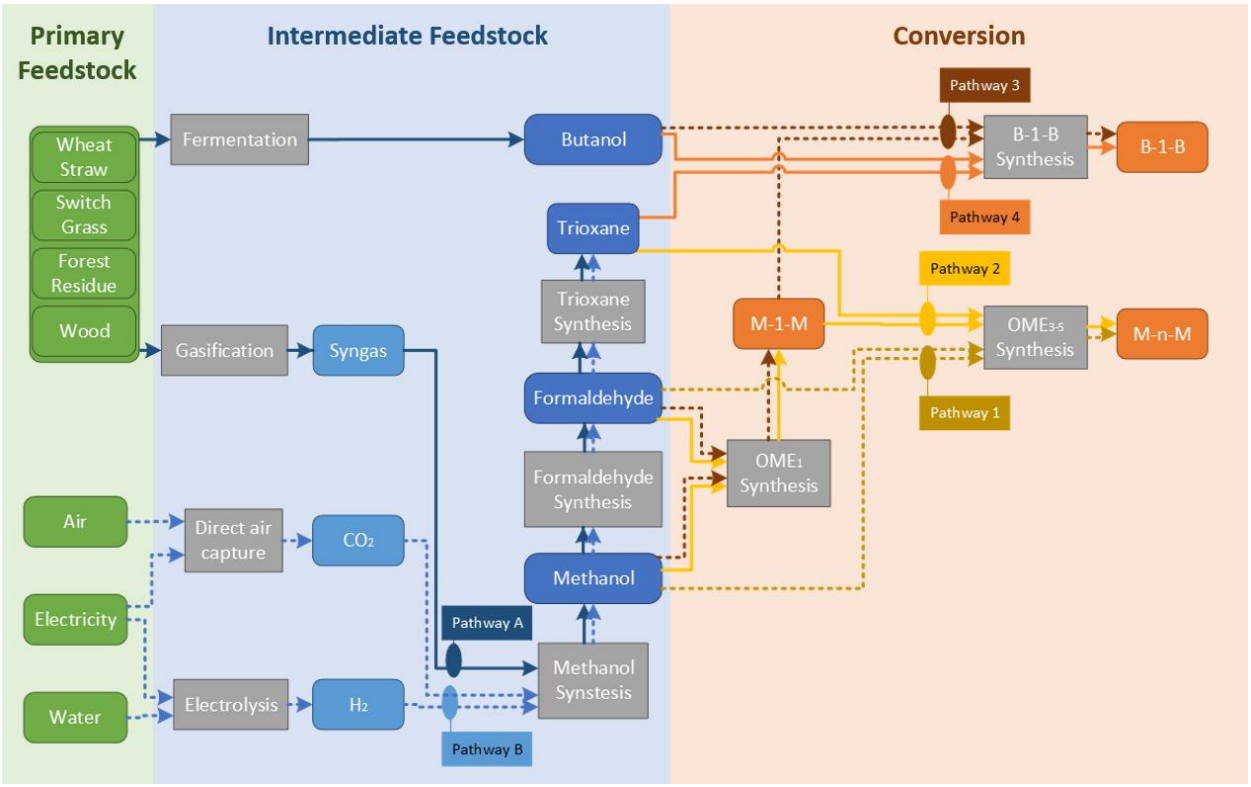

Figure 7.1. Production pathways for OMEs. Pathway A: Bio-derived intermediate products. Pathway B: Electricity derived intermediate products. Pathway 1: Methanol and aqueous formaldehyde and M-1-M. Pathway 2: M-n-M from M-1-M and trioxane. Pathway 3: B-1-B from M-1-M and butanol. Pathway 4: B-1-B from Butanol and trioxane.

TEAs have been conducted for pathways 1 and 2. There is large variability in the estimated production cost of OMEs. Production costs of 0.73–4.18 dollars per liter of diesel equivalent ($·L diesel-eq.$^{-1}$) or 2.76–15.82 dollars per diesel gallon equivalent (DGE) ($·DGE^{-1}) have been reported for synthesis from renewable feedstock [136,138,140,141,143,146]. A liter of diesel equivalent is the amount of fuel containing the energy equivalent to a liter of diesel or (36.4 MJ). Likewise a DGE is the amount of fuel containing the energy equivalent to a gallon of diesel. TEA studies of M-n-M production pathways have identified feedstock cost as a driving factor for MFSP [136,138,140,141,143,144,146,148,150]. In general, reported OME costs are largely dependent on intermediate feedstock price.

OMEs struggle to achieve a well-to-wheel greenhouse gas reduction compared to conventional diesel but the work well in some instances. Well-to-wheel greenhouse emissions have been reported to be 1.94–350 g CO_2-eq·MJ^{-1} and negative emissions, or sequestration, is possible under special circumstances [8,140–142,144,146,148]. For reference, GHG emissions from the production and combustion of diesel are 83–101 g CO_2-eq·MJ^{-1} [140,144,148,151]. In a best case scenario, Emenike et al. showed OME fuels can sequester 80 g CO_2-eq·MJ^{-1} by using biomass as a feedstock and sequestering carbon dioxide off gas from syngas cleaning although the authors do not appear to explicitly consider indirect or direct land use change emissions [141]. When 100% wind, hydro, or nuclear energy is used for direct air capture or biomass is used Rodríguez-Vallejo et al. and Hank et al. report an 18–98% reduction in well-to-wheel greenhouse gas emissions can be achieved compared to diesel [140,144,148]. Assuming a more convention grid mix paints a different picture. For example, assuming an electrical mix of 60% the German grid in 2018 and 40% on-site wind and solar, Hank et al. show that the well-to-wheel greenhouse gas emissions for direct air capture

synthesized OMEs are 209–263% of (or more than double) conventional diesel depending on thermal energy source [144]. Only OMEs produced using direct air capture via 100% renewable electricity or methanol via biomass gasification have shown greenhouse gas emissions less than conventional diesel.

The economics and sustainability of emerging OMEs with alkyl end groups has not yet been assessed. This work will focus on using biomass derived butanol. Butanol is produced via significantly different means than methanol warranting an exploration of producing these new OMEs using butanol as an intermediate feedstock. Additionally, variability in feedstock cost was analyzed with Monti Carlo analysis. This was accomplished through the construction of an engineering process model that was coupled with concurrent TEA and LCA. The model was validated with experimental and literature data. Like, Schmitz et al. and Martín et al. this work uses a truncated system boundary starting with methanol and butanol feedstock to facilitate data reproducibility in the future with updated prices for methanol and butanol. Discussion focuses on the implications of feedstock price and carbon intensity as well as addressing multi-functionality in ABE fermentation. A rigorous assessment of variability in feedstock price is included to provide a comprehensive view of uncertainty.

7.2. Methods

An engineering process model was developed and focuses on accurately capturing mass and energy flows. Mass and energy flows from the engineering process model serve as inputs for techno-economic analysis and life cycle assessment. Feedstock prices were assessed in detail during the economic assessment.

7.3. Modeling

Experimental data, Aspen Plus, and literature were used to develop and validate an engineering process model. Experimental data supported the development of novel B-1-B production pathways in Aspen Plus while stream tables for preexisting pathways were extracted from peer reviewed journal publications to validate the modeling work.

Pathway 1: M-n-M from methanol and aqueous formaldehyde. Pathway 2: M-n-M from M-1-M and trioxane.

M-1-M production consists of one reactor in which methanol reacts with aqueous formaldehyde to form M-1-M and two distillation columns using pressure swing distillation based on the process established by Weidert et al [152]. M-n-M production Pathway 2 consists of a reactor in which M-1-M reacts with trioxane to form M-n-M and two distillation columns using pressure swing distillation based on the process established by Schmitz et al [153]. M-n-M production Pathway 1 consists of a reactor in which methanol reacts with aqueous formaldehyde to for M-n-M, a membrane separation process, and two distillation columns using pressure swing distillation based on the process established by Burger et al [154]. Trioxane production was based on the process established by Grützner et al [155]. The mass and energy flows for all process in pathways 1 and 2 were retrieved from a report by Held et al [141].

Pathways 3: B1-B from butanol and M-1-M. Pathway 4: B-1-B from butanol and trioxane.

Mass and energy flows for trioxane production were derived the same as Pathway 2. The remaining processes in pathways 3 and 4 we modeled as a part of this work. Synthesis of B-1-B by pathways 3 and 4 (Figure 7.1) was modeled in Aspen Plus using Peng-Robinson and NRTL equations of state. Process flow diagrams are provided in the §7.4. Appendix. In Pathway 3, two moles of butanol react with one mole of M-1-M to form one mole of B-1-B and two moles on methanol. The methanol is separated from the B-1-B

and recycled. The fractional conversion of M-1-M in Pathway 3 is 65%. In Pathway 4, six moles of butanol react with one mol of trioxane to form three moles of B-1-B. The fractional conversion of butanol in Pathway 4 is 58%. In both pathways, the unconverted reactants are separated from the B-1-B product and recycled.

Aspen Distillation Synthesis was utilized to identify azeotropes and design the separation process. Distillation columns were first approximated using Aspen Plus shortcut distillation design and the Winn-Underwood-Gilliland methods to determine an appropriate number of stages and were subsequently modeled based on the rigorous two-phase fractionation model and Aspen Plus Column Analyzer. Decanters were used to separate heterogeneous mixtures and pressure swing distillation was used to overcome azeotropes where applicable.

Feedstock price

This section defines the uncertainty in published production cost estimates of bio-methanol and bio-butanol from lingocellulosic biomass. Techno-economic studies of bio-methanol and bio-butanol production were reviewed and their results reproduced to identify and harmonize key parameters used to estimate production cost. The probability density functions for minimum bio-methanol and bio-butanol selling prices are assessed through Monte Carlo analysis varying these parameters with distributions defined through literature review. Discussion focuses on the sources of uncertainty and the probability that methanol and butanol from lignocellulosic biomass can be produced at price points competitive with conventional fossil fuel pathways.

The price of formaldehyde was subsequently set using the methodology of Schmitz et al. based on the price of methanol and a yield of 0.823 kg formaldehyde per kg methanol [146,153,156]. The manufacturing cost of formaldehyde excluding feedstock cost is 0.017 $\$\cdot kg^{-1}$ which is 10% of the production cost, assuming the market price of fossil methanol [153]. Feedstock cost is expected to be 80–90% for chemical production, thus the assumption of Schmitz et al. was validated [157].

Literature review of feedstock price

Economic results were reproduced from key variables including reported annual operating expenditures, fixed capital investments, name plate production capacities, product yields, and capacity factors. In some cases, where this information was not available, it could be assumed or calculated from other provided information. To be considered in this work, the publication's economic results needed to be reproducible (±20%) without excessive assumptions. Values of these variables in literature are summarized in Table 7.1 and Table 7.2 and were used to validate cost distributions used in Monte Carlo simulation. Information on product yields for ABE fermentation is compiled separately in Table 7.3 because product yields are dependent on feedstock compositions, sugar yields during pretreatment, and butanol selectivity.

Table 7.1. Summary of key input variables for bio-methanol production as reported by publications prior to harmonization.

Study	Capacity ($t\cdot y^{-1}$)	Biomass Price ($\$\cdot t^{-1}$)[a,d]	Methanol Yield ($g\cdot g^{-1}$)[b]	Capacity Factor	OPEX[d] ($\$\cdot y^{-1}$)	FCI[c] ($MM)	Methanol Price[d] ($\$\cdot kg^{-1}$)
Tock et al. (2010) [158]	678,194	400	0.53	90%	154.8	856	1.38

Sarkar et al. (2011) [159]	730,000	54	0.39	85%	28.0	377	0.37
Mignard & Pritchard (2008) [160]	73,000	95	0.5	75%	11.5	185	0.92
Huisman et al. (2011) [161]	357,408	194	0.45	88%	36.2	484	0.85
Andersson et al. (2014) [162]	552,435	179	0.54	91%	66.9	728	-
Fournas and Wei (2022) [163]	84,516	91	0.63	90%	44.4	160	1.26
Zhang et al. (2021) [164]	912,500	52	0.51	-	285.8	1447	-

[a]Dollars per metric ton of dry biomass; [b]Grams per gram of dry biomass; [c]Converted to 2022 United States Dollars using the Chemical Engineering Plant Cost Index and exchange rates; [d]Converted to 2022 United States Dollars using the Producer Price Index by Commodity: Chemicals and Allied Products: Industrial Chemicals and exchange rates

FCI = Fixed Capital Investment; OPEX = Operating Expenditures Excluding Feedstock Costs; MM = million; t = metric ton or tonne

Table 7.2. Summary of key input variables for bio-butanol production publications

Study	Capacity ($t \cdot y^{-1}$)	Biomass Price ($\$ \cdot t^{-1}$)[a]	Co-product Values ($\$ \cdot t^{-1}$)		Capacity Factor	OPEX ($\$ \cdot y^{-1}$)	FCI[b] ($MM)	Butanol Price[c] ($\$ \cdot kg^{-1}$)
			Acetone	Ethanol				
Tao et al. (2013) [165]	730,000	92	990	770	96%	59.0	695	1.70
Jang and Choi (2018) [166]	356,577	83	1076	687	90%	59.2	443	3.56
Ave and Adams (2018) [167]	907,628	99	1100	900	96%	185.1	363	3.14
Kumar et al. (2012) [168]	64,843	44	810	890	90%	12.3	332	0.69
Baral and Shah (2016) [169]	736,060	161	1000	-	90%	80.9	10	2.64
Mailaram and Maity (2022) [170]	54,750	99	925	842	-	6.3	410	2.10
Meramo-Hurtado et al. (2021) [171]	2,810,462	96	1200	940	90%	-	214	-
Qureshi and Singh (2014) [172]	441,129	-	500	900	96%	82.8	64	1.72

[a]Dollars per metric ton of dry biomass; [b]Converted to 2022 United States Dollars using the Chemical Engineering Plant Cost Index and exchange rates; [c]Converted to 2022 United States Dollars using the Producer Price Index by Commodity: Chemicals and Allied Products: Industrial Chemicals and exchange rates

FCI = Fixed Capital Investment; OPEX = Operating Expenditures Excluding Feedstock Costs; MM = million; t = metric ton or tonne

Table 7.3: Product yields from ABE fermentation techno-economic literature.

Study	Feedstock Composition			Sugar Yields		ABE Yield ($g \cdot g^{-1}$)[c]	A:B:E Molar Ratio
	Cellulose (%wt.)	Hemi-cellulose (%wt.)	Lignin (%wt.)	Glucose ($g \cdot g^{-1}$)[a]	Xylose ($g \cdot g^{-1}$)[b]		
Tao et al. (2013) [165]	-	-	-	92%	92%	0.354[d]	3:6:1
Jang and Choi (2018) [166]	43%	19%	25%	77%	77%	0.339	1.2:7.2:1.6[d]
Ave and Adams (2018) [167]	37%	29%	19%	85%	96%	0.239[d]	3.6:5.9:0.6[d]
Kumar et al. (2012) [168]	37%	29%	19%	-	-	0.390	3:6:1
Baral and Shah (2016) [169]	35%	24%	16%	74%[d]	90%[d]	0.318[d]	1.8:7.7:0.5[d]
Mailaram and Maity (2022) [170]	50%	27%[d]	23%	90%	100%	0.388	3:6:1
Meramo-Hurtado et al. (2021) [171]	40%	13%	12%	91%[d]	90%	0.375[d]	2.8:5.7:1.5[d]
Qureshi and Singh (2014) [172]	-	-	-	-	-	0.38	3.3:5.2:1.4

[a] grams of glucose per gram of cellulose; [b] grams of xylose per gram of hemicellulose; [c] grams of acetone, butanol, and ethanol solution per gram of sugar; [d] calculated

Harmonization of feedstock price

Distributions for Monte Carlo assessment were taken by correlating fixed capital investment and annual operating expenditures with biomass processing capacity from peer-reviewed publications. Fixed capital investment and annual operating expenditures excluding biomass expenses were harmonized through correlating expenses with biomass processing capacity. Annual biomass expenditures were harmonized though product yields and a consistent biomass price. Likewise, co-product revenues were harmonized through co-product yields considering only acetone and ethanol and consistent co-product prices. In literature, a variety of other co-products are occasionally considered, such as hydrogen, electricity, and purified CO_2 but they are considered inconsistently and make up only a small fraction of total co-product revenues, therefore they were excluded in this work.

The fixed capital investment accounts for all inside and outside battery limits equipment, installation, and any indirect expenses. If the publication did not consider onsite utilities generation from lignin, a factor of 10% was added to the reported fixed capital investment based on of the average of results from facilities where it was included [168,170,171]. Correspondingly, steam and electricity costs were removed from reported annual operating expenditures when onsite utilities generation was not considered. Fixed capital investments were correlated with biomass processing capacity based on the sixth-tenths rule and were converted to 2022 dollars using the chemical engineering plant cost index. Equation (1), the six-tenths rule, is commonly used to approximate the fixed capital investment for a new facility based on a reference facility [157].

$$C_2 = C_1 \left(\frac{S_2}{S_1}\right)^n \quad (1)$$

Where C_2 is the approximate cost of the new facility, C_1 is the cost of the reference facility, S_2 is the capacity of the new facility, S_1 is the capacity of the reference facility, and n is a scaling exponent. The average value of n across the chemical industry is 0.6, hence it is the namesake of Equation (1) [157]. Equation (1) can be rearranged for curve fitting yielding Equation (2) [157].

$$C_2 = \left(\frac{C_1}{{S_1}^n}\right){S_2}^n = a \cdot {S_2}^n \quad (2)$$

Where a is a constant. The value of n was constrained to 0.6, S_2 was the biomass processing capacity, and a was determined from a least squares regression. In order to fit the data, the data was transformed into a logarithmic scale, specifically using the log-log transformation in Equation (3).

$$\log_{10} C_2 = \log_{10} a + n \cdot \log_{10} S_2 \quad (3)$$

The 68% and 95% confidence intervals were assessed for the regression. The regression and confidence intervals were used to determine the mean and standard of deviation of fixed capital investment at a given capacity. A Pearson's correlation coefficient was calculated, signifying the strength and direction of the linear relationship between the variables on the logarithmic scale.

The same procedures were repeated to correlate annual operating expenditures excluding biomass because there is not enough transparency in the selected publications to reproduce the published estimates of operating expenditures via more traditional methods. Some economies of scale are expected, especially in fixed operating costs such as labor and maintenance, but the value of the scaling exponent (n) for this application is undocumented, so the scaling exponent was not constrained in this application.

Monte Carlo simulation of feedstock price

The cost correlations and confidence intervals developed in Section 0 were used to determine the mean and standard deviation at a specific capacity for distributions used in Monte Carlo simulation. The capacity presented in this work corresponds to the capacity for which there is the least uncertainty in fixed capital investment and annual operating expenditures excluding feedstock costs. By nature of the statistical analysis, this is approximately the median capacity from literature. Normal distributions were selected for fixed capital investment and annual operating expenditures exuding feedstock costs because a rigorous literature review and statistical analysis was conducted. These cost were correlated using a linear regression in Section0, Equation (3), therefore the normal distribution must be applied to the logarithm to the base 10 of the values rather than the value. Triangular distributions were selected for uncertain inputs that do not have well know distributions because the triangular distribution assigns greater probability to the tails of the distribution than a normal distribution. Where there is a consensus among the review publication as to the value of an input, the value of that input is assumed to be constant throughout Monte Carlo analysis and the average value from literature was selected. The inputs for Monte Carlo analysis are listed in Table 7.4 and Table 7.5 for bio-methanol and bio-butanol, respectively. The impact of capacity was not considered in Monte Carlo analysis. Rather, a scenario analysis was conducted with scenarios for low, median, and high capacities. Results for alternate capacities can be found in the electronic supplementary information.

Table 7.4: Distributions used for Monte Carlo simulation of bio-methanol production

Input	Normal Distributions	Reference

	Mean		Standard of Deviation	
Log Base 10 of FCI ($MM)	2.652		0.0850	[158–164]
Log Base 10 of OPEX ($MM)	1.436		0.1844	[158–164]
	Triangular Distributions			
	Minimum	Peak	Maximum	
Biomass Price	45	65	90	[30]
	Constants			
Biomass Capacity ($t \cdot y^{-1}$)	354,813			Assumed
Capacity Factor	90%			[158–163]
Methanol Yield ($g \cdot g\ biomass^{-1}$)	48%			[158–164]

FCI = Fixed Capital Investment; OPEX = Operating Expenditures Excluding Feedstock Costs; MM = million; t = metric ton or tonne

Table 7.5: Distributions used for Monte Carlo simulation of bio-butanol production

Input	Normal Distributions			Reference
	Mean		Standard of Deviation	
Log Base 10 of FCI ($MM)	2.364		0.1743	[165–172]
Log Base 10 of OPEX ($MM)	1.612		0.1010	[165–170,172]
	Triangular Distributions			
	Minimum	Peak	Maximum	
Biomass Price ($\cdot dry\ t^{-1}$)	45	65	90	[173]
Ethanol Value ($\cdot t^{-1}$)	335	670	1004	[174]
Acetone Value ($\cdot t^{-1}$)	500	875	1250	[175]
	Constants			
Biomass Capacity ($t \cdot y^{-1}$)	398,107			Assumed
Capacity Factor	90%			[165–169,171,172]
Feedstock Composition				
Cellulose (%wt.)	40%			[166–171]
Hemicellulose (%wt.)	24%			[166–171]
Lignin (%wt.)	29%			[166–171]
Sugar Yields				

Glucose (g·g cellulose^{-1})	85%	[165–167,169,171]
Xylose (g·g hemicellulose^{-1})	91%	[165–167,169,171]
ABE Yield (g·g sugar^{-1})	0.36	[165–169,171,172]
A:B:E Molar Ratio	3:6:1	[165–169,171,172]

FCI = Fixed Capital Investment; OPEX = Operating Expenditures Excluding Feedstock Costs; MM = million; t = metric ton or tonne; wt. = weight

Other operational expenditures

Price of steam was calculated using the methods of Kumana base on United States national average commercial natural gas price for the past 10 years [176,177]. The price of steam is 0.010 $\$\cdot MJ^{-1}$. The price of cooling water is 0.0015 $\$\cdot MJ^{-1}$ [157]. Labor is based on the requirements for an ethanol facility [178]. Labor requirements are listed in Table 7.6. Salaries were updated to the year 2022 from the bureau of labor statistics. Labor burden is 90% of total salaries. Labor burden includes safety, general engineering, general plant maintenance, payroll overhead (including benefits), plant security, janitorial and similar services. Maintenance materials are estimated as 3% of installed equipment. Property insurance is 0.7% of fixed capital investment. It is estimated that the cost of all catalysts is about 20,000 $\$\cdot m^{-3}$, which is at the high end of the expected cost [161]. Catalysts are replaced every 3 years.

Table 7.6: Labor requirements

Position	Number	Salary (2022$)
Plant manager	1	$120,000
Plant engineer	1	$94,000
Maintenance supervisor	1	$77,000
Maintenance technician	8	$54,000
Lab manager	1	$75,000
Lab technician	2	$54,000
Shift supervisor	4	$65,000
Shift operators	20	$54,000
Yard employees	4	$38,000
Clerks & secretaries	3	$49,000

Capital expenditures:

In lieu of a bottom up assessment of CAPEX, an order of magnitude estimate is appropriate when CAPEX is not a major contributor to MFSP such as is in the production of OMEs [157,168,179]. Some have used an oil refinery of equal volumetric capacity as an appropriate proxy for CAPEX because it is a similar plant in that distillation operation units govern CAPEX at both oil refineries and an OME bio-refinery

[146,153,157,179]. While this is generally justifiable for order of magnitude estimates it can be problematic with new technologies that do not have preexisting CAPEX estimates [179]. Instead, this work calculates the capital cost based on the number of major processing steps (reactors and separators) according to (4) [157,168,179].

$$ISLB = 0.093 \cdot Q^{0.44} \cdot N^{0.486} \cdot T_{max}^{0.038} \cdot P_{mas}^{-0.02} \cdot f_m^{0.341} \quad (4)$$

Where $ISLB$ is the inside battery limits equipment cost for a CEPCI of 532.9, Q is plant capacity in metric tons per year, N is the number process steps, T_{max} is the maximum temperature, P_{max} is the maximum pressure, and f_m is the material factor. When Aspen Plus was not utilized to determine CAPEX, total CAPEX was approximated by this method. A validation of the method is provided in the electronic supplementary information. When Aspen Plus was utilized to determine CAPEX, equipment cost was approximated by the Aspen Capital Cost Estimator taking a bottom up approach. Sizing and column internals were designed using Aspen Plus Column Analyzer. Column cost from Aspen Capital Cost Estimator was validated using parametric equations from Towler et al [157]. OSLB and indirect capital costs were assessed as factors of equipment cost. OSLB can range from 20–50% with 40% usually used for initial assemenets. A portion of OSLB cost, such a cooling tower and steam plant, were accounted for in the price of steam and the price of cooling water. Therefore a value of 30% for OSLB was selected. Indirect cost were assessed as 60% of ISLB and OSLB and include prorateable expenses, field expenses, home office and construction, contingency, and other costs (such as start-up-permits, etc.) [178]. The BOMs from Aspen Capital Cost Estimator utilized to determine CAPEX are in the electronic supplementary information. Chemical engineering Plant Cost Index (CEPCI) was used to convert all costs to 2022 dollars.

The system boundary of this project forms a gate to wheel analysis including all processing steps from intermediate feedstock at the facility gate through combustion and end use. The functional unit of this study is one liter of diesel equivalent burned in an internal combustion engine where a diesel equivalent is the volume of a fuel such that the energy content is equivalent to a liter of diesel. A modified TRACI 2.1 methodology was implemented where global warming potentials of the greenhouse gases CO_2, CH_4, and N_2O were updated to 1, 27, and 273 respectively, matching the most resent ICCCP report. All scope 1 emissions and scope 2 and 3 emissions associated with the upstream feedstock and energy supply chains including transportation are accounted for.

Techno-economic analysis:

Table 7.7: Economic Assumptions

Parameter	Value
Internal rate of return	10%
Plant financing debt / equity	60% / 40% total capital
Debt financing term	10 years

Interest rate	8%
Plant life	30 years
Plant salvage value	None
Income tax rate	35%
Depreciation schedule	7-year modified accelerated cost recovery system (MACRS)
Construction period	8% year 1
	60% year 2
	32% year 3
Working capital	5% fixed capital (excluding land)
Start-up time	6 months
Start-up revenue and cost	50% revenue
	75% variable costs
	100% fixed costs
Availability	90% (329 days per year)
Indirect capita	51% total installed equipment
Base cost year	2022

Life cycle assessment

Life cycle inventory data from all scope 2 and 3 upstream and downstream processes were retrieved from life cycle inventory databases. GREET and literature data were used for to calculate feedstock carbon intensities [156]. Indirect land use change is an issue. Land use change is accounted for in GREET. The carbon intensity of bio-derived (switch grass) methanol is 0.27 kg CO_2eq.·kg^{-1}. The carbon intensity of formaldehyde 0.39 kg CO_2eq.·kg^{-1} was calculated based on the carbon intensity of methanol. The carbon intensity of butanol from ABE fermentation is dependent on attribution methodology. Using displacement method it is 2.8–11.0 kg CO_2eq.·kg^{-1} and −0.9–5.4 CO_2eq.·kg^{-1} for corn and cellulosic feed stocks are respectively [156,165,180]. Using energy allocation it is 1.2–6.5 kg CO_2eq.·kg^{-1} for cellulosic feed stocks [165,180]. The negative carbon intensity is inherent from using system boundary expansion via the displacement method. It is representative of avoided emissions rather than net removal of CO_2. The attributional approach of energy allocation is also provided for completeness. There is greater variability in reported butanol carbon intensities than methanol as butanol from cellulosic sources is a less studied/developed technology than methanol and the added uncertainty from the multifunctionality of ABE fermentation. Changes in carbon intensity can result from a difference in feedstock, land use change assumptions, and allocation methods. Impact of butanol and methanol carbon intensity is explored in a scenario analysis.

Steam from Ecoinvent. For electric scenarios the 2021 NYUP grid mix (33% Nuclear, 33% hydro, 26% natural gas, 5% wind, and 3% other) was used in the electric scenario as a representative of a low carbon intensity energy source at 29.5 g CO_2-eq·MJ^{-1}.

Distribution and utilization of fuel was derived using the methodology of Hank et al [151]. A life cycle inventory for each sub-process is provided in the electronic supplementary information. Life cycle inventory data can be compared to the work of Deutz et al. and Rodríguez-Vallejo et al [146,181].

Results and Discussion

The TEA and LCA results are discussed in this section. For each pathway, the minimum, mean, and maximum feedstock prices and carbon intensities are considered. Due to the larger contribution of steam to climate change as opposed to MFSP, electric heat is also considered as a futuristic scenario in the life cycle assessment. The four pathways are compared to conventional fossil-derived diesel as aa baseline.

Feedstock Price

Fixed capital investments from peer-reviewed publications and the linear correlations derived in Section 0 are plotted against biomass processing capacity with axes in logarithmic scale in Figure 7.2. As expected, in logarithmic scale, a positive linear correlation between fixed capital investment and capacity is observed. The Pearson's correlation coefficients for the logarithmically transformed data are 0.89 and 0.75, for bio-methanol and bio-butanol respectively. The coefficients of determination for the plotted linear regressions are 0.77 and 0.55, for bio-methanol and bio-butanol respectively. As signified by the confidence intervals plotted as dashed lines, the fixed capital investment for bio-butanol production has greater uncertainty. The process for using lingo-cellulosic biomass as a feedstock is less developed for bio-butanol and there are many subtlety different pre-treatment options leading to greater uncertainty. It was not possible to harmonize for pre-treatment type because of a lack of studies. Plotting fixed capital investments from peer-reviewed publications identifies cost projection below the 5^{th} and above the 95^{th} percentiles plotted as dotted line (Figure 7.2).

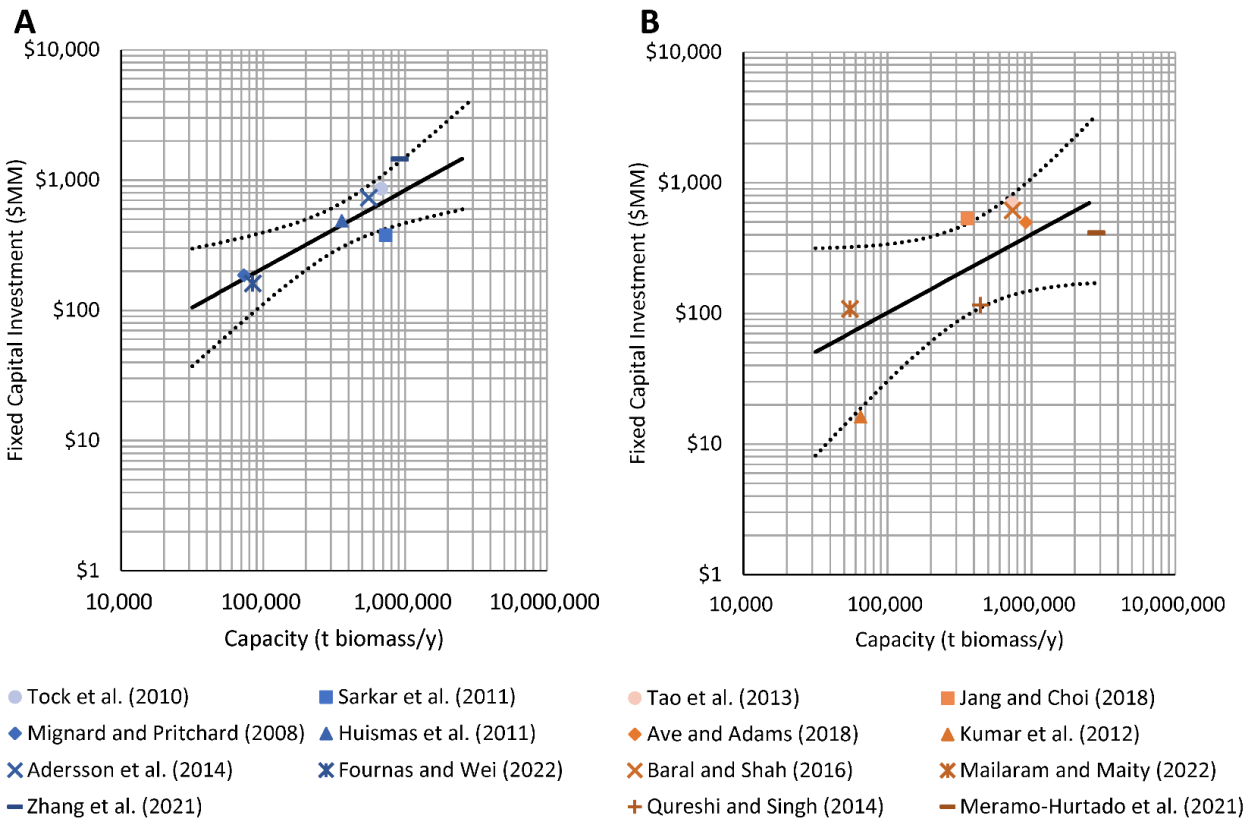

Figure 7.2. Fixed capital investments from peer-reviewed publications plotted against biomass processing capacity with axes in Log scale for A) Methanol and B) Butanol. Linear regressions are plotted with solid lines and 95% confidence intervals are plotted with dashed lines. All costs have been converted to 2022 dollars using the chemical engineering plant cost index.

The probability distributions of bio-methanol and bio-butanol price in dollars per kilogram ($\$\cdot kg^{-1}$) comparing bio-methanol and bio-butanol with their petro-chemical counterparts, fossil methanol and fossil butanol are provided in Figure 7.3. Data for fossil methanol and fossil butanol was collected between March 2020 and March 2023 for methanol and between May 2015 and May 2018 for butanol, and most closely represents the Free On Board spot price for the United States Gulf Coast region [182,183]. Based on Monte Carlo simulations, bio-methanol is expected to cost between 0.32–0.69 $\$\cdot kg^{-1}$ with 95% confidence. The mean price of bio-methanol is 0.51 $\$\cdot kg^{-1}$. Bio-butanol is expected to cost between 1.17–2.62 $\$\cdot kg^{-1}$ with 95% confidence. The mean price of bio-butanol is 1.91 $\$\cdot kg^{-1}$.

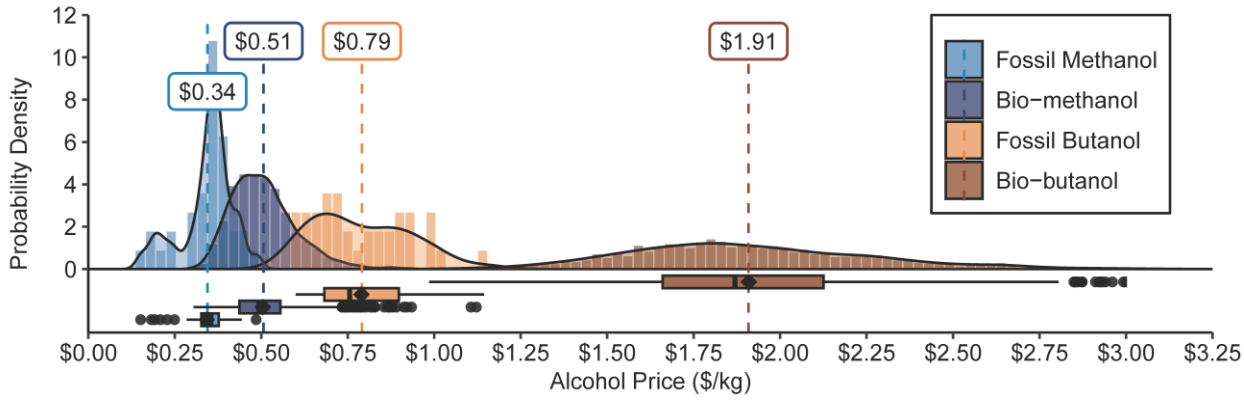

Figure 7.3. Visualization of the probability density distributions of bio-methanol and bio-butanol minimum selling price compared to petro-chemical methanol and butanol

Life cycle inventory

The life cycle inventory for each pathway is provided in Table 7.8. Pathways 1 and 2 require a larger mass of feedstock because M-1-M has a lower energy density than B-1-B. Subtle differences in feedstock requirements between Pathway 1 and Pathway 2 result from different recovery efficiencies. Likewise for Pathway 3 and Pathway 4. Pathway 2 and Pathway 4 have lower steam requirements because they have less processing steps.

Table 7.8: Mass and Energy Flows

	Output Mass Flows (t/hr)			
	Pathway 1	Pathway 2	Pathway 3	Pathway 4
M-n-M	44.6	44.6		
B-1-B			25.8	25.8
	Input Mass Flows (t/hr)			
Methanol	18.6	18.9	0.9	0
Formaldehyde	31.3	31.4	5.1	4.9
Butanol			23.9	23.9
	Input Energy flows (MW)			
Steam	111	212	87	47
Cooling water	127	182	70	44

Production cost

OME production costs for the four pathways are summarized in Figure 7.4 with detailed operational cost provided in Table 7.9 and detailed capital cost provided in Table 7.10. B-1-B can be competitive with M-n-M and has superior properties but B-1-B has the potential to be significantly more expensive due to high butanol costs. Both fuels are competitive with fossil diesel only under optimistic assumptions. M-n-M

production costs, found in literature, are within the range of 0.73–4.18 dollars per liter of diesel equivalent ($·L diesel-eq.$^{-1}$) [143,144,146,147,150,184]. The range of M-n-M production costs determined in this work is 1.27–2.26 $·L diesel-eq.$^{-1}$ which is smaller than the range found in literature because only one feedstock type (biomass derived methanol) was considered and the cost of methanol production was harmonized. Feedstock cost is the most important parameter to the assessment making recovery efficiencies critically important to minimize waste. Recovery efficiencies during distillation and separation impact feedstock requirements. In general, these results suggest that continued research effort should be conducted over feedstock production. This conclusion is applicable to e-fuels as well.

Simplifying assumptions can be made to energy calculations and CAPEX calculation without scarifying accuracy in results due to the large contribution of feedstock price. Even a large uncertainty in CAPEX does not impact the results by more than ±10% due to the high contribution of OPEX to MFSP. A rigorous assessment of CAPEX can be revisited when/if feedstock prices are reduced.

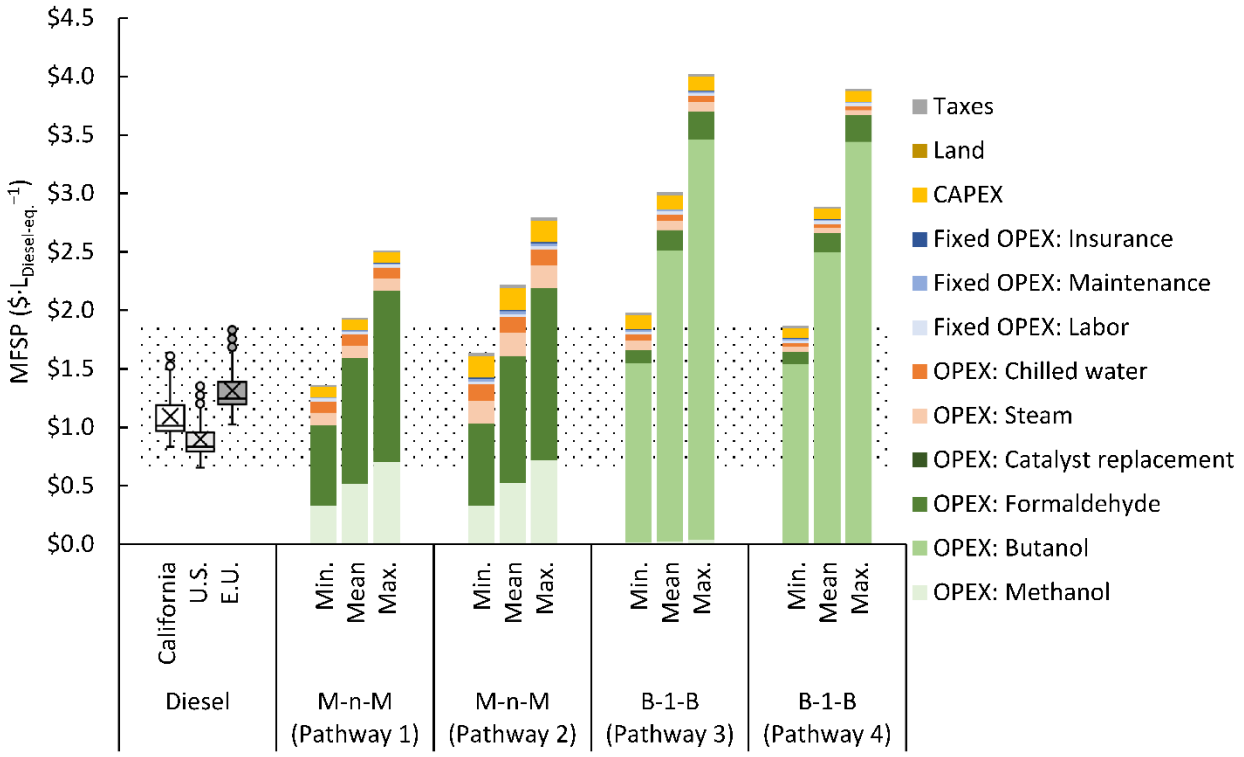

Figure 7.4: Techno economic results where “Min.,” “Mean,” and “Max” represent the minimum, mean, and maximum feedstock prices.

Table 7.9: Annual OPEX

OPEX	Fixed OPEX ($MM·y^{-1})			
	Pathway 1	Pathway 2	Pathway 3	Pathway 4
Labor	$5.0	$5.0	$5.0	$5.0
Maintenance	$2.4	$4.6	$2.8	$2.1

Insurance	$1.0	$2.2	$1.4	$1.0
	Variable OPEX ($MM·y^{-1})			
Butanol			$494.1	$496.1
Formaldehyde	$214.6	$215.6	$34.8	$33.4
Methanol	$102.3	$104.2		
Steam	$20.2	$38.7	$16.0	$8.5
Cooling Water	$5.8	$8.5	$3.2	$2.0

OPEX = Operational Expenditure

Table 7.10. CAPEX

CAPEX	ISLB ($MM)			
	Pathway 1	Pathway 2	Pathway 3	Pathway 4
Trioxane synthesis		$49.6		$25.2
B-1-B synthesis (Pathways 4)				$45.5
B-1-B synthesis (Pathway 3)			$60.0	
M-1-M synthesis		$42.5	$33.4	
M-n-M synthesis (Pathway 1)	$68.8			
M-n-M synthesis (Pathway 2)		$60.2		
	OSLB ($MM)			
OSLB	$20.6	$45.7	$28.0	$21.2
	Indirect Cost ($MM)			
Prorateable expenses	$53.6	$118.7	$72.8	$55.1
Field expenses	Included above			
Home office & construction fee	Included above			
Project contingency	Included above			
Other costs (start-up, permits, etc.)	Included above			

CAPEX = Capital expenditure; ISLB = Inside battery limits; OSLB = Outside battery limits; M-1-M = dimethoxymethane; B-1-B = Dibutoxymethane; M-n-M = blend of OMEs with methyl alkyl end groups and with oxymethylene chain lengths 3–5

Environmental impact

Attributional LCA results using energy allocation are provided in Figure 7.5A while system boundary expansion was performed in Figure 7.5B. Results are presented utilizing natural gas to generate steam "gas" and using electric heating "elec." Electric heating reduces the impact of steam but will have implications

on CAPEX and OPEX that was not explored in the TEA. Displacement of electricity, ethanol, and acetone leads to a negative carbon intensity for butanol and does not reflect a net sequestration of CO_2, but rather the avoided emissions from conventional electricity, ethanol, and acetone production. Well-to-wheel greenhouse (GHG) emissions for biomass derived M-n-M are reported as 53–74 g CO_2-eq·MJ^{-1} in literature [146,147]. In this work, emissions for biomass derived M-n-M are 24–150 g CO_2-eq·MJ^{-1}. Pathway 2 and Pathway 4 have lower onsite GHG emissions (e.g. burning of natural gas to generate steam), because these Pathways utilize less processing steps. Both fuels can meet the renewable fuel standard when utilizing feedstock with low embodied carbon, i.e. feedstock with low GHG emissions released during their manufacturing process. The assessment of feedstock carbon intensities remained outside the scope of this project but it is critically important to determining the environmental impacts of B-1-B and M-1-M. While both fuels can meet the renewable fuel standard, there are many times that they do not because the GHG emission released upstream to produce bio-methanol and bio-butanol are too large. Land use change impact of butanol production range across an order of magnitude and their impact can be 7.5 times greater than the net sum of impacts from all other emissions. In general, these results suggest that continued research effort should be conducted over feedstock production.

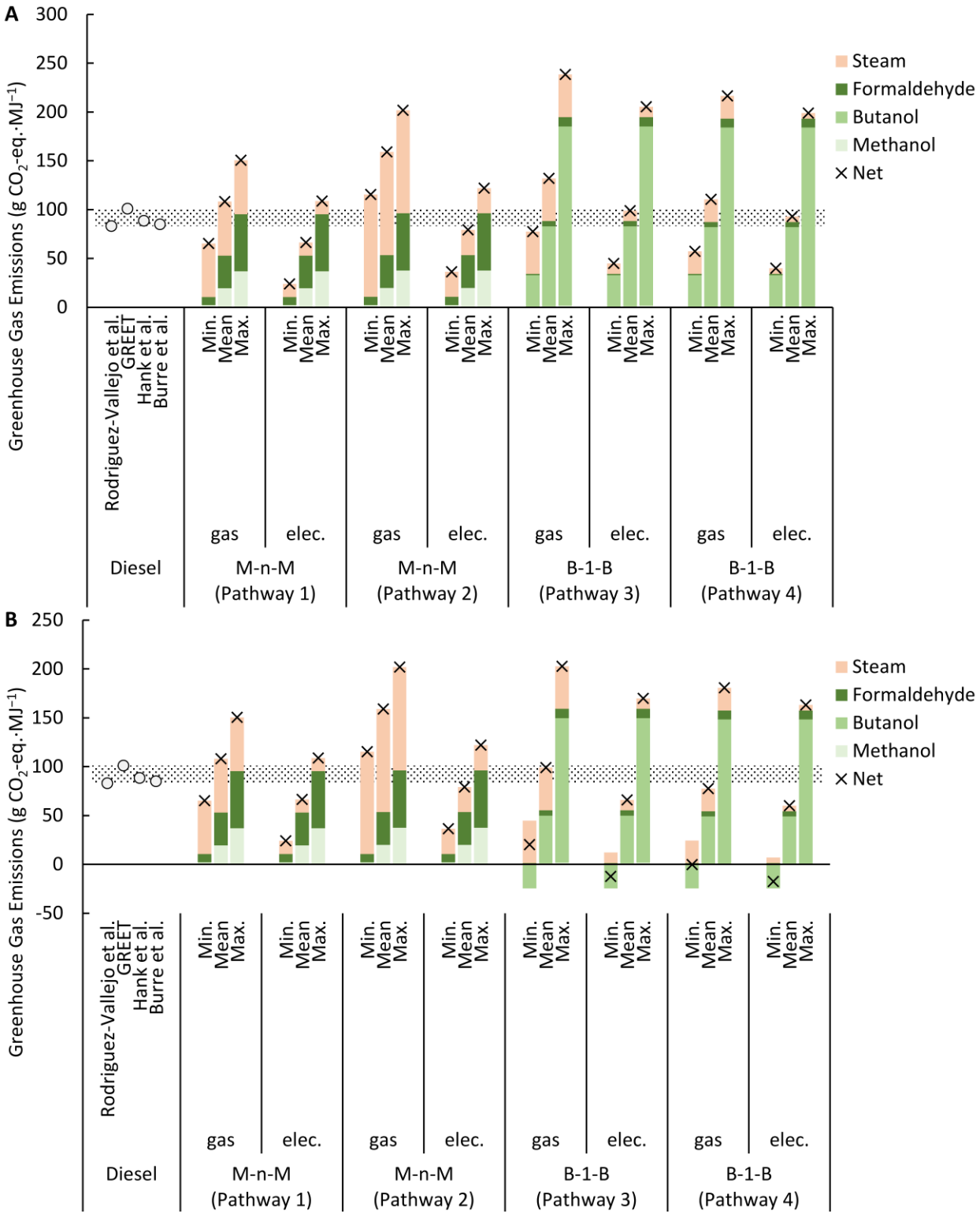

Figure 7.5. Life cycle assessment results using A) Energy allocation and B) system boundary expansion through the displacement method. Both utilizing natural gas to generate steam "gas" and using electric heating "elec." are considered.

7.4. Appendix

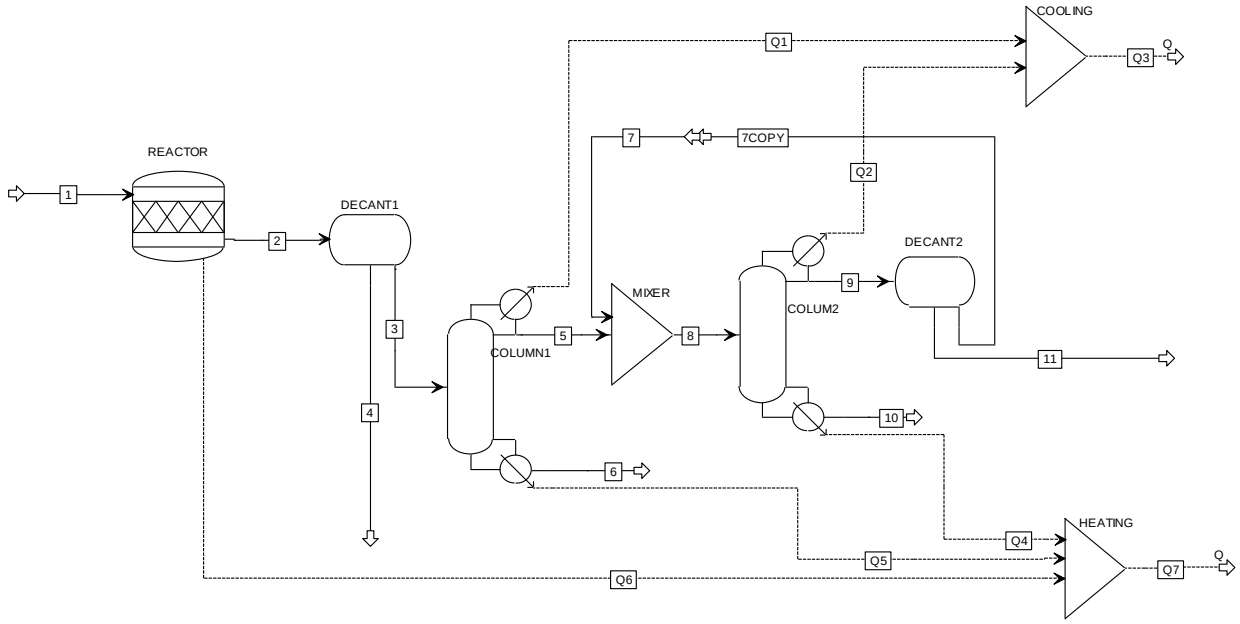

Figure A7.1. B-1-B synthesis through pathway 4.

Table A7.1. Mass flows for B-1-B synthesis through pathway 4.

	Stream					
Property	**1**	**2**	**3**	**4**	**5**	**6**
Temperature (°C)	61	80	80	80	97	179
Pressure (bar)	1.013	1.013	1.013	1.013	1.013	1.013
Enthalpy flow ($kJ \cdot s^{-1}$)	-67,859	-67,730	-57,079	-10,651	-31,117	-24,296
Mass flow ($kJ \cdot s^{-1}$)	54,471	54,471	52,031	2,440	23,705	28,326
Mass fractions ($kg \cdot kg^{-1}$)						
Water	0.000	0.059	0.014	0.999	0.032	0.000
Butanol	0.831	0.349	0.366	0.000	0.801	0.001
B-1-B	0.000	0.521	0.546	0.000	0.004	0.999
Trioxane	0.169	0.071	0.074	0.001	0.163	0.000

	Stream					
Property	**7**	**7COPY**	**8**	**9**	**10**	**11**
Temperature (°C)	80	80	96	91	114	80
Pressure (bar)	1.013	1.013	1.013	1.013	1.013	1.013
Enthalpy flow ($kJ \cdot s^{-1}$)	-2,746	-2,751	-33,864	-5,758	-27,947	-3,034
Mass flow ($kJ \cdot s^{-1}$)	1,985	1,985	25,690	2,681	23,010	695
Mass fractions ($kg \cdot kg^{-1}$)						
Water	0.045	0.046	0.033	0.293	0.003	0.999
Butanol	0.736	0.736	0.796	0.545	0.825	0.000
B-1-B	0.005	0.004	0.004	0.003	0.005	0.000
Trioxane	0.214	0.214	0.167	0.158	0.168	0.001

B-1-B = Dibutoxymethane

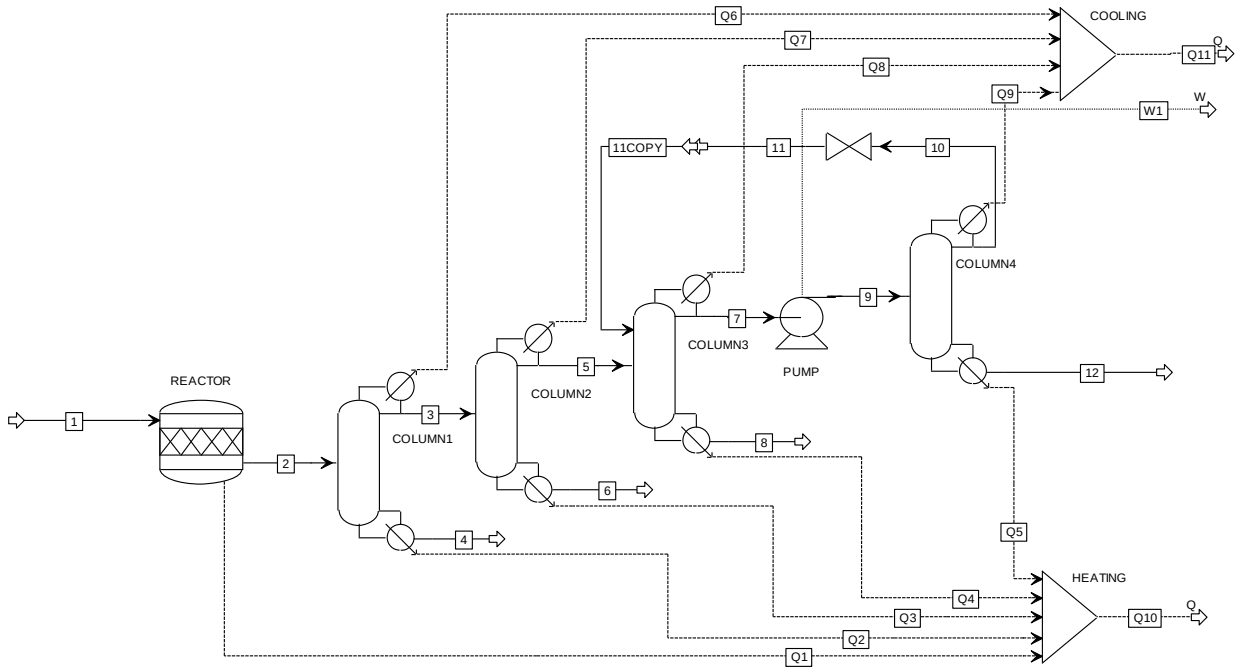

Figure A7.2. B-1-B synthesis through pathway 3.

Table A7.2. Mass flows for B-1-B synthesis through pathway 3.

	Stream						
Property	**1**	**2**	**3**	**4**	**5**	**6**	**7**
Temperature (°C)	25	60	80	179	48	118	41
Pressure (bar)	1.013	1.013	1.013	1.013	1.013	1.013	1.013
Enthalpy flow ($kJ \cdot s^{-1}$)	-11,663	-11,394	-9,193	-1,909	-2,599	-6,455	-1,911
Mass flow ($kJ \cdot s^{-1}$)	9,629	9,629	7,393	2,236	1,461	5,932	1,341
Mass fractions ($kg \cdot kg^{-1}$)							
Methanol	0.000	0.093	0.121	0.000	0.612	0.000	0.085
Butanol	0.523	0.308	0.402	0.000	0.000	0.500	0.000
M-1-M	0.169	0.059	0.077	0.000	0.388	0.000	0.915
B-1-B	0.000	0.232	0.000	0.999	0.000	0.000	0.000
M-1-B	0.308	0.308	0.401	0.001	0.001	0.499	0.000

	Stream					
Property	**8**	**9**	**10**	**11**	**11COPY**	**12**
Temperature (°C)	65	42	84	41	84	85
Pressure (bar)	1.013	4.000	4.000	1.013	1.013	4.000
Enthalpy flow ($kJ \cdot s^{-1}$)	-1,767	-1,911	-1,143	-1,143	-1,087	-730
Mass flow ($kJ \cdot s^{-1}$)	870	1,341	805	805	750	536
Mass fractions ($kg \cdot kg^{-1}$)						
Methanol	0.999	0.085	0.122	0.122	0.120	0.031
Butanol	0.000	0.000	0.000	0.000	0.000	0.000
M-1-M	0.000	0.915	0.878	0.878	0.880	0.969
B-1-B	0.000	0.000	0.000	0.000	0.000	0.000
M-1-B	0.001	0.000	0.000	0.000	0.000	0.000

M-1-M = dimethoxymethane; B-1-B = Dibutoxymethane; M-1-B = 1-(Methoxymethoxy)butane

Chapter 8 Conclusion and Future Applications

8.1. Summary

In the course of this project, many different OMEs have been used, synthesized, and studied for fuel and combustion related purposes. At a high level, the most important conclusion is this: OMEs as a class are generally excellent fuels or additives for the purpose of reducing soot production with respect to total combustion energy. The exact selection of an OME for a given purpose will be very context-dependent, and there are some fuel applications where the properties of OMEs outside of their soot reduction potential preclude their usage in certain applications.

Several types of OMEs were synthesized during this work. In the case of formation of a simple, *n*=1 OME, there are two pathways for production. In the first, M-1-M is reacted with an higher alcohol X-OH in a trans-acetalization reaction to form a target X-1-X, along with a partially-exchanged asymmetric OME M-1-X, with MeOH as an additional reaction product. This method, of course, cannot be used to formM-1-M; this must bemade in the second pathway. The second path is an acetalization reaction, where an alcohol X-OH is reacted with a formaldehyde source to produce X-1-X and water. Both reactions can be performed in acidic environments; in this work we use ion exchange resin Amberlyst 15 as the catalyst. Both reactions can be performed atmoderate temperatures, with Pathway 1 being sucessfully performed between 40°C-80°C, while Pathway 2 was performed at 60°C-100°C, where the 40°C case was insufficient to fully decompose trioxane to formaldehyde. The first pathway has fast reaction rates, but is hindered by low molar production of the target X-1-X, which is produced at approximately 10 mol% of the equilibirum concentration, while the partially exchanged product M-1-X occurs at twice this fraction, at a 2:1 X-OH :M-1-M stoichiometric ratio in the reactants. The second pathway has lower reaction rates, but shows higher mol fraction yields of the target product at 2:1 X-OH : CH2O reactant stoichiometry. The usefulness of this pathway is offset by the necessary production of water, and the equilibriumpresence of formaldehyde, which is not fully consumed. For use as fuels, both must be treated, via distillation or otherwise, to remove undesired components. Production of extended-chain OMEs can occur at similar moderate conditions in the same acidic catalyzed environment. Chain extension occurs through the addition of CH2O groups to X-n-X to produce X-(n+1)-X, where the equilibrium yield of various chain lengths is exponentially decreasing with increasing n. At the conditions used for OME production here (80°C and 0.64 min-1), the yields of various lengths was largely similar across the various alkyl groups, where *n*=1 accounted for half of the products, *n*=2 less than 25%, *n*=3 slightly greater than 10%, and so on.

Sixteen different OMEs were tested on a broad range of fuel-relevant properties. Some of these have had a subset of the tested properties already documented in literature, but a variety of untested OMEs along with new tests and properties for previously documented OMEs greatly expand the available data on the fuel properties of extended OMEs. The Indicated CetaneNumber, a crucial measure for CI fuels, is tested, and it is shown that for US and EU compatibility (ICN>51 for EU), all OMEs other than M-1-M and iP-1-iP are acceptable. Further, B-n-B is shown to have ICN independent of *n*, a useful characteristic which should improve ignition uniformity across various blend ratios. A blend study of B-1-B in diesel shows that B-1-B follows a known trend wherein ether blending has a nonlinear effect on ICN with respect to blend ratio, suppressing ICN to slightly (<5%) below a linear prediction. As is expected of oxygenated fuels, all OMEs showed reduced LHV compared to diesel, with the lower oxygen content OMEs performing the best. The flash point ofOMEs is most strongly linked to molecular weight; many lighter OMEs have FP too low for safe diesel use, however, heavier alkyl groups and longer chain lengths improve flash point to safe levels

for diesel use. The density and viscosity of OMEs followed the general trend of lower viscosity and higher density than diesel; the lower viscosity can promote droplet breakup in sprays and the higher density can offset slightly the lower LHVs of OMEs. No apparent trend in oxidative stability is seen for end groups, however, longer end groups tend to promote higher autoxidative stability. One of the largest differences between various alkyl groups arises in the water solubility. M-n-M OMEs have a significant weakness in their very high water solubility, here is is determined to be on the order of 300-500g/L depending on *n*; extending the alkyl groups produces order-of-magnitude reductions with each extension of alkyl group, to the point where B-n-B has water solubility approximately 0.2-0.3 g/L, of the same order of magnitude to diesel (about 0.1 g/L). This could have significant impacts on environmental effects due to the improved ability to isolate and clean up spills, compared to M-n-M. Another known weakness of OMEs is their high absorption into common elastomers and polymers, which could have deleterious effects on engine and fuel sealing systems. Tests with *n*=1 OMEs show that silicone is equally affected by OMEs with various end groups, while nitrile rubber shows somewhat reduced absorption with longer end groups, and FKM ("Viton") showed significant decrease in absorption with longer end groups. Polyether-ether-ketone, a common hard polymer for valve seats, was shown to be entirely resistant to OME absorption or surface degradation. Nitrile appears to leach into OMEs, causing discoloration in all tests.

The overall conclusion of the sooting tendency work is that methyl-terminated POMEs have remarkably low propensities to form soot and that this attribute is preserved even after end-group exchange to improve other fuel properties. Some more specific conclusions:

- The yield sooting index (YSI) approach can measure quantitative sooting tendencies for the full range of individual POMEs, including the extremely low soot MnM compounds, and can compare them to conventional diesel fuel.
- The YSIs of the MnM compounds are extremely low, and in some cases, they are even negative because the dilution of the base methane fuel by their product formaldehyde molecules outweighs any positive contribution they make to soot formation.
- Butyl end-group exchange increases the sooting tendency, but it is still much less than diesel, such that the tradeoff in soot may be worthwhile to get improved water solubility and heat of combustion.
- End-group exchange with alternative alcohols such as isobutyl alcohol, fusel alcohol, and tetrahydrofurfuryl alcohol also produce POME mixtures with better soot properties than conventional diesel fuels.
- The sooting tendencies of the alkyl-terminated POMEs follow clear trends with structure: the YSI decreases as the number of oxymethylene units increases, and the YSI increases as the alkyl end-groups become longer.
- The sooting tendencies of POMEs blended with conventional diesel fuel follow linear blending rules, so the POMEs improve the sooting behavior of the final blend.
- The composition and morphology of soot particles are similar for conventional diesel fuel and diesel/POME blends.

For external verification of the applicability of the chosen blend, 30 vol% of a 200°C-300°C distillation cut of B-n-B (approximately B-(2-4)-B) in cert diesel was sent to an external laboratory (FOI Laboratories, Vancouver, WA) to be tested with a battery of tests for ASTM D975 compliance. It is shown that this blend meets all ASTM D975 standards except for lubricity, where the lubricity is lower than required. A sample of this fuel blend was left in a flask for six months and shown to be fully miscible, with no apparent phase separation.

Engine testing of heavier, butyl- and propyl-terminated OMEs in a Deere Tier 3 4.5L CI engine indicate good drop-in operability of these fuels, with the engine performing at similar efficiency to diesel with no changes to the engine maps. Combustion timing was similar between diesel and OMEs, with comparable CA10 and CA50 timing, and the CA90 timing dependent on LHV. Fuel consumption naturally increased with the lower LHV of OMEs and OME blends, but lower CO emissions indicated superior combustion efficiency. PM2.5 emissions were significantly reduced compared to diesel for all OME blends, and the typical PM/NOx tradeoff was broken, where the PM emissions decrease (as a %) was significantly stronger than the NOx increase.

Fundamental combustion tests were performed for a subset of the OMEs in a rapid compression machine. E-1-E, E-2-E, P-1-P, and iP-1-iP were tested in highly dilute conditions (12:1 inert:O2, selected for consistently with past dilute OME literature), where it was shown that the three linearOMEs had qualitatively similar ignition behavior, at similar orders of magnitude to n-heptane, but without NTC. Instead, they showed regions of decreased dependence of ignition delay on temperature, verging on complete temperature independence. The three linearOMEs also demonstrated first stage ignition behavior, consistent with literature on E-1-E. In this test, iP-1-iP was unable to ignite in the measured duration (400 ms) at the 20 bar target pressure; increase to 30 bar provided high-temperature ignition at similar IDT to P-1-P at 20 bar. Comparison with a simulation of isooctane at similar conditions indicated lower reactivity than isooctane. This, combined with an exceptionally low ICN of 11, led to an investigation of iP-1-iP at several conditions to probe its potential applicability as a SI fuel. An autoignition sweep at more enginerelevant conditions (5:1 inert ratio, approximately equivalent to 25% EGR) of iP-1-iP and iC8 indicates that at these conditions, iP-1-iP has 5-10x shorter IDT than iC8. Blending with iPrOH, a necessary step in the synthesis, was able to match iC8 ignition. The NTC behavior and low reactivity relative to other OMEs is postulated to arise from low probability of O2 addition to the αC of the alkyl group, leading to RO2 cascading only from the central carbon on the oxymethylene group.

Detailed chemical kinetics models were developed for 5 prototypical POMEs (M1M, M2M, M3M, E1E, and P1P) using a combination of highly accurate first-principles based theoretical rate calculations and benchmarking through a combination of literature and new fundamental microreactor experiments to detect direct products of POME dissociation. The resultant detailed chemical kinetics models provided insight as to how POMEs react and laid the foundation for the development of mechanisms rapidly via direct analogy and rate rules for alternative POMEs with higher direct use potential such as E2E. The following conclusions were reached regarding the combustion of POMEs.

- The theoretical reaction models developed in this work were capable of reproducing the experimental results of several different studies without modification, providing significant confidence in the accuracy of the models across a wide range of operating conditions.

- The role of carbenes as an intermediate for M1M combustion as suggested in prior works was dismissed as unimportant, though it was observed that with the increase in POME chain length via monomer number increase or end group chain length, carbenes do play a more significant role. This solved a longstanding debate in the literature regarding POME kinetics.
- Both through unimolecular dissociation and abstraction, the reactive radicals for POMEs tend to form formates, which have combustion properties that can be similar to diesel. The propensity for nearly all POME combustion to go through formates explains why these fuels are particularly compatible in diesel blends.
- Both formates and the methoxy-like products formed in POME combustion form small C-O based molecules upon subsequent combustion. As a result, flames with POMEs are quickly diluted with low-sooting intermediate species, reducing the combinatorial likelihood of PAHs being formed.
- Well-skipping reactions via the combination of POME abstraction radicals (having lost a single H-atom) with flame radicals (such as H-atom itself) were shown to be important (up to 50% of radical consumption for some POMEs) and can influence the intermediate product distributions in flames. These previously not considered reactions increased the overall accuracy and reliability of the kinetic models.
- Lastly, the foundational kinetics from the 5 prototypical POMEs demonstrated distinct trends in reactivity as modifications were made to POME chain length and end groups. These trends were employed to provide reaction rate estimations for new POMEs outside the 5 prototypical POMEs. A test mechanism using these rules was created for E2E and was shown to reproduce flame speed reaction data well without modification.

The comprehensive techno-economic and life cycle assessment of four pathways for bio-methanol derived M-n-M and bio-butanol derived B-1-B production, benchmarked against conventional fossil-derived diesel, yields valuable insights. Along the way the analysis employes Monte Carlo simulation based on distributions derived from peer-reviewed publications to reveal a clear picture of feedstock price. Production cost assessments underscore the competitiveness of M-n-M and B-1-B with fossil diesel under optimistic assumptions, emphasizing the pivotal impact of feedstock costs. Environmental assessments stress the need to consider feedstock carbon intensities and the implications of land use change in butanol production. While M-n-M emerges as a more viable e-fuel, B-1-B demonstrates competitiveness and superior properties. Both, however, are only competitive with fossil diesel under optimistic assumptions.

8.2. Limitations and Future Applications

This work has several limitations, which may lead to potential areas of future work for extension of the study here. The limitations arise primarily as a result of the broad-based nature of this study, which probes a large number of fuel-relevant properties and behaviors of OMEs, but does not drill down into the deep detail of any one particular behavior. In particular, chemical kinetics is an area where significant work could be done, both for synthesis and for combustion. It is shown here that OMEs can be produced for laboratory-scale property and engine testing using reasonably simple equipment and inexpensive catalysts and reactants, however, the focus of synthesis lay in supporting the property and combustion characterization, leaving an opening for future work investigating the detailed kinetics of different

catalysts, reactant combinations, and model types to account for various inhomogeneities. Similarly, while much fundamental combustion studies provided some data to collaborators at CU Boulder, the actual quantum chemistry calculations required to model these new fuels and their reactions is well outside the scope of this work and requires specific skills which would be best left to a future studies dedicated to these calculations. Additionally, the laboratory-scale nature of the work presented here does not necessarily reflect how industrial production or use of OMEs would occur, e.g. removal of formaldehyde from equilibrium products is not likely to be performed via hand-mixing of a buffer solution and subsequent phase separation in a funnel. Pilot-scale models of real systems would more accurately demonstrate the potential industrial feasibility.

In addition to the possible work described above to rectify some of the limitations of this work, new work to build upon this study could encompass a number of options, but of particular interest is continuing the fundamental combustion studies to work with more OME molecules. B-1-B, for example, was excluded from the RCM studies due to its low vapor pressure and subsequent risk of condensation in fill lines or on internal RCM surfaces. Higher temperature mixing and improved fill lines could reduce this risk and allow more testing; also flame speeds could be evaluated for more fuels at a wider and higher resolution temperature range. iP-1-iP is on its own not an appropriate gasoline, but it is proposed to be a potential soot-reduction additive for gasoline in lower quantities, or as a sensitivity reducer for higher sensitivity fuels. This could be investigated with various gasoline surrogate blends or pump gasoline samples, and emissions monitoring could be performed to determine the PM reduction effects of low-volume blending. Finally, the TEA/LCA underscores the imperative for ongoing research in feedstock production, particularly focusing on cost-effective butanol and methanol production to enhance the overall viability of these pathways.

One of the major takeaways of this study is that OME selection for fuel blending or direct usage is a balance of various interests, e.g. soot reduction and water solubility reduction work in direct opposition. A blend of 30 vol% B-(2-4)-B in diesel was selected as an ideal legacy compatible mixture, as discussed above, but for other interests there may be better selections.

M-n-M has been studied throughout the literature for soot reduction; here we show that this remains the best choice for this purpose. OMEs with larger alkyl groups still show reductions in soot per energy with respect to diesel, but M-n-M effectively eliminates all soot production if used neat. If using M-n-M in an engine, however, care must be taken to use longer oligomers, as M-1-M and M-2-M pose handling risks due to low flash point and low cetane number; additionally, significant spill mitigation efforts must be made due to the very high-water solubility and subsequent difficulty of spill containment. Ethyl-terminated OMEs show some improvement over methyl-terminated, but generally are not ideal for many purposes. While there is some flash point and cetane number increase, water solubility remains high, flash point of shorter chains remains low, and generally all properties are not optimized for either diesel or SI use. Propyl-terminated OMEs may be of some value as jet fuel additives if oxygenates are permitted, as their moderate molecular weights place P-n-P in the light kerosene range, and while still too volatile for current diesel standards, better LHV and low water solubility would support their use in targeted applications. B-n-B remains the best selection for legacy compatibility due to its higher LHV, low water solubility, stable ICN across chain length, and low volatility and molecular weights in the diesel range. In summary:

• For best soot reduction: M-n-M

• For best legacy diesel engine compatibility: B-n-B

• For mobile applications where fuel capacity is a concern: B-n-B with a preference for lower *n*

• For lowest spill containment risk: B-n-B

• For spark ignition usage: iP-1-iP, but in limited quantity as a blendstock or in tandem with an octane booster, e.g. iPrOH

OMEs have many potential fuel applications, when selected and matched to the engine correctly. Future studies may expand on engine performance, emissions reduction, or other engine-relevant considerations as industry broadens its alternative fuels catalog. Growth of renewable fuels such as methanol and/or DME coupled with further development on industry scale OME production may eventually permit production of OMEs onboard or near refueling locations (e.g., at port for shipping applications) from a single renewable methanol or DME feedstock. Further work on dual fuel combustion (e.g., methanol or DME + OMEs) with legacy diesel engines and pilot scale/demonstrated production will be critical to enabling such applications.

Publications

List of Journal Publications

1. Lucas, S.P., Zdanowicz, A.J., Wolff, W.W. and Windom, B.C., 2024. Combustion characteristics of diisopropoxymethane, a low-reactivity oxymethylene ether. Fuel, 362, p.130727.
2. Lucas, S.P., Labbe, N.J., Marchese, A.J. and Windom, B., 2023. Pre-vaporized ignition behavior of ethyl-and propyl-terminated oxymethylene ethers. Proceedings of the Combustion Institute, 39(1), pp.765-774.
3. Lucas, S.P., Chan, F.L., Fioroni, G.M., Foust, T.D., Gilbert, A., Luecke, J., McEnally, C.S., Serdoncillo, J.J.A., Zdanowicz, A.J., Zhu, J. and Windom, B., 2022. Fuel Properties of Oxymethylene Ethers with Terminating Groups from Methyl to Butyl. Energy & Fuels.
4. Bartholet DL, Arellano-Treviño MA, Chan FL, Lucas S, Zhu J, John PC, Alleman TL, McEnally CS, Pfefferle LD, Ruddy DA, Windom B, Foust TL, Reardon, KF. "Property predictions demonstrate that structural diversity can improve the performance of polyoxymethylene ethers as potential bio-based diesel fuels", Fuel. 2021. (IF: 5.578)
5. Arellano-Treviño, Martha A., Frederick G. Baddour, Anh T. To, Teresa L. Alleman, Cameron Hays, Jon Luecke, Junqing Zhu et al. "Diesel fuel properties of renewable polyoxymethylene ethers with structural diversity." Fuel 358 (2024): 130353.
6. Arellano-Treviño, Martha A., Teresa L. Alleman, Rebecca Brim, Anh T. To, Junqing Zhu, Charles S. McEnally, Cameron Hays et al. "Blended fuel property analysis of butyl-exchanged polyoxymethylene ethers as renewable diesel blendstocks." Fuel 322 (2022): 124220.
7. Burton, Jonathan L., Jonathan A. Martin, Gina M. Fioroni, Teresa L. Alleman, Cameron K. Hays, Matthew A. Ratcliff, Michael R. Thorson et al. Fuel Property Effects of a Broad Range of Potential Biofuels on Mixing Control Compression Ignition Engine Performance and Emissions. No. 2021-01-0505. SAE Technical Paper, 2021.
8. Huq, Nabila A., Glenn R. Hafenstine, Xiangchen Huo, Hannah Nguyen, Stephen M. Tifft, Davis R. Conklin, Daniela Stück et al. "Toward net-zero sustainable aviation fuel with wet waste–derived volatile fatty acids." Proceedings of the National Academy of Sciences 118, no. 13 (2021): e2023008118.
9. Arellano-Trevino, Martha A., Danielle Bartholet, Anh The To, Andrew W. Bartling, Frederick G. Baddour, Teresa L. Alleman, Earl D. Christensen et al. "Synthesis of butyl-exchanged polyoxymethylene ethers as renewable diesel blendstocks with improved fuel properties." ACS Sustainable Chemistry & Engineering 9, no. 18 (2021): 6266-6273.
10. Cosimbescu, Lelia, Kristen B. Campbell, Senthil Subramanian, Marie S. Swita, Naijia Hao, Cameron M. Moore, Karthikeyan K. Ramasamy et al. "The properties of bicyclic and multicyclic hydrocarbons as bio-derived compression ignition fuels that can be prepared via efficient and scalable routes from biomass." Sustainable Energy & Fuels 5, no. 12 (2021): 3143-3159.

List of Conference Papers

1. Narayanan, A, Mundy, S, Thothadri, H, Gray, J, Babu, YB, Lucas, S, Windom, B, Srinivasan, KK, & Krishnan, SR. "Propyl Oxymethylene Ether-Ignited Natural Gas Dual Fuel Low Temperature Combustion – a Low Carbon Pathway for High Efficiencies and Low Emissions." Proceedings of the ASME 2023 ICE Forward Conference. ASME 2023 ICE Forward Conference. Pittsburgh, Pennsylvania, USA. October 8–11, 2023. V001T02A011. ASME. https://doi.org/10.1115/ICEF2023-110454.
2. S. Lucas, B. Windom., Rapid compression machine autoignition of diisopropoxymethane for gasoline additive use, Proceedings to 13th US National Combustion Meeting, Texas A&M University, College Station, TX, March 20-22, 2023.

3. A. Zdanowicz, S. Lucas, B. Windom, Compression ignition engine performance of butyl- and propylterminated oxymethylene ethers, Proceedings to 13th US National Combustion Meeting, Texas A&M University, College Station, TX, March 20-22, 2023.
4. Lucas, S., Zdanowicz, Cole, G., Zhu, J., McEnally, C., Labbe, N., Quinn, J., Lueke, J., Fioroni, G., Chan, F., Gilbert, A., Windom, B., Synthesis and characterization of extended-alkyl oxymethylene ethers for compression ignition engine usage. 2022 Spring Meeting of the Eastern States Section of the Combustion Institute, March 6-9, 2022, Orlando, Florida
5. Lucas, S., Gilbert, A., Chan, F., Luecke, J., Zhu, J., McEnally, C., Windom, B., Physical and chemical properties of extended-alkyl oxymethylene ethers for compression ignition fuel use. 2022 Spring Meeting of the Western States Section of the Combustion Institute, March 21-22, Stanford, California.
6. Zhu, Junqing; Chan, Fan Liang; Foust, Thomas D.; Kima, Camille A.; Kwon, Hyunguk; Lucas, Stephen; Windom, B., McEnally. C. (2021): Low sooting tendencies of individual polyoxymethylene ethers as alternative diesel fuels. figshare. Presentation. https://doi.org/10.6084/m9.figshare.14424191.v1
7. Zhu, Junqing; Chan, Fan Liang; Foust, Thomas D.; Lucas, Stephen; Montgomery, Matthew J.; Pfefferle, Lisa D.; et al. (2021): Poly(oxymethylene) ethers: potential diesel fuels with low sooting tendencies. figshare. Conference contribution. https://doi.org/10.6084/m9.figshare.14488908.v1
8. Zhu, Junqing; Chan, Fan Liang; Foust, Thomas D.; Kwon, Hyunguk; Lucas, Stephen; Pfefferle, Lisa D.; et al. (2021): Low Sooting Tendencies and Structure-Property Relationships of Individual Polyoxymethylene Ethers As Alternative Diesel Fuels. figshare. Poster. https://doi.org/10.6084/m9.figshare.17000995.v1
9. Zhu, Junqing; Chan, Fan Liang; Foust, Thomas D.; Lucas, Stephen; Montgomery, Matthew J.; Pfefferle, Lisa D.; Windom, B.; et al. (2021): Poly(oxymethylene) Ethers: Potential Diesel Fuels with Low Sooting Tendencies. figshare. Presentation. https://doi.org/10.6084/m9.figshare.13516859.v1
10. Zhu, J., Chan, F., Foust, T., Reardon, K., Pferrerle, L., McEnally, C., Poly(oxymethylene) Ethers: Potential Diesel Fuels with Low Sooting Tendencies, 2020 AIChE Annual Meeting, 2020.

References

[1] Liu, H., Wang, Z., Zhang, J., Wang, J., and Shuai, S., 2017, "Study on Combustion and Emission Characteristics of Polyoxymethylene Dimethyl Ethers/Diesel Blends in Light-Duty and Heavy-Duty Diesel Engines," Applied Energy, **185**, pp. 1393–1402.

[2] Lautenschütz, L., Oestreich, D., Seidenspinner, P., Arnold, U., Dinjus, E., and Sauer, J., 2016, "Physico-Chemical Properties and Fuel Characteristics of Oxymethylene Dialkyl Ethers," Fuel, **173**, pp. 129–137.

[3] Sun, R., Delidovich, I., and Palkovits, R., 2019, "Dimethoxymethane as a Cleaner Synthetic Fuel: Synthetic Methods, Catalysts, and Reaction Mechanism," ACS Catal., **9**(2), pp. 1298–1318.

[4] Masamoto, J., Ohtake, J., and Kawamura, M., "Process for Producing Formaldehyde and Derivatives Thereof."

[5] Satoh, S., and Tanigawa, Y., "Process for Producing Methylal."

[6] Oestreich, D., Lautenschütz, L., Arnold, U., and Sauer, J., 2017, "Reaction Kinetics and Equilibrium Parameters for the Production of Oxymethylene Dimethyl Ethers (OME) from Methanol and Formaldehyde," Chemical Engineering Science, **163**, pp. 92–104.

[7] Thavornprasert, K., Capron, M., Jalowiecki-Duhamel, L., and Dumeignil, F., 2016, "One-Pot 1,1-Dimethoxymethane Synthesis from Methanol: A Promising Pathway over Bifunctional Catalysts," Catal. Sci. Technol., **6**(4), pp. 958–970.

[8] Baranowski, C. J., Bahmanpour, A. M., and Kröcher, O., 2017, "Catalytic Synthesis of Polyoxymethylene Dimethyl Ethers (OME): A Review," Applied Catalysis B: Environmental, **217**, pp. 407–420.

[9] Lautenschütz, L., Oestreich, D., Seidenspinner, P., Arnold, U., Dinjus, E., and Sauer, J., 2016, "Physico-Chemical Properties and Fuel Characteristics of Oxymethylene Dialkyl Ethers," Fuel, **173**, pp. 129–137.

[10] Drexler, M., Haltenort, P., Zevaco, T. A., Arnold, U., and Sauer, J., 2021, "Synthesis of Tailored Oxymethylene Ether (OME) Fuels *via* Transacetalization Reactions," Sustainable Energy Fuels, **5**(17), pp. 4311–4326.

[11] He, G., Dai, F., Shi, M., Li, Q., and Yu, Y., 2018, "Hydrolysis of Methylal Catalyzed by Ion Exchange Resins in Aqueous Media," Russ. J. Phys. Chem., **92**(5), pp. 889–895.

[12] Hazra, M. K., Francisco, J. S., and Sinha, A., 2013, "Gas Phase Hydrolysis of Formaldehyde To Form Methanediol: Impact of Formic Acid Catalysis," J. Phys. Chem. A, **117**(46), pp. 11704–11710.

[13] Bartholet, D. L., Arellano-Treviño, M. A., Chan, F. L., Lucas, S., Zhu, J., St. John, P. C., Alleman, T. L., McEnally, C. S., Pfefferle, L. D., Ruddy, D. A., Windom, B., Foust, T. D., and Reardon, K. F., 2021, "Property Predictions Demonstrate That Structural Diversity Can Improve the Performance of Polyoxymethylene Ethers as Potential Bio-Based Diesel Fuels," Fuel, **295**, p. 120509.

[14] Ortiz, M. I., and Irabien, A., 1987, "Kinetic Analysis of Liquid-Phase Depolymerization of Trioxane from Programmed Temperature Data: II. Sequential Kinetic Analysis," Journal of Thermal Analysis, **32**(5), pp. 1333–1344.

[15] Kluschke, P., Gnann, T., Plötz, P., and Wietschel, M., 2019, "Market Diffusion of Alternative Fuels and Powertrains in Heavy-Duty Vehicles: A Literature Review," Energy Reports, **5**, pp. 1010–1024.

[16] Osman, A. I., Mehta, N., Elgarahy, A. M., Al-Hinai, A., Al-Muhtaseb, A. H., and Rooney, D. W., 2021, "Conversion of Biomass to Biofuels and Life Cycle Assessment: A Review," Environ Chem Lett, **19**(6), pp. 4075–4118.

[17] Ibrahim, M. F., Kim, S. W., and Abd-Aziz, S., 2018, "Advanced Bioprocessing Strategies for Biobutanol Production from Biomass," Renewable and Sustainable Energy Reviews, **91**, pp. 1192–1204.

[18] Pugazhendhi, A., Mathimani, T., Varjani, S., Rene, E. R., Kumar, G., Kim, S.-H., Ponnusamy, V. K., and Yoon, J.-J., 2019, "Biobutanol as a Promising Liquid Fuel for the Future - Recent Updates and Perspectives," Fuel, **253**, pp. 637–646.
[19] Parra, D., Izquierdo, J. F., Cunill, F., Tejero, J., Fité, C., Iborra, M., and Vila, M., 1998, "Catalytic Activity and Deactivation of Acidic Ion-Exchange Resins in Methyl *Tert* -Butyl Ether Liquid-Phase Synthesis," Ind. Eng. Chem. Res., **37**(9), pp. 3575–3581.
[20] Argyle, M., and Bartholomew, C., 2015, "Heterogeneous Catalyst Deactivation and Regeneration: A Review," Catalysts, **5**(1), pp. 145–269.
[21] Scanlon, J. T., and Willis, D. E., 1985, "Calculation of Flame Ionization Detector Relative Response Factors Using the Effective Carbon Number Concept," Journal of Chromatographic Science, **23**(8), pp. 333–340.
[22] Mcenally, C., and Pfefferle, L., 2007, "Improved Sooting Tendency Measurements for Aromatic Hydrocarbons and Their Implications for Naphthalene Formation Pathways," Combustion and Flame, **148**(4), pp. 210–222.
[23] 2022, "ASTM D1322: Standard Test Method for Smoke Point of Kerosene and Aviation Turbine Fuel."
[24] Cai, G.-Q., and Zhang, L.-Z., 2022, "Systematic Diesel Molecular Performance Evaluation Based on Quantitative Structure-Property Relationship Model," Petroleum Science, **19**(2), pp. 809–818.
[25] Fleitmann, L., Ackermann, P., Schilling, J., Kleinekorte, J., Rittig, J. G., Vom Lehn, F., Schweidtmann, A. M., Pitsch, H., Leonhard, K., Mitsos, A., Bardow, A., and Dahmen, M., 2023, "Molecular Design of Fuels for Maximum Spark-Ignition Engine Efficiency by Combining Predictive Thermodynamics and Machine Learning," Energy Fuels, **37**(3), pp. 2213–2229.
[26] Li, R., Herreros, J. M., Tsolakis, A., and Yang, W., 2022, "Integrated Machine Learning-Quantitative Structure Property Relationship (ML-QSPR) and Chemical Kinetics for High Throughput Fuel Screening toward Internal Combustion Engine," Fuel, **307**, p. 121908.
[27] 2023, "Validation of the New PM Index Formula: Phase 2. CRC Report No. RW-107-3a."
[28] Tan, Y. R., Botero, M. L., Sheng, Y., Dreyer, J. A. H., Xu, R., Yang, W., and Kraft, M., 2018, "Sooting Characteristics of Polyoxymethylene Dimethyl Ether Blends with Diesel in a Diffusion Flame," Fuel, **224**, pp. 499–506.
[29] Kwon, H., Lapointe, S., Zhang, K., Wagnon, S. W., Pitz, W. J., Zhu, J., McEnally, C. S., Pfefferle, L. D., and Xuan, Y., 2020, "Sooting Tendencies of 20 Bio-Derived Fuels for Advanced Spark-Ignition Engines," Fuel, **276**, p. 118059.
[30] McEnally, C. S., Xuan, Y., St. John, P. C., Das, D. D., Jain, A., Kim, S., Kwan, T. A., Tan, L. K., Zhu, J., and Pfefferle, L. D., 2019, "Sooting Tendencies of Co-Optima Test Gasolines and Their Surrogates," Proceedings of the Combustion Institute, **37**(1), pp. 961–968.
[31] Arellano-Treviño, M. A., Bartholet, D., To, A. T., Bartling, A. W., Baddour, F. G., Alleman, T. L., Christensen, E. D., Fioroni, G. M., Hays, C., Luecke, J., Zhu, J., McEnally, C. S., Pfefferle, L. D., Reardon, K. F., Foust, T. D., and Ruddy, D. A., 2021, "Synthesis of Butyl-Exchanged Polyoxymethylene Ethers as Renewable Diesel Blendstocks with Improved Fuel Properties," ACS Sustainable Chem. Eng., **9**(18), pp. 6266–6273.
[32] Mueller, C. J., Cannella, W. J., Bays, J. T., Bruno, T. J., DeFabio, K., Dettman, H. D., Gieleciak, R. M., Huber, M. L., Kweon, C.-B., McConnell, S. S., Pitz, W. J., and Ratcliff, M. A., 2016, "Diesel Surrogate Fuels for Engine Testing and Chemical-Kinetic Modeling: Compositions and Properties," Energy Fuels, **30**(2), pp. 1445–1461.
[33] Das, D. D., St. John, P. C., McEnally, C. S., Kim, S., and Pfefferle, L. D., 2018, "Measuring and Predicting Sooting Tendencies of Oxygenates, Alkanes, Alkenes, Cycloalkanes, and Aromatics on a Unified Scale," Combustion and Flame, **190**, pp. 349–364.

[34] Arellano-Treviño, M. A., Baddour, F. G., To, A. T., Alleman, T. L., Hays, C., Luecke, J., Zhu, J., McEnally, C. S., Pfefferle, L. D., Foust, T. D., and Ruddy, D. A., 2024, "Diesel Fuel Properties of Renewable Polyoxymethylene Ethers with Structural Diversity," Fuel, **358**, p. 130353.
[35] Cosimbescu, L., Campbell, K. B., Subramanian, S., Swita, M. S., Hao, N., Moore, C. M., Ramasamy, K. K., Sutton, A. D., McEnally, C. S., Pfefferle, L. D., and Zhu, J., 2021, "The Properties of Bicyclic and Multicyclic Hydrocarbons as Bio-Derived Compression Ignition Fuels That Can Be Prepared *via* Efficient and Scalable Routes from Biomass," Sustainable Energy Fuels, **5**(12), pp. 3143–3159.
[36] Huq, N. A., Hafenstine, G. R., Huo, X., Nguyen, H., Tifft, S. M., Conklin, D. R., Stück, D., Stunkel, J., Yang, Z., Heyne, J. S., Wiatrowski, M. R., Zhang, Y., Tao, L., Zhu, J., McEnally, C. S., Christensen, E. D., Hays, C., Van Allsburg, K. M., Unocic, K. A., Meyer, H. M., Abdullah, Z., and Vardon, D. R., 2021, "Toward Net-Zero Sustainable Aviation Fuel with Wet Waste–Derived Volatile Fatty Acids," Proc. Natl. Acad. Sci. U.S.A., **118**(13), p. e2023008118.
[37] Kessler, T., St. John, P. C., Zhu, J., McEnally, C. S., Pfefferle, L. D., and Mack, J. H., 2021, "A Comparison of Computational Models for Predicting Yield Sooting Index," Proceedings of the Combustion Institute, **38**(1), pp. 1385–1393.
[38] 2018, "ASTM D8183-18 Standard Test Method for Determination of Indicated Cetane Number (ICN) of Diesel Fuel Oils Using a COnstant VOlume Combustion Chamber - Reference Fuels Calibration Method."
[39] Abel, R. C., Luecke, J., Ratcliff, M. A., and Zigler, B. T., 2020, "Comparing Cetane Number Measurement Methods," *ASME 2020 Internal Combustion Engine Division Fall Technical Conference*, American Society of Mechanical Engineers, Virtual, Online, p. V001T02A009.
[40] Kröger, L. C., Döntgen, M., Firaha, D., Kopp, W. A., and Leonhard, K., 2019, "Ab Initio Kinetics Predictions for H-Atom Abstraction from Diethoxymethane by Hydrogen, Methyl, and Ethyl Radicals and the Subsequent Unimolecular Reactions," Proceedings of the Combustion Institute, **37**(1), pp. 275–282.
[41] Jacobs, S., Döntgen, M., Alquaity, A. B. S., Hesse, R., Kruse, S., Beeckmann, J., Kröger, L. C., Morsch, P., Leonhard, K., Pitsch, H., and Heufer, K. A., 2021, "A Comprehensive Experimental and Kinetic Modeling Study of the Combustion Chemistry of Diethoxymethane," Energy Fuels, **35**(19), pp. 16086–16100.
[42] Yanowitz, J., Ratcliff, M. A., McCormick, R. L., Taylor, J. D., and Murphy, M. J., 2017, *Compendium of Experimental Cetane Numbers*, NREL/TP--5400-67585, 1345058.
[43] Sung, C.-J., and Curran, H. J., 2014, "Using Rapid Compression Machines for Chemical Kinetics Studies," Progress in Energy and Combustion Science, **44**, pp. 1–18.
[44] Goldsborough, S. S., Hochgreb, S., Vanhove, G., Wooldridge, M. S., Curran, H. J., and Sung, C.-J., 2017, "Advances in Rapid Compression Machine Studies of Low- and Intermediate-Temperature Autoignition Phenomena," Progress in Energy and Combustion Science, **63**, pp. 1–78.
[45] Sun, W., Wang, G., Li, S., Zhang, R., Yang, B., Yang, J., Li, Y., Westbrook, C. K., and Law, C. K., 2017, "Speciation and the Laminar Burning Velocities of Poly(Oxymethylene) Dimethyl Ether 3 (POMDME3) Flames: An Experimental and Modeling Study," Proceedings of the Combustion Institute, **36**(1), pp. 1269–1278.
[46] Hanson, R. K., and Davidson, D. F., 2014, "Recent Advances in Laser Absorption and Shock Tube Methods for Studies of Combustion Chemistry," Progress in Energy and Combustion Science, **44**, pp. 103–114.
[47] Mittal, G., Chaos, M., Sung, C.-J., and Dryer, F. L., 2008, "Dimethyl Ether Autoignition in a Rapid Compression Machine: Experiments and Chemical Kinetic Modeling," Fuel Processing Technology, **89**(12), pp. 1244–1254.
[48] Phuoc, T. X., 2006, "Laser-Induced Spark Ignition Fundamental and Applications," Optics and Lasers in Engineering, **44**(5), pp. 351–397.

[49] Morsy, M. H., 2012, “Review and Recent Developments of Laser Ignition for Internal Combustion Engines Applications,” Renewable and Sustainable Energy Reviews, **16**(7), pp. 4849–4875.
[50] Mehl, M., Pitz, W. J., Westbrook, C. K., and Curran, H. J., 2011, “Kinetic Modeling of Gasoline Surrogate Components and Mixtures under Engine Conditions,” Proceedings of the Combustion Institute, **33**(1), pp. 193–200.
[51] Li, N., Sun, W., Liu, S., Qin, X., Zhao, Y., Wei, Y., and Zhang, Y., 2021, “A Comprehensive Experimental and Kinetic Modeling Study of Dimethoxymethane Combustion,” Combustion and Flame, **233**, p. 111583.
[52] Gao, C. W., Allen, J. W., Green, W. H., and West, R. H., 2016, “Reaction Mechanism Generator: Automatic Construction of Chemical Kinetic Mechanisms,” Computer Physics Communications, **203**, pp. 212–225.
[53] Zhang, P., Zsély, I. Gy., Samu, V., Nagy, T., and Turányi, T., 2021, “Comparison of Methane Combustion Mechanisms Using Shock Tube and Rapid Compression Machine Ignition Delay Time Measurements,” Energy Fuels, **35**(15), pp. 12329–12351.
[54] Wang, S., Davidson, D. F., and Hanson, R. K., 2019, “Shock Tube Techniques for Kinetic Target Data to Improve Reaction Models,” *Computer Aided Chemical Engineering*, Elsevier, pp. 169–202.
[55] Lehrheuer, B., Hoppe, F., Heufer, K. A., Jacobs, S., Minwegen, H., Klankermayer, J., Heuser, B., and Pischinger, S., 2019, “Diethoxymethane as Tailor-Made Fuel for Gasoline Controlled Autoignition,” Proceedings of the Combustion Institute, **37**(4), pp. 4691–4698.
[56] Li, R., Herreros, J. M., Tsolakis, A., and Yang, W., 2021, “Chemical Kinetic Modeling of Diethoxymethane Oxidation: A Carbon–Neutral Fuel,” Fuel, **291**, p. 120217.
[57] Zhang, C., He, J., Li, Y., Li, X., and Li, P., 2015, “Ignition Delay Times and Chemical Kinetics of Diethoxymethane/O 2 /Ar Mixtures,” Fuel, **154**, pp. 346–351.
[58] John, P. St., Yanfei Guan, Yeonjoon Kim, Kim, S., and Paton, R., 2019, “BDE-Db: A Collection of 290,664 Homolytic Bond Dissociation Enthalpies for Small Organic Molecules,” p. 32546342 Bytes.
[59] St. John, P. C., Guan, Y., Kim, Y., Etz, B. D., Kim, S., and Paton, R. S., 2020, “Quantum Chemical Calculations for over 200,000 Organic Radical Species and 40,000 Associated Closed-Shell Molecules,” Sci Data, **7**(1), p. 244.
[60] De Ras, K., Kusenberg, M., Thybaut, J. W., and Van Geem, K. M., 2023, “Unraveling the Carbene Chemistry of Oxymethylene Ethers: Experimental Investigation and Kinetic Modeling of the High-Temperature Pyrolysis of OME-2,” Proceedings of the Combustion Institute, **39**(1), pp. 125–133.
[61] Cai, L., Jacobs, S., Langer, R., Vom Lehn, F., Heufer, K. A., and Pitsch, H., 2020, “Auto-Ignition of Oxymethylene Ethers (OMEn, n = 2–4) as Promising Synthetic e-Fuels from Renewable Electricity: Shock Tube Experiments and Automatic Mechanism Generation,” Fuel, **264**, p. 116711.
[62] Würmel, J., Silke, E. J., Curran, H. J., Ó Conaire, M. S., and Simmie, J. M., 2007, “The Effect of Diluent Gases on Ignition Delay Times in the Shock Tube and in the Rapid Compression Machine,” Combustion and Flame, **151**(1–2), pp. 289–302.
[63] Ezzell, J., Wilson, D., and Allen, C., 2019, “On the Influence of Initial Conditions and Facility Effects on Rapid Compression Machine Data,” Fuel, **245**, pp. 368–383.
[64] De Ras, K., Kusenberg, M., Vanhove, G., Fenard, Y., Eschenbacher, A., Varghese, R. J., Aerssens, J., Van De Vijver, R., Tran, L.-S., Thybaut, J. W., and Van Geem, K. M., 2022, “A Detailed Experimental and Kinetic Modeling Study on Pyrolysis and Oxidation of Oxymethylene Ether-2 (OME-2),” Combustion and Flame, **238**, p. 111914.
[65] Li, R., Herreros, J. M., Tsolakis, A., and Yang, W., 2021, “Chemical Kinetic Modeling of Diethoxymethane Oxidation: A Carbon–Neutral Fuel,” Fuel, **291**, p. 120217.
[66] Jacobs, S., Döntgen, M., Alquaity, A. B. S., Hesse, R., Kruse, S., Beeckmann, J., Kröger, L. C., Morsch, P., Leonhard, K., Pitsch, H., and Heufer, K. A., 2021, “A Comprehensive Experimental and

Kinetic Modeling Study of the Combustion Chemistry of Diethoxymethane," Energy Fuels, **35**(19), pp. 16086–16100.
[67] Mehl, M., Pitz, W. J., Westbrook, C. K., and Curran, H. J., 2011, "Kinetic Modeling of Gasoline Surrogate Components and Mixtures under Engine Conditions," Proceedings of the Combustion Institute, **33**(1), pp. 193–200.
[68] Cai, L., Jacobs, S., Langer, R., Vom Lehn, F., Heufer, K. A., and Pitsch, H., 2020, "Auto-Ignition of Oxymethylene Ethers (OMEn, n = 2–4) as Promising Synthetic e-Fuels from Renewable Electricity: Shock Tube Experiments and Automatic Mechanism Generation," Fuel, **264**, p. 116711.
[69] Mehl, M., Curran, H. J., Pitz, W. J., and Westbrook, C. K., 2009, "Chemical Kinetic Modeling of Component Mixtures Relevant to Gasoline."
[70] Li, R., Herreros, J. M., Tsolakis, A., and Yang, W., 2021, "Chemical Kinetic Modeling of Diethoxymethane Oxidation: A Carbon–Neutral Fuel," Fuel, **291**, p. 120217.
[71] Lehrheuer, B., Hoppe, F., Heufer, K. A., Jacobs, S., Minwegen, H., Klankermayer, J., Heuser, B., and Pischinger, S., 2019, "Diethoxymethane as Tailor-Made Fuel for Gasoline Controlled Autoignition," Proceedings of the Combustion Institute, **37**(4), pp. 4691–4698.
[72] Merchant, S. S., Goldsmith, C. F., Vandeputte, A. G., Burke, M. P., Klippenstein, S. J., and Green, W. H., 2015, "Understanding Low-Temperature First-Stage Ignition Delay: Propane," Combustion and Flame, **162**(10), pp. 3658–3673.
[73] Mendes, J., Zhou, C.-W., and Curran, H. J., 2014, "Rate Constant Calculations of H-Atom Abstraction Reactions from Ethers by $H\dot{O}_2$ Radicals," J. Phys. Chem. A, **118**(8), pp. 1300–1308.
[74] Johnson, M. V., Goldsborough, S. S., Serinyel, Z., O'Toole, P., Larkin, E., O'Malley, G., and Curran, H. J., 2009, "A Shock Tube Study of *n* - and *Iso*- Propanol Ignition," Energy Fuels, **23**(12), pp. 5886–5898.
[75] Guo, X., Zhang, R. M., Gao, L. G., Zhang, X., and Xu, X., 2019, "Computational Kinetics of the Hydrogen Abstraction Reactions of *n* -Propanol and Iso-Propanol by OH Radical," Phys. Chem. Chem. Phys., **21**(44), pp. 24458–24468.
[76] "National Institute of Standards and Technology, Dodecane Phase Change Data, Https://Webbook.Nist.Gov/Cgi/Cbook.Cgi?ID=C112403&Units=SI& Mask=4#Thermo-Phase."
[77] "ASTM International, ASTM D93-20 Standard Test Methods for Flash Point by PenskyMartens Closed Cup Tester, 2020."
[78] "ASTM International, ASTM D7042-21a Standard Test Method for Dynamic Viscosity and Density of Liquids by Stabinger Viscometer (and the Calculation of Kinematic Viscosity), 2021."
[79] "ASTM International, ASTM D6378-20 Standard Test Method for Determination of Vapor Pressure (VPX) of Petroleum Products, Hydrocarbons, and Hydrocarbon-Oxygenate Mixtures (Triple Expansion Method), 2020."
[80] "ASTM International, ASTM D7545-14(2019)E1 Standard Test Method for Oxidation Stability of Middle Distillate Fuels—Rapid Small Scale Oxidation Test (RSSOT), 2019."
[81] "R. Stephenson, J. Stuart, M. Tabak, Mutual Solubility of Water and Aliphatic Alcohols, Journal of Chemical and Engineering Data 29 (3) (1984) 287–290."
[82] "ASTM International, ASTM D1160-18 Standard Test Method for Distillation of Petroleum Products at Reduced Pressure, 2018."
[83] Lopes, S. M., Furey, R., and Geng, P., 2013, "Calculation of Heating Value for Diesel Fuels Containing Biodiesel," SAE Int. J. Fuels Lubr., **6**(2), pp. 407–418.
[84] Gülüm, M., and Bilgin, A., 2015, "Density, Flash Point and Heating Value Variations of Corn Oil Biodiesel–Diesel Fuel Blends," Fuel Processing Technology, **134**, pp. 456–464.
[85] Bezergianni, S., and Dimitriadis, A., 2013, "Comparison between Different Types of Renewable Diesel," Renewable and Sustainable Energy Reviews, **21**, pp. 110–116.

[86] Lautenschütz, L., Oestreich, D., Seidenspinner, P., Arnold, U., Dinjus, E., and Sauer, J., 2016, “Physico-Chemical Properties and Fuel Characteristics of Oxymethylene Dialkyl Ethers,” Fuel, **173**, pp. 129–137.
[87] McAllister, S., Chen, J.-Y., and Fernandez-Pello, A. C., 2011, *Fundamentals of Combustion Processes*, Springer New York, New York, NY.
[88] Drexler, M., Haltenort, P., Zevaco, T. A., Arnold, U., and Sauer, J., 2021, “Synthesis of Tailored Oxymethylene Ether (OME) Fuels *via* Transacetalization Reactions,” Sustainable Energy Fuels, **5**(17), pp. 4311–4326.
[89] Härtl, M., Seidenspinner, P., Jacob, E., and Wachtmeister, G., 2015, “Oxygenate Screening on a Heavy-Duty Diesel Engine and Emission Characteristics of Highly Oxygenated Oxymethylene Ether Fuel OME 1,” Fuel, **153**, pp. 328–335.
[90] Deutsch, D., Oestreich, D., Lautenschütz, L., Haltenort, P., Arnold, U., and Sauer, J., 2017, “High Purity Oligomeric Oxymethylene Ethers as Diesel Fuels,” Chemie Ingenieur Technik, **89**(4), pp. 486–489.
[91] “National Fire Protection Association, NFPA 30 Flammable and Combustible Liquids Code, 2020.”
[92] Lefebvre, A. H., and McDonell, V. G., 2017, *Atomization and Sprays*, CRC Press, Taylor & Francis Group, Boca Raton London New York.
[93] Algayyim, S. J. M., and Wandel, A. P., 2021, “Macroscopic and Microscopic Characteristics of Biofuel Spray (Biodiesel and Alcohols) in CI Engines: A Review,” Fuel, **292**, p. 120303.
[94] Hayashi, J., Watanabe, H., Kurose, R., and Akamatsu, F., 2011, “Effects of Fuel Droplet Size on Soot Formation in Spray Flames Formed in a Laminar Counterflow,” Combustion and Flame, **158**(12), pp. 2559–2568.
[95] Lautenschütz, L., Oestreich, D., Seidenspinner, P., Arnold, U., Dinjus, E., and Sauer, J., 2016, “Physico-Chemical Properties and Fuel Characteristics of Oxymethylene Dialkyl Ethers,” Fuel, **173**, pp. 129–137.
[96] “National Institute of Standards and Technology, Methylal Phase Change Data, Https://Webbook.Nist.Gov/Cgi/Cbook.Cgi?ID=C109875&Units= SI&Mask=4#Thermo-Phase.”
[97] “National Institute of Standards and Technology, Methane, Diethoxy- Phase Change Data, Https://Webbook.Nist.Gov/Cgi/Cbook.Cgi?ID=C462953&Units=SI& Mask=4#Thermo-Phase.”
[98] “National Institute of Standards and Technology, Heptane Phase Change Data, Https://Webbook.Nist.Gov/Cgi/Cbook.Cgi?ID=C142825&Units=SI& Mask=4#Thermo-Phase.”
[99] “National Institute of Standards and Technology, Decane Phase Change Data, Https://Webbook.Nist.Gov/Cgi/Cbook.Cgi?ID=C124185&Units=SI& Mask=4#Thermo-Phase.”
[100] Focke, W. W., Westhuizen, I. V. D., and Oosthuysen, X., 2016, “Biodiesel Oxidative Stability from Rancimat Data,” Thermochimica Acta, **633**, pp. 116–121.
[101] Alves-Fortunato, M., Baroni, A., Neocel, L., Chardin, M., Matrat, M., Boucaud, C., and Mazarin, M., 2021, “Gasoline Oxidation Stability: Deposit Formation Tendencies Evaluated by PetroOxy and Autoclave Methods and GDI/PFI Engine Tests,” Energy Fuels, **35**(22), pp. 18430–18440.
[102] Botella, L., Bimbela, F., MartÃ-n, L., Arauzo, J., and SÃ¡nchez, J. L., 2014, “Oxidation Stability of Biodiesel Fuels and Blends Using the Rancimat and PetroOXY Methods. Effect of 4-Allyl-2,6-Dimethoxyphenol and Catechol as Biodiesel Additives on Oxidation Stability,” Front. Chem., **2**.
[103] Pélerin, D., Gaukel, K., Härtl, M., Jacob, E., and Wachtmeister, G., 2020, “Potentials to Simplify the Engine System Using the Alternative Diesel Fuels Oxymethylene Ether OME1 and OME3−6 on a Heavy-Duty Engine,” Fuel, **259**, p. 116231.
[104] Schröder, J., and Görsch, K., 2020, “Storage Stability and Material Compatibility of Poly(Oxymethylene) Dimethyl Ether Diesel Fuel,” Energy Fuels, **34**(1), pp. 450–459.

[105] Kass, M., Wissink, M., Janke, C., Connatser, R., and Curran, S., 2020, "Compatibility of Elastomers with Polyoxymethylene Dimethyl Ethers and Blends with Diesel," SAE Int. J. Adv. & Curr. Prac. in Mobility, **2**(4), pp. 1963–1973.
[106] Lockwood, K. S., Ahmed, S. F., Huq, N. A., Stutzman, S. C., Foust, T. D., and Labbe, N. J., 2022, "Advances in Predictive Chemistry Enable a Multi-Scale Rational Design Approach for Biofuels with Advantaged Properties," Sustainable Energy Fuels, **6**(23), pp. 5371–5383.
[107] Van De Vijver, R., and Zádor, J., 2020, "KinBot: Automated Stationary Point Search on Potential Energy Surfaces," Computer Physics Communications, **248**, p. 106947.
[108] "'Gaussian 16.' Gaussian, Inc., Wallingford CT, 2016."
[109] Zhao, Y., and Truhlar, D. G., 2008, "The M06 Suite of Density Functionals for Main Group Thermochemistry, Thermochemical Kinetics, Noncovalent Interactions, Excited States, and Transition Elements: Two New Functionals and Systematic Testing of Four M06-Class Functionals and 12 Other Functionals," Theor Chem Account, **120**(1–3), pp. 215–241.
[110] Jacquemin, D., Perpète, E. A., Ciofini, I., Adamo, C., Valero, R., Zhao, Y., and Truhlar, D. G., 2010, "On the Performances of the M06 Family of Density Functionals for Electronic Excitation Energies," J. Chem. Theory Comput., **6**(7), pp. 2071–2085.
[111] Georgievskii, Y., Miller, J. A., Burke, M. P., and Klippenstein, S. J., 2013, "Reformulation and Solution of the Master Equation for Multiple-Well Chemical Reactions," J. Phys. Chem. A, **117**(46), pp. 12146–12154.
[112] Golka, L., Gratzfeld, D., Weber, I., and Olzmann, M., 2020, "Temperature- and Pressure-Dependent Kinetics of the Competing C–O Bond Fission Reactions of Dimethoxymethane," Phys. Chem. Chem. Phys., **22**(10), pp. 5523–5530.
[113] Peukert, S., Sela, P., Nativel, D., Herzler, J., Fikri, M., and Schulz, C., 2018, "Direct Measurement of High-Temperature Rate Constants of the Thermal Decomposition of Dimethoxymethane, a Shock Tube and Modeling Study," J. Phys. Chem. A, **122**(38), pp. 7559–7571.
[114] "CHEMKIN-PRO 15112, Reaction Design: San Diego, 2011."
[115] Pazdera, T. M., Wenz, J., and Olzmann, M., 2022, "The Unimolecular Decomposition of Dimethoxymethane: Channel Switching as a Function of Temperature and Pressure," Faraday Discuss., **238**, pp. 665–681.
[116] Döntgen, M., Fuller, M. E., Peukert, S., Nativel, D., Schulz, C., Alexander Heufer, K., and Franklin Goldsmith, C., 2022, "Shock Tube Study of the Pyrolysis Kinetics of Di- and Trimethoxy Methane," Combustion and Flame, **242**, p. 112186.
[117] Vermeire, F. H., Carstensen, H.-H., Herbinet, O., Battin-Leclerc, F., Marin, G. B., and Van Geem, K. M., 2018, "Experimental and Modeling Study of the Pyrolysis and Combustion of Dimethoxymethane," Combustion and Flame, **190**, pp. 270–283.
[118] Al-Otaibi, J. S., Abdel-Rahman, M. A., Almuqrin, A. H., El-Gogary, T. M., Mahmoud, M. A. M., and El-Nahas, A. M., 2021, "Thermo-Kinetic Theoretical Studies on Pyrolysis of Dimethoxymethane Fuel Additive," Fuel, **290**, p. 119970.
[119] Zhong, X., Wang, H., Zuo, Q., Zheng, Z., Wang, J., Yin, W., and Yao, M., 2021, "Experimental and Kinetic Modeling Studies of Polyoxymethylene Dimethyl Ether (PODE) Pyrolysis in Jet Stirred Reactor," Journal of Analytical and Applied Pyrolysis, **159**, p. 105332.
[120] De Ras, K., Kusenberg, M., Vanhove, G., Fenard, Y., Eschenbacher, A., Varghese, R. J., Aerssens, J., Van De Vijver, R., Tran, L.-S., Thybaut, J. W., and Van Geem, K. M., 2022, "A Detailed Experimental and Kinetic Modeling Study on Pyrolysis and Oxidation of Oxymethylene Ether-2 (OME-2)," Combustion and Flame, **238**, p. 111914.
[121] Carstensen, H.-H., and Dean, A. M., 2007, "Chapter 4 The Kinetics of Pressure-Dependent Reactions," *Comprehensive Chemical Kinetics*, Elsevier, pp. 101–184.

[122] Bartholet, D. L., Arellano-Treviño, M. A., Chan, F. L., Lucas, S., Zhu, J., St. John, P. C., Alleman, T. L., McEnally, C. S., Pfefferle, L. D., Ruddy, D. A., Windom, B., Foust, T. D., and Reardon, K. F., 2021, "Property Predictions Demonstrate That Structural Diversity Can Improve the Performance of Polyoxymethylene Ethers as Potential Bio-Based Diesel Fuels," Fuel, **295**, p. 120509.
[123] Bartholet, D. L., Arellano-Treviño, M. A., Chan, F. L., Lucas, S., Zhu, J., St. John, P. C., Alleman, T. L., McEnally, C. S., Pfefferle, L. D., Ruddy, D. A., Windom, B., Foust, T. D., and Reardon, K. F., 2021, "Property Predictions Demonstrate That Structural Diversity Can Improve the Performance of Polyoxymethylene Ethers as Potential Bio-Based Diesel Fuels," Fuel, **295**, p. 120509.
[124] Herzler, J., Manion, J. A., and Tsang, W., 1997, "Single-Pulse Shock Tube Studies of the Decomposition of Ethoxy Compounds," J. Phys. Chem. A, **101**(30), pp. 5494–5499.
[125] Guan, Q., Urness, K. N., Ormond, T. K., David, D. E., Barney Ellison, G., and Daily, J. W., 2014, "The Properties of a Micro-Reactor for the Study of the Unimolecular Decomposition of Large Molecules," International Reviews in Physical Chemistry, **33**(4), pp. 447–487.
[126] Burton, J. L., Martin, J. A., Fioroni, G. M., Alleman, T. L., Hays, C. K., Ratcliff, M. A., Thorson, M. R., Schmidt, A. J., Hallen, R. T., Hart, T. R., Billing, J. M., Fox, S., Gaspar, D. J., Zhu, J., Kima, C., Pfefferle, L. D., McEnally, C. S., and McCormick, R. L., 2021, "Fuel Property Effects of a Broad Range of Potential Biofuels on Mixing Control Compression Ignition Engine Performance and Emissions," pp. 2021-01–0505.
[127] Fioroni, G., Fouts, L., Luecke, J., Vardon, D., Huq, N., Christensen, E., Huo, X., Alleman, T., McCormick, R., Kass, M., Polikarpov, E., Kukkadapu, G., and Whitesides, R. A., 2019, "Screening of Potential Biomass-Derived Streams as Fuel Blendstocks for Mixing Controlled Compression Ignition Combustion," SAE Int. J. Adv. & Curr. Prac. in Mobility, **1**(3), pp. 1117–1138.
[128] Arellano-Treviño, M. A., Alleman, T. L., Brim, R., To, A. T., Zhu, J., McEnally, C. S., Hays, C., Luecke, J., Pfefferle, L. D., Foust, T. D., and Ruddy, D. A., 2022, "Blended Fuel Property Analysis of Butyl-Exchanged Polyoxymethylene Ethers as Renewable Diesel Blendstocks," Fuel, **322**, p. 124220.
[129] Arellano-Treviño, M. A., Baddour, F. G., To, A. T., Alleman, T. L., Hays, C., Luecke, J., Zhu, J., McEnally, C. S., Pfefferle, L. D., Foust, T. D., and Ruddy, D. A., 2024, "Diesel Fuel Properties of Renewable Polyoxymethylene Ethers with Structural Diversity," Fuel, **358**, p. 130353.
[130] Das, D. D., McEnally, C. S., Kwan, T. A., Zimmerman, J. B., Cannella, W. J., Mueller, C. J., and Pfefferle, L. D., 2017, "Sooting Tendencies of Diesel Fuels, Jet Fuels, and Their Surrogates in Diffusion Flames," Fuel, **197**, pp. 445–458.
[131] Omari, A., Heuser, B., Pischinger, S., and Rüdinger, C., 2019, "Potential of Long-Chain Oxymethylene Ether and Oxymethylene Ether-Diesel Blends for Ultra-Low Emission Engines," Applied Energy, **239**, pp. 1242–1249.
[132] "ASTM International, ASTM D975-21 Standard Specification for Diesel Fuel, 2021."
[133] Gelner, A. D., Beck, H. A., Pastoetter, C., Härtl, M., and Wachtmeister, G., 2022, "Ultra-Low Emissions of a Heavy-Duty Engine Powered with Oxymethylene Ethers (OME) under Stationary and Transient Driving Conditions," International Journal of Engine Research, **23**(5), pp. 738–753.
[134] Liu, H., Wang, Z., Li, Y., Zheng, Y., He, T., and Wang, J., 2019, "Recent Progress in the Application in Compression Ignition Engines and the Synthesis Technologies of Polyoxymethylene Dimethyl Ethers," Applied Energy, **233–234**, pp. 599–611.
[135] Omari, A., Heuser, B., Pischinger, S., and Rüdinger, C., 2019, "Potential of Long-Chain Oxymethylene Ether and Oxymethylene Ether-Diesel Blends for Ultra-Low Emission Engines," Applied Energy, **239**, pp. 1242–1249.
[136] Lucas, S. P., Chan, F. L., Fioroni, G. M., Foust, T. D., Gilbert, A., Luecke, J., McEnally, C. S., Serdoncillo, J. J. A., Zdanowicz, A. J., Zhu, J., and Windom, B., 2022, "Fuel Properties of Oxymethylene Ethers with Terminating Groups from Methyl to Butyl," Energy Fuels, **36**(17), pp. 10213–10225.

[137] Subramanian, R., Khlystov, A. Y., Cabada, J. C., and Robinson, A. L., 2004, "Positive and Negative Artifacts in Particulate Organic Carbon Measurements with Denuded and Undenuded Sampler Configurations Special Issue of *Aerosol Science and Technology* on Findings from the Fine Particulate Matter Supersites Program," Aerosol Science and Technology, **38**(sup1), pp. 27–48.
[138] Pélerin, D., Gaukel, K., Härtl, M., Jacob, E., and Wachtmeister, G., 2020, "Potentials to Simplify the Engine System Using the Alternative Diesel Fuels Oxymethylene Ether OME1 and OME3−6 on a Heavy-Duty Engine," Fuel, **259**, p. 116231.
[139] Johnson, T. V., 2015, "Review of Vehicular Emissions Trends," SAE Int. J. Engines, **8**(3), pp. 1152–1167.
[140] Burre, J., Bongartz, D., Deutz, S., Mebrahtu, C., Osterthun, O., Sun, R., Völker, S., Bardow, A., Klankermayer, J., Palkovits, R., and Mitsos, A., 2021, "Comparing Pathways for Electricity-Based Production of Dimethoxymethane as a Sustainable Fuel," Energy Environ. Sci., **14**(7), pp. 3686–3699.
[141] Held, M., Tönges, Y., Pélerin, D., Härtl, M., Wachtmeister, G., and Burger, J., 2019, "On the Energetic Efficiency of Producing Polyoxymethylene Dimethyl Ethers from CO_2 Using Electrical Energy," Energy Environ. Sci., **12**(3), pp. 1019–1034.
[142] Lucas, S. P., Labbe, N. J., Marchese, A. J., and Windom, B., 2022, "Pre-Vaporized Ignition Behavior of Ethyl- and Propyl-Terminated Oxymethylene Ethers," Proceedings of the Combustion Institute, p. S1540748922003534.
[143] Martín, M., Redondo, J., and Grossmann, I. E., 2020, "Optimal Integrated Facility for Oxymethylene Ethers Production from Methanol," ACS Sustainable Chem. Eng., **8**(16), pp. 6496–6504.
[144] Oyedun, A. O., Kumar, A., Oestreich, D., Arnold, U., and Sauer, J., 2018, "The Development of the Production Cost of Oxymethylene Ethers as Diesel Additives from Biomass," Biofuels Bioprod Bioref, **12**(4), pp. 694–710.
[145] Zhang, X., Oyedun, A. O., Kumar, A., Oestreich, D., Arnold, U., and Sauer, J., 2016, "An Optimized Process Design for Oxymethylene Ether Production from Woody-Biomass-Derived Syngas," Biomass and Bioenergy, **90**, pp. 7–14.
[146] Rodríguez-Vallejo, D. F., Valente, A., Guillén-Gosálbez, G., and Chachuat, B., 2021, "Economic and Life-Cycle Assessment of $OME_{3–5}$ as Transport Fuel: A Comparison of Production Pathways," Sustainable Energy Fuels, **5**(9), pp. 2504–2516.
[147] Emenike, O., Michailos, S., Hughes, K. J., Ingham, D., and Pourkashanian, M., 2021, "Techno-Economic and Environmental Assessment of BECCS in Fuel Generation for FT-Fuel, bioSNG and OME *x*," Sustainable Energy Fuels, **5**(13), pp. 3382–3402.
[148] Mahbub, N., Oyedun, A. O., Zhang, H., Kumar, A., and Poganietz, W.-R., 2019, "A Life Cycle Sustainability Assessment (LCSA) of Oxymethylene Ether as a Diesel Additive Produced from Forest Biomass," Int J Life Cycle Assess, **24**(5), pp. 881–899.
[149] Mahbub, N., Oyedun, A. O., Kumar, A., Oestreich, D., Arnold, U., and Sauer, J., 2017, "A Life Cycle Assessment of Oxymethylene Ether Synthesis from Biomass-Derived Syngas as a Diesel Additive," Journal of Cleaner Production, **165**, pp. 1249–1262.
[150] Schemme, S., Breuer, J. L., Köller, M., Meschede, S., Walman, F., Samsun, R. C., Peters, R., and Stolten, D., 2020, "H2-Based Synthetic Fuels: A Techno-Economic Comparison of Alcohol, Ether and Hydrocarbon Production," International Journal of Hydrogen Energy, **45**(8), pp. 5395–5414.
[151] Hank, C., Lazar, L., Mantei, F., Ouda, M., White, R. J., Smolinka, T., Schaadt, A., Hebling, C., and Henning, H.-M., 2019, "Comparative Well-to-Wheel Life Cycle Assessment of $OME_{3–5}$ Synfuel Production *via* the Power-to-Liquid Pathway," Sustainable Energy Fuels, **3**(11), pp. 3219–3233.

[152] Weidert, J.-O., Burger, J., Renner, M., Blagov, S., and Hasse, H., 2017, “Development of an Integrated Reaction–Distillation Process for the Production of Methylal,” Ind. Eng. Chem. Res., **56**(2), pp. 575–582.
[153] Schmitz, N., Burger, J., Ströfer, E., and Hasse, H., 2016, “From Methanol to the Oxygenated Diesel Fuel Poly(Oxymethylene) Dimethyl Ether: An Assessment of the Production Costs,” Fuel, **185**, pp. 67–72.
[154] Burger, J., Ströfer, E., and Hasse, H., 2013, “Production Process for Diesel Fuel Components Poly(Oxymethylene) Dimethyl Ethers from Methane-Based Products by Hierarchical Optimization with Varying Model Depth,” Chemical Engineering Research and Design, **91**(12), pp. 2648–2662.
[155] Grützner, T., Hasse, H., Lang, N., Siegert, M., and Ströfer, E., 2007, “Development of a New Industrial Process for Trioxane Production,” Chemical Engineering Science, **62**(18–20), pp. 5613–5620.
[156] Wang, M., Elgowainy, A., Lee, U., Baek, K., Bafana, A., Benavides, P., Burnham, A., Cai, H., Cappello, V., Chen, P., Gan, Y., Gracida-Alvarez, U., Hawkins, T., Iyer, R., Kelly, J., Kim, T., Kumar, S., Kwon, H., Lee, K., Liu, X., Lu, Z., Masum, F., Ng, C., Ou, L., Reddi, K., Siddique, N., Sun, P., Vyawahare, P., Xu, H., and Zaimes, G., 2022, “Greenhouse Gases, Regulated Emissions, and Energy Use in Technologies Model ® (2022 Excel).”
[157] Towler, G. P., and Sinnott, R. K., 2013, *Chemical Engineering Design: Principles, Practice, and Economics of Plant and Process Design*, Butterworth-Heinemann, Oxford.
[158] Tock, L., Gassner, M., and Maréchal, F., 2010, “Thermochemical Production of Liquid Fuels from Biomass: Thermo-Economic Modeling, Process Design and Process Integration Analysis,” Biomass and Bioenergy, **34**(12), pp. 1838–1854.
[159] Sarkar, S., Kumar, A., and Sultana, A., 2011, “Biofuels and Biochemicals Production from Forest Biomass in Western Canada,” Energy, **36**(10), pp. 6251–6262.
[160] Mignard, D., and Pritchard, C., 2008, “On the Use of Electrolytic Hydrogen from Variable Renewable Energies for the Enhanced Conversion of Biomass to Fuels,” Chemical Engineering Research and Design, **86**(5), pp. 473–487.
[161] Huisman, G. H., Van Rens, G. L. M. A., De Lathouder, H., and Cornelissen, R. L., 2011, “Cost Estimation of Biomass-to-Fuel Plants Producing Methanol, Dimethylether or Hydrogen,” Biomass and Bioenergy, **35**, pp. S155–S166.
[162] Andersson, J., Lundgren, J., and Marklund, M., 2014, “Methanol Production via Pressurized Entrained Flow Biomass Gasification – Techno-Economic Comparison of Integrated vs. Stand-Alone Production,” Biomass and Bioenergy, **64**, pp. 256–268.
[163] De Fournas, N., and Wei, M., 2022, “Techno-Economic Assessment of Renewable Methanol from Biomass Gasification and PEM Electrolysis for Decarbonization of the Maritime Sector in California,” Energy Conversion and Management, **257**, p. 115440.
[164] Zhang, Z., Delcroix, B., Rezazgui, O., and Mangin, P., 2021, “Simulation and Techno-Economic Assessment of Bio-Methanol Production from Pine Biomass, Biochar and Pyrolysis Oil,” Sustainable Energy Technologies and Assessments, **44**, p. 101002.
[165] Tao, L., Tan, E. C. D., McCormick, R., Zhang, M., Aden, A., He, X., and Zigler, B. T., 2014, “Techno-economic Analysis and Life-cycle Assessment of Cellulosic Isobutanol and Comparison with Cellulosic Ethanol and N-butanol,” Biofuels Bioprod Bioref, **8**(1), pp. 30–48.
[166] Jang, M.-O., and Choi, G., 2018, “Techno-Economic Analysis of Butanol Production from Lignocellulosic Biomass by Concentrated Acid Pretreatment and Hydrolysis plus Continuous Fermentation,” Biochemical Engineering Journal, **134**, pp. 30–43.

[167] Dalle Ave, G., and Adams, T. A., 2018, "Techno-Economic Comparison of Acetone-Butanol-Ethanol Fermentation Using Various Extractants," Energy Conversion and Management, **156**, pp. 288–300.
[168] Kumar, M., Goyal, Y., Sarkar, A., and Gayen, K., 2012, "Comparative Economic Assessment of ABE Fermentation Based on Cellulosic and Non-Cellulosic Feedstocks," Applied Energy, **93**, pp. 193–204.
[169] Baral, N. R., and Shah, A., 2016, "Techno-Economic Analysis of Cellulosic Butanol Production from Corn Stover through Acetone–Butanol–Ethanol Fermentation," Energy Fuels, **30**(7), pp. 5779–5790.
[170] Mailaram, S., and Maity, S. K., 2022, "Dual Liquid–Liquid Extraction versus Distillation for the Production of Bio-Butanol from Corn, Sugarcane, and Lignocellulose Biomass: A Techno-Economic Analysis Using Pinch Technology," Fuel, **312**, p. 122932.
[171] Meramo-Hurtado, S. I., González-Delgado, Á., Rehmann, L., Quinones-Bolanos, E., and Mehvar, M., 2021, "Comparative Analysis of Biorefinery Designs Based on Acetone-Butanol-Ethanol Fermentation under Exergetic, Techno-Economic, and Sensitivity Analyses towards a Sustainability Perspective," Journal of Cleaner Production, **298**, p. 126761.
[172] Qureshi, N., and Singh, V., 2014, "Process Economics of Renewable Biorefineries," *Biorefineries*, Elsevier, pp. 237–254.
[173] Langholtz, M. H., Stokes, B. J., and Eaton, L. M., 2016, *2016 Billion-Ton Report: Advancing Domestic Resources for a Thriving Bioeconomy*, DOE/EE-1440, ORNL/TM-2016/160, 1271651.
[174] 2019, "Rising Corn Prices and Oversupply Push Ethanol Operating Margins to Multiyear Lows."
[175] Jensen, F., 2020, "INSIGHT: Record Year for Europe Acetone Market Features in Q4 Phenol Talks."
[176] "How to Calculate the True Cost of Steam."
[177] Davis, R., Markham, J., Kinchin, C., Grundl, N., Tan, E. C. D., and Humbird, D., 2016, *Process Design and Economics for the Production of Algal Biomass: Algal Biomass Production in Open Pond Systems and Processing Through Dewatering for Downstream Conversion*, NREL/TP--5100-64772, 1239893.
[178] Cheali, P., Gernaey, K. V., and Sin, G., 2015, "Uncertainties in Early-Stage Capital Cost Estimation of Process Design Â€“ A Case Study on Biorefinery Design," Front. Energy Res., **3**.
[179] Tsagkari, M., Couturier, J., Kokossis, A., and Dubois, J., 2016, "Early-Stage Capital Cost Estimation of Biorefinery Processes: A Comparative Study of Heuristic Techniques," ChemSusChem, **9**(17), pp. 2284–2297.
[180] Schmitz, N., Ströfer, E., Burger, J., and Hasse, H., 2017, "Conceptual Design of a Novel Process for the Production of Poly(Oxymethylene) Dimethyl Ethers from Formaldehyde and Methanol," Ind. Eng. Chem. Res., **56**(40), pp. 11519–11530.
[181] Deutz, S., Bongartz, D., Heuser, B., Kätelhön, A., Schulze Langenhorst, L., Omari, A., Walters, M., Klankermayer, J., Leitner, W., Mitsos, A., Pischinger, S., and Bardow, A., 2018, "Cleaner Production of Cleaner Fuels: Wind-to-Wheel – Environmental Assessment of CO_2 -Based Oxymethylene Ether as a Drop-in Fuel," Energy Environ. Sci., **11**(2), pp. 331–343.
[182] "Butanol Price."
[183] "Methanol Price and Supply/Demand."
[184] Mantei, F., Ali, R. E., Baensch, C., Voelker, S., Haltenort, P., Burger, J., Dietrich, R.-U., Assen, N. V. D., Schaadt, A., Sauer, J., and Salem, O., 2022, "Techno-Economic Assessment and Carbon Footprint of Processes for the Large-Scale Production of Oxymethylene Dimethyl Ethers from Carbon Dioxide and Hydrogen," Sustainable Energy Fuels, **6**(3), pp. 528–549.